CFD modelling of flow-induced vibration under multiphase flow regimes.

ASIEGBU, N.M.

2020

CFD MODELLING OF FLOW INDUCED VIBRATION UNDER MULTIPHASE FLOW REGIMES

NKEMJIKA MIRIAN ASIEGBU

PhD **2020**

CFD Modelling of Flow Induced Vibration under Multiphase Flow Regimes

Nkemjika Mirian Asiegbu

A thesis submitted in partial fulfilment of the
requirements of the
Robert Gordon University
(School of Engineering)
for the award of the degree of

Doctor of Philosophy

March 2020

CFD Modelling of Flow Induced Vibration under Multiphase Flow Regimes

PhD Candidate

Nkemjika Mirian Asiegbu

Supervisory Team

Dr Mamdud Hossain (Principal Supervisor)

Dr Ghazi Droubi

Dr Sheikh Z. Islam

School of Engineering, Robert Gordon University, The Sir Ian Wood Building, Riverside East, Garthdee Road, Aberdeen, AB10 7GJ, United Kingdom.

DEDICATION

To-

My Heavenly Father, Jehovah Omniscience,

my amazing parents- Mr Rapheal Asiegbu and Mrs Ifeyinwa Asiegbu,

and my awesome son- Sean Munachimso Chinenye-Kanu.

ACKNOWLEDGEMENT

My deep appreciation goes to my principal supervisor, Dr Mamdud Hossain for his guidance, support, understanding and patience throughout my PhD study. I am grateful for all the personal and technical skills he has helped me acquire and for believing in me to handle challenges. I would also like to thank my other supervisors, Dr Ghazi Droubi and Dr Sheihk Islam for their guidance and support. I appreciate Neil Barton from XODUS Group for providing me with published results from their JIP on Multiphase Flow Induced Vibration which contributed to the result analysis carried out in the present research.

I thank the entire School of Engineering for providing an enabling environment and support for my studies. In addition, I am sincerely grateful to Ms Petrena Morrison and Dr Rosslyn Shanks for being there for me when I needed support most. Your support and encouragement helped me to complete my PhD.

To my wonderful parents, Mrs Ifeyinwa and Mr Rapheal Asiegbu and most loving siblings, Ngozika Osakunu, Obinna Asiegbu, Nnaemeka Asiegbu and Obiageri Igwebuike, I will forever be indebted to you all for your unwavering love, prayers, confidence, encouragement and support. I specially appreciate Rev. Mrs Abiola Crown (and the Time to Heal charity) who made herself unconditional available for me as a parent would when I needed support most. Your support and encouragement were also crucial for me to complete this journey. I would also like to thank all my friends and colleagues in school, especially Oluwademilade Ogunsesan and other members of my research group for being another family in a foreign land. Thanks, Demmy for being extraordinarily kind.

Finally and most importantly, I recognize my sunshine and source of motivation, my amazing son, Sean Munachimso Chinenye-Kanu. I am grateful for your patience, understanding, love and care. Truly my PhD accomplishment belongs to both of us. I pray we accomplish more going forward in life. I love you, always.

ABSTRACT

Internal multiphase flow-induced vibration (MFIV) in pipe bends poses serious problems in oil and gas, nuclear and chemical flow systems. The problems include high amplitude displacement of the pipe structure due to resonance, fatigue failure due to excessive cyclic stress induced by fluctuating forces and structural wear due to relative motion of pipe and its support. Current industry guideline is based on single phase flows while the few existing MFIV models in literature are based on small scale laboratory experiments which do not completely address the complexities in multiphase flows and the differing multiphase flow mechanisms between small and large pipes. Therefore, numerical simulations of two-phase flow induced fluctuating forces, stresses, displacements and natural frequencies at 90^0 bends have been carried out to investigate the characteristics of MFIV in pipes of 0.0525m, 0.1016m and 0.2032m internal diameters (I.D.). An integrated high-fidelity CFD and FEA based numerical-analytical modelling framework was applied to predict the defining characteristics of MFIV in the pipes. The CFD simulations of 35 cases of slug, cap bubbly and churn turbulent flow induced fluctuations at the bends were carried out using the volume of fluid (VOF) model for the two-phase flows and the $k-\epsilon$ model for turbulence modelling. A one-way fluid-structure interaction was carried out to evaluate stress and displacement.

Simulations results based on 0.0525m I.D. show good agreement of the volume fraction fluctuation frequencies of slug and churn flows with the reported experiment. The behaviours of the flow induced void fraction, forces and stress as functions of gas superficial velocities in the 0.0525m I.D. pipe showed a good correlation to the observed behaviours in the 0.2032m I.D. pipe. The same correlation was not prominent in the 0.1016m I.D. pipe and was attributed to the transition behaviour of gas-liquid two-phase flows caused by Taylor instability in pipes of non-dimensional hydraulic diameter of $18.5<D_H^*<40$. Also, based on the present study, modification of Riverin correlation which was based on small scale laboratory experiment to predict RMS of flow induced forces was carried out by adjusting the constant parameter C to 20. This modification, improved the predictive capability of the model for a wider range of pipe sizes and gas volumetric fractions between 40% and 80%. The significant findings in this study would be useful input in developing a comprehensive industry guideline for MFIV.

Keywords**:** Flow induced vibration, Numerical modelling, 90^0 pipe bend, Slug/churn flow, Force fluctuations, Hydraulic diameter, Natural frequency, Fluid-structure interaction, Stress, Displacement

PUBLICATIONS

Hossain, M., Chinenye-Kanu, N.M., Droubi, G.M. and Islam, S.Z., 2019. Investigation of slug-churn flow induced transient excitation forces at pipe bend. *Journal of Fluids and Structures*, *91*, p.102733.

Chinenye-Kanu, N.M., Hossain, M., Droubi, M.G. and Islam, S.Z., 2018. Numerical Investigation of Two-Phase Flow Induced Local Fluctuations and Interactions of Flow Properties Through Elbow. *Proceedings of the 1st International Conference on Numerical Modelling in Engineering: Volume 2: Numerical Modelling in Mechanical and Materials Engineering, NME 2018, 28-29 August 2018, Ghent, Belgium*. Springer. pp. 124-141.

Chinenye-Kanu, N.M., Hossain, M., Droubi, G.M. and Islam, S.Z., 2019. CFD Investigation of the Effect of Pipe Diameter on Multiphase Flow Induced Vibration. 32nd Scottish Fluid Mechanics Meeting (SFMM2019). 30 May 2019. Dundee, UK.

Chinenye-Kanu, N.M., Hossain, M., Droubi, G.M. and Islam, S.Z., 2017. Computational Fluid Dynamics Modelling of Transient Multiphase Flow Induced Vibration in Flowlines. 15th Multiphase Flow Conference and Short Course. 14 -17 November 2017. Dresden, Germany.

TABLE OF CONTENTS

LIST OF FIGURES

LIST OF TABLES

NOMENCLATURE

A	Pipe cross sectional area, m^2
C	Constant (Riverin correlation)
F	External body forces, N
F'	Force fluctuation, N
$\overline{F_{rms}}$	Normalised RMS value of the fluctuating force, N
p	Pressure, Pa
t	Time, s
$\vec{v}_m$	Mixture velocity, m/s
v_f	Liquid phase velocity
$\overline{u}$	Velocity component in i, j = 1, 2 or 3 directions, m/s
V_{sg}	Gas superficial velocity, m/s
V_{sl}	Liquid superficial velocity, m/s
C_μ, $C_{1\epsilon}$, $C_{2\epsilon}$,	Coefficients in approximated turbulent transport equations
A_g	Surface area of gas inlet, m^2
A_l	Surface area of liquid inlet, m^2
V(t)	Instantaneous velocity, m/s
V_t	Mixture velocity, m/s
D	Pipe diameter, m
We	Weber number
Re	Reynolds number
j	Mixture velocity, m/s
j_f	Liquid superficial velocity, m/s
j_g	Gas superficial velocity, m/s
g	Gravity, m/s^2
U_G	Rising velocity of Taylor bubbles, m/s
U_L	Liquid phase velocity
U_M	Mixture velocity
D_H^*	Non-dimensional hydraulic diameter
κ_l	Surface curvature of the liquid droplet
κ_g	Surface curvature of the gas bubble
$\bar{n}_w$	Unit vectors normal to the wall

$\bar{t}_w$ Unit vectors tangential to the wall

θ_w Contact angle

k Turbulent kinetic energy

d Nodal displacements, m

U_p Time averaged velocity of fluid at point P, m/s

E Empirical constant given as 9.793

κ Von Karman constant given as 0.4187

y_p Distance of point P from the pipe wall, m

U_∞ Free stream velocity, m/s

Δy First mesh cell height, m

Greek letters

ρ Density, kg/m^3

μ Dynamic viscosity, kg/ms

σ Surface tension, N/m

$\tilde{\alpha}_g^A$ Area averaged void fraction

ρ_g Gas density, kg/m^3

ρ_l Water density, kg/m^3

$\emptyset$ Arbitrary flow property

$\Delta\rho$ Density difference between gas and liquid, kg/m^3

ρ_f Liquid density, kg/m^3

α Mean void fraction

μ_f Dynamic viscosity of liquid, kg/ms

ϵ Energy dissipation rate

ε Strain

ω Natural frequency, rad/s

τ_w Shear stress on the wall in the direction of U_p, N/m^2

Acronyms/ Abbreviations

CFD	Computational Fluid Dynamics
DES	Detached Eddy Simulation
DNS	Direct Numerical Simulation
EI AVIFF	Energy Institute's Avoidance for Vibration Induced Fatigue

	Failure
FEA	Finite Element Analysis
FFT	Fast Fourier Transform
FIV	Flow Induced Vibration
FSI	Fluid Structure Interaction
JAEA	Japan Atomic Energy Agency
JIP	Joint Industry Project
JSFR	Japan Sodium-Cooled Fast Reactor
LES	Large Eddy Simulation
LOF	Likelihood of Failure
MFIV	Multiphase Flow Induced Vibration
PSD	Power Spectral Density
Q3D	Quasi Three-dimensional
RMS	Root Mean Square
RSM	Reynold Stress Model
SST	Shear Stress Transport
URANS	Unsteady Reynolds Averaged Navier-Stokes Simulation

CHAPTER 1

INTRODUCTION

1.1 Background

BP Statistical Review of World Energy (2018) stated that global energy demand grew by 2.2% in 2017 alone, beating the 10-year average growth rate of 1.7% per year. World Energy Outlook (2018) predicts that global energy demand will further rise by more than 25% by 2040. This will be as a result of global economic growth driven by increasing prosperity in developing economies and an increase in population by 1.7 billion people (BP Energy Outlook, 2019). In order to meet this high demand, oil and gas is expected to provide about 56% of this total energy required by 2040 while renewables, coal and nuclear will jointly provide for the rest (Adam, 2018).

In 2017 alone, global oil and gas consumption rose by 1.8% (1.7 million barrels per day) and 3% (96 billion cubic meters) respectively, to meet up with the increase in demand (BP Statistical Review of World Energy, 2018). Hence, despite the development of diverse renewable energy technologies, the need for large scale investment and increased production in the oil and gas sector persists. However, the recent years' price fall in the sector continue to impose cost constraints on oil and gas exploration, production, processing and transportation from both onshore and offshore reservoirs.

In addition, due to declining production from onshore reserves while demand increases, current offshore oil production accounts for about 30% of total global oil production (Shukla and Karki, 2016). Also, depletion of shallow water fields and sophisticated advances in engineering and technology are driving increased offshore oil and gas extraction from the difficult deep (400m - 1500m) to ultra-deep (>1500m) fields while explorations are also now possible at depths of 12km (Maribus, 2014 and Shukla and Karki, 2016). Hence, with the ratio of the remaining 2P recoverable reserves of offshore to onshore oil and gas reserves by

tonnage being about 1:1.3 (Xiaoguang et al., 2018), offshore oil and gas will continue to contribute immensely to satisfy global increasing energy demand. However, this resource must also be extracted with minimum environmental risk due to flowline failure and at a competitive cost.

Conventional oil and gas are usually extracted in the form of different proportions of crude oil, natural gas and their condensates flowing together through the flowline systems. In addition to the hydrocarbons, sand and water can also be found in the flow. The complex multiphase flows are associated with inherent problems such as sand transport, erosion, hydrate formation, corrosion and flow induced vibration (FIV). Most of the mentioned problems have been the subject of considerable industry and academic investigation projects both in the past and present. However, unlike the nuclear energy industry, the multiphase FIV in the oil and gas industry has only just began to receive much needed focus due to increase in real cases and potential cases of the problem especially in offshore systems.

1.2 Motivation and justification for the present study

Extracted hydrocarbon in the offshore are transported by flowing the multiphase fluid from the Christmas tree at the seabed through important flowline sections to the topside floating platform or to the nearest flow station onshore for processing. This flowline sections include jumpers, manifold, long pipelines, rigid and flexible risers and rigid topside pipeworks. Figure 1.1 shows the complex geometries and orientations (bends, tees and S-shaped risers) of the flowline sections found at subsea. The jumpers which are usually installed to receive fluid directly from the Christmas tree are designed specially with multiple pipe bends to accommodate large expansions due to high temperature and pressure of the fluid from the tree. The manifolds which receive fluids from different wells also include different sizes and orientations of bends and T-joints. These complex geometries have been reported to be more prone to FIV (Miwa et al., 2015 and Pontaza et al., 2013).

In addition, subsea conditions are harsh to operate in; repairs, control, monitoring and measurements in such environment are also very difficult and less accessible

than onshore systems. In particular, FIV measurements are much costlier in subsea than onshore (Abuali et al., 2013) and FIV problems in such offshore oil and gas facilities constitute an unacceptable level of risk. The problems include accelerated wear, fatigue failures of the flow lines and associated structures and resonance occurrence. Fatigue failure could occur at stresses lower than the yield stress of a material making a ductile material to fail more like a brittle material due to cyclic loading. Even a hidden fatigue crack could subsequently result in through-thickness fracture or rupture in structures. Figure (1.2) shows the fatigue failure of a pipe bend due to FIV (Sanchis, 2016). Ashrafizadeh et al. (2013) investigated and reported a case where the conclusion on the cause of an existing flowline failure was misleading because dynamic loading effect was not initially considered. In addition, resonance would occur when the FIV frequency matches a natural frequency of the flowline structures hence amplifying the amplitude of the vibration and leading to failure.

In the UK, almost all oil and gas fields are located offshore (North Sea). A current study by UK Health and Safety Executive shows that fatigue and vibration-related failures lead to a high percentage of failure in the subsea topside structures (Figure 1.3). FIV in subsea systems has been reportedly aggravated due to a few cost-effective practices to optimize production including more long-distance tie-ins to existing manifolds, increase in production flow rates and use of flexible pipes. Also, Gharaibah et al. (2016) highlighted that pressure to reduce capital and operating cost encourages the use of lighter subsea pipelines. Such extra tie-in and increased flow rate have also led to reduction or complete shutdown of production until a safety measure or a case-specific solution was provided for the particular problem. This indicates that vibration issues are usually addressed reactively (Abuali et al., 2013). Therefore, high-level proactive new techniques and high-fidelity models in flow assurance and pipeline integrity are increasingly being required at both design and operational stages to address multiphase FIV.

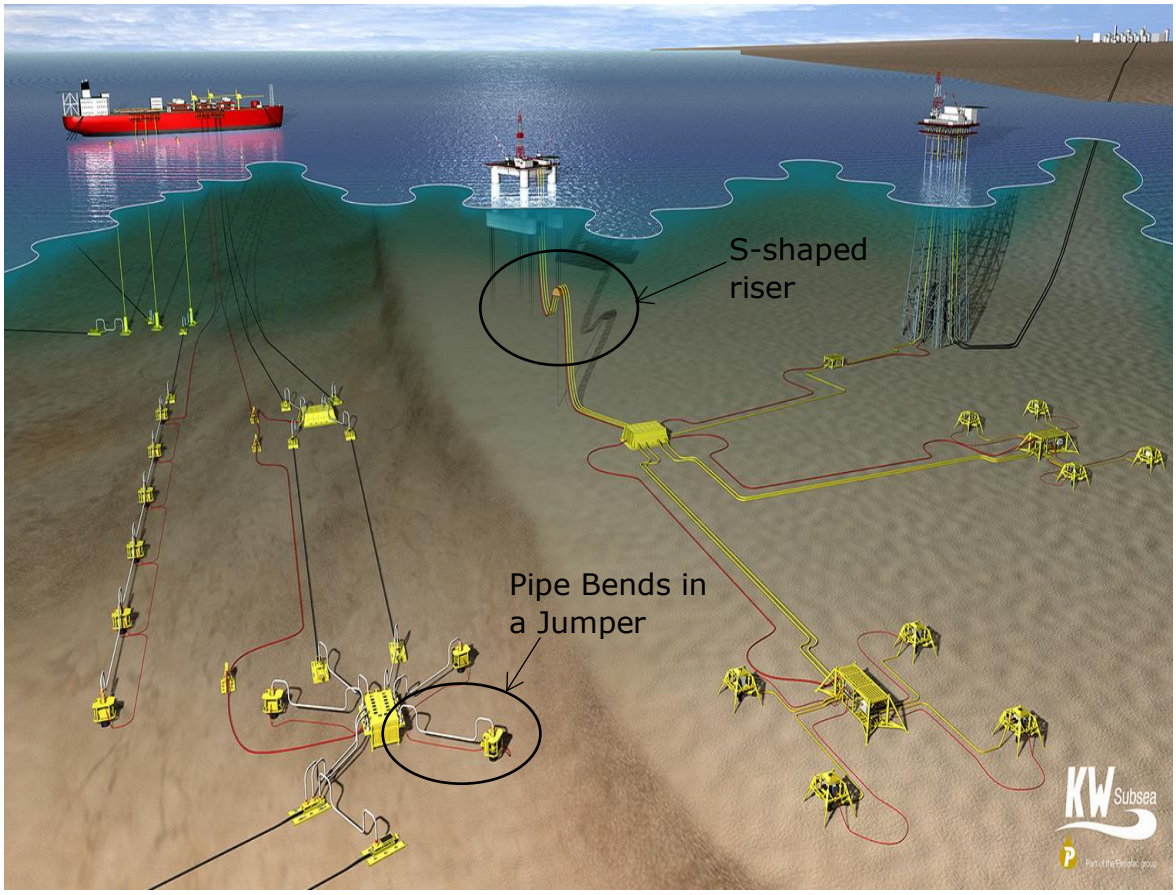

Figure 1.1: A typical subsea piping system (Offshore Energy Today, 2013)

Figure 1.2: Fatigue failure of pipe due to multiphase flow induced vibration (Sanchis, 2016).

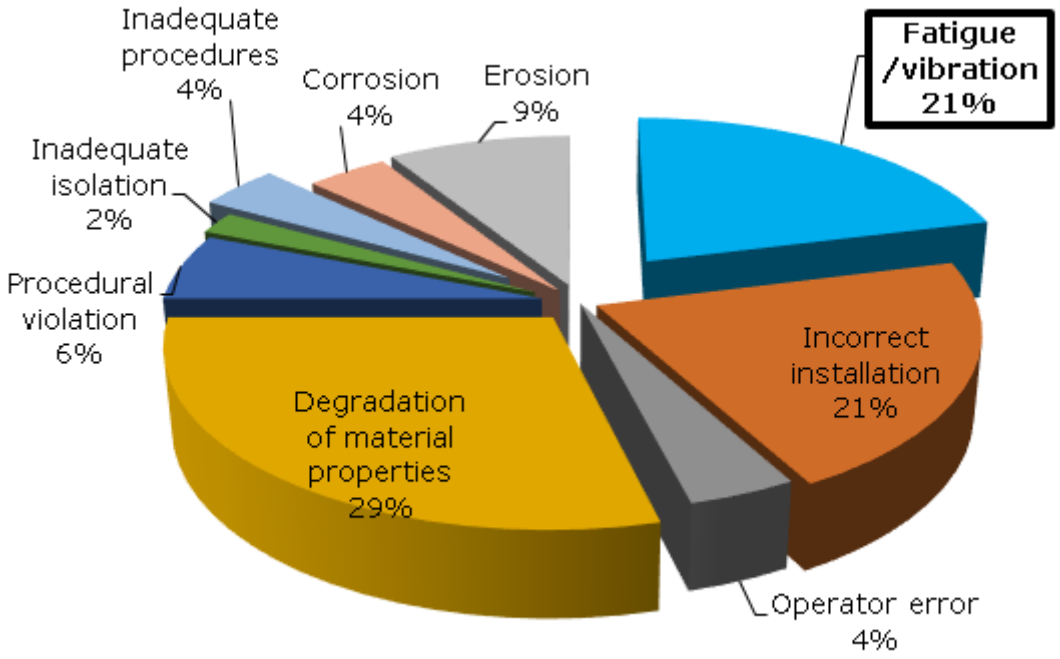

Figure 1.3: Sources of topsides pipework failure in UK offshore industry (UK Health & Safety Executive) (Hill, 2012)

1.3 Nature of multiphase FIV

Vibration of a pipe is the mechanical oscillation of the pipe about an equilibrium position. This phenomenon is initiated by excitation forces which could be an initial event leading to free vibration or a constant event leading to forced vibration. According to Siemens (2017) and Swindell (2013) the different flow mechanisms that could result in fatigue-causing excitations are:

- Pressure pulsations due to operating pumps and compressors: This could excite the associated pipe structures through which the pumped or compressed fluid flows e.g water hammer effect.
- Fluctuations due to obstructions/intrusions: When there is flow past obstructions and intrusions in flow line, e.g thermowells and other intrusive flow measurements devices, fluctuations are generated due to vortex shedding downstream of the intrusion in the flow channel.
- Cavitation and flashing: Pipes could be excited as a result of rapid changes in fluid properties e.g, phase and state change caused by large pressure variations in the pipe flow.

- Vortex induced vibration (VIV) due to external flow: When fluid flows over a cylindrical structure in a direction perpendicular to the cylinder axis, vortices are generated at the wake of the cylinder due to separation of the boundary condition. The shedding of the vortices applies oscillatory forces on the cylinder. These forces are in directions perpendicular to both the axis of the structure and the flow direction. Hence the cylinder oscillates under the influence of the forces if not fixed. In cases where the cylinder is fixed, the ratio of the predominant frequency of vortex shedding to the steady velocity of the flow is proportional to the non-dimensional Strouhal number (Gabbai and Benaroya, 2005).
- Pulsation due to piping side branches known as 'dead legs': Here vortices are generated at the entrance of the side branch due to pressure pulsation at the location. The resulting flow instability and vortex shedding generate discrete frequency excitation. The frequency can match the system acoustic frequency leading to resonance. This type of excitation is observed only in dry gas systems and frequency range can be up to 300 – 1000Hz.
- Flow-induced pulsation of flexible risers: This mechanism causes a phenomenon known as 'singing riser' and it is similar to the excitation due to pressure pulsation at the dead leg entrance region. In this case, the vortices and vortex shedding occur at the entrance of each of the corrugated grooves inside a flexible riser.
- Single-phase turbulent flows: The flow induced excitation in this case is due to the transfer of energy from fluid momentum to the pipe due to turbulent single-phase flow through pipe bends, expansions and valves. The flow velocity and fluid density directly affect the level of the flow induced excitation. In flow through pipe bends, the secondary flow large vortices, flow separation and re-attachment occurring at the bend exit excites the pipe structure. The frequency of turbulence fluctuations in single phase turbulent flows range from 1000 – 20 Hz. Hence, the lower frequency fluctuations of turbulence can excite the natural frequencies of the pipework.
- Transient multiphase flows: Excitation of pipe can also occur due to the density difference between multiple phases of materials flowing simultaneously in the pipeline. According to Swindell (2013), such process-driven excitation depends on the type/nature of process materials within the

system and contains broad band energy at low frequency similar to the characteristic flow frequencies of the multiphase flow.

In Figure 1.4, Blevins (1990) presents a wider and one of the earliest classifications of FIV and highlights some of the mechanisms mentioned. Majority of the studies of FIV have considered random turbulence excitation (Hofstede et al. 2017), acoustic resonance and vortex shedding (Pettigrew and Taylor, 1994) in single-phase flows.

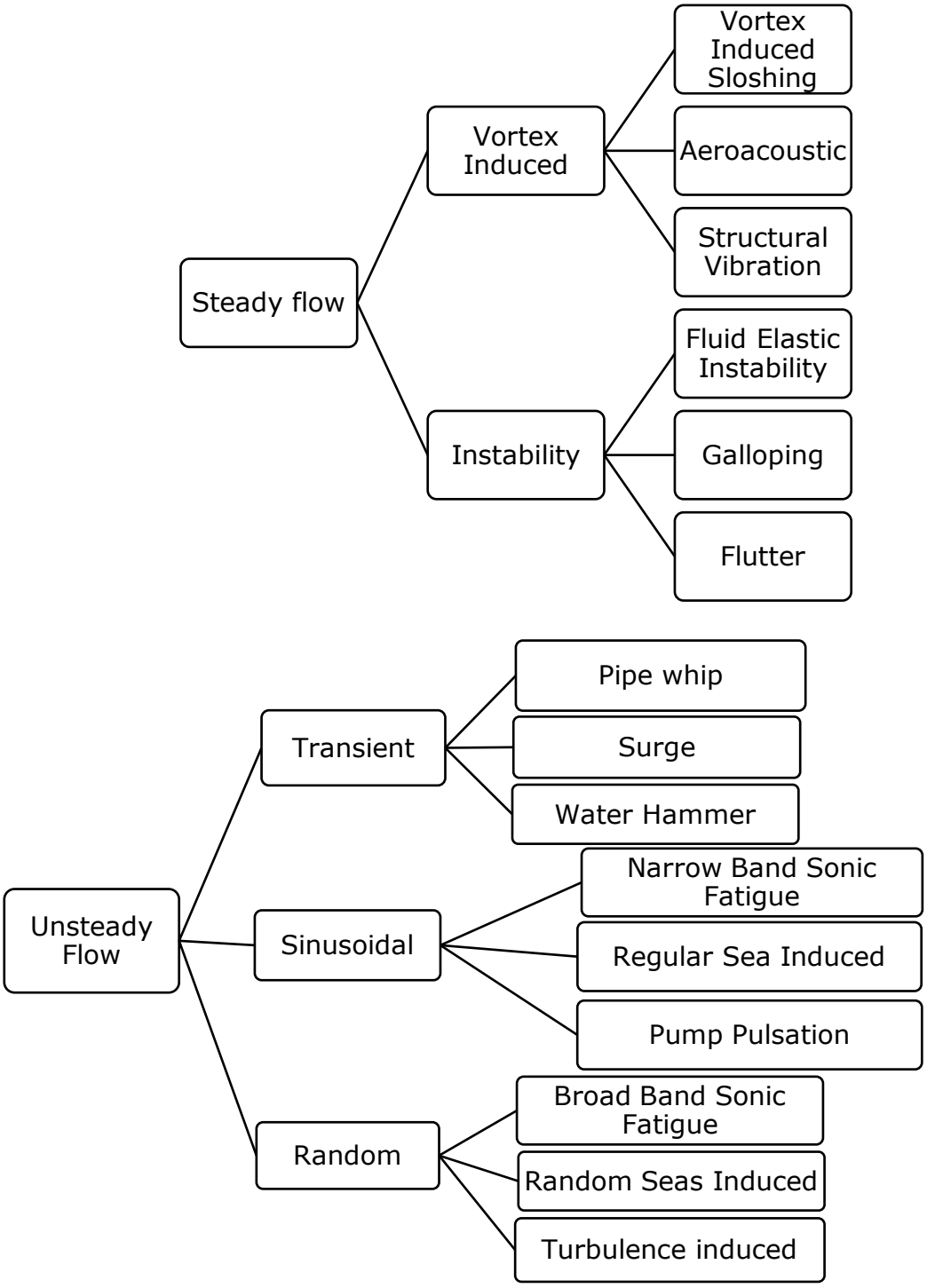

Figure 1.4: Classification of FIV (Blevins, 1990)

FIV of flow lines is a two-way fluid-structure Interaction (FSI) involving two dynamic forces: hydrodynamic forces and structural dynamic forces. When dynamic force due to fluid motion impacts on structures, it produces a response in the form of structural stress and deformations which could in turn, further disturb

the fluid flow (Blevins, 1990). The schematic of the complete FSI feedback relationship is shown in Figure 1.5.

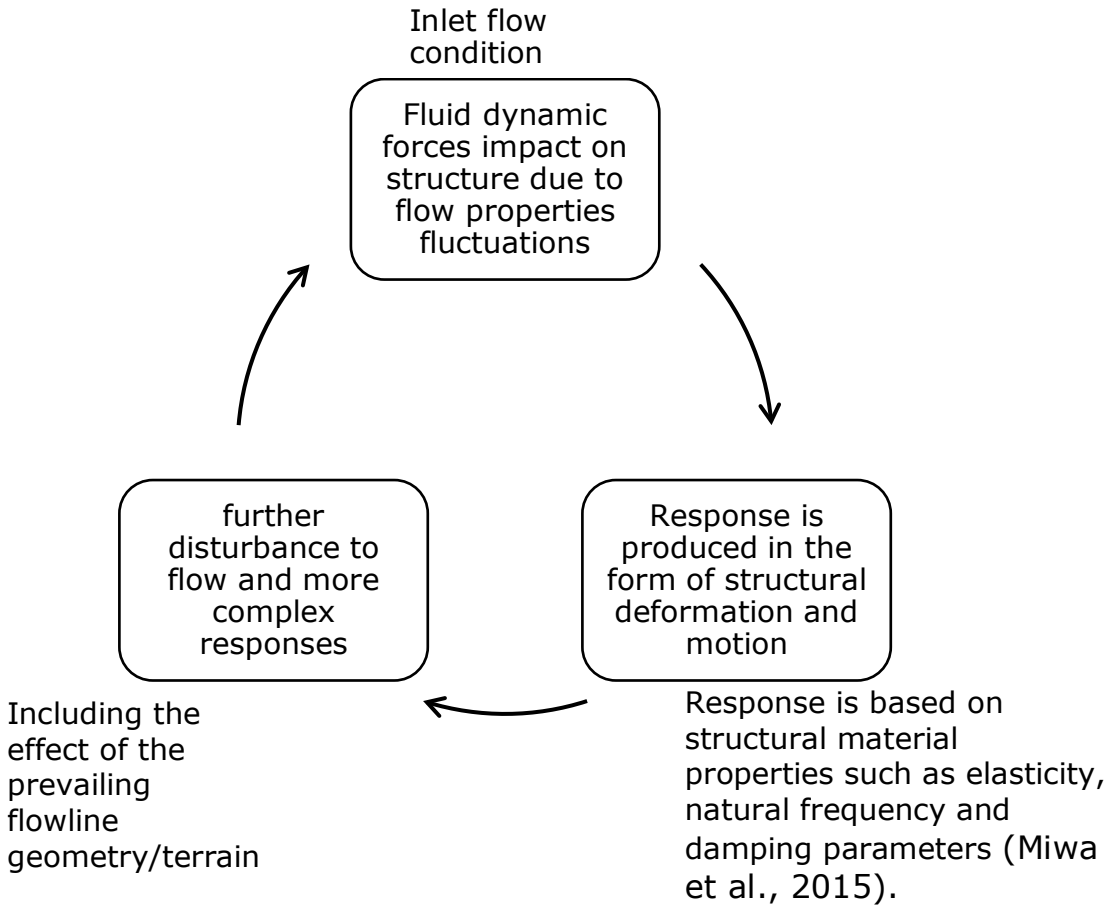

Figure 1.5: Schematic of cause and effect relationship in FIV (Blevins, 1990)

This interaction is initiated as the fluid dynamic forces excite the piping structure. However, in FSI the fluid and structure behaviours could be tightly coupled as is obtainable in fluid elastic instability. This form of FSI involving single phase turbulent flow is fairly reported in literature. The most general form of the analytical two-way FSI equation for a tightly coupled fluid elastic instability of a slender vertical pipe is based on the Euler-Bernoulli beam theory illustrated in Figure 1.6 and given by Paidoussis (1970) as:

$$EI\frac{\partial^4 y}{\partial x^4} + MU^2\frac{\partial^2 y}{\partial x^2} + 2MU\frac{\partial^2 y}{\partial x \partial t} + (M+m)g\left((x-l)\frac{\partial^2 y}{\partial x^2} + \frac{\partial y}{\partial x}\right) + (M+m)\frac{\partial^2 y}{\partial t^2} = 0 \qquad (1.1)$$

where y(x,t) is the transverse displacement, E, I, M, m, U, L and g are Young's modulus, inertial moment of cross-section area, mass per unit length of fluid, mass per unit length of pipe, steady flow velocity of fluid, length of pipe and gravitational acceleration, respectively (An and Su, 2015).

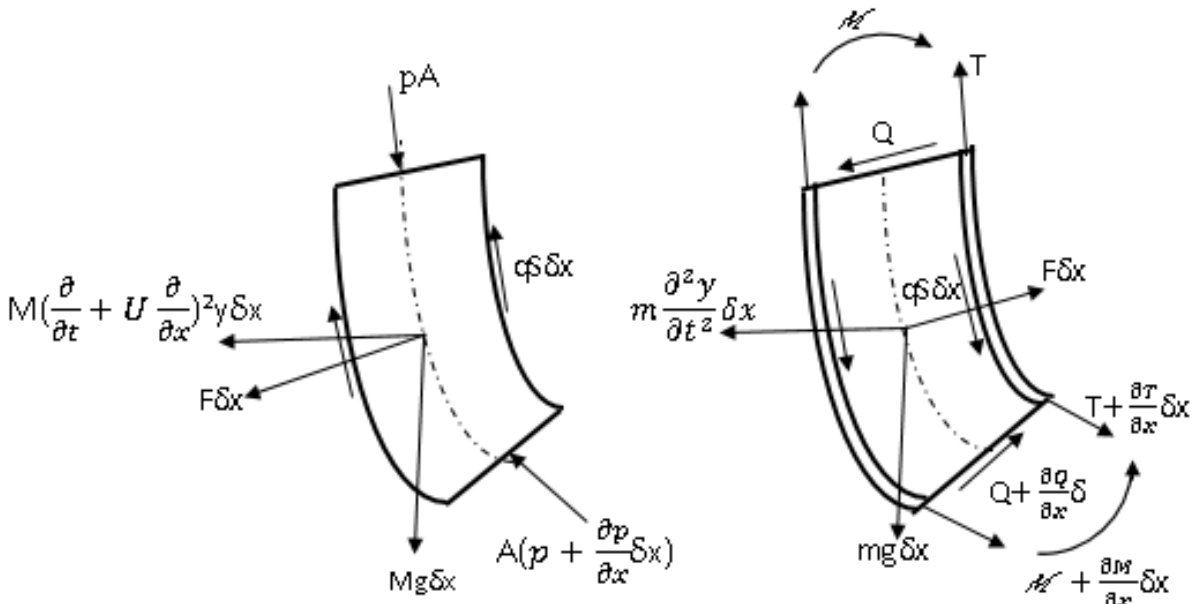

Figure 1.6: Forces and moments acting on elements of (a) the fluid and (b) the tube (Paidoussis, 1970).

EI is the flexural rigidity of the pipe and from left to right, the terms in Equation 1.1 represent respectively, flexural force, centrifugal force, Coriolis force, gravitational force and inertia force. By eliminating gravitational force, Yi-min et al. (2010) and Xu et al. (2010) applied the equation to determine natural frequencies of horizontal fluid-conveying pipes with cantilever support and simply supported boundary conditions respectively. The primary features of Equation 1.1 are that it is most suited for single phase flows in which both fluid mass (density) and flow velocity are steady and most importantly, the pipe is considered flexible and its deformation is expected to significantly modify the internal flowing fluid.

On the other hand, in another form of the FSI mechanism the fluid and structure behaviours are not tightly coupled. The force of the structural response (displacement) due to fluid force could be much less than the fluid force itself in a rigid pipe with fixed supports. Hence a one-way FSI analysis which focuses on

accounting for the stress and displacement in pipes due to internal fluid flow induced forces would be the optimum FSI approach suited for such rigid pipes rather than a two-way FSI approach.

In addition, efforts to adapt Equation 1.1 to multiphase flows were reported by An and Su (2015) and Bai et al. (2018). They implemented the equation to account for vertical pipes conveying multiphase flows. However, the former modelled a mixture flow in a long slender riser while the later attempted to capture multiphase flow by describing the variable density of multiphase flow with a mathematical model and yet considering the velocity to be steady. In reality, multiphase flows are more complex than portrayed in the two studies. Multiphase flows induced vibration (MFIV) investigations are rare. Unlike the single-phase flows, FIV in multiphase flows is more difficult to analyse and characterise due to the complex phase interactions as well as its highly unsteady and unstable nature. Initially, MFIV was addressed for nuclear industry as a result of steam-water flow system (Yih and Griffith, 1968). One of the challenges of understanding the MFIV is that it is flow regime specific. It has been shown that the slug and churn-turbulent flow patterns are the sources of the most significant dynamic forcing functions compared to other flow regimes (Bossio et al. 2014, Cooper et al. 2009, Tay and Thorpe, 2004, Riverin et al. 2006, Cargnelutti et al. 2010, Riverine and Pettigrew 2007, Liu et al. 2012, and Miwa et al. 2015). Hence, accurate identification of the particular flow regime present in the flowline is the first step to characterising the FIV due to that multiphase flow. For gas-liquid flows, depending on the orientation of flow and void fraction (gas fraction), the flows can be identified as the different flow regimes shown in Figure 1.7 (a) and (b). In a single flow line, one flow regime can transit into another flow regime as the superficial velocities of the individual phases change. For instance, in a vertical flowline starting with bubbly flow, increase in gas superficial velocities can change the flow to slug flow regime where smaller bubbles join to form bigger ones. The big bubbles called Taylor or cap bubbles, with surrounding liquid film, form gas slugs which are followed by liquid slugs. As the gas superficial velocities increase, the slugs distort resulting in a more disturbed and turbulent flow regime called churn flow. Further increase in the velocity will lead to annular flow regime where the gas phase maintains the

middle portion of the flow line in axial direction while the liquid forms film on the pipe wall (Abdulkadir, 2011).

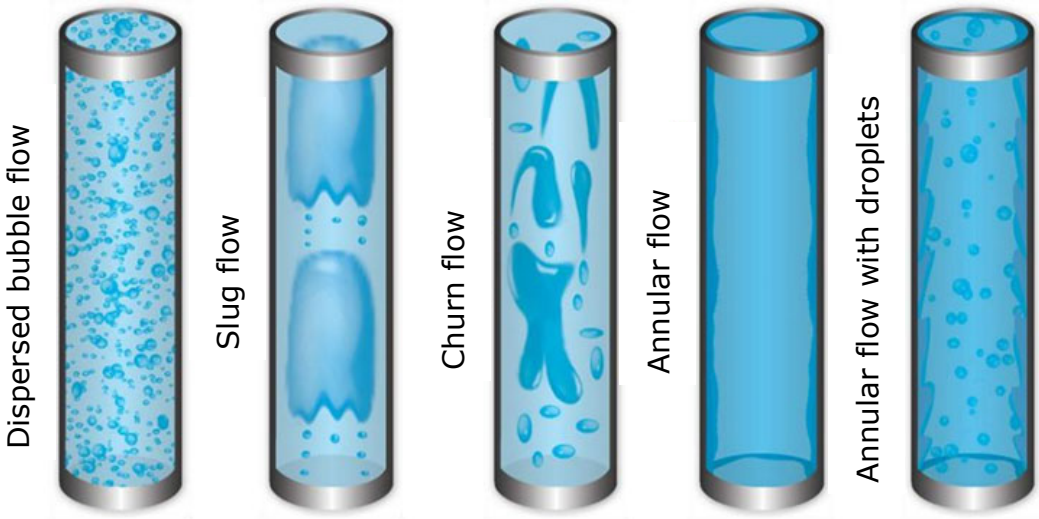

(a)

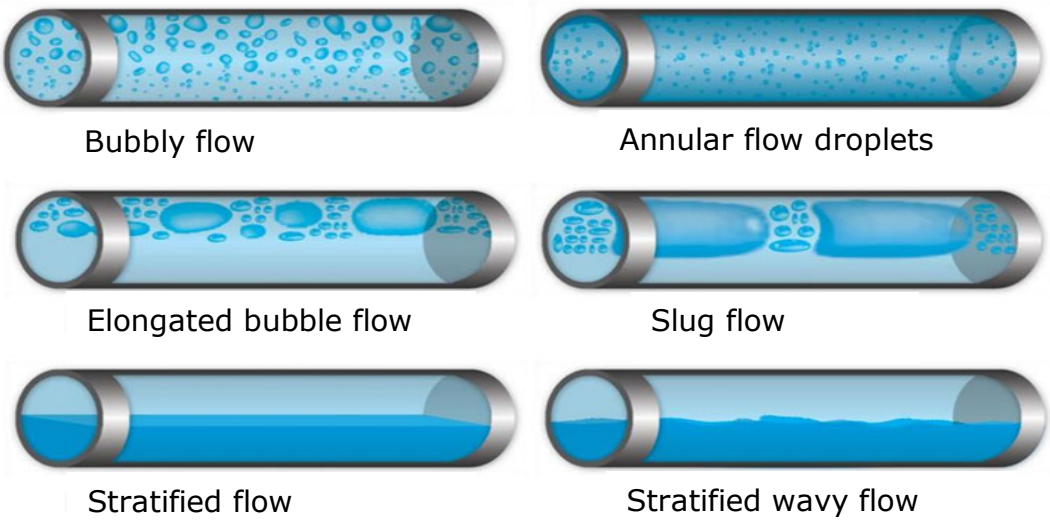

(b)

Figure 1.7: (a) flow regimes in vertical pipes; (b) flow regimes in horizontal pipes (Bratland, 2016).

In the case of horizontal flow lines, the obtainable flow regimes are shown in Figure 1.7 (b). Increase in superficial gas velocity leads to the formation of waves on the surface of the liquid. As gas velocity increases, these waves rise and contact the upper portion of the flow line until alternate slugs of liquid and gas are formed.

Further increase in the velocity will also lead to annular flow regime (Hua and Pan, 2015).

A lot of complex phase motions and interactions exist in multiphase flowlines between the phases as well as between phases and pipe wall. This is as a result of differences in phase densities, viscosity and surface tension which influence momentum interactions at phase boundaries; phase change processes involving energy transfer/generation; turbulence and pressure drop (Miwa et al., 2015). These lead to instabilities and flow properties fluctuations. The fluctuations are the sources of the dynamic loading that excites flow line structures conveying the multiphase flows. The excited flowline will vibrate and increase the threat of fatigue failure due to stress, fretting wear due to displacements, deformation and resonance effect. In practical systems, FIV is observed to have frequency content generally up to 100 Hz (Miwa et al., 2015 and Ashrafizadeh et al., 2013). The pioneering investigations of FIV were carried out for nuclear energy applications. In fact, multiphase flows-induced vibration investigations were initially addressed as steam-water FIV in nuclear energy power plants (Yih and Griffith, 1968). Many of the earlier studies were experimental, but thanks to the development of high-speed computers, recent MFIV investigations are applying coupled one-way and two-way transient FSI approach to flow modelling in CFD and structural finite element analysis (FEA).

1.4 Modal Parameters and dynamic response of Structures

A complete assessment of the dynamic behaviour of a structure vibrating under loading includes the determination of the modal parameters of the structure. When a structure vibrates, the frequency response of the structure within a given frequency range can be divided in a way that individual modes of vibration are isolated. These individual modes have characteristic parameters which are the resonance/natural frequency, the modal damping and the mode shape of the structure. Hence, they are called the modal parameters. Determining these parameters constitute the modal analysis of structures.

Modal analysis can be carried out experimentally using accelerometer to measure the time varying acceleration response of the vibrating structure and carrying out

Fast Fourier Transform of the signal. Another method to carry out modal analysis involves solving the equation of motion of an undamped system under free vibration in a FEA computer application. With the development in computing capabilities, power and speed, this method is able to model complex structure designs and new systems. Due to increasing reliability and validation data, the computer FEA method presents a more feasible and economic method of determining modal parameters of new and existing complex large structures where risk of failure might be high, rather than large scale costly experimentation.

One of the main risks of structural vibration is the risk of resonance. Resonance occurs when the frequency of structural vibration matches any of the natural frequencies of the structure. The natural frequencies are simply identified as the frequencies at which peaks appear in the magnitude of the frequency response function. Then, the modal damping can be described using the damping ratio which is a function of the frequency bandwidth between the two half power points of the magnitude of the frequency response function and the natural frequency of the particular mode of vibration. Finally, the mode shapes are more difficult to determine. They can be constructed using the modal displacements obtained at different points on the structure under vibration.

1.5 Approaches to investigating FIV issues

There are a number of approaches to investigate FIV in new design systems, systems to be modified and operational systems. Such approaches include:

- Experimental investigations for both new systems and operational systems. This approach usually involves developing a scaled-down physical model representing the real-life system set-up and measuring vibration in terms of the dynamic acceleration of the structure using accelerometer. Also, the transient force and pressure capable of inducing vibration or fatigue in the structure could be measured using force and pressure transducers, respectively. A reliable experimental result should also involve investigating the effect of scale on the observed behaviors and interactions of the vibration parameters.
- Analytical calculations to predict vibration levels and fatigue risk for both new systems and operational systems. This method would require

assumptions in the physical description of the system and excitation mechanisms in order to simplify calculations.

- In-situ measurements of vibration modal parameters in operational systems followed by comparison with previous data or standards from manufacturers' specification and industry standards.
- CFD and FEA modeling of the system. Due to developments in computing, this method of investigation is gaining more favorable attention in recent years. This approach also allows the details of complex geometries and excitation mechanisms to be more accurately modelled compared to analytical modelling. Full scale models of systems under vibration can also be investigated using computer simulations.

A few joint industry projects (JIP) have made efforts to develop procedures in some cases, involving a combination of the outlined approaches to address some of the FIV excitation mechanisms presented in Section (1.3) as direct sources of fatigue failures. The result of such efforts includes the DNV-RP-F204. This recommended practice is focused on riser fatigue assessment which considered wave-induced, low-frequency and vortex-induced stress-cycles as the main contributors to fatigue damage. There is also the DNV-OS-F101 which is a more general offshore standard for submarine pipeline systems. However, complex internal multiphase flow as an excitation mechanism has not been properly addressed. Current practice for assessing internal FIV generally refers to the Energy Institute guideline for Avoidance of Vibration Induced Fatigue Failure (EI AVIFF) (2008). The guideline laid down a systematic approach to undertaking a proactive assessment of process pipework and systems against FIV. This assessment is predominantly carried out at three different stages namely; initial design stage of a process system, operating stage of an existing system and during modification of existing systems. There are two aspects of the assessment, these are qualitative and quantitative assessments which give a likelihood of failure (LOF) score for the system. The qualitative assessment identifies and ranks the possible excitation mechanisms for each system unit while quantitative assessment addresses each of the excitation mechanisms and provides the LOF score.

The LOF calculations are based on simple and conservative models with a very high LOF score assumed and assigned to multiphase flows (e.g slug flow) and

environmental loading-based excitation mechanisms. By doing this, the guideline shows that multiphase FIV in subsea pipeworks are not yet well understood. Usually, high LOF value warrants more comprehensive predictive approaches such as computational fluid dynamics (CFD) as advised in the guideline. Also, assumption of such high LOF values leads to over conservativeness and over engineering which is not sustainable in the current global scenario of competitiveness and cost savings. In addition, the guideline was not initially intended for subsea application. Most importantly, literature also shows that slug and churn flows induce the highest vibration at bends and T-joints in flow lines. The fact that slug flows occurs more often than not in subsea oil and gas flowlines due to hydrodynamic slugging, terrain slugging, and operational induced slugging gives an indication of how often FIV due to slug flow induced force and pressure fluctuations would occur in pipework. Hence, this flow regime is inherent in subsea and onshore flowlines and hydrocarbon process systems. They have been recorded to cause FIV related interruptions in oil and gas operations (Lu et al. 2014, Abuali et al., 2013 and Pontaza et al., 2013). Hence, accurate models and correlations are required to proactively address the multiphase FIV and pipeline integrity challenges.

1.6 Research Aim and Objectives

The aim of this study is to develop a high-fidelity integrated framework of CFD model, structural FEA and analytical calculations to predict the critical multiphase flow and pipe properties fluctuations due to slug, churn, cap-bubbly and churn-turbulent flows through 90^0 pipe bends. One of the main bases for validating the fidelity of this framework was comparing the RMS of forces predicted in this study using the present approach with the prediction of the empirical-analytical model developed by Riverin et al. (2006) and optimizing the performance of the model for large pipes. In order to achieve the aim, the following objectives were accomplished:

1. Investigate the characteristic interface evolution and phase distributions in gas-liquid two phase slug and churn flow regimes in an upward small pipe flow through bend, and the quantitative and qualitative validation of the

multiphase model and numerical approach that accurately describes the flow by comparing numerical predictions to published experimental data.

2. Numerically simulate of cap-bubbly and churn-turbulent flow regimes in large pipe bends in order to investigate and validate the phase distribution and evolution through a 90^0 pipe bend.
3. Analytical modelling and validation of the fluctuating impact forcing signals with emphasis on the effect of increasing gas superficial velocities and liquid superficial velocities.
4. Determine the effect of pipe diameter on the flow properties fluctuations with particular interest in the peak frequency and maximum magnitude of the void fraction and flow induced forces fluctuations.
5. Evaluate the pipe structure natural frequencies and responses in the form of stress and deformation magnitude and frequency due to MFIV and their behaviours as a function of pipe diameter.

Original contributions of present research

Based on the knowledge gaps in the following literature survey, the original contributions of the present research include:

- Validation and implementation of an integrated framework of CFD modelling and analytical calculations to accurately predict MFIV.
- This study provides an extensive result database from numerical experiment that will be useful for identifying and estimating LOF due to MFIV under slug and churn flow regimes in practical pipe sizes. Such database will also be useful for validation purposes and development of more robust models suitable for a wider range of pipe sizes than is currently available in literature.
- Quantified the effect of void fraction/liquid hold-up on the RMS of flow induced forces as a function of the ratios of pipe diameters of 0.0525m, 0.1016m, 0.2032m.
- Estimated the correlation between the RMS of flow induced forces and pipe diameters in order to assess the applicability of the relationships established between the RMS of force and flow superficial velocities based on laboratory scale experiments to pipes of industrial scale.

- Quantified the interaction between flow induced forces magnitude and stress magnitude as a function of pipe diameter for geometrically similar pipes. Findings can directly contribute to ongoing development of new industry standards and guidelines for addressing MFIV in subsea jumpers and risers by proffering high fidelity factors for scaling up laboratory tests-based results to predict RMS of force fluctuation and maximum magnitude of stress fluctuation in industrial scale pipes of 0.2032m diameter.
- Evaluated the effect of added mass due to internal multiphase flow on the natural frequencies of pipe structure as a function of pipe diameter.

1.7 Thesis organization

This study presents detailed investigation of multiphase flow induced vibration in the bends in pipes of different diameters by carrying out numerical simulations of similar flow conditions in all the pipe sizes. The results are analysed using analytical calculations and statistical processes. The results are also validated with similar experimental case studies in literature before the investigation methodology is extended to a wider range of FIV scenarios. These are presented in a step by step fashion in the following chapters:

Chapter 1 introduces the background of the problem of MFIV and presents the justification of this research. This chapter also presents the aim and objective of this research.

Chapter 2 presents a comprehensive review of literature on experimental and numerical gas-liquid multiphase FIV in small and large diameter pipes. Considerable attention was paid to identifying the multiphase and turbulence models which were adopted in the numerical studies of MFIV found in literature. Then results obtained for the characteristic FIV parameters were highlighted where obtainable in the literature.

Chapter 3 details the theoretical background and methods used in this numerical investigation. The models used for flow regime identification are explicitly discussed before the appropriate multiphase flow models fitting the flow regimes

are presented. The finite element modelling approach used for stress and modal analysis is also discussed.

Chapter 4 presents the numerical solution procedures adopted in solving the multiphase flow governing equations and the structural finite element equations. The mesh sensitivity analysis and the validation of the numerical modelling approach for the flow regimes of interest are also discussed.

Chapter 5 discusses the results on the effect of gas and liquid superficial velocities on the characteristics of slug and churn flow induced fluctuations of the void fractions and excitation forces in 90^0 bends.

Chapter 6 presents detailed results of the effect of pipe diameter on the defining characteristics of MFIV.

Chapter 7 discusses the result of one-way FSI due to MFIV to explore stress response magnitudes and frequencies as a function of pipe diameter. Result of effect of global gas volumetric fraction on the natural frequencies of the pipes as a function of pipe diameters is also presented. Finally, the interaction between the dominant frequencies of force fluctuation, stress fluctuation and the natural frequencies of the pipe structure is assessed to predict the risk of resonance.

Chapter 8 presents the conclusions derived from the significant findings in the present research and the suggested recommendations for future work.

CHAPTER 2

LITERATURE REVIEW

2.1 Gas-liquid two-phase FIV in vertical pipes and bends

Knowledge of two-phase FIV due to internal flowing fluid along with its fluctuating forces and predominant frequencies has become increasingly important in several engineering applications including chemical process systems, oil and gas flowlines, and nuclear energy generation systems (Parameshwaran et al. 2016). The two phase flows are generally problematic in any system that they exist, for instance the nuclear energy power plant and oil and gas flowlines. This is because of the complex flow regime transition behaviours as well as the interactions between phases in fully developed flows (Abdulkadir et al. 2015 and Abdulkadir et al. 2019). When two phase fluids flow through bends, the associated complexities are even more. The abrupt change of flow direction introduces parameters such as impact force, momentum change, centrifugal force and Coriolis force which could equally or disproportionately contribute to physical mechanisms such as re-circulation, separation, secondary flow, re-attachment, mixing and change of flow pattern at bends. These are the excitation mechanisms of MFIV in pipe bends.

The flow behaviours in small pipes and bends also differ from that of large diameter pipe bends. According to Schlegel et al. (2010) pipes with non-dimensional hydraulic diameter, D_H^*, less than 18.6 are considered small pipes while pipes with non-dimensional hydraulic diameter, D_H^*, greater than 40 are considered large pipes. In the context of this study involving air-water multiphase flow, the D_H^* value for the small pipe refer to pipes with diameters ≤ 0.0507 m (D_H^* = 18.6) while diameters > 0.1091 m corresponding to D_H^* = 40, are referred to as large pipes. The intermediary range is referred to as the transition region where both small pipe and large pipe effects are present but at different intensities. Based on the findings by Mishima and Ishii (1984) and Schlegel et al. (2009), bubbly flow regime exists in both small and large pipes for all values of liquid superficial velocities at gas superficial velocities below ~0.1 m/s. As gas superficial velocity begins to increase, large bubbles begin to form in both small and large pipes.

However, in small pipes, the large bubbles grow into stable long slugs that fill the entire pipe cross-section and are called slug flow regimes but in large pipes, the large bubbles are only able to form short cap bubbles called cap-bubbly flow regime. As gas superficial velocity increases to ~0.2-0.3m/s (for 0.1m/s liquid superficial velocity), the cap-bubbly flow in large pipes begins to evolve into churn-turbulent flow regime. On the other hand, a fairly stable slug flow regime will still exist in small pipes up to gas superficial velocities above ~1.1m/s (for 0.1m/s liquid superficial velocity) where churn flow regime begins to form. Understanding the two-phase flow behaviour in pipes of different sizes and at pipe bends is crucial to predicting FIV. Some of the literature that exposed the complex behaviours at bends include Pour et al. (2018) and Abdulkadir et al. (2012, 2013, 2014).

In order to develop flow assurance and pipeline integrity assessment approach and predictive models for MFIV, its characteristic features, e.g. time-history of void fraction, velocity, forces, pressure, stress, displacements and their magnitudes and frequencies need to be investigated and quantified for different flow conditions and pipe geometry. The following subsections present efforts reported in literature to investigate MFIV as well as the significant findings on the characteristic features obtained in their results for small diameter pipes and then for large diameter pipes. Then summary of the literature which have successfully applied relevant CFD and turbulent models to the flow regimes of interest in this study is presented in the next section. Finally, the knowledge gaps and the original contributions of this research based on the knowledge gaps are presented in the last section of this chapter.

2.1.1 Experimental studies of MFIV measurements in pipes having D< 0.1091 m

A number of experimental studies have been reported and some correlations to predict multiphase flow induced force characteristics have been developed. Yih and Griffith (1968) investigated the two-phase flows through a vertical duct impacting on a beam structure and studied the momentum flux fluctuations. They investigated flows with a velocity range of 15-75 m/s, duct diameters of 6.35 mm, 15.9 mm and 25.4 mm, with volume fraction of gas of 50-100%. Their key findings

were that the maximum void fraction fluctuations are high in slug and annular flows and the predominant fluctuation frequency were less than 30Hz.

Tay and Thorpe (2004) carried out experiments to study the effects of density, viscosity and surface tension of liquid on slug flow induced forces on a horizontal 90^0 pipe bend. The pipe internal diameter was 70 mm and the gas and liquid superficial velocities were 0.38 – 2.87 m/s and 0.2 – 0.7 m/s respectively. The piston flow model (PFM) developed in the study over predicted the maximum resultant forces more significantly for gas superficial velocities above 2.5 m/s. The square root of the maximum resultant force predicted with PFM showed a linear relationship with mixture velocity. The study also concluded that no significant effect of liquid physical properties was observed on the force characteristics. Furthermore, Tay and Thorpe (2014) whose study was based on the PFM model and equations adopted from literature to predict the time varying velocity and pressure at the inlet and outlet of the control volume extended the upper limit of gas superficial velocities to 3.18 m/s and reported similar results as Tay and Thorpe (2004).

Riverin et al. (2006) studied the FIV in a pipe diameter of 20.6 mm with a U-bend and a T-junction. They have investigated 11 test cases within the gas volume fraction 50% and 75% and the mixture velocities of 2 – 12 m/s. For both volumetric qualities and geometries, the predominant frequenies of force fluctuations were reported to increase from approximately 2 Hz to 30 Hz with increasing mixture velocities. The root mean squares of the equivalent bend forces were observed to be between 1 – 12 N. Riverin et al. (2006) developed a correlation of the dependence of dimensionless RMS force on Weber number based on their experimental data and the previously reported data of Yih and Griffith (1968) and Tay and Thorpe (2004). The model is given as:

$$\overline{F_{rms}} = \frac{F_{rms}}{\rho V_t^2 (\frac{\pi D^2}{4})} = CWe^{-0.4} \qquad (2.1)$$

where, $\overline{F_{rms}}$ is the normalised RMS value of the fluctuating force, C is a constant given as 10 and We is the Weber number defined as:

$$We = \frac{\rho_m V_t^2 D}{\sigma} \tag{2.2}$$

where ρ, V_t, D and σ are the liquid density, mixture velocity, pipe diameter and surface tension, respectively.

Cargnelutti et al. (2010) investigated the stratified, slug and annular flows in pipes of internal diameter of 25.4 mm in a horizontal orientation. The gas and liquid superficial velocities ranged from 0.1 to 30 m/s and 0.05 to 2 m/s respectively. Forces were measured for straight pipe, T-joint, T-joint with one of the arms closed off (T-bend), 90^0 sharp bend and large radius bend. The measured dimensionless slug flow induced forces in the bend and T-bend agreed well with the values predicted by Riverin et al. (2006)'s model. However, the stratified and annular flows data did not conform well to Riverin et al. (2006) model. Further, Cargnelutti et al. (2010) proposed a simple analytical model based on the momentum change due to the slug flow to calculate the resultant force at a bend. The model performed better for slug flows compared to annular and stratified flow. The model was modified to be based on the mixture velocity so that the model would predict the annular and stratified flow induced forces.

Riverin and Pettigrew (2007) extended the experimental study of Riverin et al. (2006) on a pipe diameter of 20.6 mm to four vertical bend configurations of R/D= 0.5, 2, 5 and 7.2 and volumetric qualities of 25, 50, 75 and 95% corresponding to mixture velocities from 1 m/s to 20 m/s. Their study shows that the predominant frequencies and root mean squares of forces (F_{rms}) matched the previously developed correlation of Riverin et al. (2006).

Nennie et al. (2013a), carried out experiments on horizontal 180^0 bend and 90^0 bend with pipe diameter of 4 inches (0.1016m) to compare their experimental measurements of air-water slug flow-induced forces to that from CFD and a simplified analytical model by Cargnelutti et al. (2010). Force values measured in the 180^0 degree bend for gas and liquid superficial velocities of 2.2 m/s and 2.4

m/s respectively compared well with CFD simulation results but did not compare well with the simplified model. The RMS of $F_y$in the first bend were obtained as 116.2 N and 131.1 N in the CFD simulation and experimental measurement respectively. Total RMS value of F_x (summed for both bends) are 62.2 N and 59.4 N in the CFD simulation and experimental measurement respectively. Although the frequency range for both forces in both CFD and experiment spread over a range of 0.01 – 100, maximum prominent frequencies generally existed between 0.1 and 10.

Nennie et al. (2013a) also compared the non-dimensional RMS of resultant forces measured from both 180^0 and 90^0 bend experiments as a function of no-slip liquid hold-up between the 4 inches (0.1016m) diameter pipes and previous experimental measurements from a 1 inch (0.0254m) and a 0.25 inch (6mm) pipes. Results show that the dimensionless forces were generally within the range of 0.1 – 30 for liquid hold-up values between 0 – 1 for the slug flow regimes. On comparison of dimensionless force for all geometries with the exception of only the 0.25 inch pipe, maximum values were obtained during slug flow in the single bend of the 4 inch pipe between no slip liquid hold up values of 0.1 – 0.4. This study concluded that liquid hold-up had equal influence on the forces on the bend notwithstanding the pipe diameter. However, this conclusion is based on the scope of the small pipe sizes and horizontal orientation that were investigated. More details on the FIV measurements in the 6mm pipe could be found in Cargnelutti et al. (2010).

Recently, Wang et al. (2018) carried out experimental tests to evaluate the pressure and displacement fluctuations amplitude and frequencies in a pipe having inner diameter of 0.0514m and thickness of 0.0058m. The flow is downward through an inclined horizontal pipe and then up through a riser connected to it at a bend. The test cases for the pressure fluctuation are, at gas superficial velocity of 0.07m/s, liquid superficial velocities were varied from about 0.08 – 1.2m/s making a total of about 12 flow cases. Another 8 flow cases were obtained by varying gas superficial velocities between 0.02 – 0.3m/s for a liquid superficial velocity of 0.60m/s. Additional 16 flow cases were defined at void fraction 70% with a range of unspecified pairs of liquid and gas superficial velocities. Most of the flow cases fall within dispersed bubbly to churn flow regimes in the riser. The

pressure and displacement sensors are installed at the bottom of the pipe to measure the fluctuation of both parameters in vertical direction. Results show that mean pressures measured for all flow cases were generally between 16 - 31 KPa. For gas superficial velocity of 0.07m/s, predominant frequency of pressure fluctuation increased with liquid superficial velocity from about 0.01 – 0.3 Hz while the amplitude of fluctuation decreased from about 5.5 – 0 kPa. On the other hand, predominant frequency of pressure fluctuation did not vary significantly as gas superficial velocity increased with fixed liquid superficial velocity of 0.6m/s rather the amplitude of the fluctuation increased from 0.5 – 3.5 kPa. Lastly, the observations in the pressure fluctuations for the 16 flow cases having void fraction of 70% were more random since these flow cases cut across bubbly, slug and churn flows. Generally, predominant frequencies increased with mixture velocities while significantly high amplitudes of fluctuations were observed at very low and very high mixture velocities. Visualization test at these two extremes show that slug and Taylor bubbles flow regimes dominate these regions. In addition, the maximum amplitude of displacement fluctuation was observed for flow regimes existing at the two extremes. Also, the maximum predominant frequency of displacement fluctuation was observed in slug flow regime. Generally, displacement fluctuated within 0.2 – 0.8 mm and the general behaviours of pressure fluctuations correlated with displacement fluctuations. This study provides a good resource for validation of numerical and analytical modelling. However, it is limited in both the superficial velocities and pipe diameter that was investigated. In addition, their focus was only on vibration in vertical direction.

Finally, Liu et al. (2012) and Miwa et al. (2015) conducted experimental studies in flow induced vibration (FIV) in vertical and horizontal (Miwa et al. 2016) 90^0 bends of 52.5 mm diameter pipe with a bend radius of 76.2 mm. 36 multiphase flow cases of flows encompassing bubbly, slug, churn and annular flow regimes were investigated in the vertical bend. Gas and liquid superficial velocities were in the range of 0.1–18 m/s and 0.61–2.31 m/s respectively. The horizontal and vertical components of RMS of forces for all the slug and churn flow were reported to be within 2–60 N. The corresponding force frequencies were in the range of 1–7 Hz and 1–11 Hz, respectively. In the slug flow, the experimental values for the maximum magnitude of force fluctuation was approximately 5 N while the predominant frequency was approximately 8 Hz. The corresponding values for the

churn flow were approximately 6 N and 3 Hz, respectively. They developed an analytical model to predict the frequency of force fluctuations based on the two-fluid model. In Miwa et al. (2015), the developed model included an impact force term, which performed better in predicting force fluctuations frequency compared to the previous model without the term. The accuracy of the force frequency model was reported to be approximately 30% and 25% respectively in the two studies as reported in Miwa et al. (2015) and Miwa et al. (2016).

2.1.2 Numerical studies of MFIV measurements in pipes having D<0.1091 m

In parallel to experimental studies, CFD technique has been used for FIV studies. The volume of fluid (VOF) model in computational fluid dynamics (CFD) has been reported to perform satisfactorily in slug flow (Abdulkadir et al., 2015, Gayet et al., 2013, Emmerson et al. 2015, Araujo et al. 2015 and Ratkovich et al. 2013) and churn turbulent flow (Da Riva and Del Col, 2009 and Parsi et al., 2015) modelling. In addition, CFD technique has shown good potentials in FIV investigations (Nennie et al., 2013b, Hofstede et al., 2017, Pontaza et al., 2013, Abuali et al. 2013b, Gayet et al. 2013, Zhu et al. 2015, Zhu et al. 2017 and Montoya-Hernandez et al. 2014).

In a subsequent study by Nennie et al. (2013b), they carried out CFD simulations to investigate the effect of entrance length on slug flow induced forces at bend in pipe of 4 inch diameter. They observed that the calculated forces at the bends when entrance length was short (1.5m) were less than the values obtained in the validated 4 inch pipe of 3m entrance length reported in Nennie et al. (2013a). This was attributed to the fact that slug velocity did not reach the theoretical slug velocity expected at the bend. On the other hand, a long pipe (6m) gave comparable slug velocity and force levels as the validate geometry of 3m entrance length.

Hofstede (2017) applied a coupling of CFD and solid mechanics modelling to study FIV of nuclear fuel rods in axial turbulent flows. They tested the effect of $k-\omega\ SST$ and RSM URANS models on the outcome of Turbulence Induced Vibration (TIV)

simulation in a two-way coupled FSI simulation and observed no direct influence of the URANS models on the FSI simulation. Emmerson et al. (2015) used CFD to study flow induced forces in a horizontal 180^0 pipe bend of 4" (101.6 mm) diameter. The VOF model was used for the two-phase flows modelling while LES was used to model turbulence to predict slug flow with superficial liquid and gas velocities of 2.4 m/s and 2.2m/s respectively. They also modelled a second case from Tay and Thorpe (2004) experiment with superficial liquid velocity of 1.8 m/s and superficial gas velocity of 0.5 m/s within a 70mm diameter pipe of 90^O bend. The RMS value of the horizontal-component of force obtained from CFD was 137.3 N compared to their own experimental value of 131.1 N. Power spectral analysis of the time domain signal of forces gave predominant frequencies in the range of 0 – 5 Hz (1 Hz peak) and 0.5 – 10 Hz (1.8 Hz peak) for the CFD and experimental method respectively. The RMS value of the vertical components of forces obtained with CFD of 22 N did not match with the experimental value of 59.4 N. However, their simulation of Tay and Thorpe (2004) shows good prediction of peak force frequency and average resultant force. Further CFD analyses has been carried out for FIV by Zhu et al. (2015) and Zhu et al. (2017). Their FIV measurement was focused on pipe deflection and they used single-phase CFD analysis to model gas flow with dispersed liquid droplets and sand particles. These studies show that CFD method can perform well in FIV predictions.

Finally, Wang et al. (2018) also presented numerical results of the modal analysis they conducted to predict resonance. They observed that the first 3 orders of natural frequencies of the pipeline-riser system increased as the gas volume fraction at pipe inlet increased. 1^{st} order varied between 2 – 4 Hz while the ranges of the 2^{nd} and 3^{rd} orders were about 5 – 10 Hz and 10 – 20 Hz respectively. Finally, they concluded that although no risk of resonance existed in the flowline, yet the high amplitude and frequency of pressure and displacement fluctuations observed within slug flow regime could induce excessive stress and fatigue failure in the flowline.

2.1.3 Experimental studies of MFIV in pipes having D>0.1091 m

Experimental studies on MFIV in large pipes above 4 inch are very recent. The most relevant of such studies were conducted on pipes of 6 inches (0.1524m)

diameter with different configurations of bend as part of a recent joint industry project (JIP) to define MFIV behaviours and develop CFD approach to predict them in subsea structures. The parameters that were analysed included, time histories, magnitudes and frequencies of hold-up, force, pressure and acceleration obtained at both upstream and downstream of bends (Nennie and Belfroid, 2016 and Belfroid et al. 2016). These experiments were also used to validate CFD studies that were conducted in a subsequent phase of the project (Ponatza et al. 2016, Emmerson et al. 2016a, and Emmerson et al. 2016b).

Nennie and Belfroid (2016) reported MFIV experiments carried out on a 6 inches diameter pipe with a bend of 1.5D. This study experimented on both single phase and multiphase flows. The gas and liquid superficial velocities ranges are 0.9 – 40m/s and 0.0001 – 4m/s respectively. The test section geometries were a horizontal 90^0 bend, vertical and horizontal U-bends. The dimensionless RMS of force as a function of mixture velocities varied between 0.03 – 100 for mixture velocities range of 0.01 – 41m/s. A maximum dimensionless force RMS of 100 was observed in the vertical U-bend. Nennie and Belfroid (2016) compared forces measured directly from the experimental flow loop using force sensors to that calculated by substituting the time history of liquid hold-up obtained by electrical resistance tomography (ERT) and video in a simplified model. The calculated forces compared well with the direct force measurements especially for the calculated forces based on the ERT liquid hold-up measurement. Slug flow induced force fluctuations were in the range of -550 – 1500 N for gas superficial velocities range of 0.9 – 9.4m/s and liquid superficial velocity of ~2m/s, Finally, both studies concluded that the fluctuations of the hold-up dominates the multiphase flow induced forces at bends.

Belfroid et al. (2016a), summarised the results of all the test cases that were investigated by Nennie and Belfroid (2016) for the same flowline geometries and test conditions. Important observations with regards to the behaviour of the non-dimensional force fluctuation as a result of Weber number were reported and compared to the model by Riverin et al. (2006). At higher liquid fractions, their results were mostly outside the 50% accuracy range although, similar trends reported in literature (Liu et al. 2012 and Riverin et al. 2006) were generally observed. At low liquid fractions, their measured force dropped sharply as Weber

number increased indicating a different slope with weber number compared to the Riverine model with constant C given as 10.

Belfroid et al. (2016b) also reported more summaries of the findings in the study by Nennie and Belfroid (2016). They evaluated the critical gas fraction at which the behaviour of the multiphase flow induced forces at the bend transition from single phase gas flow to multiphase flow behaviour. The measured forces were approximately constant at low liquid fractions and the showed a sudden increase at liquid fractions in the range of 1 – 10%. This is due to increased momentum flow as liquid flow rate increases. Finally, at constant gas superficial velocity PSD of Fy fluctuation dropped continuously with increase in frequency for liquid volume fractions below ~2%. On the other hand, a clear pick was observed in PSD for liquid volume fractions above 2%.

In the case of pipe diameters larger than 6 inches, this study is only able to report FIV experimental investigation due to single phase flows. Most of the reports are based on the report by Yamano et al. (2011) on the investigations carried out by Japan Atomic Energy Agency (JAEA) on the FIV characteristics in large 90^0 pipe bends for the purpose of developing FIV evaluation methodology for Japan sodium-cooled fast reactor (JSFR). The operating conditions of the JSFR have ranges of 0.56 – 1.27m pipe diameter, 12.7, 17.5mm pipe thickness, 7.3 – 9.1m/s flow velocity, 1.3 $X10^7$ – 4.2 X 10^7 Reynolds numbers and 395 - 550^0C temperature. Therefore, experiments had to be carried out only by using scaled down models of the real system. However, in order to increase the fidelity of extrapolating the experimental observations to the JSFR system, their evaluation approach involved examining the dependency of FIV characteristics on the Reynolds number (velocity, viscosity and scale). The ranges of the test section scale, Re number, velocity and temperature (viscosity) that were examined in the experiment are, 1/15 – 1/3, $3X10^5$ – $8X10^6$, 0.8 - 9.2m/s and 20^0C – 60^0C respectively.

Yamano et al. (2011a) focused on investigating the transient flow separation behaviours at the elbow as the main source of pressure fluctuation at the bend. In the 1/3 scale L-shaped elbow test section which is a 0.41m diameter pipe, 124 pressure transducers were installed at different positions on the elbow test section to measure pressure fluctuations on the pipe wall which correspond to the FIV

exciting forces. Flow visualization showed flow separation at the intrados of the elbow exit area accompanied by vortex shedding and then a subsequent re-attachment at about 0.29m downstream of the separation. This observation was not dependent on velocities within the scope of their study. Also, velocity distribution in the radial direction was observed to be independent of the Re number. The non-dimensional PSD of pressure fluctuation within the region of separation was dominant with a peak of about 0.1 PSD at ~0.45 Strouhal number. A comparison between velocities of 7.0m/s and 9.2m/s as well as fluid temperature of 20^0C and 60^0C show that the non-dimensional PSD of pressure fluctuation was not dependent on Reynolds number. Inlet conditions were also varied between 0% and 5% of swirl flow velocity ratio at 20^0C and 9m/s. Although the trends seen in the values of PSD as a function of Strouhal number for both inlet conditions were similar at each of the elbow regions, PSDs in the case of 5% were higher than the 0% but not in a significant way. Generally, the non-dimensional PSD of pressure fluctuation range was obtained to be 10^{-6} – 10^{-1} for Strouhal number range of 10^{-1} – 10 and results concluded that the inlet swirl flow had no significant effect on pressure fluctuations on the pipe wall although a slight deformation of flow separation was observed.

In another study based on the JSFR test conditions by Yamano et al. (2011), Yamano et al. (2011b), compared the time-averaged velocity profiles obtained at a position of 0.17D downstream of elbow between the 1/3 and 1/10 scale test sections for Re = 3.2 X 10^5 and observed no dependence on the test scale. They also, carried out tests to investigate the effect of elbow curvature on FIV. In this case they used a 1/8 scale experiment and elbow radius of curvatures of 1.0 and 1.5 were understudied. They observed that at the elbow exit, flow separation occurred continuously in the short elbow while occurring intermittently in the long-elbow. Also, the observation of secondary flows in the elbows show that the radius of curvature influenced both the position of the separation region and high-turbulence intensity region.

2.1.4 Numerical studies of MFIV in pipes having D>0.1091 m

Generally, MFIV in large pipes are rare and most of the few available recent investigations are actively exploring the applicability of numerical methods to predict FIV. This is because carrying out comprehensive life scale experiments of oil and gas and nuclear energy pipework where the effect of all characteristic MFIV parameters could be tested might be hazardous and very costly. This section presents the most relevant literature that implemented numerical method to investigate the problem of FIV for pipes having diameters of >5inches (0.127m).

Montoya-Hernandez et al. (2014) conducted a study on multiphase flow in large pipes with diameter up to 5 inches. However, they assumed the multiphase flow to be a homogenously mixed single phase in their formulation. This assumption could lead to invalid conclusions if the formulation is applied to slug and churn flow patterns.

Pontaza et al. (2016) carried out a CFD study on slug flow and annular dispersed flow regimes FIV in a pipe of 0.1524m diameter with a 90^0 bend and radius of curvature of 1.5D in order to compare CFD results to experimental results in literature. The VOF model and LES approach were used to model the multiphase flow and turbulence respectively. Two flow cases were used in their analysis. The annular flow gas and liquid superficial velocities were 20.1 and 2.0 m/s while that of the slug flow were 10.45 and 1m/s. Force fluctuations range for slug flow was -500 - 1000 N and the predominant frequencies of the PSD of force fluctuation in both x and y direction were ~1Hz. Their most significant finding is that the standard deviation of flow induced forcing for both CFD prediction and experimental measurement s had a level of agreement within ±20%.

A similar study was carried out by Emmerson et al. (2016a). They implemented the VOF model in CFD method to model the multiphase flow while turbulence was modelled with LES. The Quasi Three-dimensional (Q3D) CFD approach described by Emmerson et al. (2015) was used in this study to define inlet conditions in the 90^0 horizontal 0.1524m (6”) pipe bend. CFD results were compared to experimental measurements obtained from a flow loop with firstly, a straight horizontal inlet pipe section and secondly, a vertical U-bend section upstream of the horizontal bend of interest. For a slug flow case having gas and liquid superficial

velocities of 3.2 m/s and 2.1 m/s, the force fluctuations were generally in the range of 0 - 400 N for CFD and 100 - 300 N for experimental measurements in the test section having U-bend. The magnitude of this force fluctuation was about 30% lower compared to the case of the straight horizontal inlet pipe section. Also, the predominant frequency of the PSDs of Fx and Fy fluctuations were ~0.8Hz in both experiment and CFD prediction. In conclusion, the CFD was able to predict the magnitude of force fluctuation within 2% and 7% for the straight inlet and the U-bend upstream section cases, respectively.

Pontaza et al. (2013a) have applied CFD and FEA to investigate flow induced vibration on a subsea pipe jumper and compared the effects on Tee and Bend. Their modelling has the weakness of neglecting liquid phase volume fraction of 1.5% and treating the flow as single-phase. Subsequently, Pontaza et al. (2013b) used the CFD technique to carry out a FIV assessment of an operational subsea oil and gas manifold with a combination of bends and T-joints for a single mixture velocity with 2.2% liquid gas condensate using two-phase flow modelling. Their flow domain consisted of 8”X6” connection leading to 12” pipe. Force calculations were carried out on the T-joint and a vertical 6” 90^0 bend upstream of the joint. The study reported a predominant frequency in the range of 10-40 Hz from the power spectral analysis of the time domain signal of the three components of forces. They also showed that including liquid phase broadens the frequency range compared to single-phase gas only flow modelling. The pipe vibration was seen as displacement fluctuations in the range -0.1 – 0.1 mm at the pipe bends. The PSD of the predicted nominal stress fluctuation signal showed important frequencies within 20 – 70 Hz where the frequencies of the predominant stress magnitudes were at ~23 Hz for the 6’’X8’’ connection and ~50 Hz for a 2”X6” small bore connection.

Yamano et al. (2011a) also used numerical simulation-based methodology in their study. This was a one-way FSI coupling because the pipe vibration feedback force due to pipe displacement/motion is significantly less than the fluid flow induced force in such a way that its feedback effect on the fluid flow will not be significant. Hence, the time-history of the fluid force obtained from CFD simulation is directly fed into the structural analysis simulation code to evaluate the structural stresses due to vibration. They applied U-RANS approach by solving the Reynold stress

models (RSM) equations. The normalised velocity profiles from the simulation match the experiments. The result validates the applicability of URANS approach to flow separation because such flow is mostly influenced by the convective term and not the turbulence term. This suggests that the URANS method can model the large-scale vortices generated by the flow separation. However, the method is not very suitable for modelling small-scale vortices. The simulation was able to capture the two peaks at 0.5 and 1.0 Strouhal Number obtained in experiment. Finally, the modelling approach satisfactorily modelled the pressure fluctuation PSD although the amplitude level of the PSD was generally underestimated in the Re = 1.2 $X10^6$ (3.0m/s) compared to the Re = 3.6 X 10^6 (9.2m/s).

Yamano et al. (2011b) also carried out CFD simulations using URANS, LES and DES approaches and compared results to experimental measurements. The first approach showed better conformity to experiment than the others. For the 1/3 scale experiment (Re = 3.6 $X10^6$ and Velocity = 9.2m/s), the URANS approach was able to predict the backflow due to separation which occurred at a position of 0.18D downstream of elbow within the z/D<0.2 region as well as the re-attachment and attenuation of the low-velocity region which occurred at 0.61D (z/D<1) and 1.1D respectively. They also reported that the pressure fluctuation PSD results agreed with experiment. Peak frequency of 10Hz and 12Hz were obtained near the separation region boundary for the experiment and URANS calculation respectively. Although a second peak was observed at 24 Hz in the simulation which was attributed to the alternating supply of secondary flows from both sides of the separation region and PSD amplitude was also generally underestimated.

Takaya et al. (2017) also carried out a numerical investigation of the same 1/3 scaled model of the hot-leg elbow piping of JSFR system that was evaluated by Yamano et al. (2011a) under the inlet uniform rectified flow condition. They equally solved the U-RANS with RSM to capture the complex behaviours of the high velocity turbulent flow induced vibration at the elbow. Vibration analysis and stress on the piping was calculated using the pressure fluctuation data obtained from the U-RANS modelling of the flow on a 304 stainless steel elbow section. The flow condition in this study include, a short elbow having diameter of 0.41m, mean flow velocity of 9.2m/s and temperature of 60^0C corresponding to Reynolds number of

8 X 10^6. This numerical study is assumed to be an improvement of the modelling carried out by Yamano (2011) for the same flow condition because a better agreement was observed between their numerically calculated PSD of pressure fluctuations results and the experimental measurements at the downstream of the elbow. Generally, the non-dimensional PSD of pressure fluctuation varied between $1X10^{-6}$ – $1X10^{-1}$ for Strouhal number range of 10^{-1} – 10 within the flow separation region in both experiment and numerical results. Results obtained numerically for the upstream (bend inlet), within the bend and outer region of the separation zone at the downstream didn't agree very well with experiment compared to the separation zone results, although the trends were similar. The non-agreeing numerical results consistently underestimated the experimental results and varied between ~$1X10^{-10}$ – $1X10^{-3}$ while the experiment varied between $1X10^{-6}$ – $1X10^{-2}$ for the same Strouhal number range. In addition, the numerical PSD results generally underestimated the experiment results at high Strouhal numbers for all locations on the test section. The discrepancies and agreement in results from both methods were attributed to the time average approach of URANS and its ability to predict large vortexes at the separation region respectively. Nevertheless, the calculated stress which varied between ~0.03 and 0.3 MPa showed good agreement with experimental measured stress indicating that the accurate prediction of pressure fluctuation within the main recirculation location is mostly important for FIV prediction in the high velocity single phase (liquid) large pipe flow.

Sanchis and Jakobsen (2012) also carried out URANS CFD simulations to investigate the capability of the two-equation SST turbulence to accurately predict the characteristic FIV behaviours in bends of subsea oil and gas production systems. Firstly, a single phase oil flow at 3.21 m/s and Re number of 5.4 X 10^5 through a pipe of diameter 0.15 m is simulated. Then multiphase phase flow having liquid as continuous phase and gas as dispersed phase is also simulated using the Eulerian-Eulerian multiphase model and a single SST URANS turbulence model solved for both phases. Their main conclusions are that the separation zone is larger in multiphase flow and mainly filled with the gas phase and that the magnitude of wall pressure fluctuation is much higher in multiphase flow but at similar frequency as in the single phase flow. Generally, the risk of FIV is increased in the case of multiphase flow.

Finally, as part of an ongoing JIP to develop MFIV predictive models for subsea flowlines, Kim and Srinil (2018) reported their numerical simulation of a full scale M-shaped subsea jumper transporting slug flows. The pipe diameter is 0.240m and both gas and liquid superficial velocities where 5m/s each. A one-way FSI analysis was carried out by coupling CFD simulation of fluid flow with static structural analysis of the jumper structure. The VOF and the $k-\omega$ SST RANS model were used to model the slug flow and turbulence respectively. They observed a successive decrease in the amplitude of the pressure forces acting on the bend wall from the jumper inlet to the outlet. This was attributed to drop in both momentum and pressure along the jumper. A modal analysis showed the range of the first six natural frequencies of the subsea jumper to be 3.5 – 14.7 Hz. A risk of resonance effect was also established because the predominant frequencies of the stress and displacement fluctuations are around some of the natural frequencies of the jumper. However, none of these results were validated with experimental results.

2.2 Turbulence modelling in FIV investigations

Turbulence has been modelled in different MFIV studies by solving the URANS equations with any one of the turbulence models; $k-\epsilon$ models, SST transition models, $K-\omega$ SST models and RSM equations. A few large pipe investigations have also applied LES and DES approaches to predict turbulence. Depending on the MFIV excitation mechanism, different turbulence models could perform optimally for the different mechanisms. For instance, in the study by Hofstede (2017) in which they examined the effect of linear $k-\omega\,SST$ and non-linear RSM (with Elliptic Blending) URANS model on turbulence induced vibration (TIV) due to liquid single-phase flow. They observed that the frequencies of the pipe vibration in the x and y direction are similar and match closely to experimentally obtained values, however the frequency in the x-direction differed from the experimental results by 10%. The difference was attributed to the fact that unlike the LES, the URANS models couldn't capture the random high frequency fluctuations emanating from the turbulent pressure and velocity field but could capture the pressure oscillations due to low frequency large vortical structures. The effect of such low frequency structures is captured in the time averaged turbulent fluctuations solved by URANS

and they are uniform in the x and y direction. Hence, when the focus is to predict single phase flow induced turbulence, the URANS model has limitations. However, although the results are not exact match but close enough and since in the present study simulation, the vibration was due to a uniform body force introduced as the initial perturbation and not just the turbulent pressure fluctuations, it is concluded that the URANS model performed well.

In addition, Emmerson et al. (2015) compared the effect of realizable $k-\epsilon$ and Large Eddy Simulation (LES) turbulence models in the MFIV investigation in horizontal pipe. When realizable $k-\epsilon$ model was applied, they observed smearing of the interface between the gas and liquid phase due to increased turbulence generation, hence damping out wave initiation at the interface. This behaviour was not observed when LES was used. However, since multiphase flow effects are considered to contribute more to the force fluctuations compared to turbulence effect, the $k-\epsilon$ model was used in addition to the Q3D CFD section used to spontaneously develop slug flow.

Pontaza et al. (2016) and Emmerson et al. (2016a) applied LES model with VOF model to simulate slug flow. The former modelled the smallest turbulent eddies using the Smagorinsky eddy viscosity model and the filter cut-off was the local grid size. The turbulent scales larger than the grid size are resolved directly. Their result compared favourably with experimental measurements. However, LES requires more mesh-resolution and computing resources compared to URANS equation. Although Pontaza et al. (2016) were able to perform their simulation on high-performance computer (HPC) that distributes workload on 128 processors in parallel, such computing resources are not commonly available.

Finally, Yamano et al. (2011a), Yamano et al. (2011b) and Takaya et al. (2017) observed that although RSM URANS model are not able to capture the small-scale vortices, the model was able to capture the large-scale vortices generated by the flow separation and its re-attachment downstream of the bend. The pressure fluctuations on the wall of the pipe downstream of the bend due to the flow separation and re-attachment were the main source of FIV in their investigation of single-phase flow through large pipe bend. This mechanism of FIV due to single phase flow is different from the MFIV mechanism in the sense that the effect of

the density difference due to multiphase flow impacting the inner wall of a pipe bend is more significant than the effect of turbulence on the flow induced force fluctuations on the pipe wall in multiphase flow. In addition, RSM is more computationally intensive than two-equation URANS models such as the $k-\epsilon$ model which requires a modest computing resources to produce a reasonably accurate solution compared to the rest models and approaches of calculating turbulence (Versteeg and Malalasekera, 2007). Hence, in typical cases of slug/churn flow induced vibration at pipe bend where the interest is in the impact forces at pipe bend due to in-flow of the alternating/large waves multiphase flow rather than the vibration induced by flow separation at the downstream of the bend, it might not be necessary to apply RSM URANS model.

2.3 Knowledge gaps

In summary, above literature reviews show that the most relevant MFIV predictive models are based on small pipes. For instance, the analytical model presented in Liu et al. (2012) and Miwa et al. (2015) which is capable of predicting the frequency of excitation forces within 30% accuracy. However, in addition to the relatively high margin of error of the model, the proposed analytical model also requires void fraction data from experimental measurement as input to calculate impact force fluctuations term. Thus, in order to use the model to solve flow problems at both operating and design stages of practical systems, experiments have to be conducted to extract void fraction signals using the problem specific flow conditions and geometry. On the other hand, the RMS of fluctuating force could be predicted using Riverin et al. (2006) empirical correlation within 50-75% gas volume fraction. However, this model's error margin is up to 50%. Furthermore, an attempt to fit the measured forces from a practical large pipe experiment to the model has shown that the model will predict RMS of fluctuating force in large pipe further outside the 50% error margin (Belfroid et al., 2016a).

In addition, since the physical mechanisms resulting to phase distributions of multiphase flows in pipes would differ between small pipes and large pipes and between horizontal and vertical pipes, it would be inaccurate to generalise conclusions on MFIV parameters behaviours and interactions that were obtained

for small pipes to be applicable to large pipes. For instance, Nennie et al. (2013a)'s conclusion that the effect of liquid hold-up on flow induced forces is equal for different pipe sizes was based on small pipes and might not hold for a large pipe of 0.203m diameter with a bend in vertical upward flow orientation. Hence, for the confidence level of a conclusion to be adequate, different diameters need to be tested. This is also an impractical solution if experimental method is to be used. On the other hand, CFD method has been performing satisfactorily in multiphase modelling in recent times making this method a viable tool to predict both frequency and the RMS of force fluctuations with all operating ranges. However, current literature on the comprehensive application of CFD for MFIV study, encompassing a range of flow velocities in a range of pipe diameters from small to large pipes is rather limited.

Finally, correlating stress and displacement magnitudes and predominant frequencies with pipe diameter is an important aspect of FIV evaluation which can give more insight into the best approach to scale up lab measurements to practical-sized system of pipe bends. Such analysis is lacking in literature. Also, the effect of added mass due to internal multiphase flow quality is crucial in evaluating the natural frequencies of a pipe structure and should not be ignored in an MFIV evaluation. Although, the extent of the influence of this factor for different pipe sizes has not been reported in literature. Furthermore, reduced or zero risk of resonance does not eliminate the effect of excessive stress and fatigue failure, hence detailed calculation of stress is required in MFIV evaluation.

In conclusion, studies on CFD modelling of multiphase flows and MFIV have been gaining more attention in recent times over experiments due to advantages such as less cost compared to the high cost of carrying out large scale or hazardous experiments. However, due to inherent complexities associated with interfaces and turbulence behaviours in different multiphase flow regimes, optimum application of CFD modelling technique requires in-depth in-sight to the predominant interface and turbulence behaviours as well as validation of the defining characteristics of the flow with experiment. Some of the mentioned studies validated some or all of their CFD results with experimental results and the various agreements reported in literature between these two methods have increased the confidence level in CFD method for research. Generally, VOF model has been applied both in small

and large pipes to predict void fraction advection in slug and churn flows. Therefore, the present study applies a CFD modelling technique using VOF and RANS turbulence models to simulate flow induced fluctuating forces for a wide range of flow conditions covering slug, cap bubbly, churn-turbulent and churn flows. The CFD simulations of flow induced properties has been validated against the experimental data of Liu at al. (2012) and the empirical model of Riverin et al. (2006) using the small scale pipe, thus giving confidence in extending the CFD method for investigating flow induced vibration in larger pipes of similar geometry containing the flow of similar flow regimes.

CHAPTER 3

METHODOLOGY

This chapter starts by presenting the fundamental theory of two-phase flow modelling in fluid dynamics engineering. The discussion forms a good pre-requisite understanding of the theories of flow regime identification which is discussed next. Since literature shows that MFIV is flow regime specific, in-depth understanding of the physical mechanisms in such flows and the accurate identification of the flow regimes in both the small and large pipes are the first steps to characterising the vibration behaviours of pipe bends conveying such flows. Then the CFD method is presented with a detailed presentation of the multiphase and turbulence models that were implemented in the present study. Finally, the transient structural dynamic modelling and modal analysis which are based on finite element analysis of structures are presented. The schematic overview of the methods and process implemented in the present study are shown below in Figure 3.1.

3.1 Theory of two-phase flow modelling

Many material flows in real life industry are multiphase flows. However, the basis of the theories of such flows rest on the accurate understanding and modelling of single phase flows. The analysis of single phase flow is based on the concept that the fluid is a continuum. This fundamental theory in analysing the behaviour of fluids is that if the scales of time and lengths are much greater than the characteristic molecular lengths and times, then describing the fluids as a continuum gives accurate quantitative analysis of the fluid dynamics behaviour of the system. This means that fluid properties at a point in space are treated mathematically as continuous functions of space and time. Therefore, the basic conservation equations are developed using the standard method of continuum mechanics (Jakobsen, 2014 and Ishii and Hibiki, 2010).

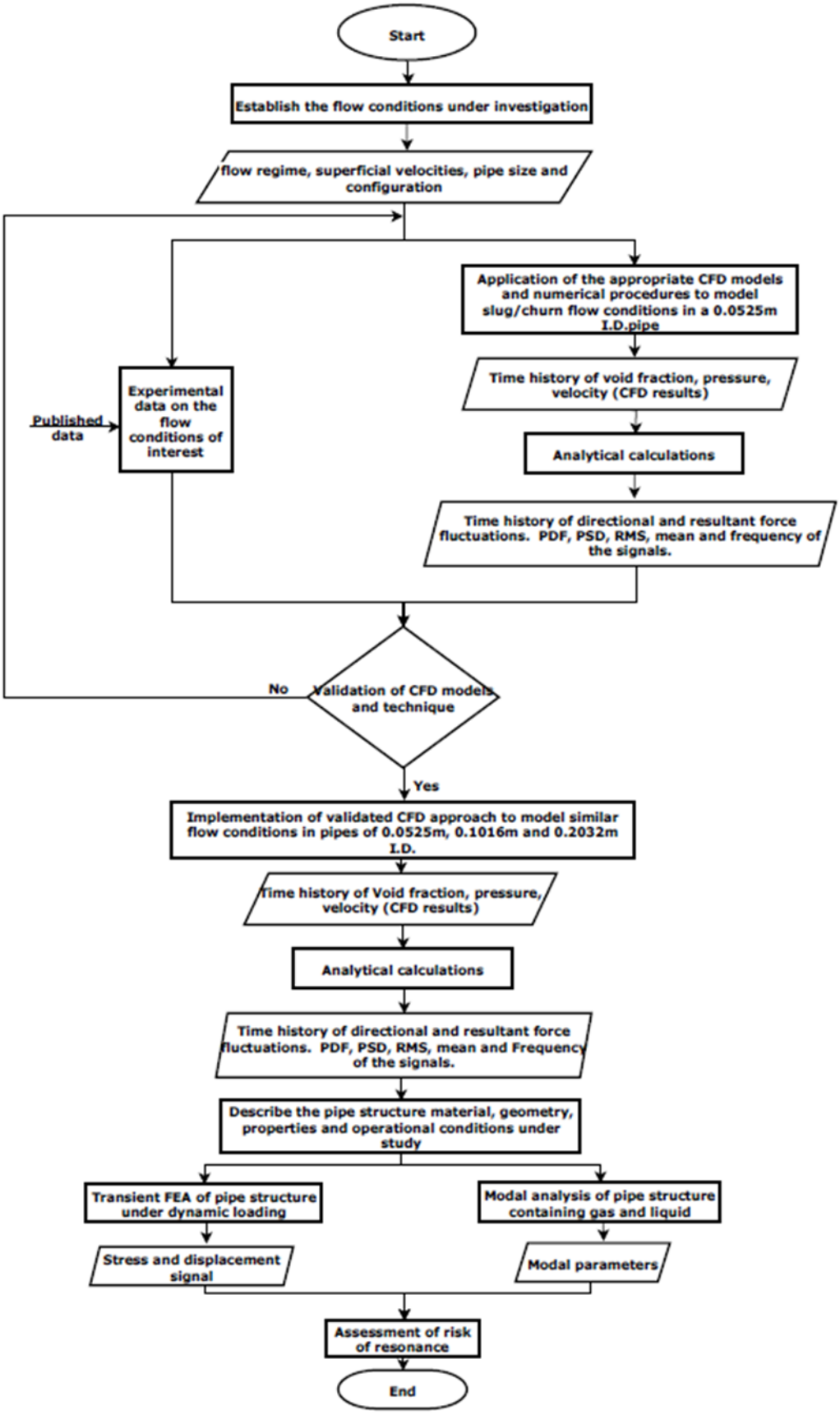

Figure 3.1: Schematic overview of the investigation

Ishii and Hibiki (2010) termed the formulation of the governing equations of flow problems based on the local instant variation of flow properties as local instant formulation. The equations are of two categories known as balance equations and constitutive equations. The balance equations demonstrate that fluid flow quantities in motion are always balanced. The balance equation is generally given in differential form for the transport of a property ∅ as (Versteeg and Malalasekera, 2007):

$$\frac{\partial(\rho\emptyset)}{\partial t} + div(\rho\emptyset\boldsymbol{u}) = div(\Gamma\, grad\, \phi) + S_\phi \qquad (3.1)$$

where, ρ, u, ∅, Γ, S_ϕ are given as density, velocity, arbitrary flow property, diffusion coefficient and rate of increase of ∅ due to sources. From the first term on the left-hand side to the last term on the right-hand side, the terms are described as, the rate of change, the convective, the diffusive and the source terms respectively.

For mass, momentum and total energy which are conservable quantities, the version of balance equations which express their classical laws are called conservation equations. In addition, the balance equations for quantities which may not be conserved are called transport equations, example the transport equation for turbulent Reynolds stresses (Jakobsen 2014). On the other hand, the constitutive equations give quantitative description of the physical properties of fluids and these equations can be classified as:

- Mechanical constitutive equations e.g, Newton's viscosity law,
- Energetic constitutive equations e.g, Fourier's law of heat conduction,
- Constitutive equation of state e.g; the equation of state.

In single phase flows, the set of the balance and appropriate constitutive equations is expected to form a closed set of equations ready for solving. In two-phase flows, the local instant formulations based on the continuum theory is also applied by considering the two-phase flow field to be a multi-region field of single phases resulting in a multi-boundary problem in which the boundaries between the phases

are moving. These equations form the basis for the macroscopic two-phase flow models when different averaging methods are applied to them. The main distinguishing feature of the two phase formulations is the treatment of the balance equations and the constitutive equations at the interfaces between the phases. According to Ishii and Hibiki (2010), the balance of flow quantities at the interface is called a jump condition while the application of the constitutive laws at the interface yields interfacial boundary conditions. From the ongoing discussion, it follows that continuum formulations of two-phase flow problem involve, the derivation of:

- the field equation,
- the constitutive equation,
- and the interfacial conditions.

The interfacial structure of two-phase flows directly influences the steady and dynamic characteristics of the flow on a macroscopic level, for instance the rate of momentum transfer between the phases. Therefore, any chosen averaging method applied to the local properties of the flow must be able to fully capture the prevailing combined interfacial dynamics, particle-particle and particle-continuous phase interaction.

In order to obtain the macroscopic mean values of two-phase flow properties, three main averaging procedures can be used. The Eulerian, the Lagrangian and the Boltzmann statistical averaging (Ishii and Hibiki, 2010). The first averaging method is most widely used because the standard field equations of continuum mechanics conform to its time-space definition of physical phenomena. This method levels out the instant local variations of flow properties within a domain by integration. The second method is useful when the mean behaviour of an individual flow particle over some finite time interval is required. Lastly the Boltzmann statistical averaging is useful when the interest is no longer on a single particle but on the collective behaviour of a group of many particles. In the context of mixture, separated and bubbly two-phase flows, several researchers (Ishii 1971, Ishii, 1977, Ishii and mishima, 1984, Zuber 1964, Zuber et al. 1964, Zuber 1967, Delhaye 1968, Venier and Dehaye 1968, Kocamustafaogullari, 1971, Arnold et al.

1989, Zhang and Prosperetti, 1994a, Zhang and Prosperetti, 1994b) have applied the different averaging methods to derive two fundamental formulations of the macroscopic field equations: the drift flux (mixture) and the two-fluid model. In mixture model, the two phases are considered to be a mixture, therefore one equation each is solved for mass, momentum and energy conservation including an extra diffusion (continuity) equation to account for the changes in phase concentration. The drift flux model is a type of mixture model that involves models to account for the diffusion, slip and homogeneity of flow. On the other hand, two-fluid model treats the phases in two-phase flow separately and therefore solves a complete set of the mass, momentum and energy equations for each of the phases including three jump conditions for coupling both fields. More details on the averaging methods can be found in Ishii and Hibiki (2010).

The drift-flux (mixture) and two fluid model formulations form the bases of the mixture, VOF and Eulerian multiphase flow models used in CFD modelling of two-phase flows. Choice of the model to apply for a particular multiphase flow problem depends on:

- Identification of the flow regime of interest to be modelled
- Matching the flow physical mechanisms and properties such as interfacial area geometry as well as the intrinsic phases' interaction to the appropriate multiphase model which was developed based on the identified features.

Literature surveyed in the present study has established that MFIV is flow regime dependent with emphasis on slug and churn flows in both small and large pipes as the flow regimes with the most significant forcing functions. It follows that individual flow regimes result in different hydrodynamic characteristics and turbulence behaviours which influence important FIV mechanisms such as momentum transfer and pressure drop across pipe bends. The most significant behaviours of these flow regimes would also depend on the interface structure and wave dynamics. Hence, in order to accurately characterise and predict MFIV it is important to identify the flow regime present at particular flow velocities so that the most appropriate multiphase flow models and turbulence models can be applied to accurately predict the fluctuations of the hydrodynamic flow properties that would induce the vibrations and stresses in the flowline structures.

3.2 Flow regime identification

Two-phase gas liquid flow regimes in pipes having circular cross-section depend on the flow rates, pipe size, pipe orientation, fluid properties and operating conditions. The four basic flow regimes which occur in upward flow in pipes of circular cross-section are bubbly, slug, churn and annular flow regimes. However, the slug flow regime can appear differently in the form of bubbly-cap flow in pipes of larger diameter. In addition, the transition mechanism from one flow regime to another also differ from small pipes to large pipe sizes. Hence, this section discusses pertinent flow regime maps and their transition mechanisms for small and large diameter pipes in order to accurately identify the flow case studies of interest to this study.

3.2.1 Two-phase flow in small diameter pipes

The presence of interfacial shear, drag, surface tensions, associated discontinuities and the resulting complex transfer mechanisms between phases and between phases and flow channel wall lead to complexities in identification of flow regimes and modelling of their transitions. Earlier flow maps which are based on empirical correlations and experimental observation were limited to the conditions near those of the experimental measurements. Recent studies have been based on the flow regimes descriptions by Taitel et al. (1980) and Mishima and Ishii (1984). They developed transitions models based on mechanistic modelling of the flow regimes mechanisms. Taitel et al. (1980) postulated that their mathematical models which were based on the physical mechanisms of the flow regimes and transitions are largely free of the shortcomings of empirically based transition maps since they included the effect of fluid properties and pipe size in their formulation. The criteria for flow regime transition based on Mishima and Ishii (1984) with reference to Taitel et al. (1980) are discussed below.

- Bubbly to slug flow transition

The physical mechanism which has been discussed in literature (Mishima and Ishii, 1984 and Taitel et al. 1980) are the collision and agglomeration or coalescence of small gas bubbles as gas rate increases. Here, discrete gas bubbles combine into

larger bubbles having diameters that are approximately equal to the pipe diameter. Taitel et al. (1980) described these larger bubbles observed at the transition stage as having lengths of 1-2 diameters. Mishima and Ishii, (1984) referred to these bubbles as cap bubbles and reported a further coalescence at the wake region of the bubble which invariable increases the length of the cap bubble to the full size of Taylor or slug bubble. They proposed a tetrahedral lattice pattern of bubble distribution from which they calculated that transition occurs at void fraction of 0.3 due to maximum packing of the lattice structure. The gas and liquid superficial velocities which gives this transition on a 2-dimensional flow map is given below (Mishima and Ishii, 1984):

$$j_f = \left(\frac{3.33}{C_o} - 1\right) j_g - \frac{0.76}{C_o}\left(\frac{\sigma g \Delta\rho}{\rho_f^2}\right)^{1/4} \tag{3.2}$$

$$C_o = 1.2 - 0.2\sqrt{\left(\frac{\rho_g}{\rho_f}\right)} \tag{3.3}$$

$$j = j_g + j_f \tag{3.4}$$

where, $j, j_f, j_g, \sigma, g, \Delta\rho, \rho_g \text{ and } \rho_f$ are respectively, mixture velocity, liquid superficial velocity, gas superficial velocity, surface tension, gravity, density difference between gas and liquid, gas density and liquid density.

- Slug to churn flow transition

The slug to churn flow transition is more difficult to identify accurately due to the complexity in describing churn flow mechanism itself. According to Taitel et al. (1980), churn flow has been identified by gas froths, liquid film instability adjacent to the Taylor bubble or the oscillation of the short liquid slug between two successive gas slugs. Their experimental observation indicate that churn flow is an entry region phenomenon associated with the existence of slug flow further into the flow channel. Hence, depending on the flow rates and pipe size, churn flow will eventually disappear and stable slug will appear at some distance from the inlet

along the flow direction in any flow which is initially observed as churn flow. The entrance length is given as:

$$\frac{l_E}{D} = 40.6\left(\frac{U_M}{\sqrt{gD}} + 0.22\right) \tag{3.5}$$

D is pipe diameter and U_m is obtained from substituting Nicklin et al.'s (1962) relation for the rising velocity of Taylor bubbles U_G in a concurrent flow of liquid U_L in to the relation for total volumetric flow rate:

$$Q = U_M A = U_L A(1 - \alpha_T) + U_G A \alpha_T = (U_{GS} + U_{LS})A \tag{3.6}$$

Where $\alpha_T = 0.25$ is the void fraction for slug flow to occur and U_G is given by Nicklin et al.'s (1962) as:

$$U_G = 1.2U_L + 0.35\sqrt{gD} \tag{3.7}$$

Conversely, Mishima and Ishii (1984) defined the slug to churn flow transition to be based on the physical condition that slug flow transits into churn flow when the mean void fraction over the entire flow region attains the average void fraction in the slug-bubble section. The slug to churn flow transition is given as:

$$\alpha \geq 1 - 0.813 \times \left\{ \frac{(C_0 - 1)j + 0.35\sqrt{\Delta\rho g D/\rho_f}}{j + 0.75\sqrt{\left(\Delta\rho g D/\rho_f\right)\left(\Delta\rho g D^3/\rho_f v_f^2\right)^{1/18}}} \right\}^{0.75} \tag{3.8}$$

The last term in the denominator in Equation (3.8) above can be simplified for weak viscous fluids such as water as:

$$\left(\Delta\rho g D^3/\rho_f v_f^2\right)^{1/18} \approx 3 \qquad (3.9)$$

Finally, Mishima and Ishii (1984) represented the transition criterion given above in terms of j_f and j_g using a relationship from the drift-flux model given as:

$$\alpha = \frac{j_g}{C_0 j + 0.35(\Delta\rho g D/\rho_f)} \qquad (3.10)$$

- Churn to annular flow

Taitel et al. (1980) developed a model to identify churn to annular flow transition based on the physical mechanism underlying the upward flow of the liquid film against gravity, the breakaway of the wavy interface of the film and the entrainment of the liquid droplet in the upward flowing gas core. Interfacial shear and drag were the mechanisms in play. The opposing gravity and drag forces acting on a liquid droplet entrained in an upward fast flowing gas core were balanced to obtain the velocity below which stable annular flow could not exist. By treating the interaction between the crests of the upward flowing liquid film wave and the gas core exactly as the interaction between the liquid droplet and gas core, they gave the transition model as:

$$\frac{U_{GS}\rho_G^{1/2}}{[\sigma g(\rho_L - \rho_G)]^{1/4}} = 3.1 \qquad (3.11)$$

Mishima and Ishii (1984) suggested that churn flow to annular flow transition is based on two mechanisms. Firstly the flow reversal mechanism in the liquid film surrounding large bubbles. Secondly, similar to Taitel et al. (1980), they also suggest that the transition could be based on balancing the interaction between interfacial shear and drag forces of the gas core on the film wave crests and the surface tension force of the liquid film. Based on the initial mechanism, the first criterion was developed as:

$$j_g = \sqrt{\left(\frac{\Delta\rho g D}{\rho_g}\right)(\alpha - 0.11)} \tag{3.12}$$

where α is given by equation (3.8).

The second mechanism was used to develop another churn to annular flow transition criterion given as:

$$\alpha = \frac{j_g}{C_0 j + \sqrt{2\left(\sigma g \Delta\rho / \rho_f^2\right)^{1/4}}} \tag{3.13}$$

Equation 3.13 is used for flow in large diameter pipes for which diameter is given as (Mishima and Ishii, 1984):

$$D > \frac{\sqrt{(\sigma/\Delta\rho g) N_{\mu f}^{-0.4}}}{[(1 - 0.11 C_0)/C_0]^2} \tag{3.14}$$

3.2.2 Two-phase flow in large diameter pipes

The characteristics of two-phase flow in large pipes differ from that in small pipes within some ranges of gas and liquid superficial velocities. An important defining characteristic which differentiates large and small pipes lies in the mechanism known as surface instability which causes large gas bubbles to break-up. In large pipes, the surfaces of large bubbles experience distortions caused by turbulent fluctuations or Kelvin-Helmhotz instability. Due to the distortions, Taylor instability encourages the growth of the disturbance manifesting as break-up of the large bubbles (Shen et al. 2014). On the other hand, the instability and distortions which would have occurred on the upper surface of bubbles in small pipes are damped out due to the restraining effect of the pipe walls. Therefore, large gas slugs cannot exist in large pipes but they exist in small pipes. Kataoka and Ishii (1987) defined the critical diameter at which the large slug bubble disintegrates to cap bubbles as:

$$D_H^* = \frac{D_H}{\sqrt{\sigma/g\Delta\rho}} \geq 40 \qquad (3.15)$$

As mention in preceding chapter, pipes with non-dimensional hydraulic diameter, D_H^*, less than 18.6 are considered small pipes. In small pipes, where stable Taylor bubbles exist, the pipe wall forms a boundary limiting bubble growth in terms of increasing bubble diameter. Therefore, rather than increasing bubble diameter, the bubble elongates in the longitudinal direction of the pipe forming slug bubbles that entirely bridges the pipe cross section. Schlegel et al. (2010) and Shen et al. (2014) recommend a transition region of $18.6<D_H^*<30$ and $18.5<D_H^*<40$ respectively where the bubble stability caused by the pipe wall begins to reduce drastically until the upper limit of the range where pipe wall will have no more effect on the cap bubbles.

Therefore, the absence of long slug bubbles in large pipes indicate that the flow regime transition criteria proposed for small pipes may not entirely be applicable to large pipes. Before discussing the flow regime transitions in large pipes, it is important to clarify to a good extent, the generally accepted flow regimes/flow patterns obtainable in large pipes. The earliest study to identify flow regimes in large pipes was by Ohnuki and Akimoto (2000). They carried out experiments to investigate the characteristics of flow pattern and phase distribution in upward air-water two-phase flow in two large vertical pipes. One of the pipes has I.D 0.48m and L/D of about 4.2 while the other has I.D of 0.2m and L/D of about 60. They proposed the undisturbed bubbly, the agitated bubbly and the churn bubbly flows as the three different patterns of bubbly flow regimes obtainable in large pipes. They also proposed churn-slug and churn-froth flows which can loosely be likened to the slug and churn flow regimes in small pipes. However, based on the investigation of Schlegel et al. (2009), Shen et al. (2014) recommends that the flow regimes in large pipes be regarded as bubbly flow, cap-bubbly or cap-turbulent flow and churn-turbulent flow. These flow regimes (phase distributions) were characterised based on bubble drag and relative velocity which influence two-phase flow properties. The characteristics described by Schlegel et al. (2009) have been summarised here:

1) Bubbly flow: This flow regime is characterised by discrete small spherical or distorted bubbles which are fairly uniformly distributed in a continuous flowing liquid phase. Both the bubbles sizes and concentration do not vary much, therefore the time domain signal of the void fraction due to bubbly flow will show relatively low fluctuations. A PDF plot of the cross sectional area averaged void fraction data will peak below a void fraction of 0.3 (Schlegel et al. 2009).

2) Cap bubbly flow: Based on the drag behaviour of bubble, bubbles are categorized into Group 1 and Group 2 bubbles. The initial group represents small spherical, ellipsoid or distorted bubbles while the later describes larger cap-shaped or irregularly shaped bubbles. The cap bubbly flow regime is characterised by the presence of the short cap shaped bubbles (Group 2) with small bubbles (Group 1) flowing concurrently in the liquid film around the cap bubbles unlike the long gas slugs which completely fills the pipe cross section as is obtainable in small pipes. The break-up of the unstable slugs into the more stable cap bubbles creates additional interfaces which increase bubble-induced turbulence and more locations where shearing-off and recirculation of small bubbles can occur (Shen et al. 2014). This flow regime corresponds to the churn slug flow regime described by Ohnuki and Akimoto (2000). According to them, the presence of a consistent slug flow (in this case, a cap bubbly flow regime) is also significantly affected by the entry length (L/D) of the flow channel. The coalescence of bubbles in a relatively long flow channel resulted in a churn slug/cap bubbly flow further along the flow channel in some of the cases where 'churn bubbly' flow was initially observed at a smaller L/D section. The PDF is characterised by two peaks with the first peak being higher and more prominent than the trailing peak. The peaks represent the liquid phase with entrained Group 1 bubbles and the Group 2 bubbles with surrounding liquid film entrained with Group 1 bubbles respectively. The highest peak is also much lower than the peak in bubbly flow as reported by (Schlegel et al. 2009).

3) Churn-turbulent flow: The surface distortion and instability of cap bubbles which are attempting to increase in size, and the increased collision of such cap bubbles due to their increased number leads to both rapid production

of longer distorted bubbles and their destruction into smaller bubbles. This behaviour increases the turbulence further compared to cap-bubbly flows. Greater mixing and distribution of bubbles and liquid phase is also seen compared to the fairly intermittent nature of cap bubbly flows, therefore, the PDF shows a single peak at a higher void fraction.

Few studies have been carried out to develop flow regime transition maps for large pipes based on the physical mechanisms of the flow regimes. Some of the difficulties lie in the unpredictable behaviour of large cap bubbles. Flow regime transition in large pipes are observed to be a slower process compared to transition in small pipes (Shen et al. 2014). However, Schlegel et al. (2009) have developed transition criteria for large pipes (D^*_H) based on the analytical models for flow regime transition in small pipes by Mishima and Ishii (1984). The transition criteria have been summarised as follows:

- Bubbly to Cap Bubbly flow

A similar mechanism which causes the bubbly flow to slug flow regime transition has been attributed to also cause the bubbly flow to cap bubbly flow transition in large pipes. Therefore, the transition criterion relation developed by Mishima and Ishii (1984) is applicable here.

- Cap bubbly to churn turbulent flow transition.

This transition occurs when the cap bubbles become densely packed to the extent they begin to coalesce into larger unstable cap bubbles which equally disintegrate. The tetrahedral lattice structure for bubble distribution which was proposed by Mishima and Ishii (1984) has been applied to obtain the void fraction at maximum packing of cap bubbles and small distorted bubbles at which churn turbulent flow behaviours begin to occur. The lattice structure is shown in Figure 3.1 below.

The void fraction is given by Schlegel et al. (2009) as:

$$\langle \propto_{CT} \rangle = \langle \propto_{mp} \rangle + \langle \propto_{mp} \rangle \left(1 - \langle \propto_{mp} \rangle\right) = 0.506 \qquad (3.16)$$

$\langle \propto_{CT} \rangle$ and $\langle \propto_{mp} \rangle$ are the void fractions at the churn turbulent transition and maximum packing respectively.

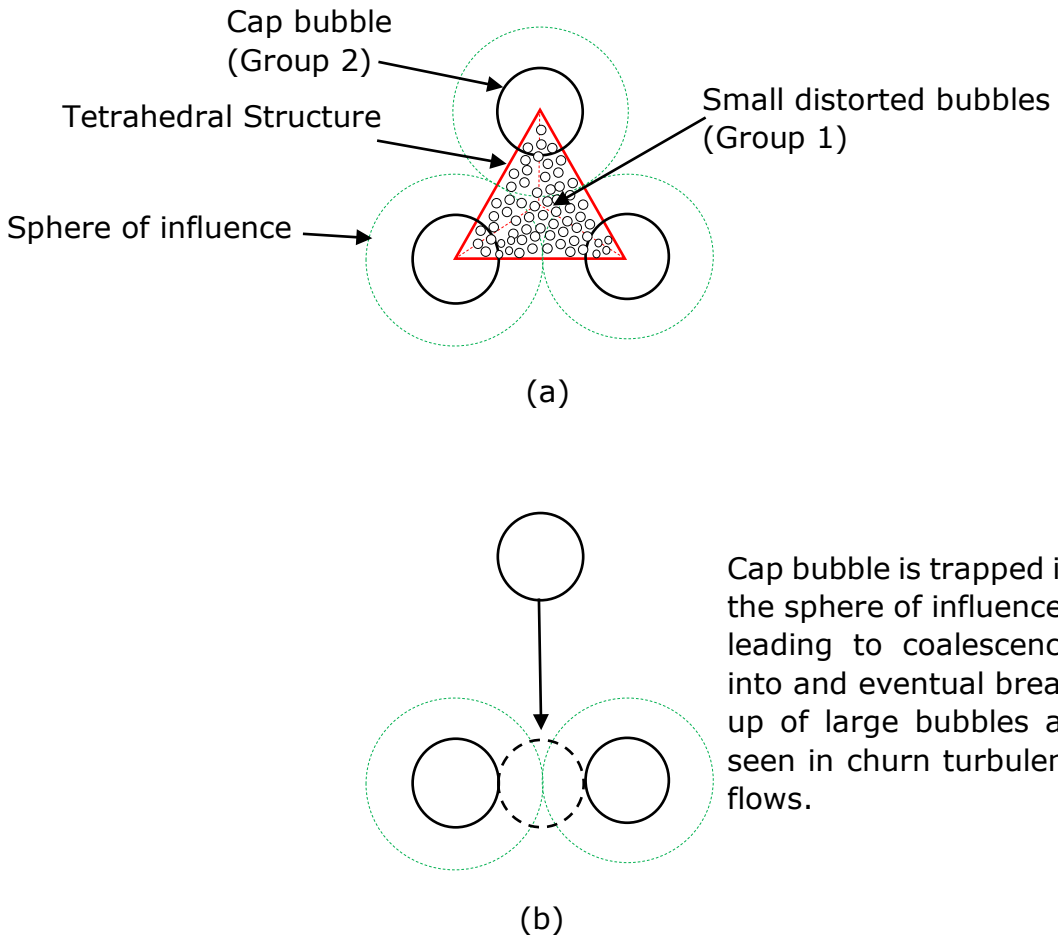

Figure 3.2: Cap-bubbly to churn-turbulent flow regime transition mechanism (Schlegel et al. 2009 and Mishima and Ishii, 1984).

Figure 3.2 shows that cap bubble cannot flow through the sphere of influence, rather it is trapped in the tetrahedral structure leading to coalescence into larger cap bubbles which eventually breaks up into smaller cap bubbles once again due to Taylor instability.

- Transition to annular flow regime

Two transition mechanisms were proposed by Mishima and Ishii (1984). The first mechanism which involves flow reversal in the liquid film surrounding the Taylor/slug bubbles is not applicable to large pipes because slug bubbles cannot exist in large pipes. The second mechanism is the breaking off of liquid from liquid slugs and long waves and their entrainment into the gas core. The transition criterion developed from this second mechanism is given as:

$$\langle j_g \rangle = \left(\frac{\sigma g \Delta\rho}{\rho_g^2}\right)^{1/4} N_{\mu f}^{-0.2} \tag{3.17}$$

Where,

$$N_{\mu f} \equiv \mu_f \Big/ \left[\rho_f \sigma \sqrt{\left(\frac{\sigma}{g\Delta\rho}\right)}\right]^{1/2} \tag{3.18}$$

3.3 CFD modelling of two-phase flow

After identifying the flow regime characteristics of the flows to be modelled using their superficial velocities, the next step is to apply the Computational Fluid Dynamics (CFD) technique to extract fluctuating flow properties due to the transient multiphase flows. This technique basically involves the prediction of the variation and fluctuation of fluid flow properties by converting the integral of the governing equations over a control volume into a system of algebraic equations and solving them by computer calculations. In the last two decades, the CFD method for fluid flow analysis have received increased application and development because of its unique capabilities over the experimental method. Such capabilities include its ability to cost-effectively model industrial scale systems whose flow conditions might be too difficult or hazardous to set-up in a lab experiment e.g long spans of subsea oil and gas pipeline stretching a few

kilometres. CFD will also allow detailed observation of the flow features which could be difficult to measure in most real-life or experimental cases.

The main three stages involved in CFD modelling include the pre-processing, the solving and the post-processing stages. The pre-processing stage involves the definition of the computational domain, the generation of a grid of finite control volumes, the choice of the flow physical phenomenon of interest, the fluid properties and the appropriate boundary condition. In the present study involving a time-dependent flow analysis, the solver stage involves firstly a macroscopic averaging of the governing equation by first integrating the conservation equations over the control volume. This control volume integration is the distinguishing feature of the finite volume technique that has been used in the present CFD method. The next integration is carried out over a finite time interval to account for the transient nature of the flow. Then the equation is converted into a system of algebraic equations and solved iteratively. The post processing involves interpretation of results using plots, animations etc. A comprehensive application of CFD to solve a flow problem must involve validation of results using experimental results. In cases where it is impossible to carry-out experiments of any kind, then validation can be done by comparing CFD results with analytical solutions and high-quality data from similar problems reported in literature (Versteeg and Malalasekera, 2007).

Selecting the most appropriate modelling approach is crucial in modelling multiphase flows. In the pre-processing stage, the in-sight and hence choice of the flow physical characteristics stipulates the equations to be solved. Different physical mechanisms dominate in different flow regimes leading to distinguishing features such as the length scale of the interface between the phases and turbulence behaviours. In the context of the present study, coalescence is the major physical mechanism leading to predominantly large interfaces within slug and churn flow regimes. In extension to cap-bubbly and churn-turbulent flows in large pipes, coalescence of smaller bubbles and break-up of large bubbles due to Taylor instability result in the characteristic presence of large Group 2 bubbles in large pipes. Also, coalescence due to wake entrainment and random collisions due to bubbles induced turbulence as well as break-ups due to shearing-off from Group 2 bubbles and turbulent eddies impact are additional mechanisms mostly present

within the liquid slugs entrained with Group 1 bubbles. For gas liquid two-phase flows, the VOF, two-fluid Eulerian, and Mixture models are the available multiphase models. In the Eulerian model, the phases exist simultaneously and a set of conservation equations are solved for each phase and interfacial terms are used to account for interactions between phases. The Eulerian model is more suitable for dispersed, droplet and bubbly flow and the interfacial terms makes convergence difficult. The mixture model combines the phases into a single mixture. It solves one mixture continuity and one mixture momentum equation as well as a volume fraction transport equation for the secondary phase while phase interactions are treated using the slip velocities, which depend on the flow regime. It is also more applicable for dispersed, bubbly and droplet flows but computationally less intensive than the Eulerian model. The VOF model tracks the interface between phases and is more suitable for stratified, slug or churn flow modelling. The present study of MFIV is focused on the flow induced forces due to alternate impact of liquid and gas bubbles or waves due to slug and churn flows at pipe bends. A specialised VOF model known as Multifluid-VOF model solves separate conservation equations for each phase as the Eulerian model and it is able to model both large bubbles and the smaller entrained bubbles dynamics in the liquid slug. This method is also computationally intensive and difficult to converge. However, although VOF model cannot model the small entrained bubbles breakage and coalescence, it can accurately track some of the entrained bubbles interfaces so long as the computational grid is small compared to the interface length. Therefore, VOF method is used to track the predominantly large interfaces between liquid and gas phases in slug, cap-bubbly and churn flow regimes in the present study. In addition, this method of multiphase flow modelling considers both phases to share velocity and pressure field and thus a single set continuity and momentum equations is solved. In comparison, the multifluid-VOF model solves for the individual phase properties which are required if the flow has numerous arbitrarily shaped and sized interfaces. In such flows, it is important to predict drag, lift and the development of vorticial structures which give rise to mechanisms such as shearing-off, wake entrainment and bubbles induced turbulence obtainable in bubbly flows. In slug flows, the large interfaces which dominate the flow are accurately predicted by solving a continuity equation for the volume fraction. The effect of the large interfaces which means that phases exist separately in relatively large regions within the flow, is more significant than the

effect of the smaller bubbles and droplets which could be entrained in the phases. Hence in the present study, the homogenous multiphase flow model applied in VOF is capable of modelling the slug/churn flow patterns while consuming fewer computing resources and time due to fewer equations and ease of convergence. Any droplet and bubble smaller than mesh size, are not captured in VOF modelling. The standard $k-\epsilon$ URANS turbulence model which calculates mixture properties and models all time and length scales of turbulent structures, is computationally inexpensive and can implement proper near walls treatment, have been applied to account for turbulence in the present multiphase flow. These methods are described in the following sections.

3.3.1 Volume of Fluid Method

The VOF method models multiple immiscible fluids by solving a single set of momentum equations which is shared by the phases (here, air and water). In addition to solving one continuity equation for both phases, an equation representing the space conservation of the volume fraction α is also solved. This ability to track the volume fraction of each phase through the computational domain is the characteristic feature of the VOF method.

The tracking technique was originally developed by Nichols and Hirt (1975) and extended by Hirt and Nichols (1981). They compared three different pre-existing techniques for free boundary modelling and based on the shortcomings and strengths of the techniques, they developed the VOF approach. The techniques are:

- the surface height functions which applies lagrangian style of calculation and cannot treat bubbles and drops surfaces,

- the line segments which is lagrangian-like in approach, cannot treat intersection of two surfaces and three-dimensional surfaces,

- and the surface marker-particles techniques which is Eulerian in approach but it is computationally expensive.

An important feature in their comparison is the performance of the Lagrangian and Eulerian approaches. VOF which uses the Eulerian representation was developed as a direct improvement of the surface marker-particles and it is simple and economical for tracking free boundaries both in 2 and 3-dimensional grid. They choose the Eulerian coordinate representation of fluid flow over the Lagrangian. In Lagrangian technique the free surface coincides with mesh boundary and this boundary moves with the free surface flow. Hence, their rational was based on the fact that in cases of highly contorting or shearing free surface flows, the meshes would be severely distorted and the Lagrangian technique would perform poorly resulting in questionable accuracy. The mesh in the Eulerian technique cannot distort with flow since the mesh is a free reference frame and the fluid flows through it. However, there are instances when free boundaries are located within mesh cells. Special means will then be required to locate such surface and to apply boundary conditions to them. More details on how VOF method was initially applied in a numerical code can be found in Nichols and Hirt (1975) and Hirt and Nichols (1981).

Therefore, VOF method which solves the applicable system of Navier-Stokes equation and the volume fraction continuity equation for one of the phases (water in this case) is solved:

$$\frac{\partial \alpha_q}{\partial t} + \vec{u}.\nabla \alpha_q = 0 \tag{3.19}$$

where subscript q represents each phase component.

Air volume fraction is obtained from the relation

$$\sum_{q=1}^{2} \alpha_q = 1 \tag{3.20}$$

The continuity and momentum equations are given below (Ishii and Hibiki, 2010):

Continuity:

$$\frac{\partial \rho}{\partial t} + \nabla.(\rho \overline{u}) = 0 \tag{3.21}$$

Momentum:

$$\frac{\partial (\boldsymbol{\rho \overline{u}})}{\partial \boldsymbol{t}} + \nabla.(\boldsymbol{\rho \overline{u}\,\overline{u}}) = -\nabla \boldsymbol{P} + \nabla.\boldsymbol{\mu}(\nabla \overline{\boldsymbol{u}} + \nabla \overline{\boldsymbol{u}}^{T}) + \boldsymbol{F} \tag{3.22}$$

The properties appearing in the transport equations are determined by the presence of the component phases in each control volume. For example, the density is considered to be:

$$\rho_m = \sum_{q=1}^{2} \alpha_q \rho_q \tag{3.23}$$

Therefore, the momentum equation is dependent on the volume fractions of the gas and liquid through density ρ and viscosity μ.

The surface tension force in the momentum equation is represented by F. In fluid dynamics, surface tension is expressed as a normal boundary condition at interfaces. The expression is given as the fluid pressure jump across the interface under surface tension:

$$p_s \equiv p_2 - p_1 = \sigma\kappa \tag{3.24}$$

Where p_s is the surface pressure and $p_2$and p_1 are the pressures in the two fluids on either side of the interface. However, the surface tension force is expressed as

a volume force and added to the momentum equation as a source term in VOF method by Brackbill et al. (1992). They re-formulated the force as a volume force called the continuum surface force (CSF). They achieved this by replacing the fluids boundary across which the gas and liquid properties change discontinuously requiring pressure jump treatment by a transition region with finite thickness over which surface tension acts everywhere by varying smoothly over the finite thickness across the interface. Therefore, the surface tension effects between liquid water and air has been considered by using the continuum surface force (CSF) model. According to this model, the volume force is added to the momentum source as,

$$F = \sigma \left(\frac{\rho \kappa_l \nabla \alpha_l}{1/2(\rho_l + \rho_g)} \right) \tag{3.25}$$

Where, σ is the surface tension coefficient, ρ is calculated using equation (3.23) and κ_l is the surface curvature of the liquid droplet defined in terms of the divergence of the unit normal, and is given by,

$$\kappa_l = \nabla . \bar{n}_l \tag{3.26}$$

Also, $\kappa_l = -\kappa_g$ and $\nabla \alpha_l = -\nabla \alpha_g$. The unit normal vector, n_1 is calculated from the local gradients in the surface normal at the interface as,

$$\bar{n}_l = \frac{\nabla \alpha_l}{|\nabla \alpha_l|} \tag{3.27}$$

More on the CSF model and its implementation in numerical calculations using the VOF method can be seen in Chung (2002).

Wall adhesion effects are accounted for by adjusting the surface curvature near the wall, where gas-liquid interface meets the solid wall. The local curvature of this interface is determined by the contact angle, θ_w, which represents the angle between the wall and the tangent to the interface at the wall. The surface normal vector at the wall is given by,

$$\bar{n} = \bar{n}_w cos\theta_w + \bar{t}_w sin\theta_w \tag{3.28}$$

Where, $\bar{n}_w$ and $\bar{t}_w$ are the unit vectors normal and tangential to the wall, respectively.

3.3.2 Turbulence Model

According to Pope (2000) century old experience and effort has still proved ineffective in developing a simple analytic theory to completely describe and calculate turbulence. Turbulence exist in many practical flows at different Reynolds numbers. For instance, in pipe flows, it exists at Reynolds number values greater than 4000. The difficulty in developing an accurate turbulence theory or model lies in its peculiar complex features and their interactions with the other fluid flow properties. The presence of turbulence in a flow indicate the presence of rotational flow structures having different length scales ranging from the characteristic length of the flow channel to very small length scales (0.1 to 0.01mm) called the Kolmogorov microscales. These rotational flow structures are called turbulent eddies. The turbulent eddies introduce fluctuations in the instantaneous velocity field $U(x,t)$ making it a function in all direction and time. The largest eddies are considered to be anisotropic while the smallest eddies at high mean flow Reynolds numbers are isotropic. These eddies contain kinetic energies which starts from the stretching work done by mean flow on the large eddies. The energy vary from the highest values in the largest eddies to the smallest values in the smallest eddies in a fashion called energy cascade. At the smallest eddies, energy is dissipated by conversion into thermal internal energy. These complex behaviours make the calculation of turbulent flows difficult. The methods available in CFD to calculate turbulence are usually assessed based on range of applicability, accuracy, level of

description, simplicity and cost of use. Brief description of the methods are given below.

- Direct numerical simulation (DNS): Here, the Navier-Stokes equations are solved directly to obtain the instantaneous velocity $U(x,t)$ for one realization of the flow. All the length and time scales of velocity fluctuations are resolved with no need for closure equations. This makes DNS the most accurate and simplest approach to calculating turbulence. On the other hand, these advantages make DNS the most computationally expensive model with cost increasing as Re^3 (Pope, 2000).
- Large-eddy simulation (LES): This approach is more economical than DNS but not as accurate and simple. Here, only the large-scale three-dimensional time-dependent turbulent motion are resolved. This is done by directly solving equations for the filtered velocity field $\overline{U}(x,t)$ corresponding to the large eddies while the smaller-scale motions are modelled.
- Turbulence models for Reynolds-averaged Navier-Stokes equations: Here the flow variables (*u, v, w,* and *p*) are represented with a sum of the mean and the fluctuating component of the variable. This operation is known as Reynolds decomposition (Pope, 2000). Also, the presence of vortical eddy motions and velocity gradient in a turbulent flow which result in the appearance of turbulent velocity fluctuations act in such a way that faster moving fluid layers are decelerated while the slower layers are accelerated. This behaviour leads to momentum exchange across control volume boundaries. Hence, the time average of the instantaneous continuity and momentum equation would now contain additional turbulent shear stresses known as Reynolds stresses as a result of the variances and second moment of the velocity fluctuations (Versteeg, 2007). The new set of governing equations which has been modified by Reynolds stresses is known as Reynolds-averaged Navier-Stokes (RANS) equations and it contain six additional unknowns. In order to close the system of equations, turbulence models are required to predict the Reynolds stresses. Different classical turbulence models have been created with the most complex being the Reynolds stress model (RSM) which solves additional seven equations alongside the RANS flow equations. The simplest is the mixing length model which solves no extra transport equation and simply solves for the Reynolds

stresses by solving for the turbulent viscosity (μ_t) with simple algebraic formulae. Somewhere in between these two models and in terms of computing resources and accuracy is found the Standard $k-\epsilon$ model.

The decomposed velocity and pressure components and the RANS equations are given in Equation (3.29) and (3.30) - (3.31) respectively:

$$u_i = \bar{u}_i + u'_i$$

$$p = \bar{p} + p' \tag{3.29}$$

And

$$\frac{\partial \rho}{\partial t} + \frac{\partial}{\partial x_i}(\rho \overline{u_i}) = 0 \tag{3.30}$$

$$\frac{\partial}{\partial t}(\rho \overline{u_i}) + \frac{\partial}{\partial x_j}\left(\rho \overline{u_i}\,\overline{u_j}\right) = -\frac{\partial \bar{p}}{\partial x_i} + \frac{\partial}{\partial x_j}\left[\mu\left(\frac{\partial \overline{u_i}}{\partial x_j} + \frac{\partial \overline{u_j}}{\partial x_i} - \frac{2}{3}\delta_{ij}\frac{\partial \overline{u_i}}{\partial x_i}\right)\right] + \frac{\partial}{\partial x_j}\left(-\rho \overline{u'_i u'_j}\right) \tag{3.31}$$

In this study, the standard $k-\epsilon$ models are used. The $k-\epsilon$ model is well established and performs well for many industrial flows. In order to describe the Reynolds stresses, only two additional equations are solved alongside the RANS equations. This equation was developed by Launder and Spalding (1974) based on single phase flow. The mixture turbulence model applied in this study is the simplified extension of the single phase $k-\epsilon$ model. In this model, it is deemed that the mixture properties and mixture velocities could adequately capture the main features of turbulent flow.

The mixture turbulent kinetic energy k is given by Launder and Spalding (1974):

$$\nabla.(\rho_m \vec{v}_m\, k) = \nabla.\left(\frac{\mu_{t,m}}{\sigma_k}\nabla k\right) + G_{k,m} - \rho_m \epsilon \tag{3.32}$$

The mixture energy dissipation rate ϵ is given by:

$$\nabla.(\rho_m \vec{v}_m\, \epsilon) = \nabla.\left(\frac{\mu_{t,m}}{\sigma_\epsilon}\nabla \epsilon\right) + \frac{\epsilon}{k}(C_{1\epsilon} G_{k,m} - C_{2\epsilon}\rho_m \epsilon) \tag{3.33}$$

Where, the mixture density and velocities are given by:

$$\rho_m = \sum_{i=1}^{N} \alpha_i \rho_i \tag{3.34}$$

And

$$\bar{v}_m = \frac{\sum_{i=1}^{N} \alpha_i \rho_i \bar{v}_i}{\sum_{i=1}^{N} \alpha_i \rho_i} \tag{3.35}$$

The turbulent viscosity, $\mu_{t,m}$ is computed from:

$$\mu_{t,m} = \rho_m C_\mu \frac{k^2}{\epsilon} \tag{3.36}$$

And the production of turbulent kinetic energy, $G_{k,m}$ is computed from:

$$G_{k,m} = \mu_{t,m}(\nabla \bar{v}_m + (\nabla \bar{v}_m)^T) : \nabla \bar{v}_m \tag{3.37}$$

The turbulent model constants are:

$C_{1\epsilon} = 1.44$, $C_{2\epsilon} = 1.92$, $\sigma_k = 1.0$, $\sigma_\epsilon = 1.3$

These constants are originally intended for single phase flows, however, since a mixture $k - \epsilon$ model is solved in the present study, the constants are applicable.

3.4 Transient dynamic modelling of pipe structure

The flow induced forces due to transient multiphase flows are equally time-dependent. As described in Figure 1.4 (Chapter 1), the response to this dynamic loading appear in the form of displacement or deformation of the pipe structure which in turn can further disrupt the flow regime. In the context of the analysis carried out here, the structure is a rigid steel pipe with fixed end supports. Hence, the response is expected to be mostly in the form of displacements and stress. No significant large deformation due to the flow induced forces is expected as would have been the case with flexible flow lines. Also, no significant shell type deformation of the pipe wall is expected. Hence, theoretically the expected pipe mesh deformation type of structural response is too negligible to produce a feedback response in the form of any significant flow regime disruption which would have changed the characteristics of the subsequent flow induced forces. Consequently, a one-way FSI analysis will perform well to obtain the time-varying displacement and stresses in the present study.

The basic finite element equation of motion is solved by a linear transient dynamic analysis given in matrix form as (Pavlou, 2015 and Meirovitch, 2001):

$$[k]\{d\} + [c]\{\dot{d}\} + [m]\{\ddot{d}\} = \{F\}(t) \tag{3.38}$$

where d, $\dot{d}$ and $\ddot{d}$ are the time-dependent vectors of the nodal displacements, its first derivative and second derivative with respect to time respectively while, {F}, [k], [c] and [m] are the time-dependent applied load vector, the stiffness matrix, the damping matrix and the mass matrix respectively. The time history of the displacement and stress fluctuations are obtained from the computations. The expressions relating the nodal displacements to strains is given as:

$$\{\varepsilon\} = [B]\{d\} \tag{3.39}$$

while the expression relating the stress to the strain is given by:

$$\{\sigma\} = [D]\{\varepsilon^{el}\} \tag{3.40}$$

Where

{ε} = total strain vector = $\left\lfloor \varepsilon_x \varepsilon_y \varepsilon_z \varepsilon_{xy} \varepsilon_{yz} \varepsilon_{xz} \right\rfloor^T$

[B] = strain-displacement matrix, based on the element shape functions

{σ} = stress vector = $\left\lfloor \sigma_x \sigma_y \sigma_z \sigma_{xy} \sigma_{yz} \sigma_{xz} \right\rfloor^T$

[D] = elasticity matrix

$\{\varepsilon^{el}\} = \{\varepsilon\} - \{\varepsilon^{th}\}$ = elastic strain vector

$\{\varepsilon^{th}\}$ = thermal strain vector

3.5 Modal analysis

The natural frequencies and mode shapes are important parameters in the design of a structure for dynamic loading conditions. These are the characteristics of a structure under the assumption of no damping and no time-dependent loading. A modal analysis determines these free vibration characteristics by solving the equation of motion for an undamped system (Meirovitch, 2001). The equation is given in matrix form as (Pavlou, 2015):

$$[k]\{d\} + [m]\{\ddot{d}\} = \{0\} \tag{3.41}$$

Assuming a linear system whose motion is harmonic under free vibration, the solution of Equation (3.39) above becomes an Eigenvalue problem of the form:

$$\left(-\omega_i^2[M] + [K]\right)\{\phi_i\} = \{0\} \tag{3.42}$$

Where ω_i is the ith natural frequency of the pipe structure in radians per unit time and ϕ_i is the displacement vector (eigenvector) representing the mode shape of the pipe structure at the ith natural frequency.

Furthermore,

$$\omega^2 = \frac{k}{m} \tag{3.43}$$

But, in the case of m, the multiphase flow in the pipe adds to the mass of the pipe structure depending on the global volumetric fractions of the gas and liquid flowing in the system. Equation (3.41) shows that the natural frequency of the pipe will change according to the added mass of each of the contained two-phase flow cases under study. The ANSYS Mechanical FEA tool employed in this study uses a special algorithm known as HSFLD242 3-D Hydrostatic Fluid elements to include contained fluid inside a solid structural model in a Finite Element model to capture the effect of fluid pressure and mass on the natural frequency and modes of a structure in modal analysis modelling. Further details are given in APPENDIX A for the HSFLD242 3-D Hydrostatic Fluid Elements code.

CHAPTER 4

NUMERICAL SOLUTION PROCEDURES AND VALIDATION

The applicability of numerical procedures depend largely on their level of accuracy and the extent to which they realistically reproduced the physical behaviours of a real life process. Hence in this chapter, the flow conditions of interest are identified on the flow regime map. Then the appropriate solution procedure of VOF multiphase model and K-e turbulence model in CFD as well as the procedures of transient structural dynamics and modal analysis in FEA that are used to model the flows are presented. Furthermore, accuracy of the numerical predictions were established by carrying out mesh sensitivity and validation studies. The validation of the numerical approaches is done by comparing numerical predictions obtained in the present study with published experimental data. However, experimental data on MFIV especially in large pipes are limited. Hence, the major validation in this study is carried out using the published experiments by Liu et al. (2012) and Miwa et al. (2015) for small diameter pipe. This process involved comparing void fraction predictions obtained using the VOF model and Geo-reconstruct scheme for interface treatment implemented in three different mesh sizes to the experimental results of Liu et al. (2012). The aim is to establish the accuracy of the numerical procedure before applying the same technique to investigate MFIV in larger but geometrically similar pipes in subsequent chapters of this study.

4.1 Multiphase flow solution procedure

The set of governing equations, turbulence models and boundary conditions describing the multiphase flow regimes of interest in the present study have been implemented in a commercial CFD software known as FLUENT 18.0.

4.1.1 Interface tracking and treatment

In slug and churn flow interface distribution and geometry are the defining futures that directly influence the flow induced forces because the interfaces define the liquid and gas regions which have different densities and hence lead to fluctuating

momentum and reaction forces impacting pipe bends. Hence, accurate prediction of the evolution and position of interfaces are important in the present study. The volume fraction equation (Equation 3.19) has been solved using explicit time formulation which gives better numerical accuracy in comparison to the implicit formulation. The explicit formulation is time dependent and it calculates the present volume fraction using values from previous time step as given in Equation 4.1:

$$\frac{\alpha_q^{n+1}\rho_q^{n+1}-\alpha_q^n\rho_q^n}{\Delta t}V+\sum_f\left(\rho_q U_f^n \alpha_{q.f}^n\right)=0 \qquad (4.1)$$

where, n+1 is index for current time step while n is index for previous time step. $\alpha_{q.f}$ is the face value of the q[th] phase volume fraction, V is the cell volume and U_f is the volume flux through the face based on normal velocity. Hence, the explicit formulation does not require the solution from the iteration of the transport equation at each time step and the volume fraction is solved once each time step.

The choice of the time step size is conditioned by the Courant number-based stability criterion. The numerical algorithm used in this study applies a different time step each for the volume fraction and the rest transport equations calculations. Based on a pre-assigned maximum allowable Courant Number of 0.25 and the smallest time spent by fluids in cells (control volume) in the region near the free surface to empty out of the cell, the present numerical algorithm automatically refines the sub-time step for the volume fraction calculation. The sub-time step size is calculated as:

$$\Delta t = C\frac{V}{\sum_{cell}U_f} \qquad 4.2$$

where, C is the Courant Number, V is the cell volume and U_f are the outgoing fluxes in the cell.

A few Interface capturing schemes have been applied in literature to interpolate the face fluxes of the volume fraction based on the type of interface that is expected from the gas-liquid two-phase flow. The schemes include the geometric reconstruction (Geo-Reconstruct), the CICSAM, the Compressive and the Modified HRIC schemes. In the first scheme a special interpolation treatment is applied to the cells that are located near the interfaces between fluid phases while in the last three schemes the same treatment used on cells that are completely filled with one of the fluid phases is applied to these cells. In the present study, a sharp interface is required to accurately describe slug and churn flow regimes. Therefore, the Geo-Reconstruct scheme is applied. This scheme is based on the volume fractions description of fluids layout in each cell as was presented by Hirt and Nichols (1981). The treatment by Youngs (1982) is able to locate interfaces more accurately by a straight line. The slope of the straight line in a cell is approximated by the volume fraction of one fluid phase in the cell and that of the same fluid phase in the cell's eight neighbouring cells. Then the sloped straight line is moved to a position where it divides the cell into two volumes matching the two volume fractions of the two phases contained in the cell. Finally, the volume of each fluid phase flowing through a cell side is obtained as a result of the interface position in the control volume δV.

4.1.2 Computational geometry and boundary conditions

The geometry is a vertical pipe with a 90^0 bend at the upper end connected to the horizontal section of the pipe. The inlet, outlet and pipe wall are shown in Figure 4.1. Three different sizes of this geometry were investigated in the present study. The size and orientation of the 0.0525 I.D. pipe is based on the pipe geometry that was investigated by Liu et al. (2012). In that case, the R/D of the bend radius is ~1.45 of the pipe I.D. The pipes of 0.1016m (4 in) and 0.2032m (8 in) I.D. were selected to reflect standard sizes obtainable in subsea jumpers and manifolds. These sizes also coincide with the transition and large-pipe ranges described by (Kataoka and Ishii, 1987) in their definition of pipe sizes using non-dimensional hydraulic diameter given in equation (3.15). Also, the same R/D of ~1.45 reported in Liu et al. (2012) was equally adopted in the pipes of 0.1016m and 0.2032m I.D. Table 4.1 presents the sizes.

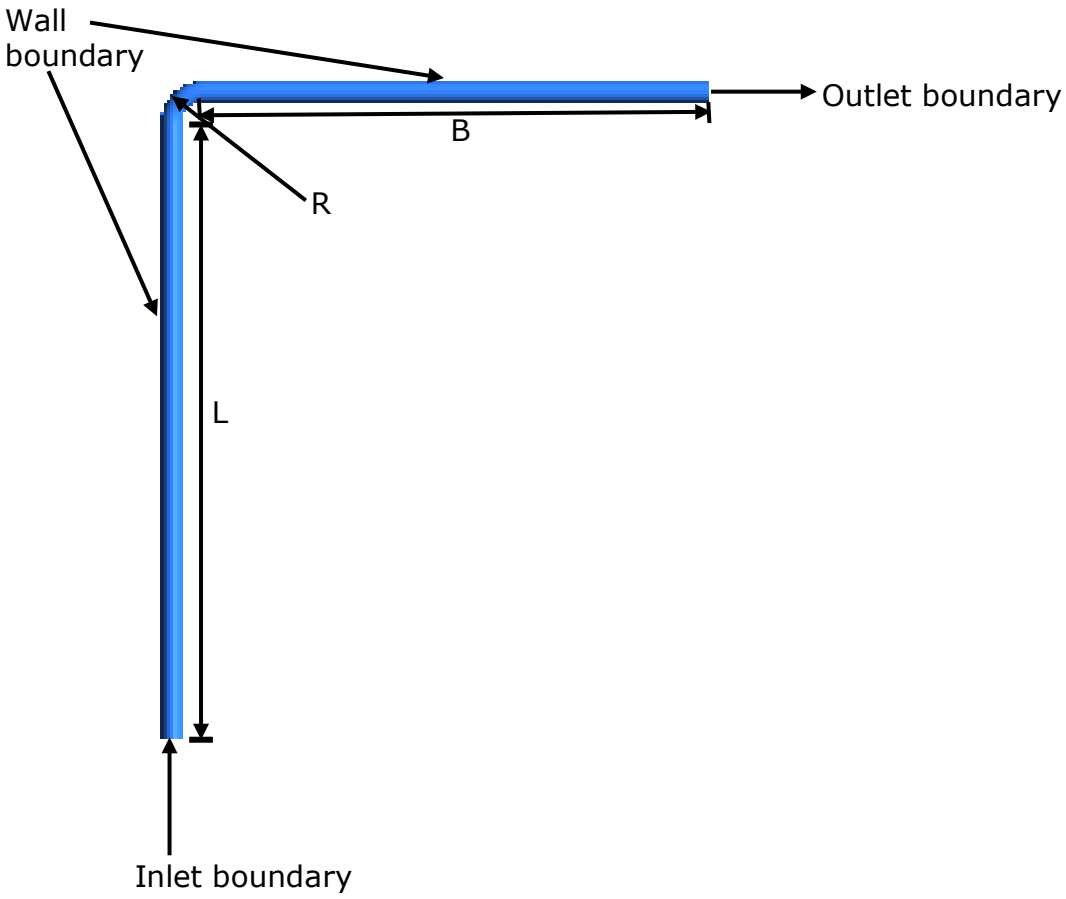

Figure 4.1: Boundaries of the computational domain

Table 4.1: Pipe sizes under investigation in present study

Parameter	**Values**	**Values**	**Values**
$\mathbf{D_H^*}$	19.2	37.2	74.5
Diameter, D[m]	0.0525	0.1016	0.2032
Bend Radius, R[m]	0.0762	0.1473	0.295
Length, L[m]	4	10	16
Breadth, B[m]	4	6	12

4.1.2.1 Inlet and Outlet boundary conditions

It is challenging to set up the inlet flow velocity for multiphase flows, especially for slug and churn flows, where phases are separated. One way to deal with this, would be to set an inlet mixture velocity and no-slip gas volume fraction in the inlet. Flow would eventually separate out within the flow domain, however, a very long flow domain would be needed. A more efficient method of setting inlet boundary condition for slug and churn flows have been described in Parsi et al. (2016) and has been utilised in the present study. This method involves splitting the inlet into two sections as shown in Figure 4.2 in order to expedite the development of multiphase flow regimes. The central core (A_g) is used for air flow and the surrounding annular (A_l) for water flow

Though the inlet areas, A_g and A_l were selected arbitrarily, it is expected the particular choice of the areas and thus the inlet velocities would not affect the final outcome as the development of specific flow patterns is dependent on the superficial velocities only. The selection of inlet areas would only affect the length of the flow pipe needed for the flows to develop and to distribute themselves into specific patterns. In the present study, the inlet length is sufficiently long for flow to develop and separate into expected slug and churn flow patterns.

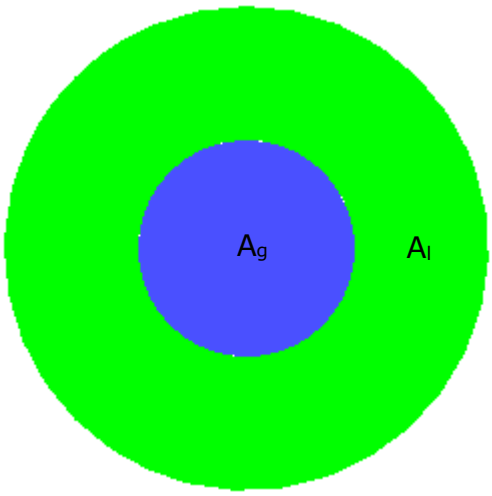

Figure 4.2: Domain inlet

Fluids are introduced into the flow domain at the inlets by setting the phase velocities. The gas and liquid phase velocities are calculated respectively as:

$$v_g = \frac{v_{sg} A}{A_g} \tag{4.3}$$

and

$$v_l = \frac{v_{sl} A}{A_l} \tag{4.4}$$

where v_g and v_l are specified gas and liquid inlet velocities, v_{sg} and v_{sl} are superficial gas and liquid velocities, A is the cross-sectional area, A_g and A_l are the area of gas and liquid area inlets. Hence, both inlets are defined as velocity-inlets. The turbulence parameters at both inlets are specified as turbulent intensity, I and hydraulic diameter D_H. The turbulent intensity is estimated with Equation 4.5:

$$I = \frac{0.16}{Re_{D_H}^{1/8}} \tag{4.5}$$

The pipe outlet is a single outlet and its boundary condition is defined as pressure outlet. Zero value is defined for the gauge pressure at the outlet to specify that the outlet is at atmospheric condition.

4.1.2.2 Wall boundary condition

Walls are usually the main origin of turbulence in flows. Hence, in a wall bounded turbulent flow, the main stream flow behaviours which are affected by the presence of turbulence are consequently affected by the no-slip wall condition of the flow. Within the near-wall region having boundary layer thickness δ, there are three layers known as the viscous sublayer which is dominated by viscous effect,

the outer layer which is called the fully turbulent layer and the interim layer which is equally affected by both viscosity and turbulence. Due to the layers and their dominating mechanisms, flow variables exhibit large gradients in the near-wall region compared to the main flow and the exchange of momentum and mass is more significant. Hence implementing the right treatment of the near wall region is highly important in numerical calculations to produce the most accurate solution of the pipe flow. When using the URANS turbulence models, the near wall region could be treated by completely resolving the viscous sublayer or by using a wall function to model the layer.

In the present study where the $k-\epsilon$ turbulence model has been used to model turbulence, the appropriate treatment is to use wall functions. Here, a relatively lower number of meshes is required compared to cases where the viscous sublayer has to be completely resolved. The available wall functions in the CFD code used in the present study are the standard wall function, the non-equilibrium wall function and the enhanced wall treatment. The code also permits the input of a user-defined wall function. However, the standard wall function which was developed by Launder and Spalding (1974) has been implemented in this study. Here the height from the wall of the first cell in the computational domain is chosen so that the first node P, is outside the viscous sub-layer region. The height is represented by a dimensionless distance y^+ given as $30 < y^+ < 300$. The mean velocity in the near wall region can be obtained according to the law-of-the-wall as given in Equation 4.6:

$$U^* = \frac{1}{\kappa} In\left(E y_p^*\right) \tag{4.6}$$

where the dimensionless velocity

$$U^* \equiv \frac{U_p C_\mu^{1/4} k_p^{1/2}}{\tau_w/\rho} \tag{4.7}$$

and the dimensionless distance from the wall is given as:

$$y^* \equiv \frac{\rho C_\mu^{1/4} k_p^{1/2} y_p}{\mu} \tag{4.8}$$

The turbulent kinetic energy and rate of dissipation for the fluid at the near wall region are given as:

$$k_p = \frac{U^{*2}}{\sqrt{C_\mu}} \tag{4.9}$$

$$\varepsilon_p = \frac{U^{*3}}{\kappa y_p} \tag{4.10}$$

where U_p, τ_w, y_p, ρ, μ, *E, and* κ are respectively given as, the time averaged velocity of the fluid at point P, the shear stress on the wall in the direction of U_p, the distance of point P from the wall, the density of fluid, the dynamic viscosity of the fluid, an empirical constant which is a function of the wall roughness given as 9.793 in present calculation, and von Karman constant given as 0.4187. Finally, a stationary wall is defined at the wall for the pipe motion and the mesh is not dynamic since the pipe is rigid and any shell mode deformation is expected to be too negligible to cause any significant change in the flow regime structure. In summary, mixed boundary conditions involving Dirichlet and Neumann boundary conditions have been adopted in the present CFD simulations.

4.1.3 Solver methods and controls

Table 4.2 presents the solution methods that have been adopted in this study. All the simulations in this study are transient and are carried out in pressure-based solver. A negative gravity (-9.81m/s^2) is specified since the flows are in vertical upward direction. The explicit scheme is adopted for this VOF model formulation and the volume fraction cut-off and courant number are set as 1 X 10^{-6} and 0.25 respectively. Also, implicit body force formulation is used to account for the density difference between water and air in the present separated flow regimes. The surface tension between the two fluids was set at a constant of 0.0728 N/m. Water was assigned as the primary phase (phase 1) while air was assigned the secondary phase (phase 2).

All residuals were set to 0.001. The under-relaxation factors for; pressure, density, body forces, momentum, turbulent Kinetic energy, turbulent dissipation rate and turbulent viscosity are given as 0.3, 1, 0.5, 0.3, 0.6, 0.6, 0.5 respectively. Finally, a fixed time step of 0.00001s was used for a maximum iteration of 30.

Table 4.2: Solution discretization scheme

S/N	**Variable**	**Scheme**
1	Pressure-Velocity coupling	SIMPLE
2	Pressure	PRESTO
3	Momentum	Second order upwind
4	Volume fraction	Geo-Reconstruct
5	Turbulent kinetic energy	First order upwind
6	Turbulent dissipation rate	First order upwind
7	Transient formulation	First order implicit

4.1.4 Flow regime identification of the two-phase flow case studies

Based on Equation (3.15) and Table 4.1, the pipe having a diameter of 0.203 m is a large pipe while the other two pipes with diameters of 0.0525 m and 0.1016 m fall within the range where stable slug flow regime could still exist. Identifying the flow regimes that are responsible for observed FIV behaviours is necessary in order

to draw useful conclusions and accurately inform predictive models and proactive approaches in addressing MFIV problems. Equation (3.2) – (3.18) have been used to construct the flow regime maps shown in Figure 4.4 (a) and (b), describing both the small and large pipe transitions based on liquid and gas superficial velocities. The transition criterion (Curve A) coincide for the bubbly-slug flow regime transition in both small and large pipes. However, the physical mechanisms for the other transition regions in the two-phase flow differ in the small and large pipes hence, the transitions criteria differ. Curve B defines the transition for cap-bubbly to churn turbulent flow regime while Curve C defines the slug to churn flow regime transition in a pipe of 0.0525m diameter. Curve D and E represent the transition to annular flow regime in a large pipe and a small pipe respectively. In Figure 4.4 (b), the flow regime map presents the slug-churn transition based on the entrance length phenomenon suggested by Taitel et al. (1980). Curve F represents entry length L_e of 3.8 m and L_e/D of 72.4 m. According to Taitel et al. (1980), at a pipe cross-section located at 3.8 m from inlet in a pipe of 0.0525 m diameter, flow rate pairs found in the area bounded by curves A and F will be stable slugs while the flow rate pairs found within curves F and E and bounded above by a section of curve A, will be churn flows. Similar explanation goes for curve G which represents an entrance length of 9.6 m in a pipe of 0.1016 m diameter while curve H represents an entrance length of 15.4m in a pipe of 0.2032m diameter. Table 4.3 shows the superficial velocity pairs and the calculated (Equations (4.3) and (4.4)) inlet velocity pairs of the two-phase flow regime that have been investigated in the present study.

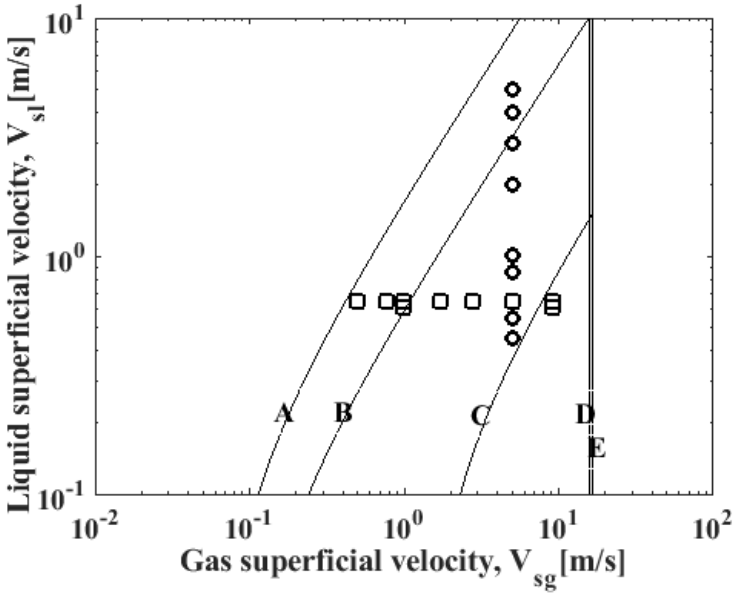

(a)

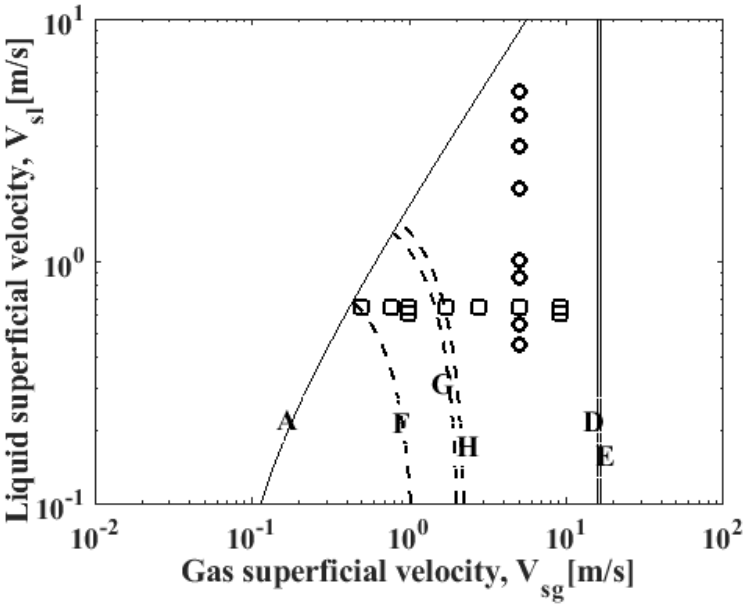

(b)

Figure 4.3: Flow regime maps based on (a) Mishima and Ishii (1984) transition criteria in addition to Schlegel et al. (2009) criterion for cap-bubbly to churn turbulent flow transition in large pipes, (b) Taitel et al. (1980) entry length phenomenon for slug to churn flow transition.

Table 4.3a: Two phase flow case studies

Pipe Diameter = 0.0525m						
S/N	**V_{sl} [m/s]**	**V_{sg} [m/s]**	**V_l [m/s]**	**V_g [m/s]**	**Flow regime**	**Gas fraction, β[-]**
1	0.61	0.978	0.725	6.189	Slug flow	0.616
2	0.61	9.04	0.725	57	Churn flow	0.937
3	0.642	0.5	0.763	3.164	Slug flow	0.438
4	0.642	0.773	0.763	4.89	Slug flow	0.546
5	0.642	0.978	0.763	6.189	Slug flow	0.604
6	0.642	1.7	0.763	10.76	Slug flow	0.726
7	0.642	2.765	0.763	17.5	Slug flow	0.812
8	0.642	5	0.763	31.64	Slug flow	0.886
9	0.642	9.04	0.763	57	Churn flow	0.934
10	0.45	5	0.534	31.64	Churn flow	0.917
11	0.55	5	0.653	31.64	Slug flow	0.901
12	0.85	5	1.01	31.64	Slug flow	0.855
13	1	5	1.188	31.64	Slug flow	0.833
14	2	5	2.375	31.64	Slug flow	0.714
15	3	5	3.563	31.64	Slug flow	0.625
16	4	5	4.751	31.64	Slug flow	0.556
17	5	5	5.939	31.64	Slug flow	0.500
Pipe Diameter = 0.1016m						
S/N	**V_{sl} [m/s]**	**V_{sg} [m/s]**	**V_l [m/s]**	**V_g [m/s]**	**Flow regime**	**β[-]**
18	0.61	0.978	0.812	3.938	Slug flow	0.616
19	0.61	9.04	0.812	36.4	Churn flow	0.937
20	0.642	0.5	0.854	2.013	Slug flow	0.438
21	0.642	0.773	0.854	3.11	Slug flow	0.546
22	0.642	0.978	0.854	3.938	Slug flow	0.604
23	0.642	1.7	0.854	6.845	Slug flow	0.726
24	0.642	2.765	0.854	11.133	Slug flow	0.812
25	0.642	5	0.854	20.133	Slug flow	0.886
26	0.642	9.04	0.854	36.4	Churn flow	0.934

Table 4.3b: Two phase flow case studies

Pipe Diameter = 0.2032m						
S/N	**V_{sl} [m/s]**	**V_{sg} [m/s]**	**V_l [m/s]**	**V_g [m/s]**	**Flow regime**	**Volume fraction, β[-]**
27	0.61	0.978	0.769	4.943	Cap bubbly flow	0.616
28	0.61	9.04	0.769	45.69	Churn turbulent flow	0.937
29	0.642	0.5	0.81	2.53	Cap bubbly flow	0.438
30	0.642	0.773	0.81	3.91	Cap bubbly flow	0.546
31	0.642	0.978	0.81	4.94	Cap bubbly flow	0.604
32	0.642	1.7	0.81	8.59	Churn turbulent flow	0.726
33	0.642	2.765	0.81	13.976	Churn turbulent flow	0.812
34	0.642	5	0.81	25.27	Churn turbulent flow	0.886
35	0.642	9.04	0.81	45.69	Churn turbulent flow	0.934

4.2 CFD mesh sensitivity and validation studies

The computational domain and flow conditions used for mesh sensitivity and validation studies are similar to the experimental set-up of Liu et al. (2012) which is an upward flow in vertical 90^0 elbow of diameter 0.0525m and radius of curvature of 0.0762m shown in Figure 4.1. The same geometry was scaled up to the two more similar geometries having diameters of 0.1016m and 0.2032m and presented in Table 4.1. The following two subsections present the mesh independence studies and the validation studies respectively. The multiphase flow case studies which were used for the mesh sensitivity and validation studies are given in Table 4.4.

Table 4.4: Flow conditions used for validation and mesh independence studies

Flow properties	**Air**	**Water**
Slug flow Superficial velocities [m/s]	0.978	0.61
Churn flow Superficial velocities [m/s]	9.04	0.61
Density [kg/m^3]	1.225	998.2
Viscosity [kg/m-s]	1.7894 X 10^{-5}	0.001003
Surface tension [N/m]	0.0728	

4.2.1 Mesh independency

Mesh independency tests have been carried out using three different mesh sizes for each of the pipe sizes that have been investigated. The pipe geometries were created in ANSYS Design-Modeller. Then all the computational domains were divided into hexahedral meshes by exporting them to ICEM CFD 18.0 meshing software were the O-grid method was used to create the structured mesh with appropriate refinement and spacings within the near-wall region. Figure 4.5 show the typical mesh of the pipe wall for all the pipe sizes and Figures 4.6 (a), (b) and (c) show the mesh sizes under study for the pipe diameters of 0.0525m, 0.1016m and 0.2032m respectively. Table 4.5 show the refinement parameters that were adopted for each of the mesh sizes in each of the pipe sizes. The near wall cell size was predicted using the expression:

$$\Delta y = \frac{y^+ \mu}{U_\tau \rho} \tag{4.14}$$

and

$$U_\tau = \sqrt{\frac{\tau_w}{\rho}} \tag{4.15}$$

$$\tau_w = 0.5 C_f \rho U_\infty^2 \tag{4.16}$$

For internal pipe flows, C_f is given as:

$$C_f = 0.079 Re_d^{-0.25} \tag{4.17}$$

where Δy and U_∞ are the first cell height and the free stream velocity respectively. The y^+ values were chosen between 30 and 100.

The mesh sensitivity study carried out in this study involves determining the optimum mesh for each pipe size that would accurately and economically model the turbulent flows of interest based on the appropriate turbulence model and near wall modelling approach that has been chosen.

Figure 4.4: Meshing on pipe wall

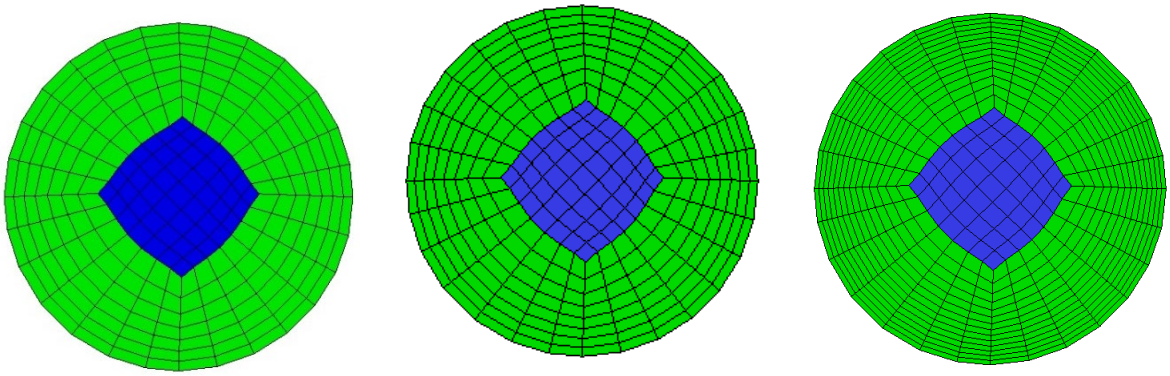

154840 cells 277136 cells 366912 cells

(a)

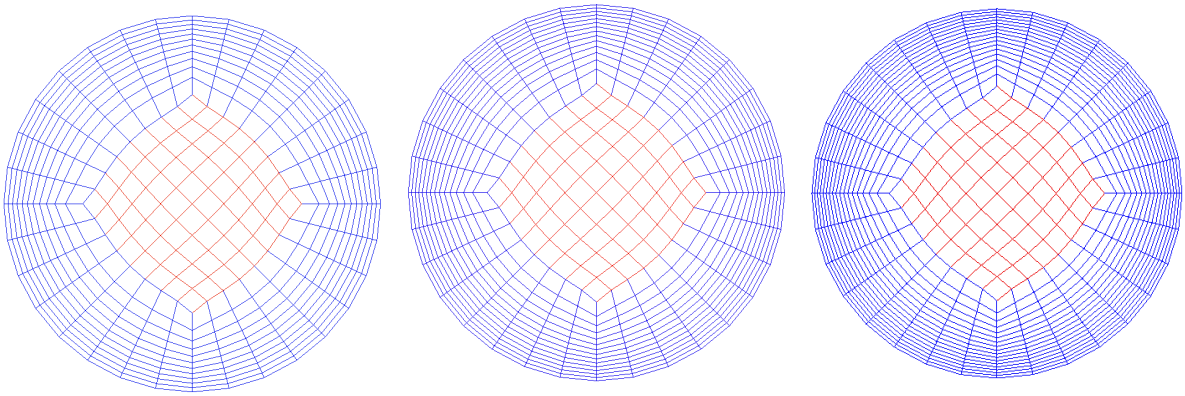

688896 cells 428032 cells 690688 cells

(b)

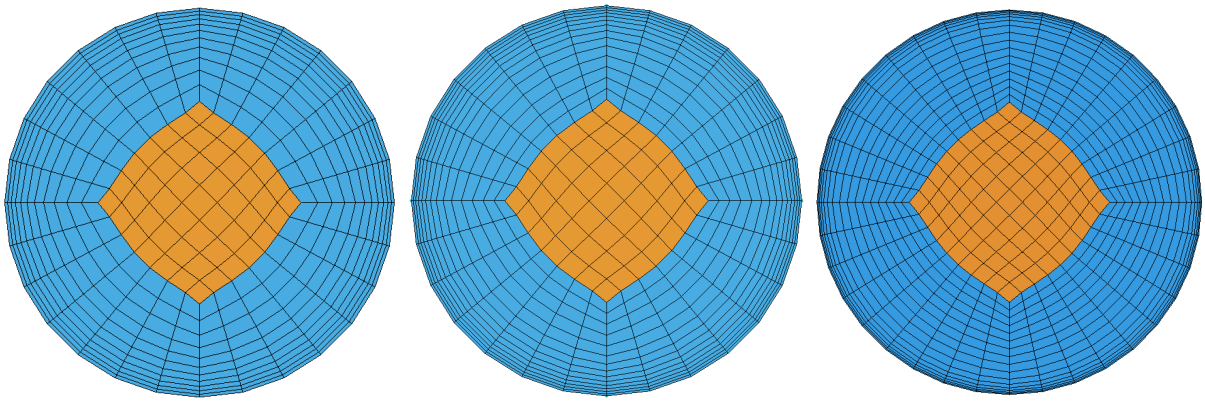

352002 cells 269010 cells 647802 cells

(c)

Figure 4.6: Pipe meshes for (a) D = 0.0525 m, (b) D = 0.1016 m and (c) D = 0.2032 m.

Table 4.5: Mesh parameters

D = 0.0525 m		**D= 0.1016 m**		**D = 0.2032 m**	
Mesh sizes	**1st cell, Δy[m]**	**Mesh sizes**	**1st cell, Δy[m]**	**Mesh sizes**	**1st cell, Δy[m]**
154840	0.0012	688896	0.0011	353002	0.0015
277136	0.001	428032	0.00089	269010	0.001
366912	0.00054	690688	0.0007	647802	0.0005

Velocity profiles were respectively obtained in the 0.0525m, 0.1016m and 0.2032m pipes at planes positioned at 0.2 m, 0.4 m and 0.6 m upstream of the bends. Figures 4.7 (a), (b) and (c) show respectively, that the velocity profiles for all three meshes in each of the pipe sizes are almost similar and they represent typical velocity profile of a fully developed turbulent flow in pipe. The slug flow regime properties were implemented as homogenous mixture properties to calculate the velocity profiles.

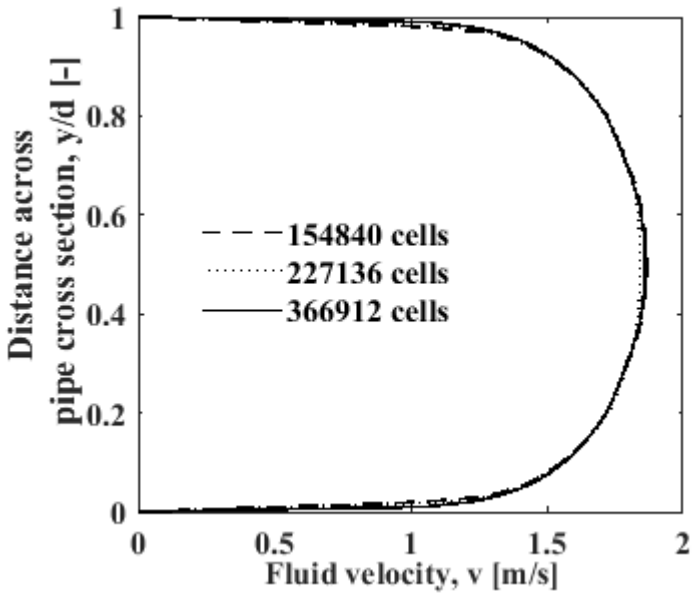

(a)

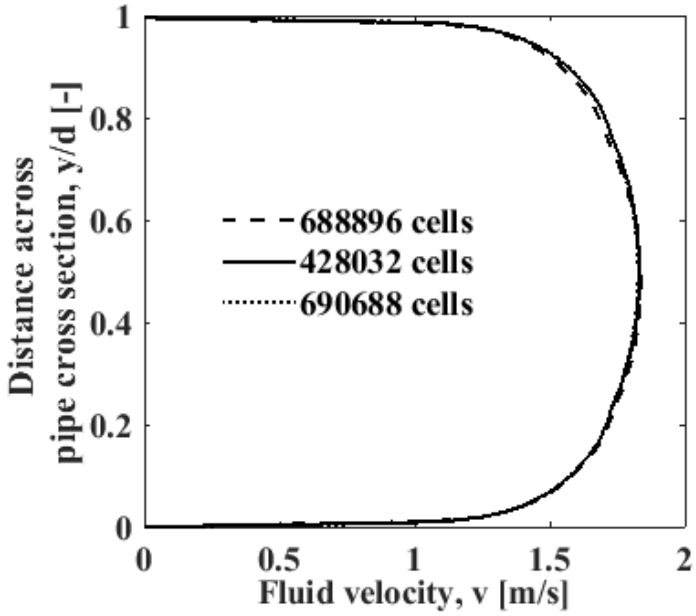

(b)

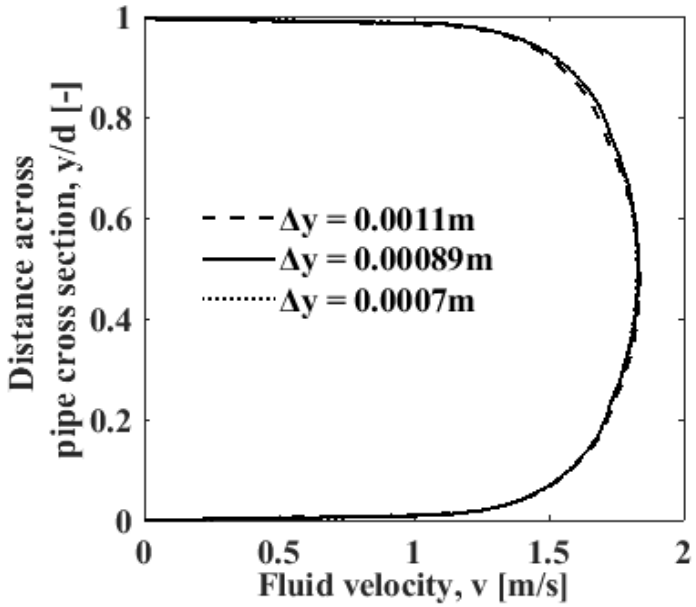

(c)

Figure 4.7: Predicted velocity profiles for the three mesh sizes in pipe diameters of (a) D = 0.0525 m, (b) D = 0.1016 m and (c) D = 0.2032 m

4.2.2 Validation studies

In order to validate the numerical models which were used in this study, void fraction data was collected from the three different meshes that were tested for

the pipe of 0.0525m I.D. The predicted void fraction signal were compared to the void fraction data which is available from the experiment of Liu et al. (2012) for the same pipe geometry and flow condition. The location for this data extraction was at the position of 0.2m from upstream of the bend. Figure 4.8 (a) shows the effects of mesh size on the variation of the void fraction signal for the three mesh sizes and the experiment (Liu et al. 2012) while Figure 4.8 (b) shows the effect of mesh size on the predicted PSD of the signal.

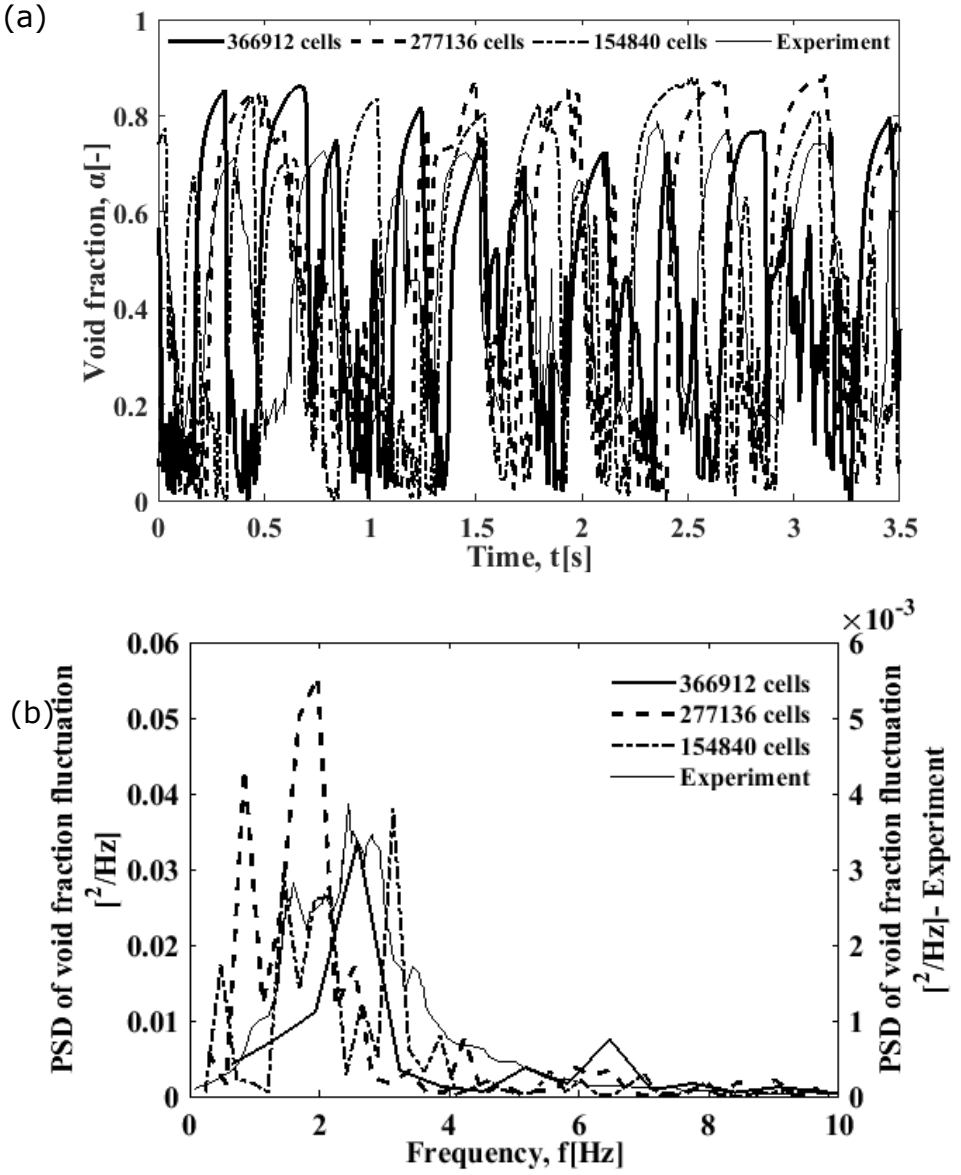

Figure 4.8: Comparison of the void fraction (a) time series and (b) PSD of fluctuation for the same geometry and flow condition from the experiment (Liu et al. 2012) to that obtained from numerical predictions using the three mesh sizes.

Flow development is dependent on the mesh size and the fluctuations vary significantly among different meshes as seen in Figure 4.8 (a). However, Figure 4.8 (b) shows a good agreement between the prediction using the mesh size of 366912 and the experimental data. Nevertheless, mesh independency testing based on void fraction time series is quite challenging as discussed by Parsi et al. (2016) and thus discrepancies in void fraction fluctuations have been quantified using the average data obtained for each mesh size in the present study. The time-averaged mean volume fraction at the reference location was calculated to be 0.438, 0.476 and 0.439 for mesh sizes of 154840, 227136 and 366912, respectively. The experimental value of Liu et al. (2012) was 0.427. The experimental data of Liu et al. (2012) were extracted from their reported work using plot digitisation tool. The possible errors involved in using this method include data precision/human error, round-off error and errors emanating from using only the data sample size that was available from the reported experimental plot to calculate average value. However, to reduce precision/human error, the plot digitisation was carried out twice and on comparison, the two sets of extracted data matched each other. Also, round-off error was avoided by increasing the precision of numbers to up to 5 decimal places. Finally, since slug/churn flows have highly alternating nature and the void fraction signal has a consistent repetitive pattern, it is assumed that the reported 5s of flow signal reported in the experiment is very representative of the flow behaviour hence, the calculated average value is reliable.

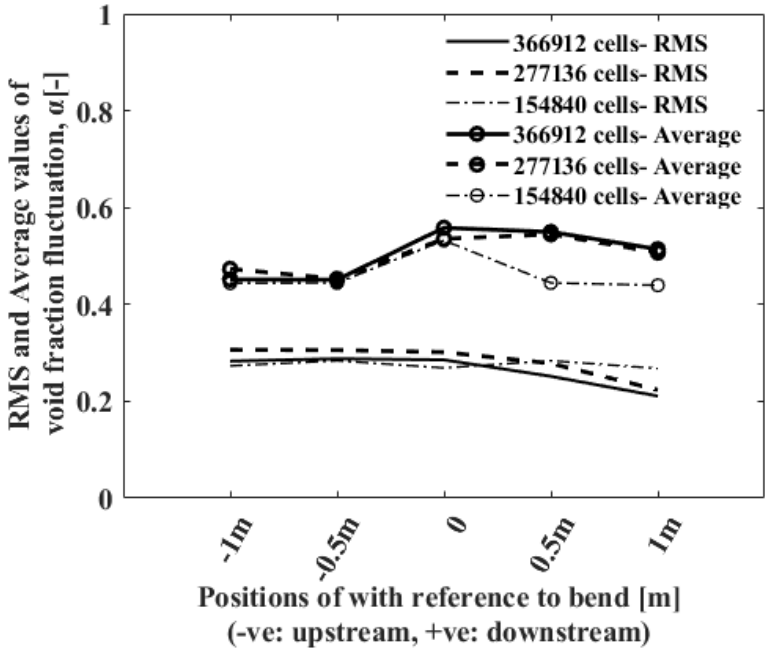

Figure 4.9: RMS and average of void fraction signal obtained for meshes in Figure 4.6 (a).

Figure 4.9 shows a comparison of the RMS and the average values of the signal for the three meshes used in the mesh sensitivity analysis of the pipe of 0.0525m I.D. This figure also confirm that the average values as well as RMS values in the present study give more clearer comparison of void fraction predictions obtained for different meshes. It is inherently difficult to predict transient phenomenon of slug flows. This difficulty is visible in Figure (4.8b) as well. Although, based on the prediction of velocity profile and void fraction, the mesh of size 366912 was treated as grid independent and used for more validation studies subsequently.

4.3 Structural FEA

The pre-processing stage in full transient structural finite element analysis involves accurate definition of structural model geometry and its material properties. These definitions as well as the analysis settings make up the inputs in the analysis. Under the analysis setting, the fundamental physical behaviours of the system under study including boundary and initial conditions are defined. The next stage in the analysis is the processing stage. Here the most appropriate numerical

calculations technique for the problem is implemented. This has been presented under the solution procedure section below.

4.3.1 Structural model

The structural response to flow induced forces depends on the nature of the forcing signal as well as the properties and geometry of the structural model. The structural model used in the present numerical study have geometry and properties given in Tables 4.6 and 4.7, respectively. The pipe thicknesses are selected according to the API 5L grade line pipes. The length, breadth and bend radius are as given in Table 4.1 for the fluid model. The pipe model and mesh are shown in Figure 4.10.

Table 4.6: Details of pipe geometry, mesh sizes and boundary condition

Properties	**Small Pipe**	**Medium Pipe**	**Large Pipe**
Inner diam6eter, D[m]	0.0525	0.1016	0.2032
Outer diameter, D_o[m]	0.06032	0.1143	0.2191
Thickness, t[m]	0.00391	0.00635	0.00795
Elbow breadth, b[m]	0.2	0.4	0.6
Mesh type	Tetrahedral	Tetrahedral	Tetrahedral
Mesh size [-]	66247	109039	119040

Table 4.7: Property details of the pipe structure

Property	**Definition**
Pipe material	Structural steel
Steel density [kg/m^3]	7850
Young's Modulus [Pa]	2X10^{11}
Tensile Yield strength [Pa]	2.5X8^{08}
Tensile Ultimate strength [Pa]	4.6X8^{08}
Poisson's ratio	0.3

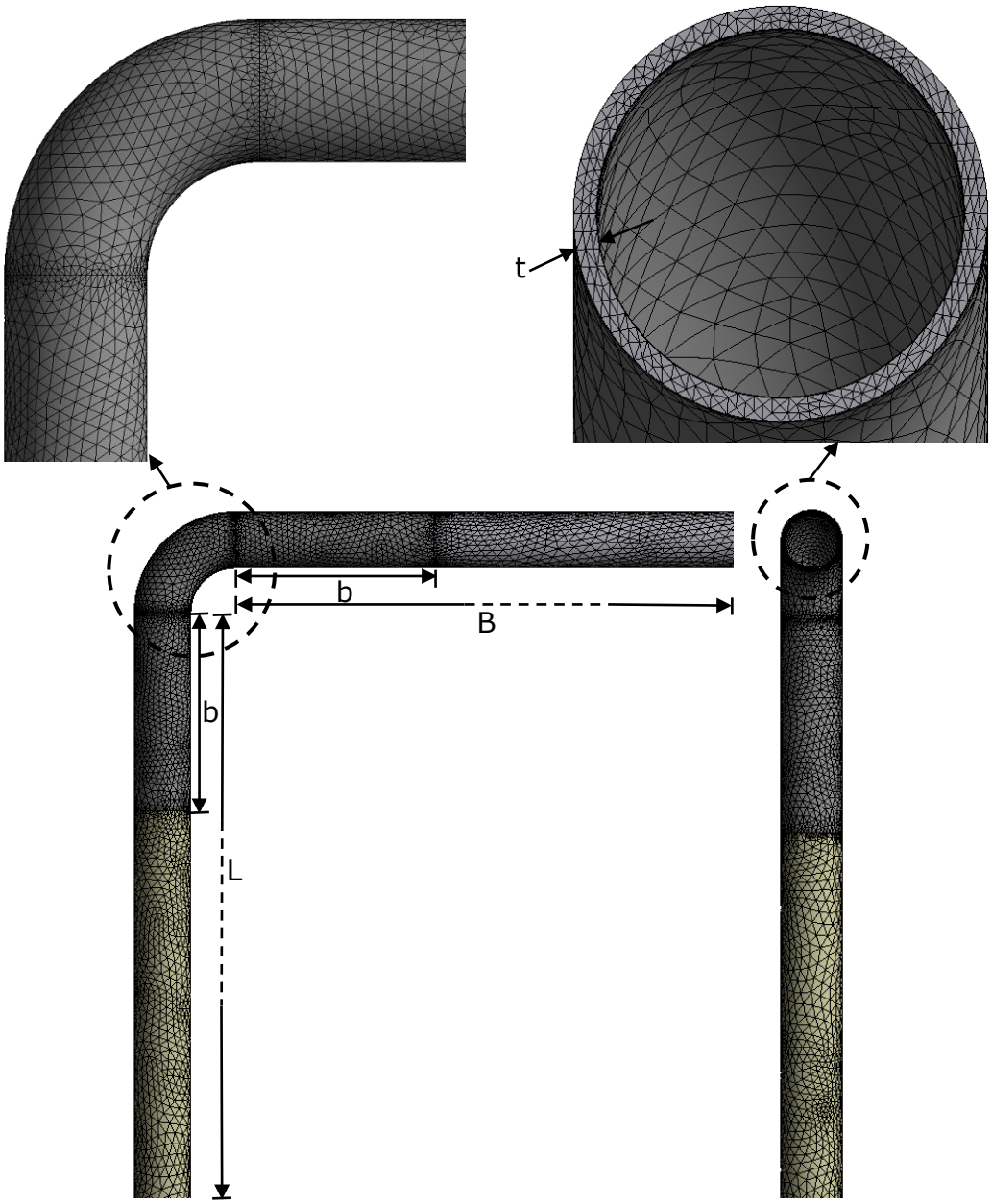

Figure 4.10: Geometry and mesh of structural model.

4.3.2 Analysis settings

Since the pipe geometry is a slender structure and transverse displacement could be assumed to be upto 10% of the pipe thickness, setting large deflection parameter to 'on' allows the numerical calculation to account for stiffness changes resulting from change in element shape and orientation. Large rotation and strain also contribute to the changes. Hence, this analysis which accounts for large

deflection requires iterative solution and takes longer to solve, however, it is more accurate than solutions which ignores the occurance of large deflection.

Table 4.8: Analysis setting

Parameter	**Setting**
Large deflection	On
Solver type	Iterative solution
Time step [s]	0.002s
Boundary condition (pipe ends)	Fixed support
Initial displacement	Zero
Initial velocity	Zero

Further more, this type of analysis also require that the load be applied in small increments. Hence, the time history of the flow induced forces computed using CFD simulation results will be applied in increaments at a small time step size as given in Table 4.8. The force is applied on the inner surface of the elbow bounded by two cross sectional planes that are cut off at distances of 'b', upstream and downstream of the elbow as shown in Figure 4.10.

The present transient structural analysis tool (ANSYS Mechanical) allows damping to be specified for the structure through damping controls. The controls include specifying values for stiffness coefficient (Beta damping), mass coefficient (alpha damping) and numerical damping. These damping controls can also be applied as material damping when assigning material properties in the Engineering Data section. In the present study, the numerical damping which is also called the amplitude decay factor, γ has been assigned a default value of 0.1. This damping option controls the numerical noise produced by the higher frequencies of a structure since the contributions of the higher frequency modes are usually not accurate.

4.3.3 FEA solution procedure

To solve equation (3.38) the program uses the Hilber-Hughes-Taylor method called HHT-α method and developed by Hilber et al. (1977). This is an implicit time

integration method which offers some improvement over the Newmark time-integration method developed by Newmark (1959). Both methods are unconditionally stable and second-order accurate. However, the HHT- α method is also second-order accurate while being able to control numerical dissipation in higher frequency modes hence damping out the associated unwanted numerical noise. On the other hand, the Newmark method cannot control numerical dissipation without jeopardizing second-order accuracy of low frequency modes (Hughes, 1987). The HHT- α time integration scheme solves three finite difference equations for the three unknowns $\{\ddot{d}_{n+1}\}$, $\{\dot{d}_{n+1}\}$ and $\{d_{n+1}\}$ using the algebraic equations:

$$[k]\left\{d_{n+1-\alpha_f}\right\} + [c]\left\{\dot{d}_{n+1-\alpha_f}\right\} + [m]\{\ddot{d}_{n+1-\alpha_m}\} = \{F^a\}(t_{n+1-\alpha_f}) \tag{4.11}$$

$$\left\{\dot{d}_{n+1-\alpha_f}\right\} = \{\dot{d}_n\} + [(1-\delta)\{\ddot{d}_n\} + \delta\left\{\ddot{d}_{n+1-\alpha_f}\right\}]\Delta t \tag{4.12}$$

$$\left\{d_{n+1-\alpha_f}\right\} = \{d_n\} + \{\dot{d}_n\}\Delta t + \left[\left(\frac{1}{2}-\alpha\right)\{\ddot{d}_n\} + \alpha\left\{\ddot{d}_{n+1-\alpha_f}\right\}\right]\Delta t^2 \tag{4.13}$$

where:

$$\{\ddot{d}_{n+1-\alpha_m}\} = (1-\alpha_m)\{\ddot{d}_{n+1}\} + \alpha_m\{\ddot{d}_n\}$$

$$\left\{\dot{d}_{n+1-\alpha_f}\right\} = (1-\alpha_f)\{\dot{d}_{n+1}\} + \alpha_f\{\dot{d}_n\}$$

$$\left\{d_{n+1-\alpha_f}\right\} = (1-\alpha_f)\{d_{n+1}\} + \alpha_f\{d_n\}$$

$$\left\{F^a\left(t_{n+1-\alpha_f}\right)\right\} = (1-\alpha_f)\{F^a_{n+1}\} + \alpha_f\{F^a_n\}$$

Equation (4.11) then give the finite difference form:

$$\left(a_0[M] + a_1[C] + (1-\alpha_f)[K]\right)\{d_{n+1}\} = (1-\alpha_f)\{F^a_{n+1}\} + \alpha_f\{F^a_n\} - \alpha_f[K]\{d_n\} + [M]\left(a_0\{d_n\} + a_2\{\dot{d}_n\} + a_3\{\ddot{d}_n\}\right) + [C]\left(a_1\{d_n\} + a_4\{\dot{d}_n\} + a_5\{\ddot{d}_n\}\right) \tag{4.14}$$

Where:

$$a_0 = \frac{1-\alpha_m}{\alpha \Delta t^2}$$

$$a_1 = \frac{(1-\alpha_f)\delta}{\alpha \Delta t}$$

$$a_2 = a_0 \Delta t$$

$$a_3 = \frac{1-\alpha_m}{2\alpha} - 1$$

$$a_4 = \frac{(1-\alpha_f)\delta}{\alpha} - 1$$

$$a_5 = \left(1-\alpha_f\right)\left(\frac{\delta}{2\alpha} - 1\right)\Delta t$$

Equation (4.14) calculates $\{d_{n+1}\}$ while $\{\dot{d}_{n+1}\}$ and $\{\ddot{d}_{n+1}\}$ are calculated using the expressions:

$$\{\dot{d}_{n+1}\} = a_1(\{d_{n+1}\} - \{d_n\}) - a_4\{\dot{d}_n\} - a_5\{\ddot{d}_n\} \quad (4.15)$$

$$\{\ddot{d}_{n+1}\} = a_0(\{d_{n+1}\} - \{d_n\}) - a_2\{\dot{d}_n\} - a_3\{\ddot{d}_n\} \quad (4.16)$$

α and δ, are originally Newmark integration parameters but α has been amended as α_m (Wood et al., 1981) and α_f (Hilber et al., 1977). γ is the amplitude decay factor. The values for α, α_m, α_f, δ and γ are respectively, 0.3025, 0, 0.1, 0.6 and 0.1. These equations are solved at discrete time points. The time increment between successive time points is called the integration time step.

CHAPTER 5

CHARACTERISTICS OF TWO-PHASE FLOW INDUCED EXCITATION FORCES AT A 90^0 PIPE BEND

This chapter discusses the main CFD investigations that were conducted based on the small pipe geometry of 0.0525 m diameter. Two-phase air-water flow simulations have been carried out to investigate the effects of liquid and gas velocities on excitation force characteristics at the pipe bend. In the CFD analysis, the superficial gas velocity was varied from 0.5 m/s to 9.04 m/s, while keeping the liquid superficial velocity at 0.642 m/s encompassing the slug to churn flow regimes. Further, the effects of liquid superficial velocity have been captured by varying the velocity from 0.45 m/s to 5 m/s, while keeping the superficial gas velocity constant at 5 m/s. Figure 4.4 shows the simulation conditions plotted on the superficial gas and liquid velocity plane together with flow transition plot of Mishima and Ishii's (1984) for upward two-phase flows. The simulation conditions mainly falls within the slug and churn flow regimes.

5.1 Two-phase volume fraction results

The force fluctuations in the bend is primarily due to the momentum flux at the bend. As given in Liu et al. (2012) under homogeneous flow conditions, the momentum flux in two phase-flow can be calculated as:

$$M = AV_t^2\left[\rho_g \tilde{\alpha}_g^A(t) + \rho_l\left(1 - \tilde{\alpha}_g^A(t)\right)\right] \qquad (5.1)$$

where, $\tilde{\alpha}_g^A$ represents the area averaged void fraction and V_t is the mixture velocity. Therefore, it is interesting to analyse the void fraction fluctuations under different flow conditions.

5.1.1 Effects of gas velocity

Figure 5.1 shows the volume fraction contour plots of gas within the flow domain for different superficial gas velocity after 5 seconds of flow. The figure shows that the CFD model captures the flow features of slug, churn and churn-annular flow well. The slug is clearly visible up to superficial gas velocity of 1.7 m/s, characterised by large gas bubbles surrounded by thin liquid films and cyclic liquid structures. As expected in slug flows, gas bubbles are also entrained within the liquid structures. It should be noted that the VOF model is good at tracking large interfaces between the phases. Thus, the smaller bubbles and their interactions entrained within the liquid structures are not well captured in the simulation. Particularly, small bubbles whose volumes are much less than the cell volume or whose interface do not cross the cell faces could not be captured. As the superficial gas velocity increases further to 2.765 m/s and 5 m/s, the liquid structure's integrity is lost due to the penetration of gas into the liquid at higher gas velocities and the flow is characterised by large scale liquid waves at the wall and breaking down of large gas bubbles into smaller ones or continuous core. These behaviours can be identified as flow regime transition behaviours from slug to churn flow as well as established churn flow behaviours. With further increase of superficial gas velocity to 9.04 m/s, the flow is churn flow regime and approaching the boundary to annular flow transition. At this velocity, the flow is characterised by gas core and discontinued liquid wavy structures at the wall. Despite the shortcoming of the VOF model to capture smaller bubbles and droplets, larger scale flow features of slug and churn flows are captured well.

The area averaged void fraction fluctuations seems to be a key parameter in flow induced vibration study (Liu et al. 2012). Figures 5.2 and 5.3 show comparison of the time domain signals and the power spectrum densities (PSD) of the void fraction obtained from the present CFD study and reported experiment (Liu et al. 2012) for a slug and churn flow respectively. The CFD prediction represents well the void fraction fluctuations of both slug and churn flows as can be seen in Figures 5.2 (a) and 5.3 (a), respectively. In particular, the slug flow is characterised by the liquid slug bodies with void fraction averaging around 20% and the gas bubbles with void fraction of 80%. The PSD of the slug flow, Figure 5.2 (b), shows a peak

at 2.5 Hz which matches well with the experimental value. Churn flow is inherently more complex to predict, but the CFD simulation reproduced the experimental signal well as shown in Figure 5.3 (a). As expected, the PSD (Figure 5.3 (b)) shows a range of frequencies and similar trend as reported in the experiment (Liu et al. 2012). The most predominant frequency has been predicted to be around 0.6 Hz. Relative to the slug flow (Figure 5.2 (b)), the PSD of the churn flow is smaller by an order of magnitude.

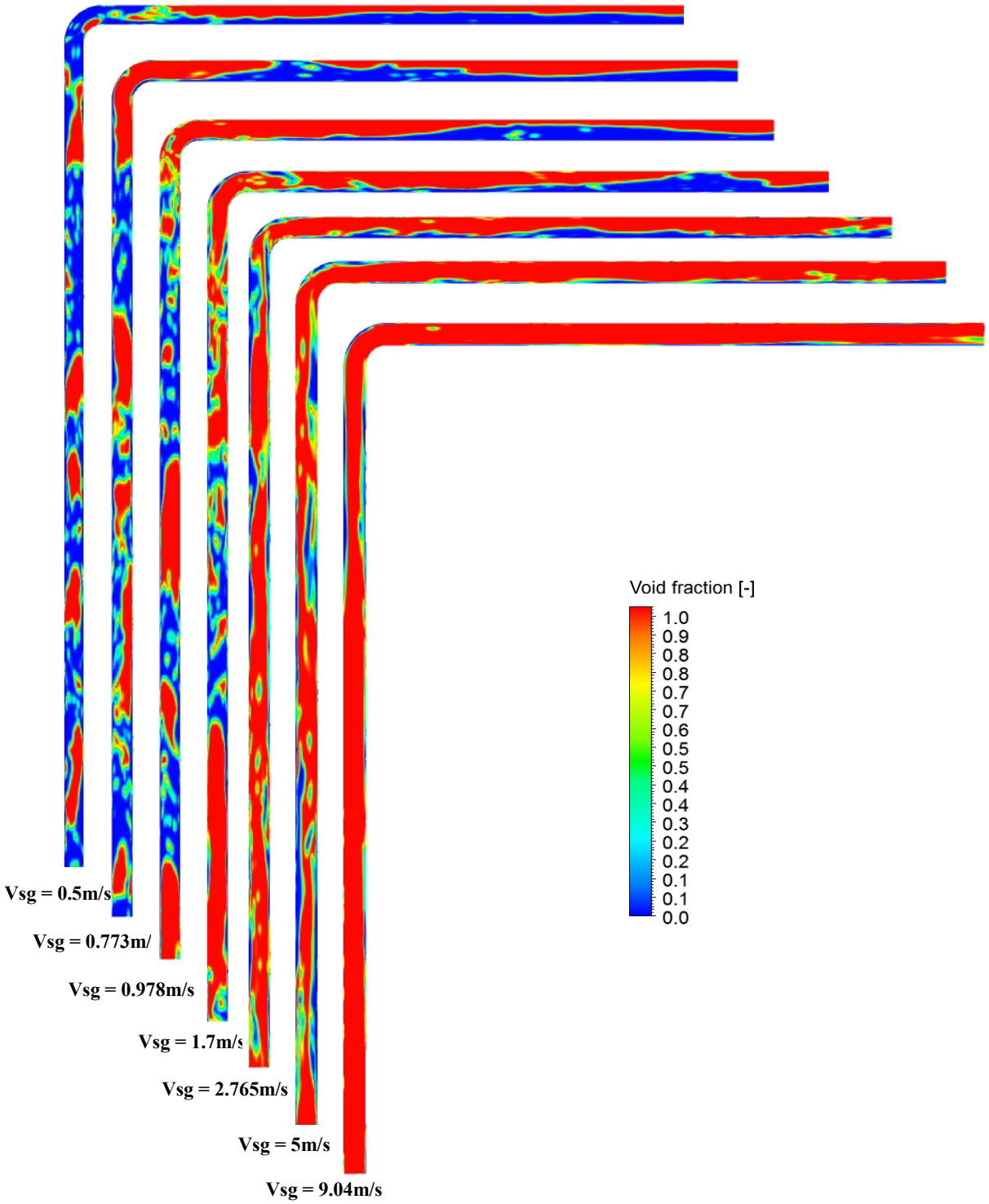

Figure 5.1: Contour Plot of gas void fraction distribution for different superficial gas velocities for a fixed superficial liquid velocity of 0.642 m/s

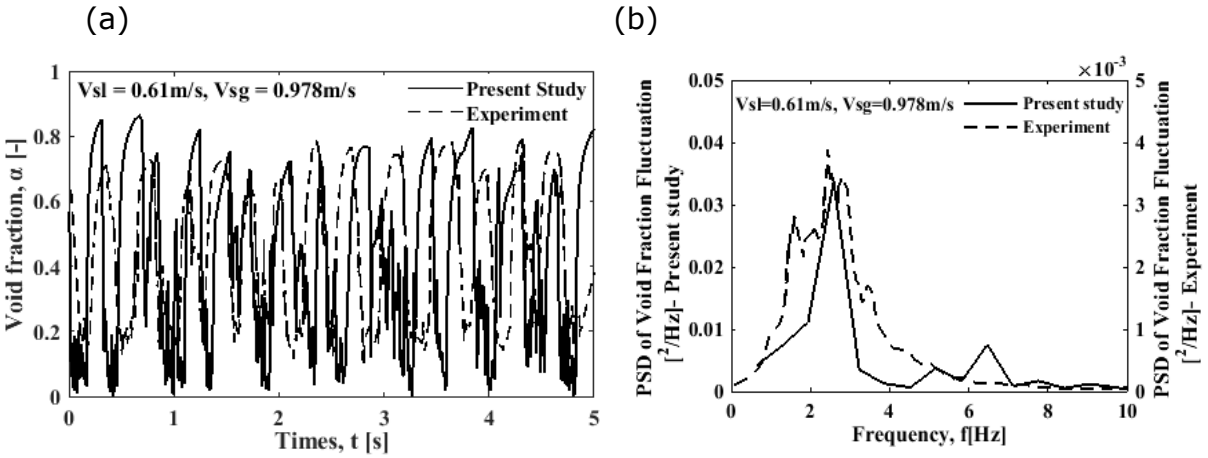

Figure 5.2: Comparison of void fraction variation with time for present study and experiment (Liu et al., 2012) result of a typical slug flow (a) Void fraction fluctuation and (b) PSD.

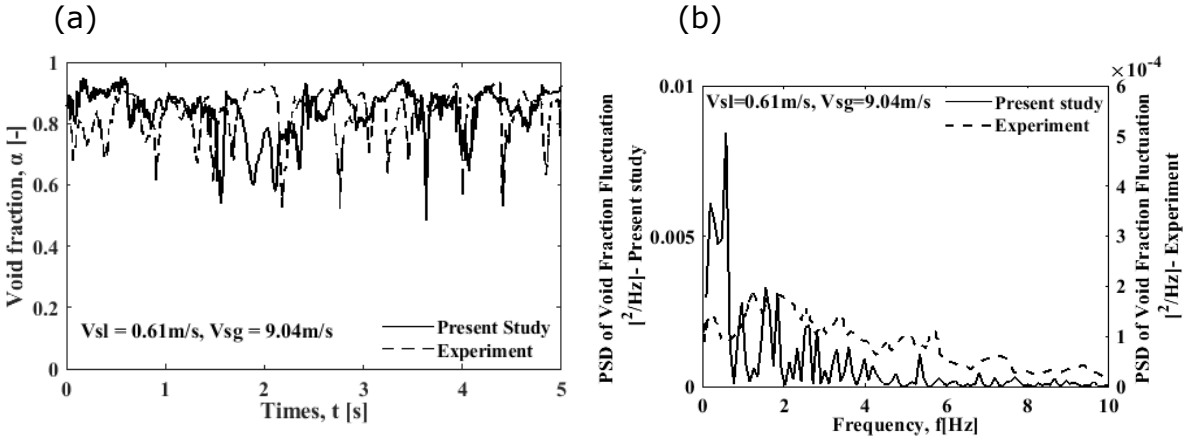

Figure 5.3: Comparison of void fraction variation with time of present study and experiment (Liu et al., 2012) result of a typical churn flow (a) Void fraction fluctuation and (b) PSD.

Figure 5.4 shows the predicted void fraction fluctuations and their power spectrum density for different flow regimes keeping the liquid velocity fixed at 0.642 m/s. Figures 5.4(a) (i) – (iii) show the consistent slug flow regimes, where the void fraction has been dominated by liquid slugs with average void fraction of around 20% and gas bubbles with void fraction of 80%. The corresponding PSD in Figures 5.4(b) (i) - (iii) show the dominant frequency is approximately 2 Hz, which drops slightly with the increase of gas velocity. The spread of PSD is between 0 and 10 Hz. Figures 5.4 (a) and (b) (iv) – (vii) show that the slug structure starts to break

down as the gas superficial velocity increases to churn flow velocities. The PSD of churn flow is characterised by more than one distinct peak and the range of frequencies drops compared to slug flow to between 0 and 5 Hz, with the predominate frequencies also diminishing with higher gas velocities. The main flow features observed in the time series are as follows:

- At lower gas superficial velocities (below 1.7 m/s), the time averaged void fraction fluctuations broadly vary between two distinct values of 80% and 20%.
- While at the higher end of the void fraction of 80%, the time series is generally uniform, at the lower end of void fraction of 20%, the time series shows high frequency fluctuations which is representative of the randomly distributed and variable sized bubbles entrained in the liquid slug. Here, the entrained bubbles were large enough to be captured by the present sizes of mesh cells using VOF model.
- At higher superficial velocities (above 2.765 m/s), the cyclic fluctuations in the time series is characterised by sudden drops of the void fraction.
- The amplitude of the drops decreases with the increase of superficial gas velocities.
- At lower end of the superficial gas velocities (2.765 m/s), a broad range of amplitudes in drops is observed.
- With further increases of superficial gas velocities, the drop in amplitude becomes more uniform.

These observations can be interpreted as follows: at lower superficial gas velocities, the flow is characterised by slug flows with the transport of alternative structures of gas and liquid. Gas bubbles generally has uniform structures, while the liquid structures often entrained gas bubbles as characterised by high fluctuation frequency and low amplitude vibrations at around 20% of void fraction. It should be noted though, the present VOF model can only predict the presence of the larger bubbles within the liquid body. The presence of smaller bubbles and its associated fluctuations are not captured in the present study. With the increase of superficial gas velocities, the flow is transitioned to churn flows, which is characterised by the sudden drops in void fraction fluctuations. These drops indicate the passage of liquid structures. As the superficial gas velocity increases

(to 9.04 m/s), more and more gas penetrates through the liquid structures, liquid structures lose their integrity and breaks into large wavy structures along the wall, which is at the boundary of transition from churn to slug flows.

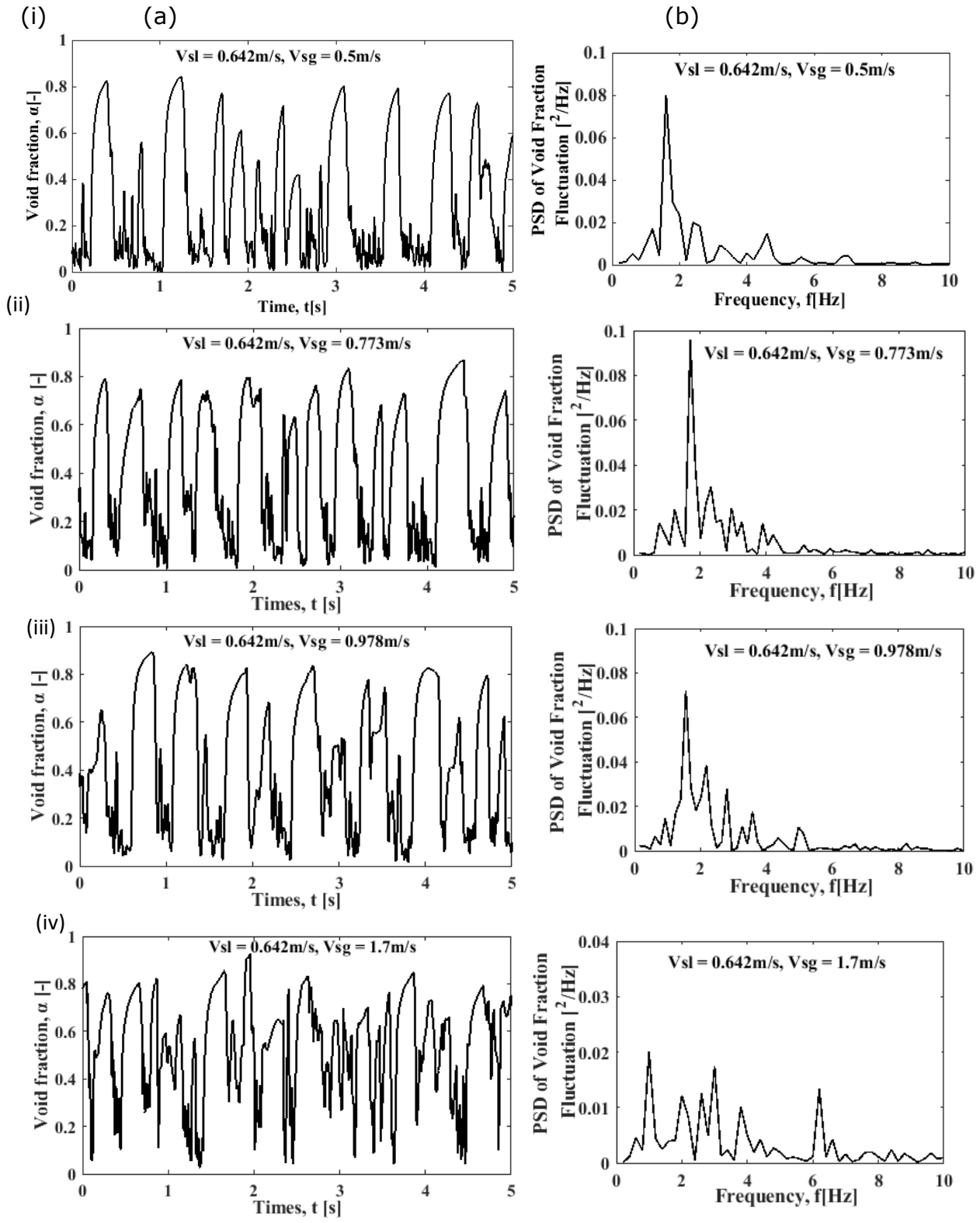

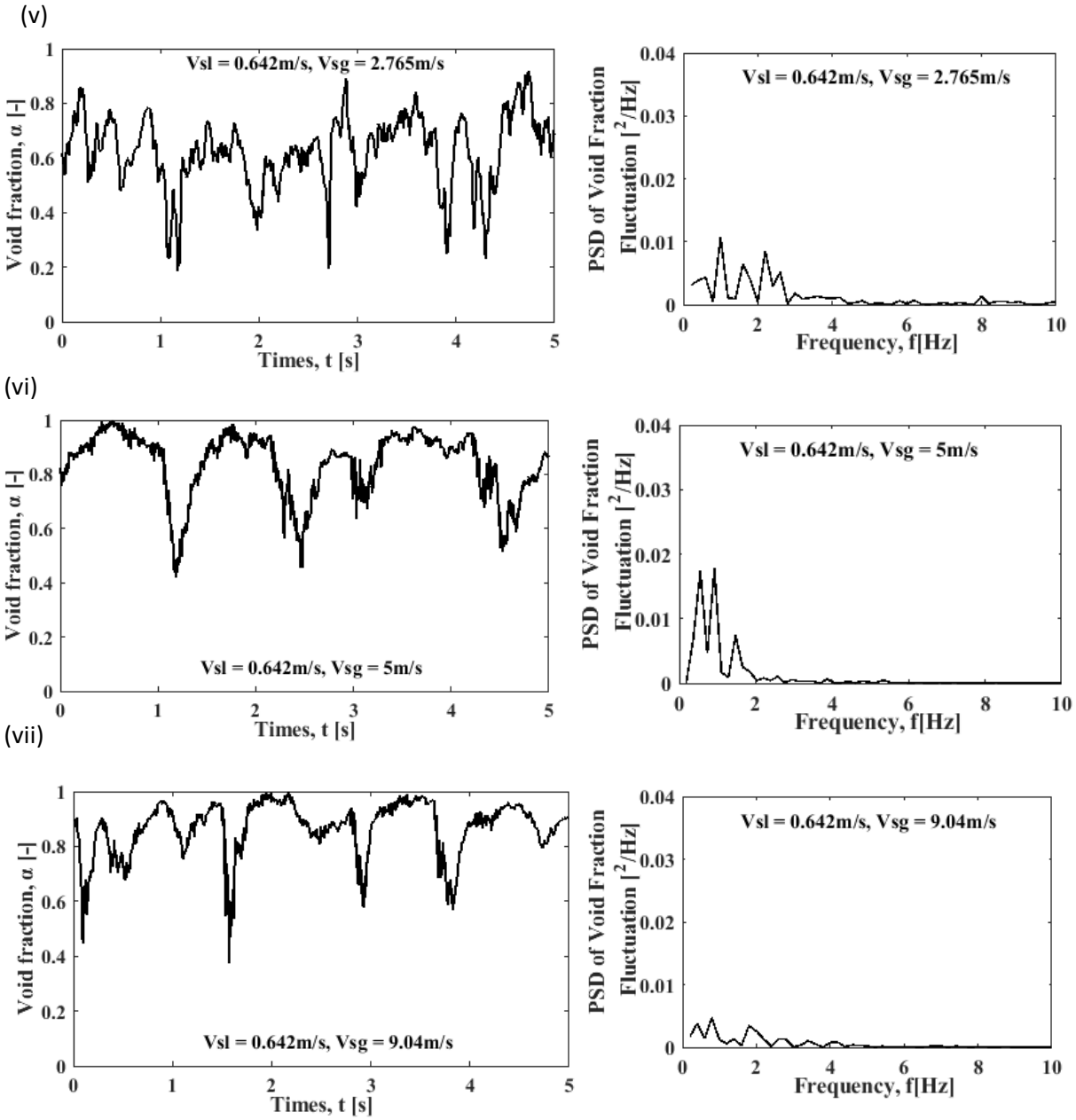

Figure 5.4: The effect of superficial gas velocity for a fixed superficial liquid velocity of 5 m/s (a) Void fraction fluctuation and (b) PSD.

Figures 5.5 (a) and (b) show the peak frequency and the RMS of void fraction fluctuations. Figure 5.5 (a) shows that the peak frequency varies between 0.75 Hz to 1.8 Hz and the value drops with the increase of gas flowrate. This could be explained as, with the increase of gas flow rate, the smaller gas bubbles coalesce into larger bubbles leading to the reduction of high frequency components. As the flows approach churn flows, this study observed a range of dominant frequencies (Figure 5.4 (b)) due to complex interaction between phases with the most

significant frequencies remaining constant at about 0.8 - 1Hz as seen in Figure 5.5 (a). Figure 5.5 (b) shows that the RMS of void fraction fluctuations drops with the increase of the superficial gas velocity. This observation can be explained as the increased chaotic nature of churn flows demonstrated by random void fractions appearing at diverse frequencies compared to the more periodic nature of moderate slug flow patterns where fluctuation energy is concentrated within a narrow band of frequencies. The fluctuation energies in flows close to or in churn flows are distributed over a large frequency ranges and the RMS of void fraction fluctuations drops considerably.

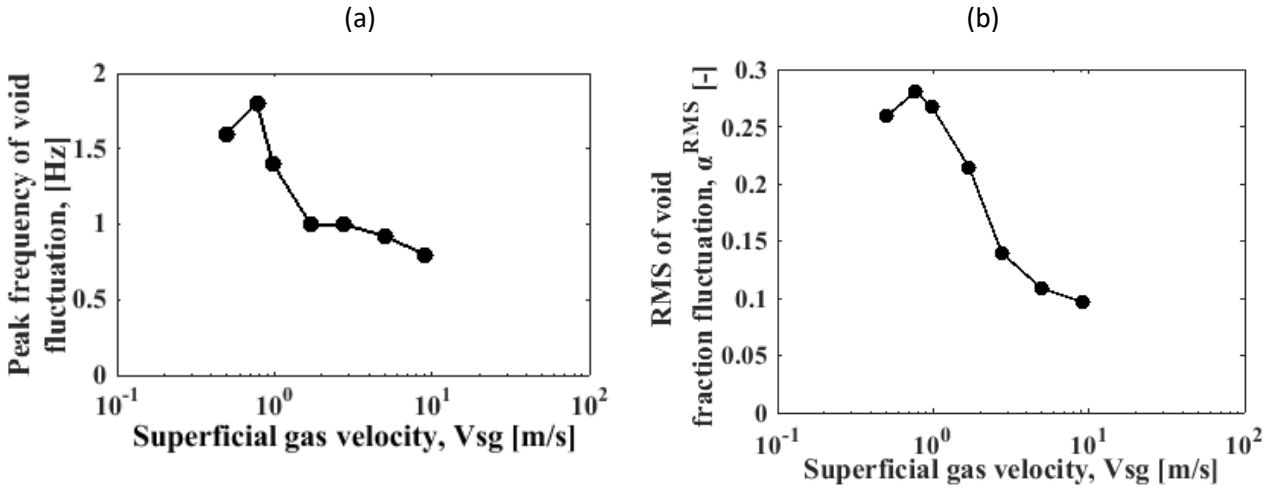

Figure 5.5: (a) Peak frequency and (b) RMS of void fraction fluctuation for different superficial gas velocities while keeping the superficial liquid velocity fixed at 0.642 m/s.

5.1.2 Effects of liquid velocity

Figure 5.6 shows the predicted void fraction fluctuations and their power spectral density for superficial liquid velocities varied between 0.45 m/s and 5m/s, while keeping the superficial gas velocity constant at 5 m/s. According to the flow regime map of Mishima and Ishii (1984) (Figure 4.4 (a)) these velocities falls within the slug flow regime, with the lowest liquid velocity at the slug-churn boundary, while the highest liquid velocity falls near the slug-bubbly flow boundary. As shown in Figure 5.6, the volume fraction contour plot at 5 seconds of flow development has been captured well in the simulation

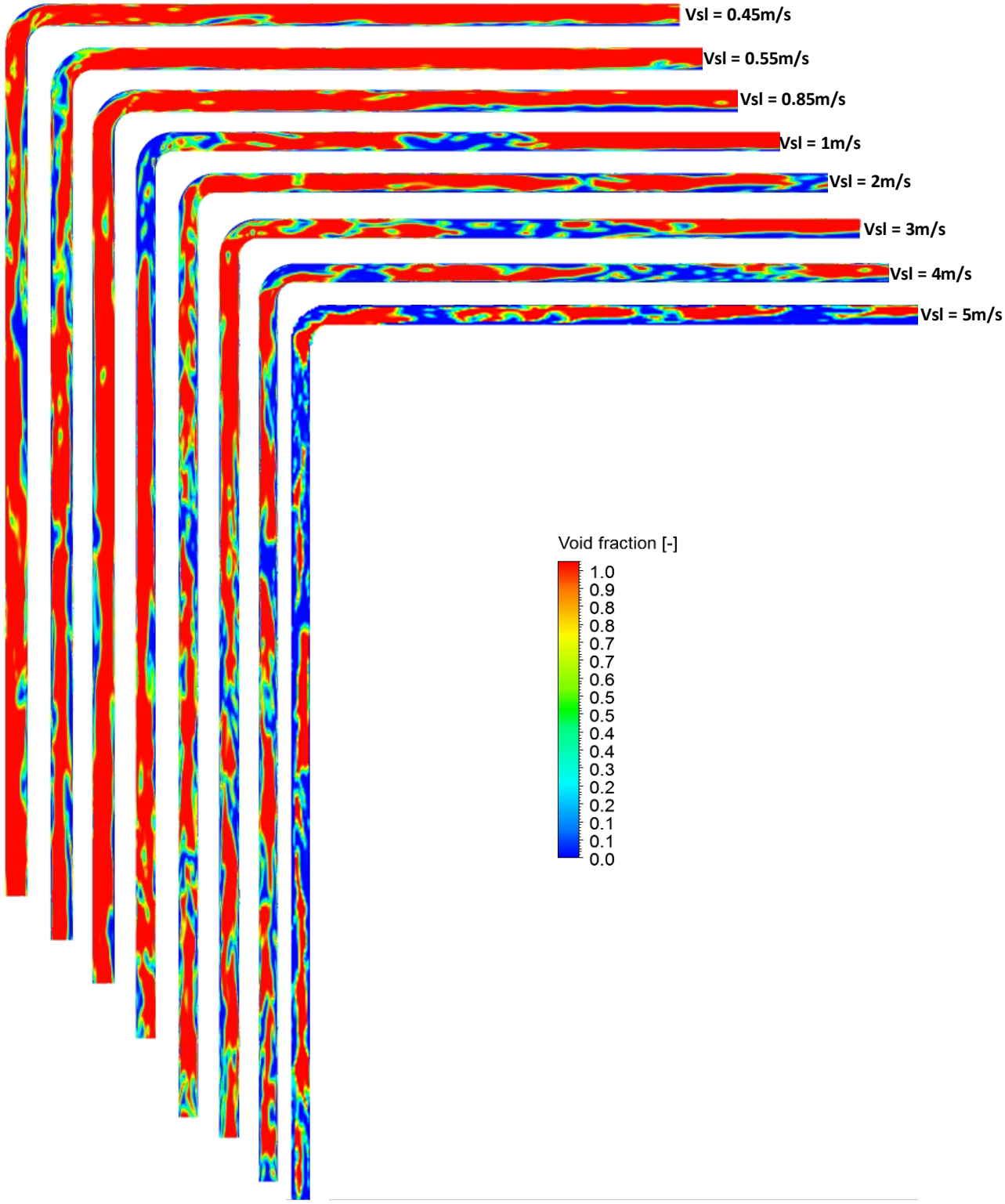

Figure 5.6: Contour Plot of gas void fraction distribution for different liquid superficial velocity for a fixed superficial gas velocity of 5m/s.

Figure 5.7 shows the predicted void fraction fluctuations and their power spectral density for different superficial liquid velocities. Main features of these plots are that as the liquid velocity increases the void fraction fluctuations tends towards higher frequency and the void fraction values vary between 20% to 80%. The PSD plots show that the effects of increasing liquid are to broaden the frequency range up to 0-30Hz.

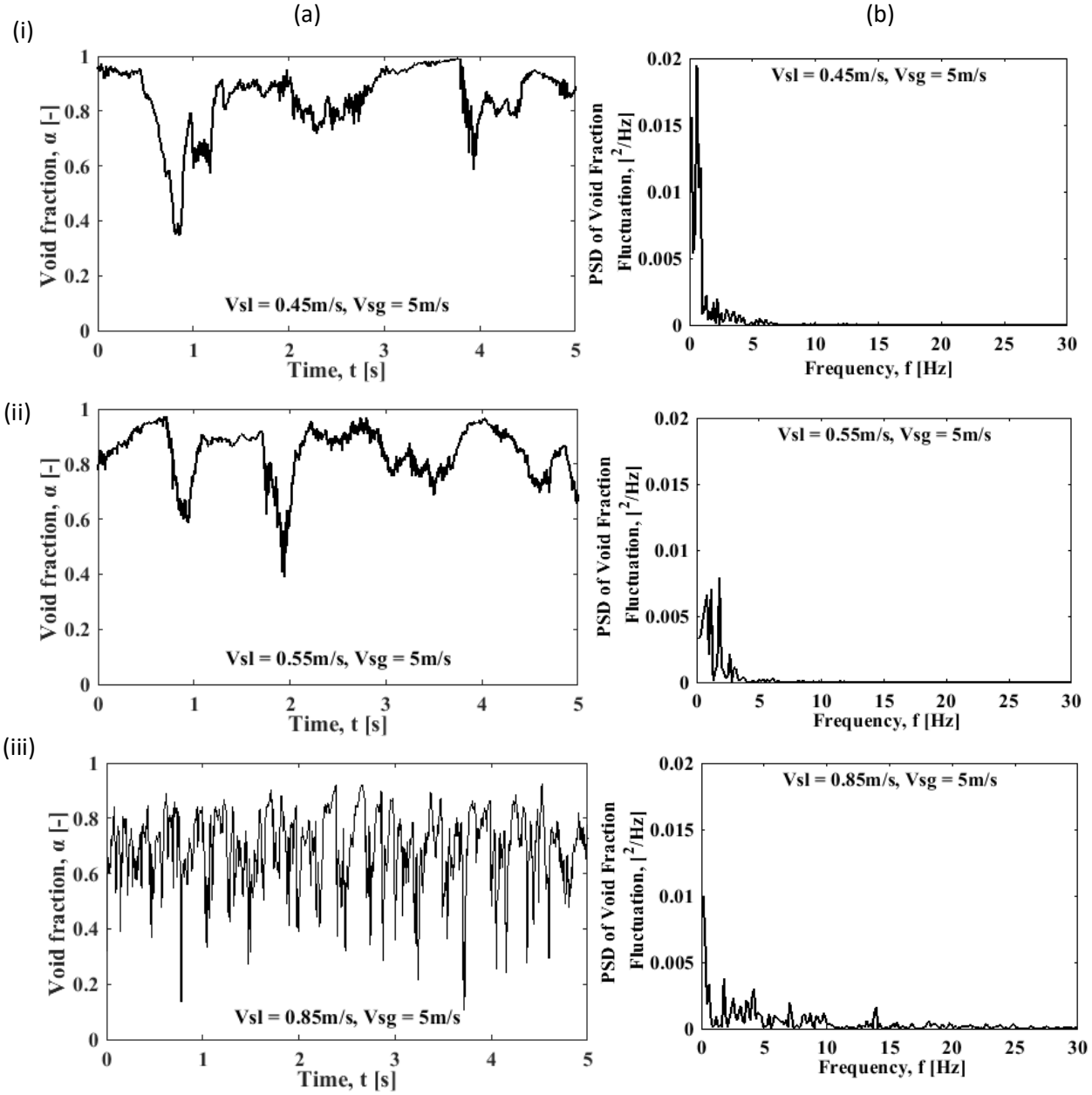

(iv)

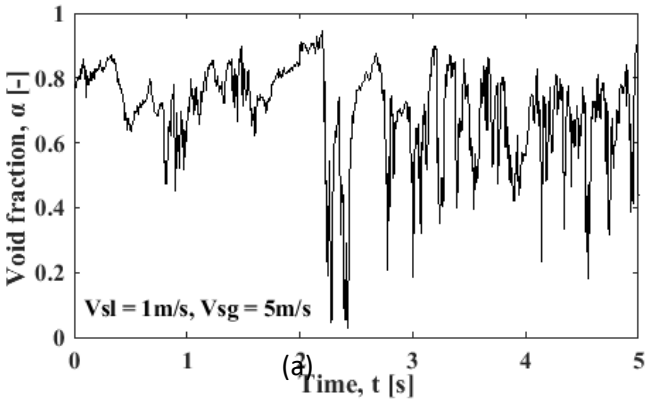
Void fraction, α [-]
Time, t [s]
Vsl = 1m/s, Vsg = 5m/s

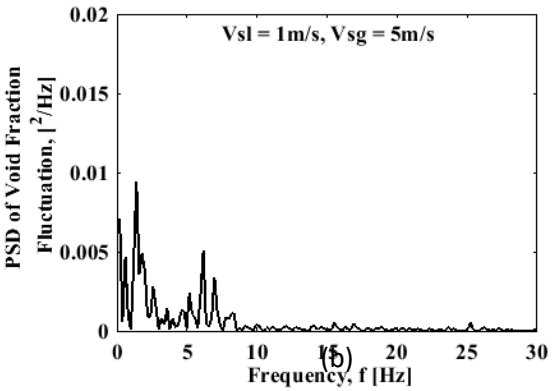
PSD of Void Fraction Fluctuation, |²/Hz|
Frequency, f [Hz]
Vsl = 1m/s, Vsg = 5m/s

(a) (b)

(v)

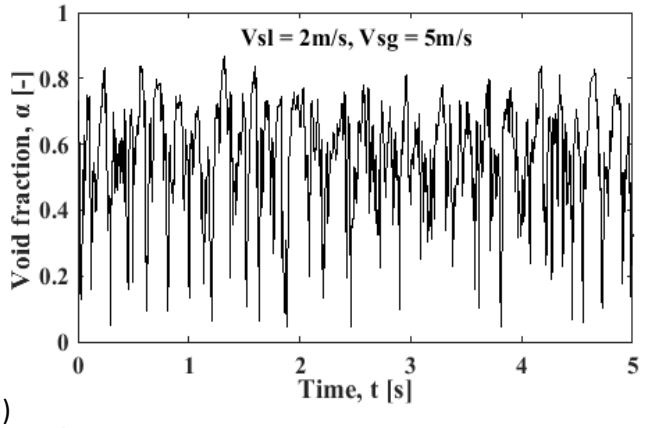
Void fraction, α [-]
Time, t [s]
Vsl = 2m/s, Vsg = 5m/s

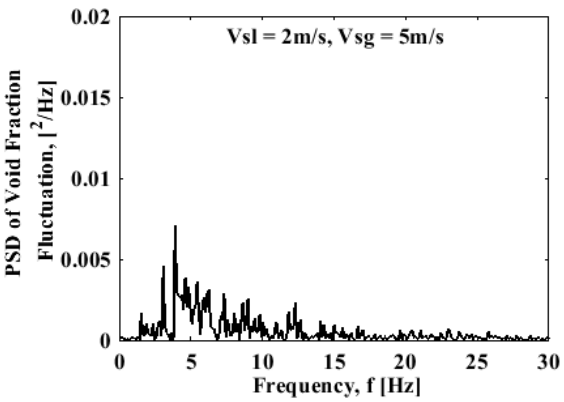
PSD of Void Fraction Fluctuation, |²/Hz|
Frequency, f [Hz]
Vsl = 2m/s, Vsg = 5m/s

(vi)

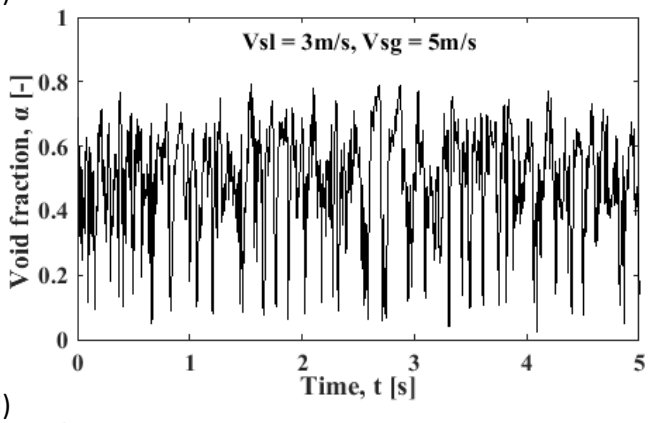
Void fraction, α [-]
Time, t [s]
Vsl = 3m/s, Vsg = 5m/s

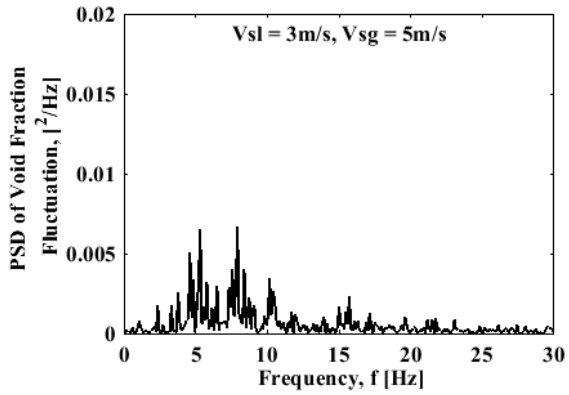
PSD of Void Fraction Fluctuation, |²/Hz|
Frequency, f [Hz]
Vsl = 3m/s, Vsg = 5m/s

(vii)

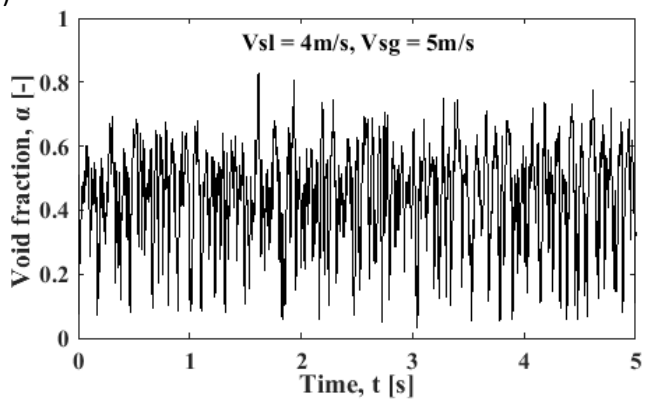
Void fraction, α [-]
Time, t [s]
Vsl = 4m/s, Vsg = 5m/s

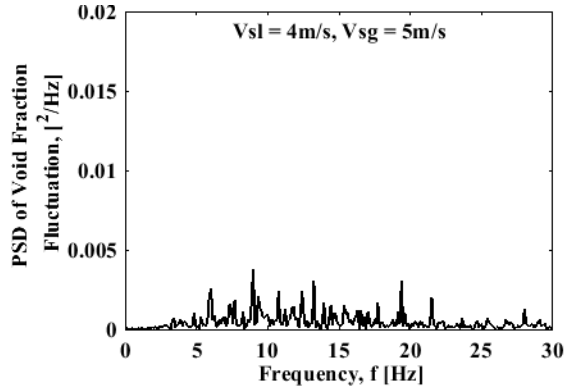
PSD of Void Fraction Fluctuation, |²/Hz|
Frequency, f [Hz]
Vsl = 4m/s, Vsg = 5m/s

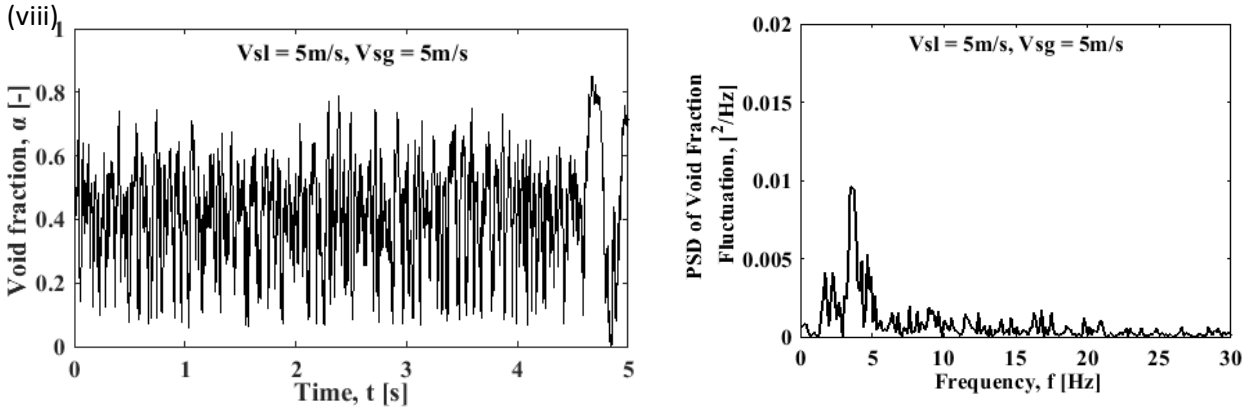

Figure 5.7: The effect of superficial liquid velocity for a fixed superficial gas velocity of 5 m/s (a) Void fraction fluctuation and (b) PSD.

Figures 5.8 (a) and (b) show the dominant frequency and the RMS value of volume fraction fluctuations. The peak frequency increases with the increase of the liquid velocity as the higher liquid content creates greater number of liquid slug while keeping the length and velocity of each liquid slug body constant for a given gas flow rate (as shown in Figure 5.6). Thus, with the increase of liquid velocity, more slug bodies collide with the bend resulting in the higher frequency at the increased liquid velocity. With further increase of liquid velocity, the two-phase flow regime reaches near the bubbly flow and thus, the peak frequency drops significantly. The RMS of void fraction fluctuation shows a slight upward trend with the increase of superficial liquid velocity.

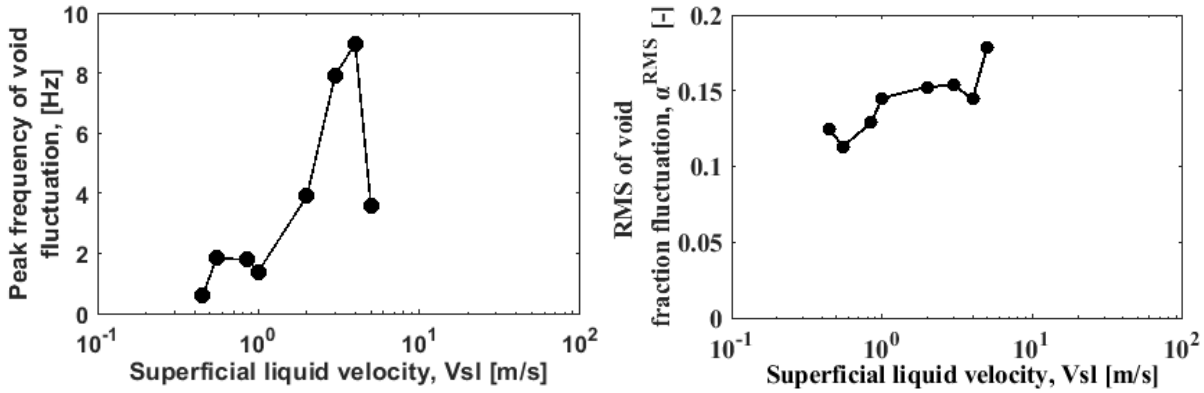

Figure 5.8: (a) Peak frequency and (b) RMS of void fraction fluctuation for different superficial liquid velocities while keeping the superficial gas velocity fixed at 5 m/s.

5.2 Two-phase flow induced force

The following subsections present the time domain signals, PSD and RMS of the flow induced forces due to increasing gas superficial velocity and liquid superficial velocity, respectively. The next subsection also presents momentum balance analysis carried out at the elbow control volume to obtain the analytical expressions used for calculating the time history of flow induced forces.

5.2.1 Effects of gas velocity

The fluctuating force acting on the elbow has been calculated using momentum balance on a control volume at the elbow. Figure 5.9 shows the control volume at the elbow used for the force calculation. The time dependent forces acting on the elbow can be calculated from the CFD simulation data using the momentum balance equations:

$F_x(t) = \dot{m}(t)V(t) + p(t)A$ -at the exit plane of the bend (5.2)

$F_y(t) = -\dot{m}(t)V(t) - p(t)A$ -at the inlet plane of the bend (5.3)

$\dot{m}(t) = \left[\alpha(t)\rho_g + \left(1 - \alpha(t)\right)\rho_l\right]AV(t)$ (5.4)

where, $\dot{m}(t)$ is instantaneous mass flow rate at inlet or outlet plane of the control volume, $\alpha(t)$ is instantaneous area-averaged gas volume fraction at the inlet or outlet plane of the control volume, $p(t)$ is instantaneous area averaged pressure perpendicular to the flow direction at the inlet or outlet plane of the control volume, $V(t)$ is instantaneous area averaged velocity at the inlet or outlet plane of the control volume.

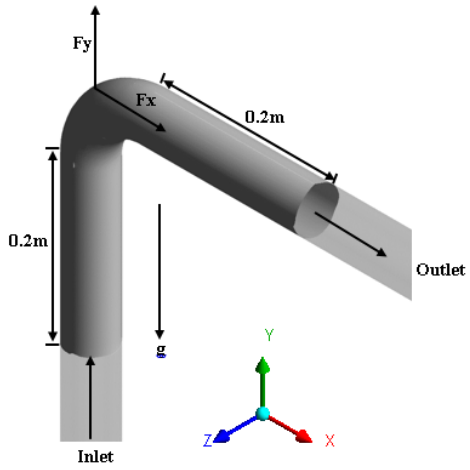

Figure 5.9: Control Volume around the bend for force calculation

While applying the momentum balance calculations using Equations (5.2) and (5.3) it should be noted that the unsteady $k-\epsilon$ turbulence model used in the present study cannot predict the turbulence pressure fluctuations. In present study, the unsteady $k-\epsilon$ model predicts the fluctuating force stemming predominantly from the intermittent impact of liquid structures on the elbow. However, for the slug and churn flows impacting at the elbow, almost all unsteady behaviour stems from the interface surface dynamics and the impact of liquid and gas structures. Indeed, Liu et al. (2012) shows that the RMS of fluctuating forces are strongly correlated to the RMS of fluctuating momentum fluxes based on the experimental data analyses. Therefore, the application $k-\epsilon$ turbulence model with VOF multiphase model is well capable of flow model for predicting the force fluctuations in multiphase slug and churn flows within reasonable accuracy.

Figures 5.10(a) and (b) show the comparison of simulated and experimental force fluctuations and their PSDs for the churn flow pattern ($V_{sl} = 0.61$m/s and $V_{sg} = 9.04$m/s). The present CFD prediction shows very good agreement with the experimental results of Liu et al. (2012) for time signal as well as PSD. A predominant frequency of approximately 1.9 Hz and the maximum PSD of approximately 99 N^2/Hz were observed for both present study and reported experiment (Liu et al. 2012).

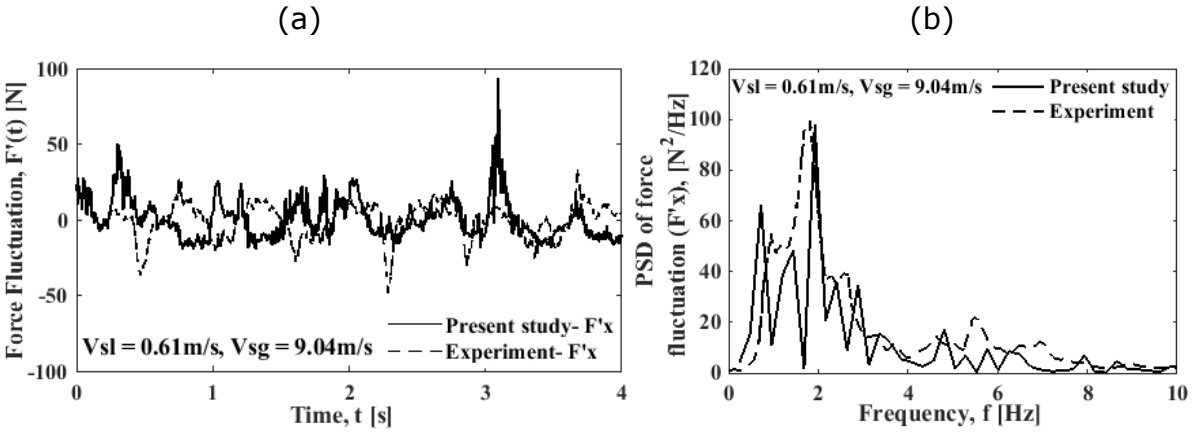

Figure 5.10: Comparison of present study and experiment (Liu et al. 2012). for (a) Force fluctuation and (b) PSD for superficial liquid velocity of 0.61 m/s and superficial gas velocity of 9.04 m/s.

Figures 5.11 (a) and (b) show the simulated time signals of force fluctuations in x and y directions and their corresponding PSDs. In slug flow regime, the y-component of force fluctuations are higher than the x-components. However, as the flow regime change with the increase of gas superficial velocity, the force fluctuations in x and y direction becomes similar. In slug flows, the impact of liquid on the bend cause the higher fluctuations in the y-direction similar to water hammer effect. The force fluctuations in slug flows spread over a range of frequency level and the relative importance of higher frequency (>2Hz) is also observed in Figures 5.11 (b) (i) – (v). However, in churn flow regime the importance of higher frequencies diminishes as shown in 5.11 (b) (vi) – (vii). This is in contrast to the presented frequency domain results for void fraction fluctuations shown in Figures 5.5 (a) and 5.5 (b). Force fluctuations spread over smaller ranges compared to the void fraction fluctuations. Liu et al. (2012) also reported similar observations.

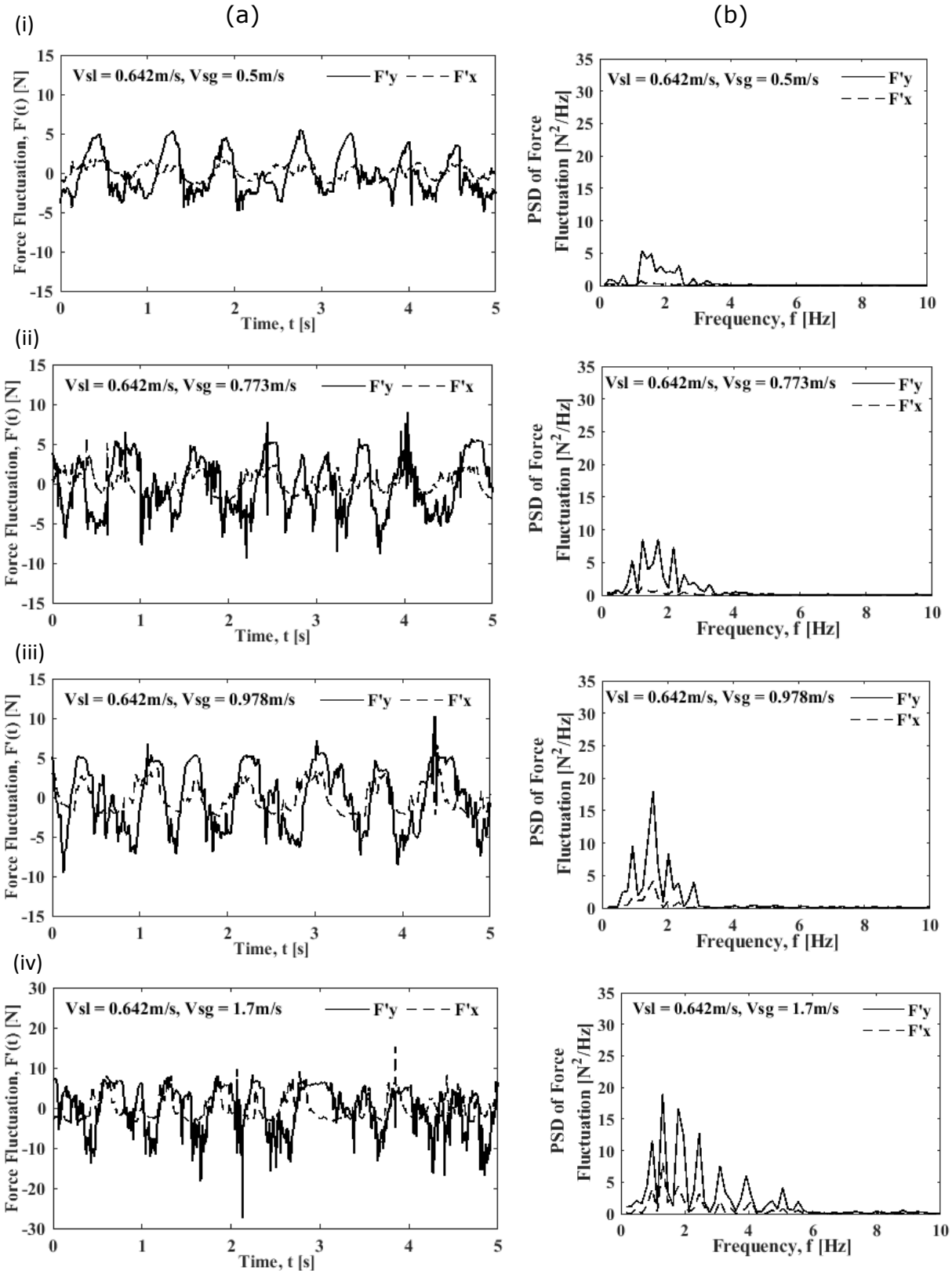
(a)
(b)
(i)
Vsl = 0.642m/s, Vsg = 0.5m/s
F'y
F'x
Force Fluctuation, F'(t) [N]
Time, t [s]
PSD of Force Fluctuation [N²/Hz]
Frequency, f [Hz]
(ii)
Vsl = 0.642m/s, Vsg = 0.773m/s
(iii)
Vsl = 0.642m/s, Vsg = 0.978m/s
(iv)
Vsl = 0.642m/s, Vsg = 1.7m/s

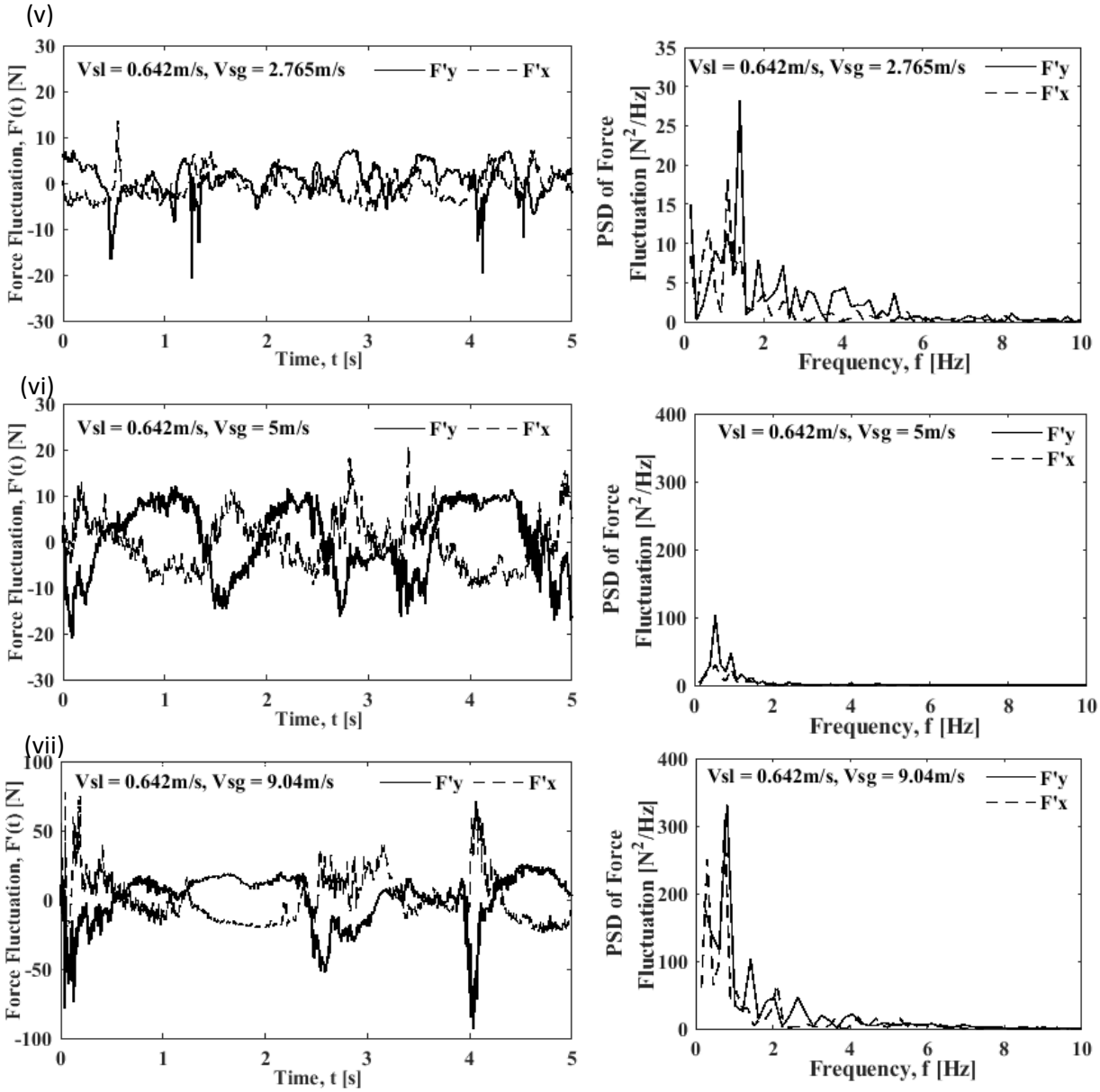

Figure 5.11: The effect of superficial gas velocity on (a) Force fluctuation and (b) PSD for a fixed superficial liquid velocity at 0.642 m/s.

Figures 5.12 and 5.13 present the predominant frequency and the RMS of force fluctuations in the x and y direction, respectively. The predominant frequencies of x and y component forces are higher in slug flows and increases with the superficial gas velocity and drops as gas superficial velocity increases towards churn flow regime before increasing again. Liu et al. (2012) observed similar behaviour in their experimental study. The range of RMS values for the x and y force components were 0.89 – 16.6 N and 2.5 – 18.5 N respectively for a mixture velocity of 1.142 – 9.682 m/s. Liu et al. (2012) obtained values of approximately 2 – 14 N and 4 – 24 N for similar velocity range. The RMS values obtained by Riverin et al. (2006) was from 1 - 12 N for similar flow conditions and mixture velocities 2 – 12 m/s. It should be noted that the multiphase flow regimes and the transformation from slug to churn flows depends on many factors including fluid properties, pipe size, shape, developing length and the injection methods and thus direct comparison of force fluctuation frequencies, PSDs and RMS values are rather difficult among different studies. However, the present results replicate the previous studies within a good accuracy level.

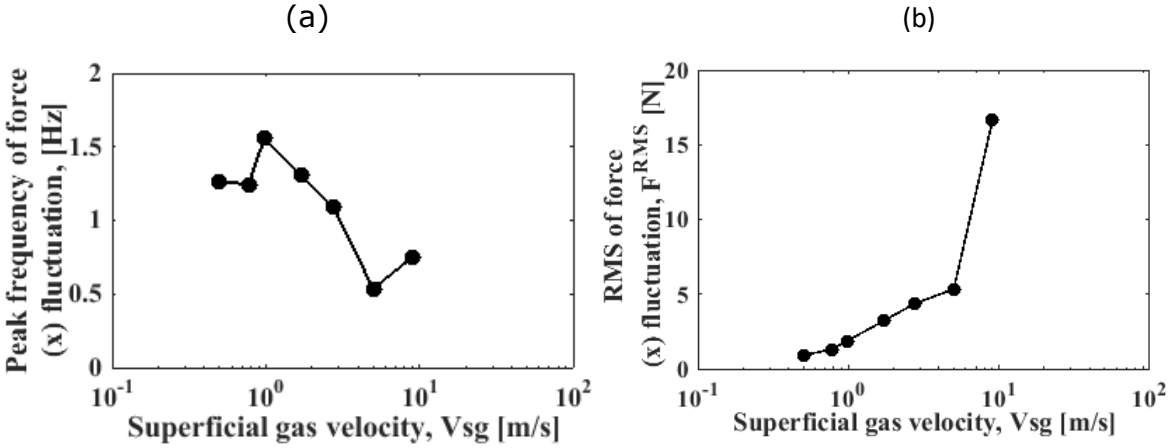

Figure 5.12: The effect of superficial gas velocity on (a) Peak frequency and (b) RMS values of x-component of force fluctuation for a fixed superficial liquid velocity at 0.642 m/s.

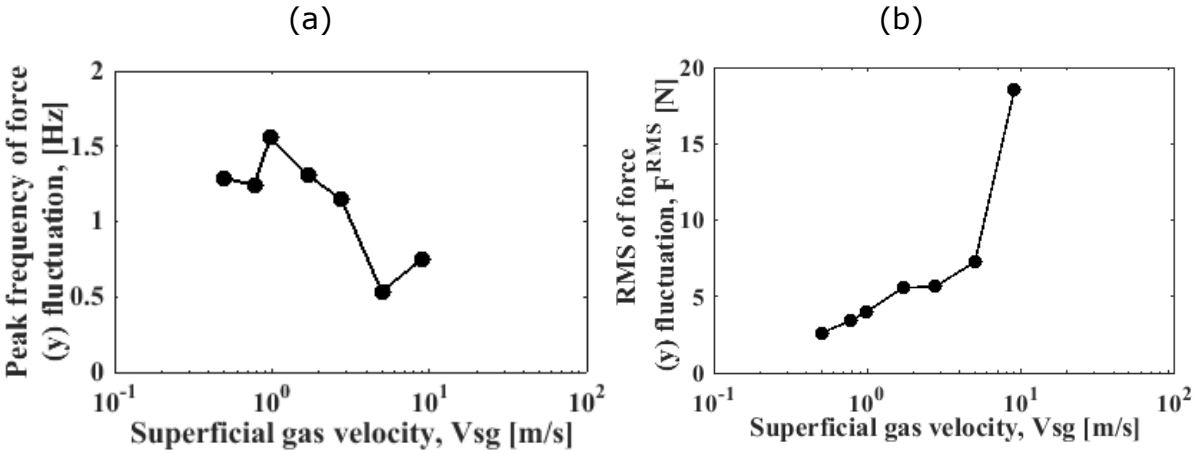

Figure 5.13: The effect of superficial gas velocity on (a) Peak frequency and (b) RMS values of y-component of force fluctuation for a fixed superficial liquid velocity at 0.642 m/s.

5.2.2 Effects of liquid velocity on forces at the bend

Figures 5.14(a) and (b) show the time series of force fluctuations and PSDs of force fluctuations. With the increase of liquid superficial velocity, the fluctuations of both vertical and horizontal components increase and show very similar patterns between them. The PSD plots also show that with the increase of the superficial velocity, the range of frequencies reach above 20 Hz and shows multiple peak frequencies. Figures 5.15 and 5.16 show the predominant frequency and the RMS values of fluctuations of forces for different superficial liquid velocities. The predominant frequency increases with the increase of superficial liquid velocity quite rapidly initially and starts to drop as the flow tends to approach bubbly flows. On the other hand, higher liquid content increases the RMS of force fluctuations with the increase of superficial liquid velocity rapidly.

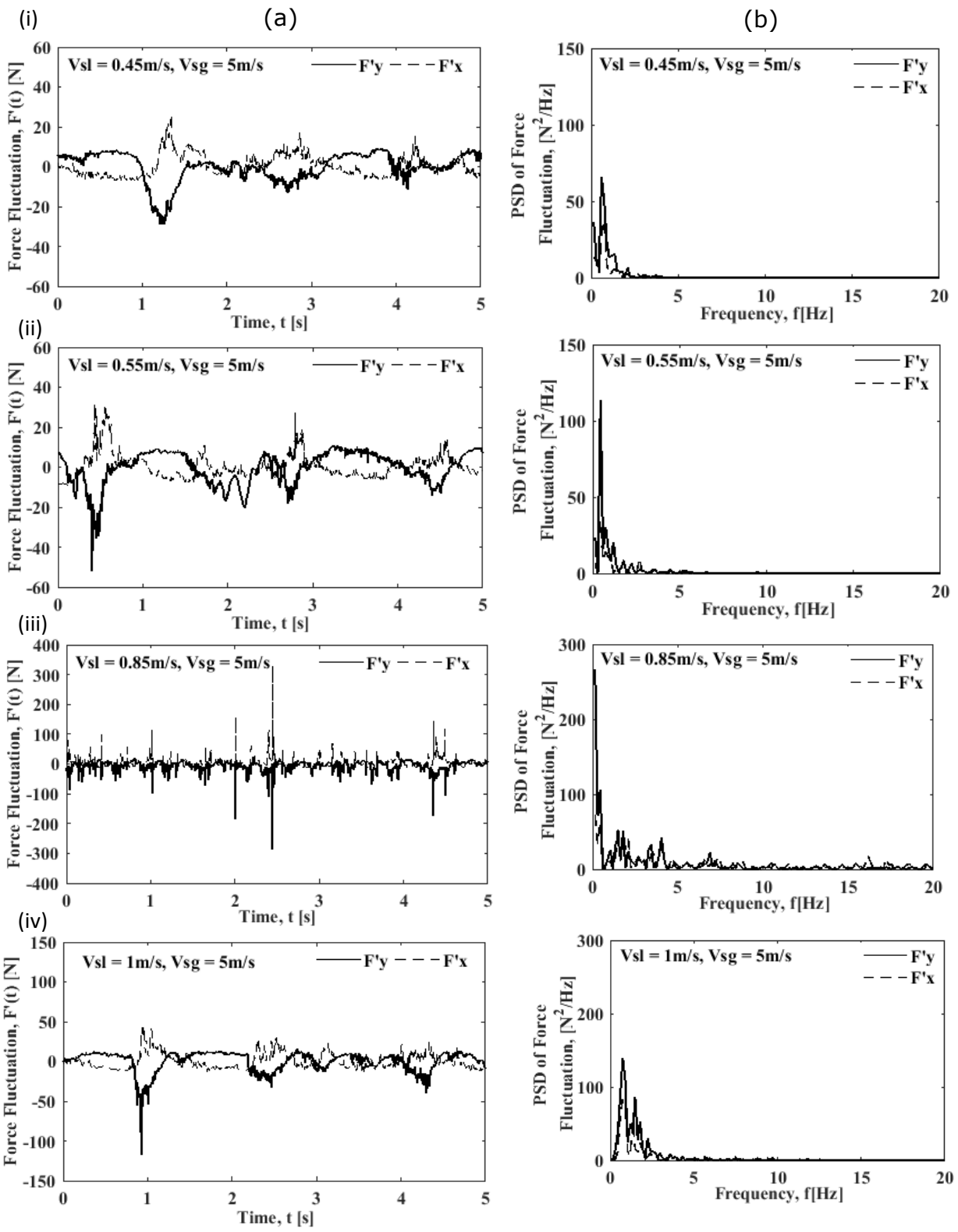
(i)
(a)
(b)
Vsl = 0.45m/s, Vsg = 5m/s
F'y
F'x
Force Fluctuation, F'(t) [N]
Time, t [s]
PSD of Force Fluctuation, [N²/Hz]
Frequency, f[Hz]
(ii)
Vsl = 0.55m/s, Vsg = 5m/s
(iii)
Vsl = 0.85m/s, Vsg = 5m/s
(iv)
Vsl = 1m/s, Vsg = 5m/s

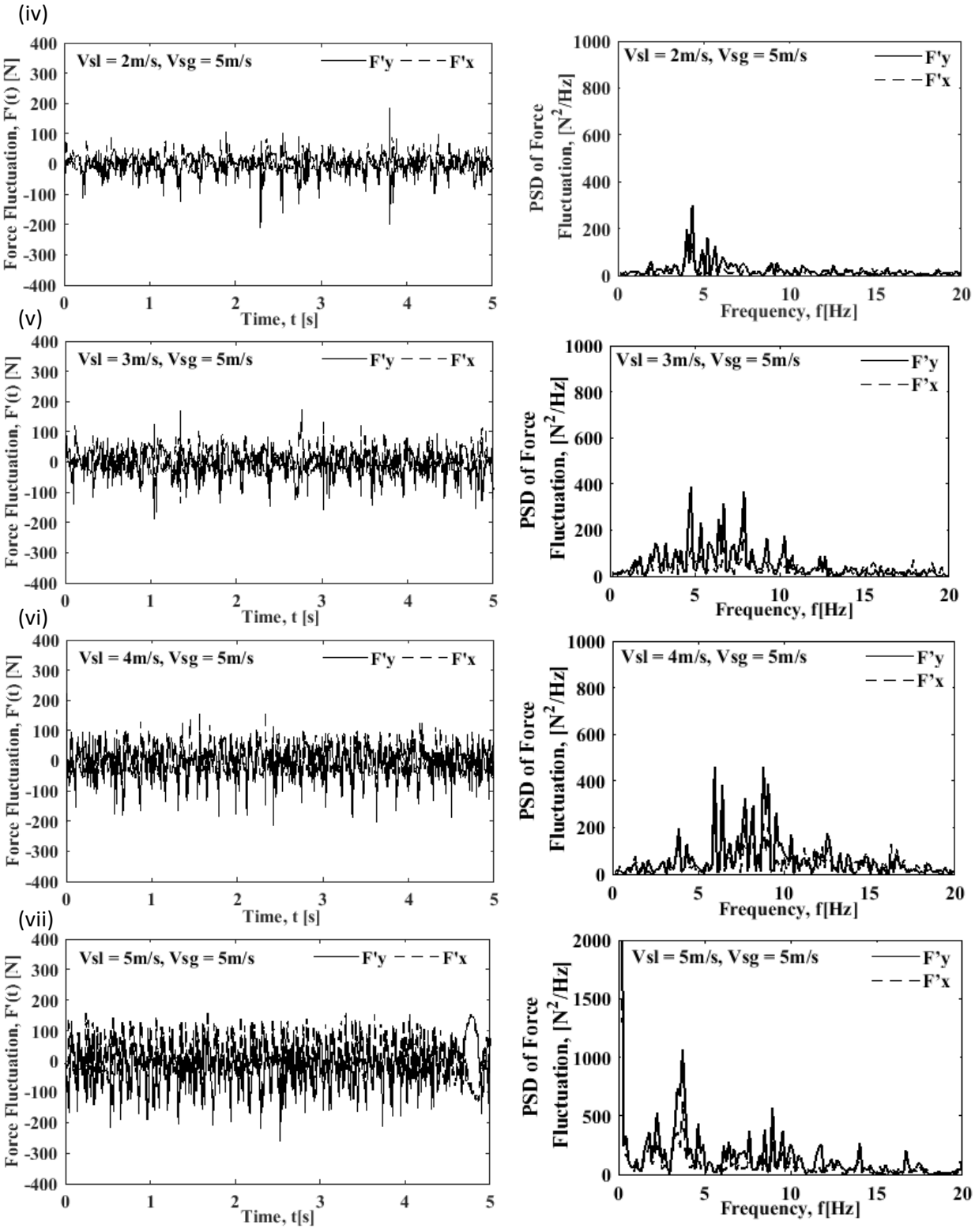

Figure 5.14: The effect of superficial gas velocity on (a) Force fluctuation and (b) PSD for different superficial liquid velocity for a fixed gas velocity at 5 m/s.

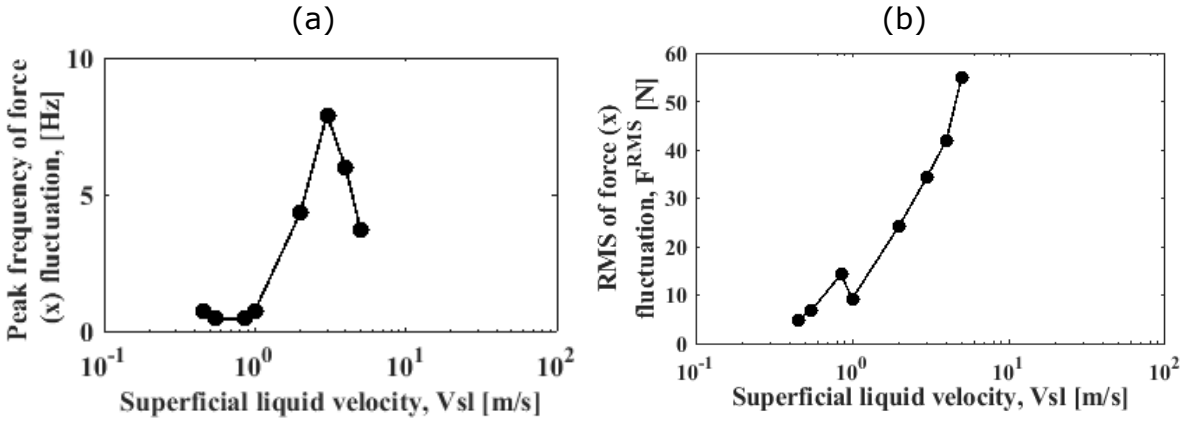

Figure 5.15: The effect of superficial liquid velocity on (a) peak frequency and (b) RMS values of x-component of force fluctuation for a fixed superficial gas velocity at 5m/s.

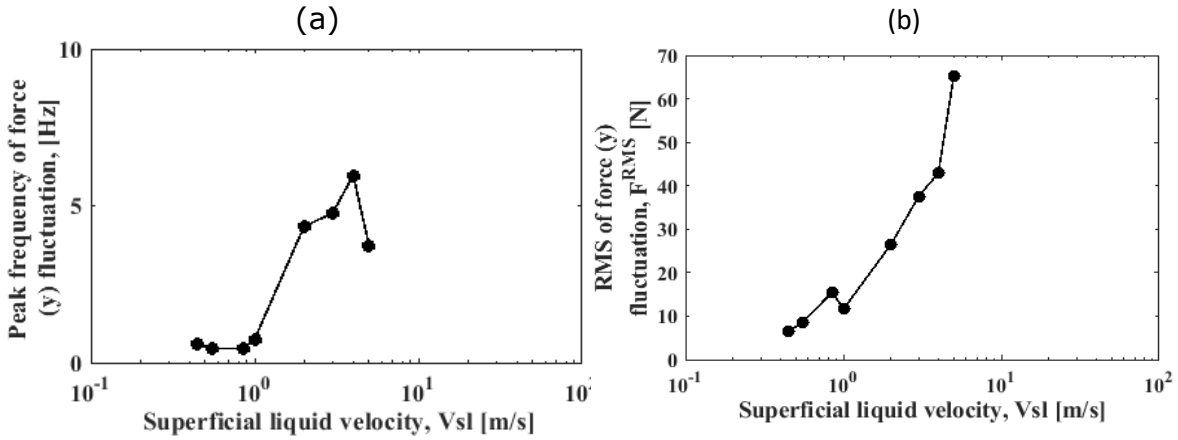

Figure 5.16: The effect of superficial liquid velocity on (a) peak frequency and (b) RMS values of y-component of force fluctuation for a fixed superficial gas velocity at 5m/s.

In summary, the increase of gas reduces the range of frequency of force fluctuations, while the increase of liquid broadens the range of frequency of the force fluctuations. Figures 5.17 and 5.18 present the RMS of the fluctuating components of the force as functions of the fluctuating components of momentum flux and pressure terms for the 17 flow case studies in the pipe of 0.0525 I.D. There is a correlation between the force and momentum flux fluctuations as shown in Figures 5.17 (a) and (b). Also, the correlation were stronger with the x-components of the parameters than was observed in the y-components. The most

significant deviations of the momentum flux fluctuations seen in Figure 5.17 (b) were due to the moderate slug flows. This deviation was compensated for by the pressure term as explained with Figure 5.18.

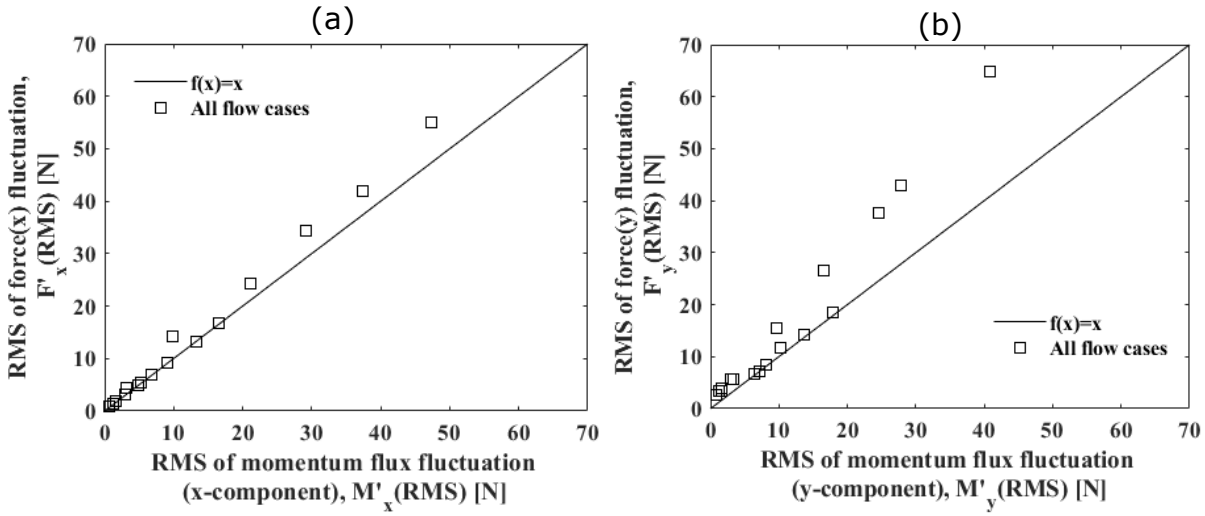

Figure 5.17: RMS of the contribution of (a) x-component and (b) y-component of momentum flux fluctuation on the force fluctuation for all flow case studies.

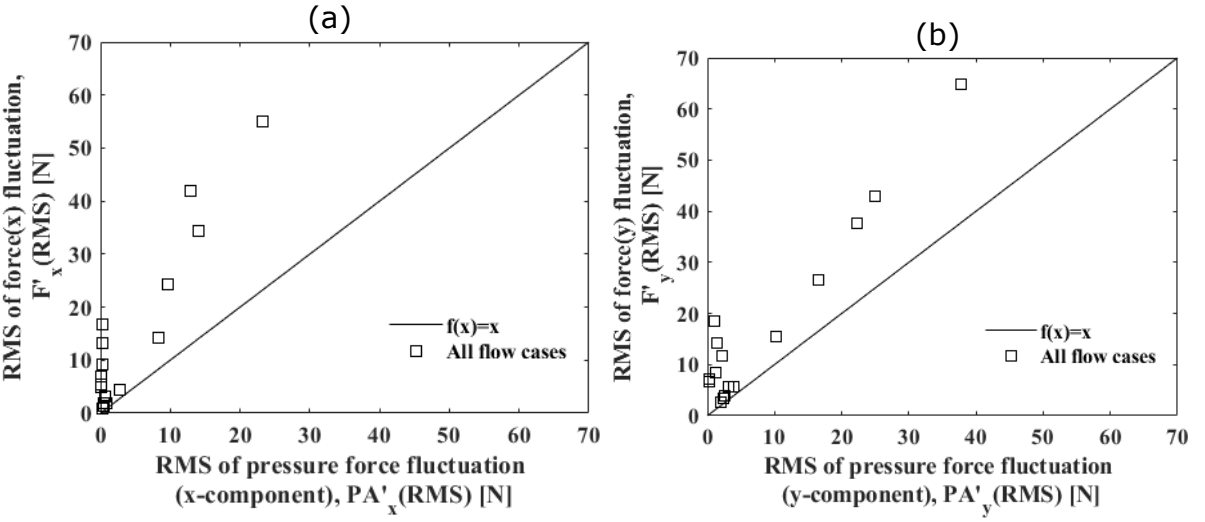

Figure 5.18: RMS of the contribution of (a) x-component and (b) y-component of fluctuation of the pressure term on the force fluctuation for all flow case studies.

Figure 5.18 shows that there is little or no correlation between the fluctuations in the pressure term and the force fluctuations. The little correlation seen in Figure 5.18 (b) is for the moderate slug flows. In slug flows, the flow is dominated by the

presence of the distinct, intermittent gas and liquid slugs separated by continuous interfacial areas which is not present in churn flows. Due to this distinct nature of slugs and the low liquid superficial velocities of the flow cases under study, higher pressures were observed during the passage of liquid slugs through the elbow as reported. The force fluctuations in the churn flows were only dependent on the momentum flux fluctuations. Generally, the simulated results show that the momentum flux fluctuations dominate the fluctuations in force, whereas the fluctuating pressure components is not well correlated with force fluctuations.

These relative importance of the fluctuations of the momentum flux over the fluid pressure on the resultant force fluctuations can be further explained based on the momentum theory applied in the present study to calculate fluctuating forces. The theory whose application yielded Equations (5.2) and (5.3) indicated that the wall shear stress and pressure forces acting on the wall is equivalent to the momentum flux fed into and out of the control volume around the elbow as well as pressure on the face of inlet and outlet of the control volume. Further details on the control volume analysis has been given by Liu et al. (2012). In addition, it should be noted that the applied U-RANS modelling in the present study is not capable of predicting pressure fluctuations due to turbulence. The pressure fluctuations observed in the present study stems from cyclic flow of fluid and gas bodies in the slug flow and churn flows. Hence, the conclusion that the major force fluctuations are caused by the momentum flux fluctuations. In physical sense that means the force fluctuations originate from the cyclic impact of liquid structures on the bend similar to water hammer effects. In single phase flows, the impact force may not be significant, as the established pressure gradient in the flow is enough for negotiating the bend from vertical to horizontal direction. In slug and churn flows, the established pressure gradient by continuous gas phase is not enough to overcome the inertia of liquid elements. The impact of these liquid elements on the elbow bend structure causes the force fluctuations as evidenced in the RMS of force fluctuations closely related to the RMS momentum flux fluctuation. The impact of liquid elements on the bend can also be observed in the contour plots of void fraction in Figures 5.1 and 5.6. These figures show that after the liquid impacts on the bend, the liquid bodies lose their structures and flow mostly as stratified/stratified-wavy film along the horizontal section of the pipe. Therefore the explained physical mechanisms support the conclusions that RMS values of the

force fluctuations are well correlated with that of the momentum flux, while that of pressure fluctuations are weakly correlated.

5.3 Non-dimensional RMS of excitation force

Riverin et al. (2006) developed a correlation to predict the RMS of force fluctuations using their experimental data of U-bend and T-junction and other available reported data. Their correlation has been developed for the gas volume fraction in the range of 50-75% and are given by:

$$\overline{F_{rms}} = \frac{F_{rms}}{\rho V_t^2 (\frac{\pi D^2}{4})} = 10We^{-0.4} \tag{5.5}$$

where, $\overline{F_{rms}}$ is the normalised RMS value of the fluctuating force, We is the Weber number defined as

$$We = \frac{\rho_m V_t^2 D}{\sigma} \tag{5.6}$$

Figure 5.19 shows the comparison of the present simulation data of normalised resultant RMS force fluctuation against the Riverin et al. (2006) correlation. The ranges of gas void fraction in the present study varied between 40%-100% representing a wider spread compared to the data set used by Riverin et al. (2006). Their correlation was developed for gas volume fraction in the range of 50%-75%. Nevertheless, most of the present prediction data fall within $\pm 50\%$ of the correlation and produces excellent match with the Riverin et al. (2006) correlation.

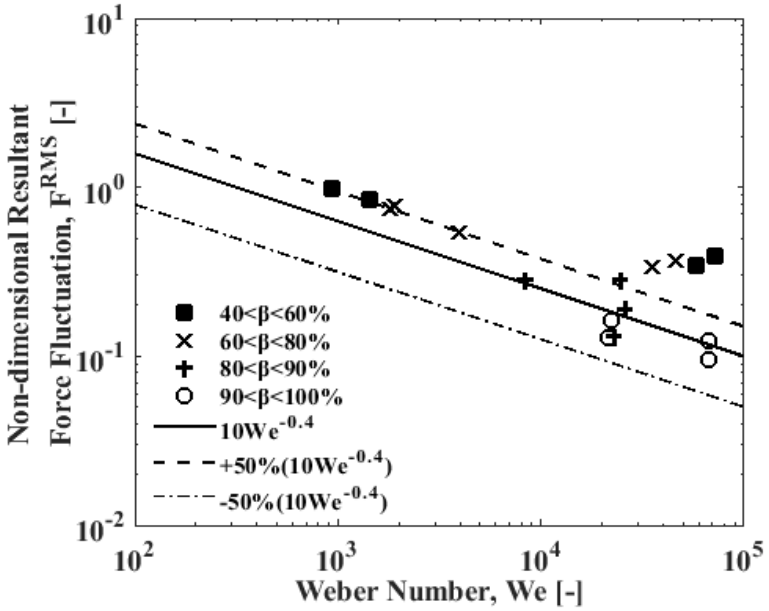

Figure 5.19: Comparison of RMS values of fluctuating forces with Riverin et al. (2006) correlation. The 17 cases of simulation data are grouped according to volume fraction of gas.

In summary, the slug and churn flow induced forces on a 90^0 pipe bend of 0.0525 m I.D. were characterised without the effect of pipe structure response. The simulation results were compared with the time history of volume fraction and excitation forces reported in the experiment and the results show a very good conformation of CFD results with the experimental data. The simulation results show that the peak gas volume fraction frequency varies between 0.5–9 Hz with the values decreasing with the increase of superficial gas velocity, and increasing with the increase of superficial liquid velocity in the slug flow regimes. The gas volume fraction fluctuation frequencies drop as the flow approach the transition boundary from slug flows to annular or bubbly flow. The frequency of gas volume fraction fluctuations is broadband and spreads over 30 Hz.

Furthermore, the force time variations have been calculated using momentum balance at the pipe elbow. The simulated time domain signal of forces for churn flow and its frequency domain PSD matched well with the experiment data. The peak frequency of the fluctuations of force varied between 0.5–1.7 Hz and dropped with the increasing superficial gas velocity. The frequency of fluctuations of force spreads below 10 Hz and contrary to volume fraction fluctuations, the RMS of force fluctuations increases with the superficial gas velocity.

On the other hand, with the increase of superficial liquid velocity, the peak frequency of fluctuations of force varies between 1–7 Hz and increases initially before dropping at higher superficial liquid velocity as the flow approaches bubbly flow. The PSD of fluctuation of force spreads over 20 Hz with the increase of superficial liquid velocity. The RMS of force fluctuations increases with the increase of superficial liquid velocity. It can be concluded that the increase of gas fraction narrows the range of frequency ranges, while increasing the liquid fraction expands the frequency ranges of force fluctuations. Finally, the present results obtained for pipe of 0.0525 m I.D. show very good match of RMS of resultant force fluctuations with Riverin et al. (2006) correlation.

CHAPTER 6

EFFECT OF PIPE DIAMETER ON MFIV

This chapter compares the characteristics of slug and churn flow induced fluctuations of the void fractions and excitation forces in 90^0 pipe bends of internal diameters (I.D) given as 0.0525m, 0.1016m and 0.2032m. Based on the criterion given by Kataoka and Ishii (1987) (Equation 3.15), the non-dimensional hydraulic diameters D_H^* for the three pipe sizes are respectively given as 19.2, 37.2 and 74.5. These three pipe bends are considered to be geometrically similar since the bend orientation are the same and they are all 90^0 bends. Based on the pipe diameter, bend radius and entrance length the scales are given in Table 6.1.

Table 6.1: Scales of the three pipe sizes with reference to the largest pipe

Geometric properties	**I.D (0.0525m)**	**I.D (0.1016m)**	**I.D (0.2032m)**
$\mathbf{D_H^*}$	19.2	37.2	74.5
Diameter scale	1/4	1/2	1
Bend radius scale	1/4	1/2	1
Entry length scale	1/4	5/8	1

Hence the next subsection describes in detail the predicted void fraction distribution in small and large pipes followed by calculation and comparison of excitation forces using CFD predicted flow properties. Finally, the performance of

the Riverine et al. (2006) model which was based on small pipe experiment is evaluated for larger pipes.

6.1 Comparison of volume fraction prediction in small and large pipes

The volume fraction distribution has been shown to directly correlate with force fluctuation through the area averaged void fraction parameter in Equation (5.1). This behaviour is also evident in the correlation of RMS of momentum flux fluctuation and RMS of force fluctuation that has been presented in Chapter 5. Hence accurate qualitative and quantitative interpretation of void fraction distribution is important in characterising the flow induced forces due to multiphase flows. In order to achieve this based on qualitative observations, the same size of pipe sections has been cut out from all three pipe sizes. For each of the cut-out sections, the upstream pipe length is 4m and the downstream is 2m. Figures 6.1 – 6.9 present the contour plots and PDFs of the same pairs of gas and liquid superficial velocities simulated in the three different pipe sizes. For the real life sizes of the three pipe geometries, a scale of ~43:1 has been used to depict the pipe geometries in Figures 6.1 – 6.9 to better compare the slug geometries. In each pipe size, the flows were allowed to become fully developed before results were extracted for analysis. Generally, result data were extracted after ~5s, ~12s and ~20s in the 0.0525m, 0.1016m and 0.2032m I.D. pipes respectively. These figures show that the CFD modelling approach was able to capture the prominent features of the slug, cap-bubbly, churn and churn turbulent flows regimes well.

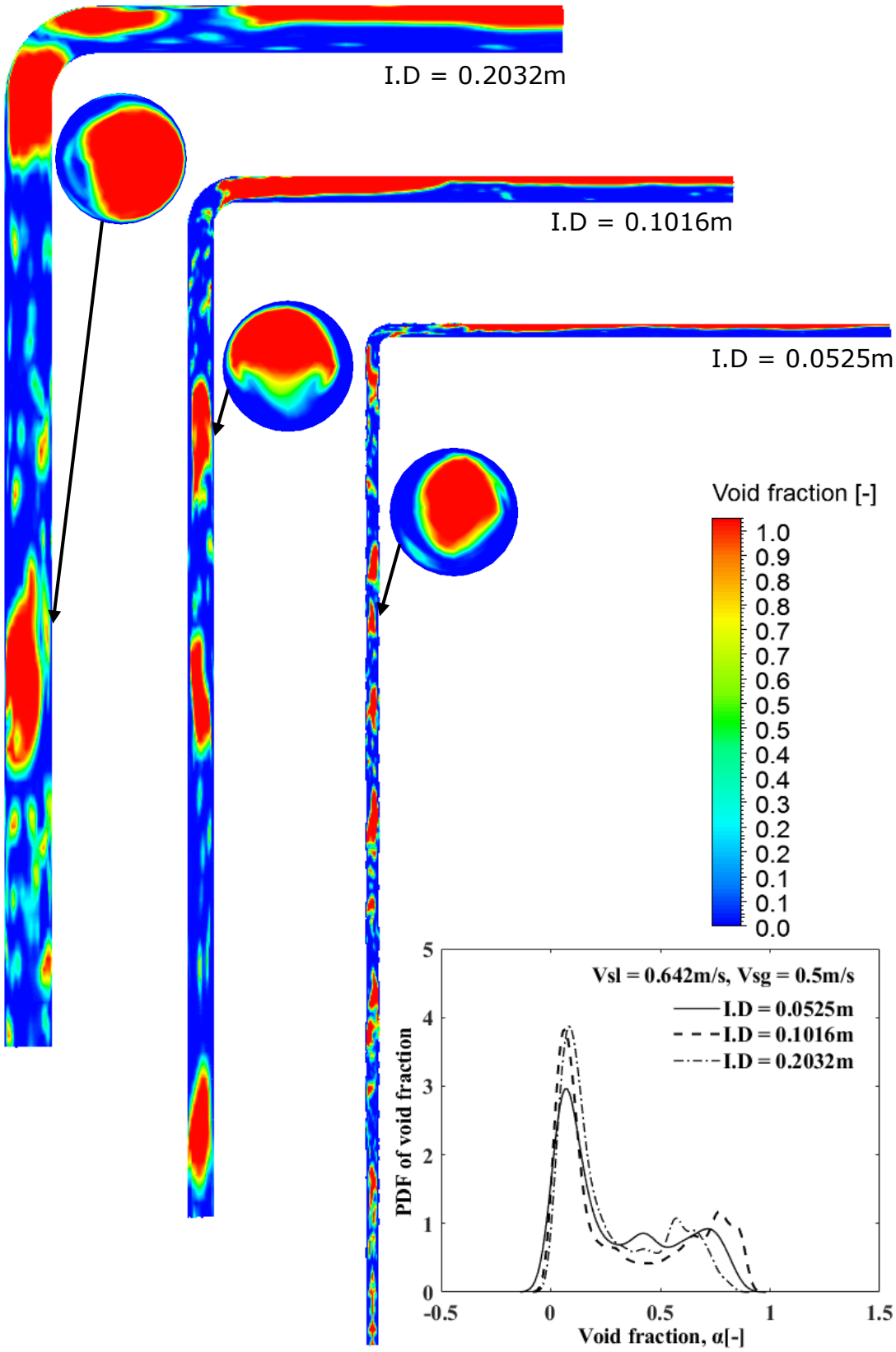

Figure 6.1: Contour of air volume fraction and PDF for Vsl=0.642m/s and Vsg=0.5m/s in the three pipe sizes.

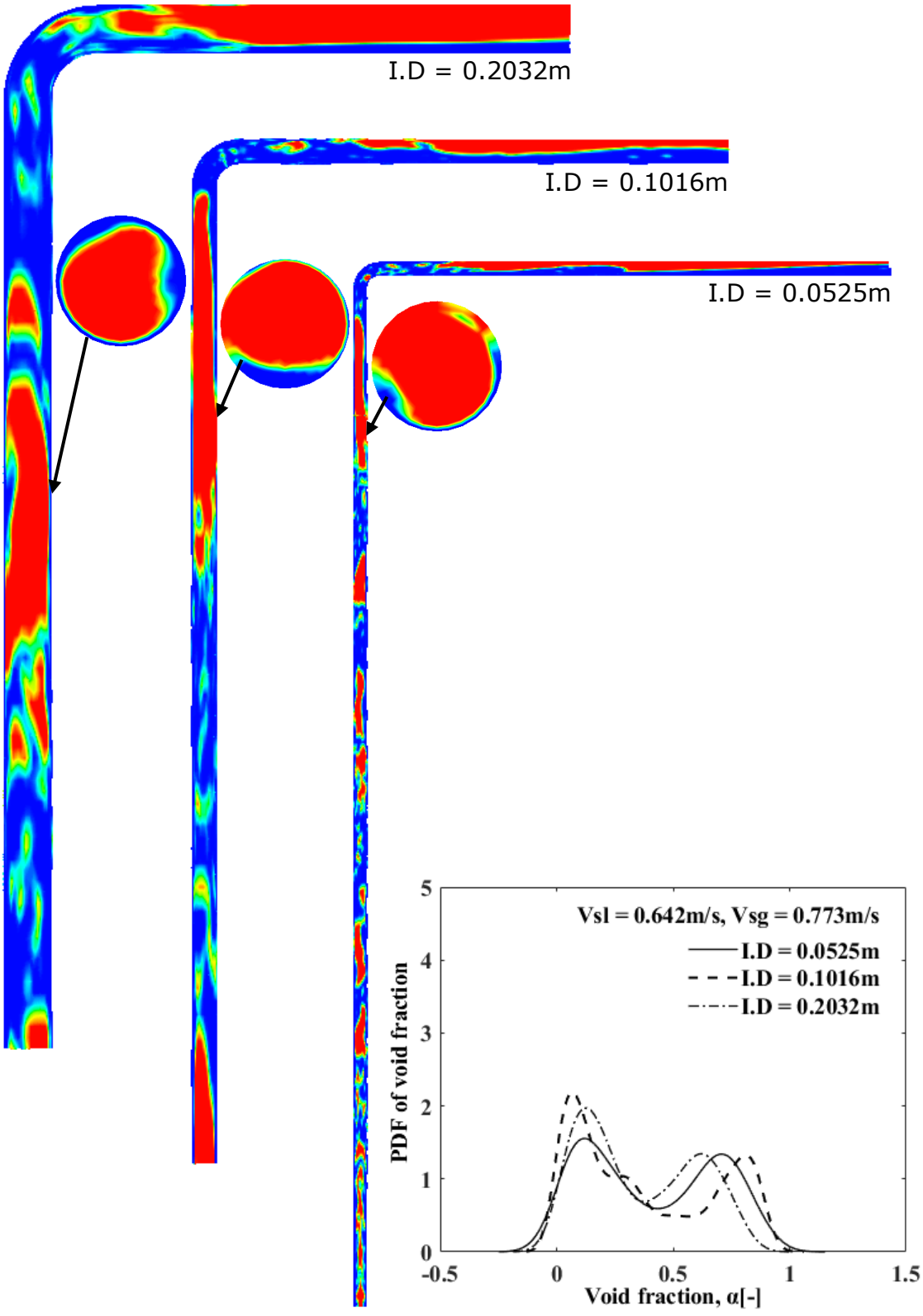

Figure 6.2: Contour of air volume fraction and PDF for Vsl=0.642m/s and Vsg=0.773m/s in the three pipe sizes.

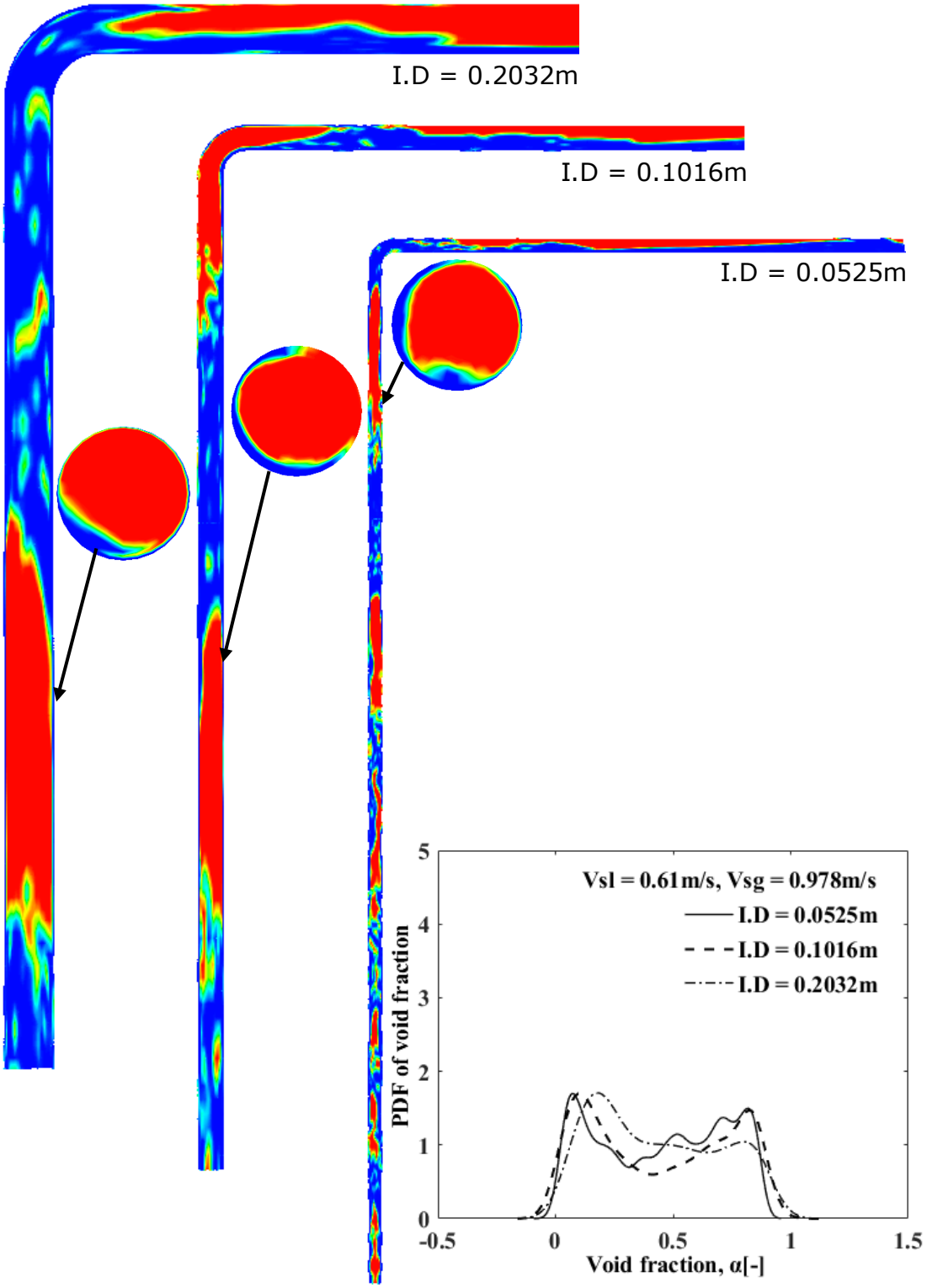

Figure 6.3: Contour of air volume fraction and PDF for Vsl=0.61m/s and Vsg=0.978m/s in the three pipe sizes.

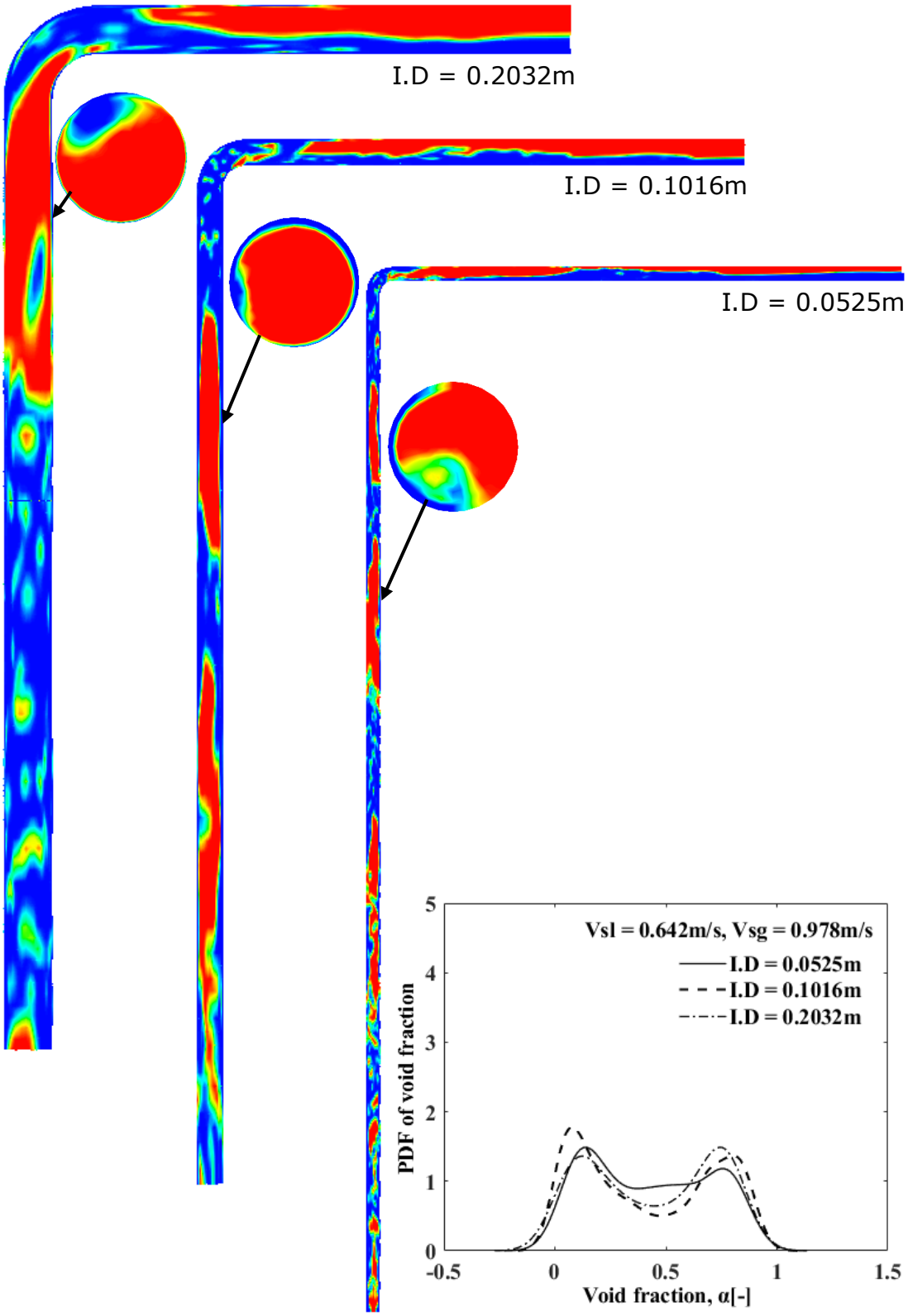

Figure 6.4: Contour of air volume fraction and PDF for Vsl=0.642m/s and Vsg=0.978m/s in the three pipe sizes.

Figure 6.1 shows the two phase flow having liquid and gas superficial velocities of 0.642 m/s and 0.5m/s respectively. Based on the flow regime transition maps described by Mishima and Ishii (1984) and Schlegel et al. (2009), this flow regime lies very close to the bubbly to slug flow transition and this transition is the same for both small and large pipes. Therefore, as shown in the contour plot, the gas slug length l_s and cross sectional area α, are less compared to that of higher gas superficial velocities of 0.773m/s and 0.978m/s in fully developed slug flows shown in the contour plots in Figures 6.2, 6.3 and 6.4 especially for I.D.s of 0.1016m and 0.0525m. The slug length l_s, in these two smaller diameter pipes are approximately 15D which agrees with the range 8D<l_s<16D reported by Taitel et al. (1980). In the large pipe (I.D = 0.2032), there was no significant increase in the l_s obtained close to the bubbly to slug flow transition as the gas superficial velocity increased up to 0.978m/s. The l_s within this cap bubbly flow regime could not grow significantly due to the surface instability that prevents development of long slugs in large pipes (Shen et al. 2014), therefore $l_s \approx$ 4D.

The PDF of the void fraction for Vsl=0.642m/s and Vsg=0.5m/s in the three pipe sizes are similar since bubbly flow transition mechanism and behaviours are the same irrespective of pipe sizes. The PDF peaked at a void fraction less than 0.3 which is representative of void fraction in bubbly flows while a broad trailing tail extends to void fractions above 0.5. As gas superficial velocity increased up to 0.978m/s, the two peaks in the PDFs of void fraction in the small pipe became almost equal while in the larger pipes, the leading peak representing low void fraction of liquid slug containing small bubbles was higher than the trailing peak representing cap bubbles. These behaviours are consistent with the experimental observations reported by Schelgel et al. (2009), Costigan and Whalley (1997) and Lowe and Rezkallah (1999).

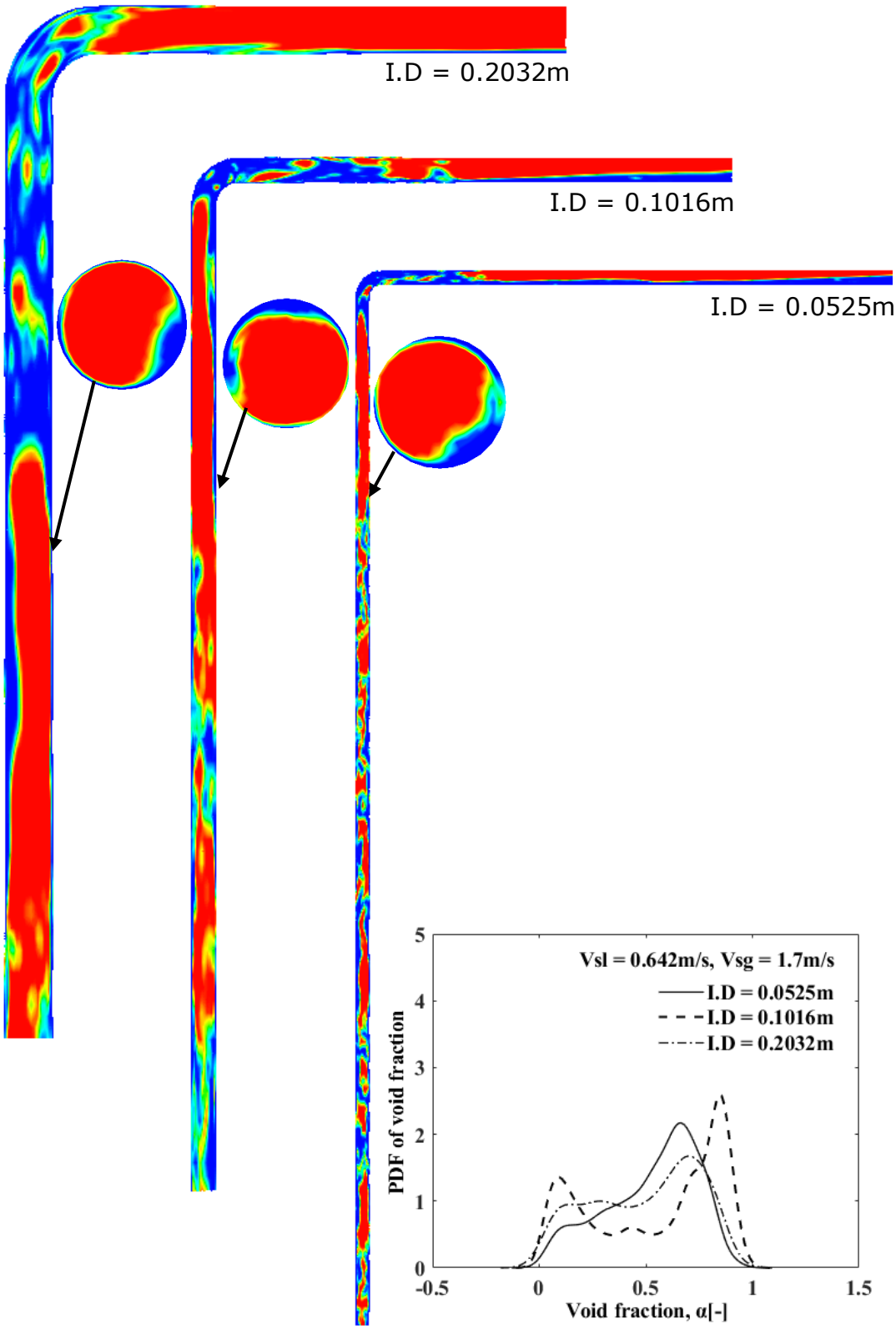

Figure 6.5: Contour of air volume fraction and PDF for Vsl=0.642m/s and Vsg=1.7m/s in the three pipe sizes.

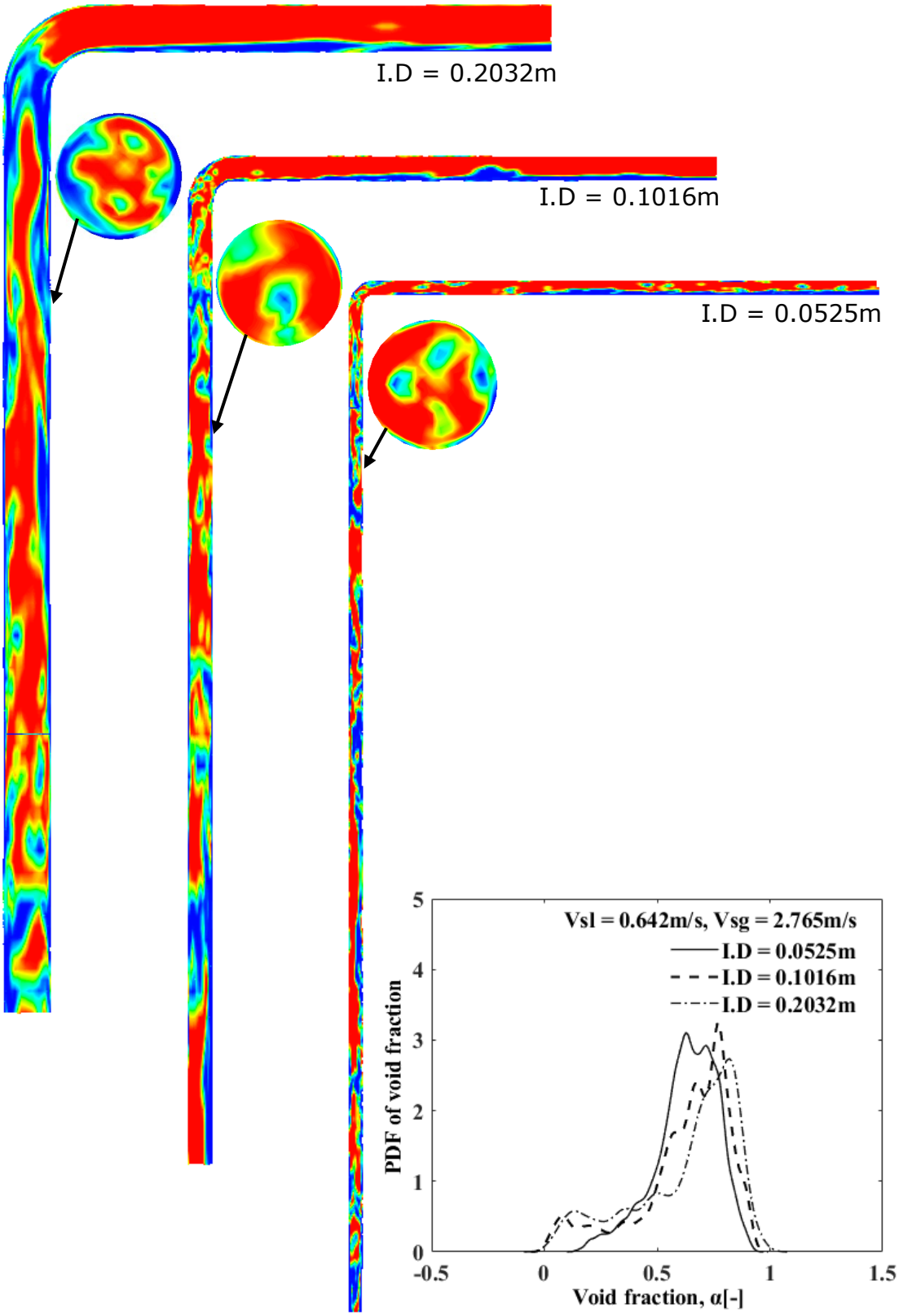

Figure 6.6: Contour of air volume fraction and PDF for Vsl=0.642m/s and Vsg=2.765m/s in the three pipe sizes.

The PDFs in Figures 6.5 and 6.6 represent typical PDFs of unstable slug flow regime as described by Costigan and Whalley (1997). A dominant peak is seen at higher void fraction up to 0.8 while a trailing tail is seen below 0.4. However, the tail shows consistent visible peaks in the pipes of I.D = 0.1016m and 0.2032m while this was not the case in the small pipe of I.D = 0.0525m in which the shape of the PDF at Vsg of 2.765m/s does not show a peak in the trailing edge below 0.5. This is more consistent with a churn flow behaviour and conforms to the suggested physical mechanism of slug to churn flow transition by entry length phenomenon by Taitel et al. (1980). Figure 4.4 (b) indicates that at Vsl and Vsg of 0.642m/s and 2.765m/s in the pipe of 0.0525m I.D, the two phase flow is in churn flow regime as shown in the flow map. Furthermore, in Figures 6.1 – 6.6, the contour plots show that the liquid slug could still bridge the pipe cross-section.

On the other hand, the contour plots of the gas void fraction in Figures 6.7 – 6.9 show that the liquid slugs could rarely bridge the pipe cross-section. The large liquid wave structures which are characteristic of churn flows are also visible in the figures and the observation is consistent with the findings of Montoya et al., (2016), Costigan and Whalley (1997), Da Riva and Del Col (2009) and Lowe and Rezkallah, (1999). Based on the review reported by Montoya et al. (2016) and the findings of Da Riva and Del Col (2009), the VOF in the present study has accurately modelled the liquid wave structures observed in Figures 6.8 and 6.9 since these waves have large interface scales while the mesh individual cell volume dimensions in each of the present pipe geometries are relatively much smaller. Hence the condition for accurate implementation of VOF method is largely met. However, the gas cores in the large pipe (0.2032m I.D.) in Figures 6.8 and 6.9 are seen to be carrying entrained liquid droplets which are large enough to be captured in the flow model. Similar entrainments were not seen in the two other pipes in the figures. This observation can be explained as the onset of droplet entrainment caused by shearing off of liquid from the liquid wave crest due to vapour drag. A mechanism described by Mishima and Ishii (1984) as the churn-turbulent to annular flow transition behaviour in large pipes. Presently, curves D and E in Figures 4.4 (a) and (b) represent the churn-annular flow transitions in the large (0.2032m I.D.) and small (0.0525mI.D.) pipes respectively. Curve D also correspond to slightly lower values of Vsg compared to curve E. In addition, for

the same Vsl, Curve B which is the cap-bubbly to churn-turbulent flow transition in the large pipe exist at a much lower Vsg compared to Curve C which represents slug to churn flow transition in small pipes. Hence in the case of the large pipe (0.2032m I.D.), the positions of curves B and D (Figure 4.4 (a)) suggest that at Vsg = 9.04m/s and Vsl = 0.642m/s and 0.642m/s, both flow cases would already be exhibiting the churn-turbulent to annular flow regime transition behaviour described by Mishima and Ishii (1984). This explains the liquid droplets seen breaking off from the wave crests in the pipe of 0.2032m I.D. in Figures 6.8 and 6.9.

The PDFs all show peaks above 0.8 in the three pipe sizes. Although the peaks are more defined and narrower in the smallest pipe than the two larger ones indicating less fluctuation of void fraction and the dominance of a narrow range of void fraction in the pipe due to churn flow compared to the two larger pipes. In summary, the CFD method was able to reproduce the fundamental physical behaviours of the cap-bubbly, slug, churn and churn turbulent flow regimes across the small to large diameter pipes in the present study.

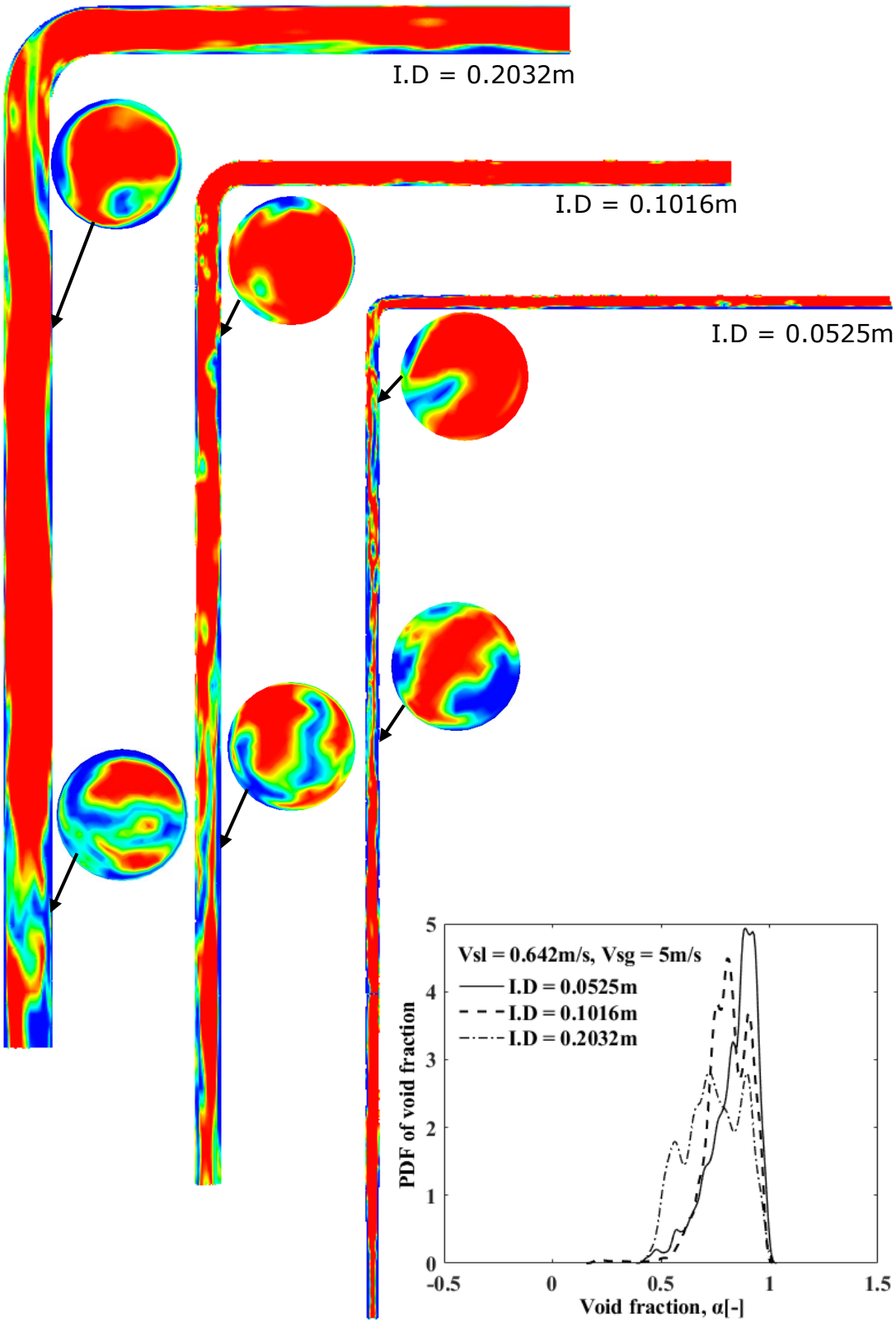

Figure 6.7: Contour of air volume fraction and PDF for Vsl=0.642m/s and Vsg=5m/s in the three pipe sizes.

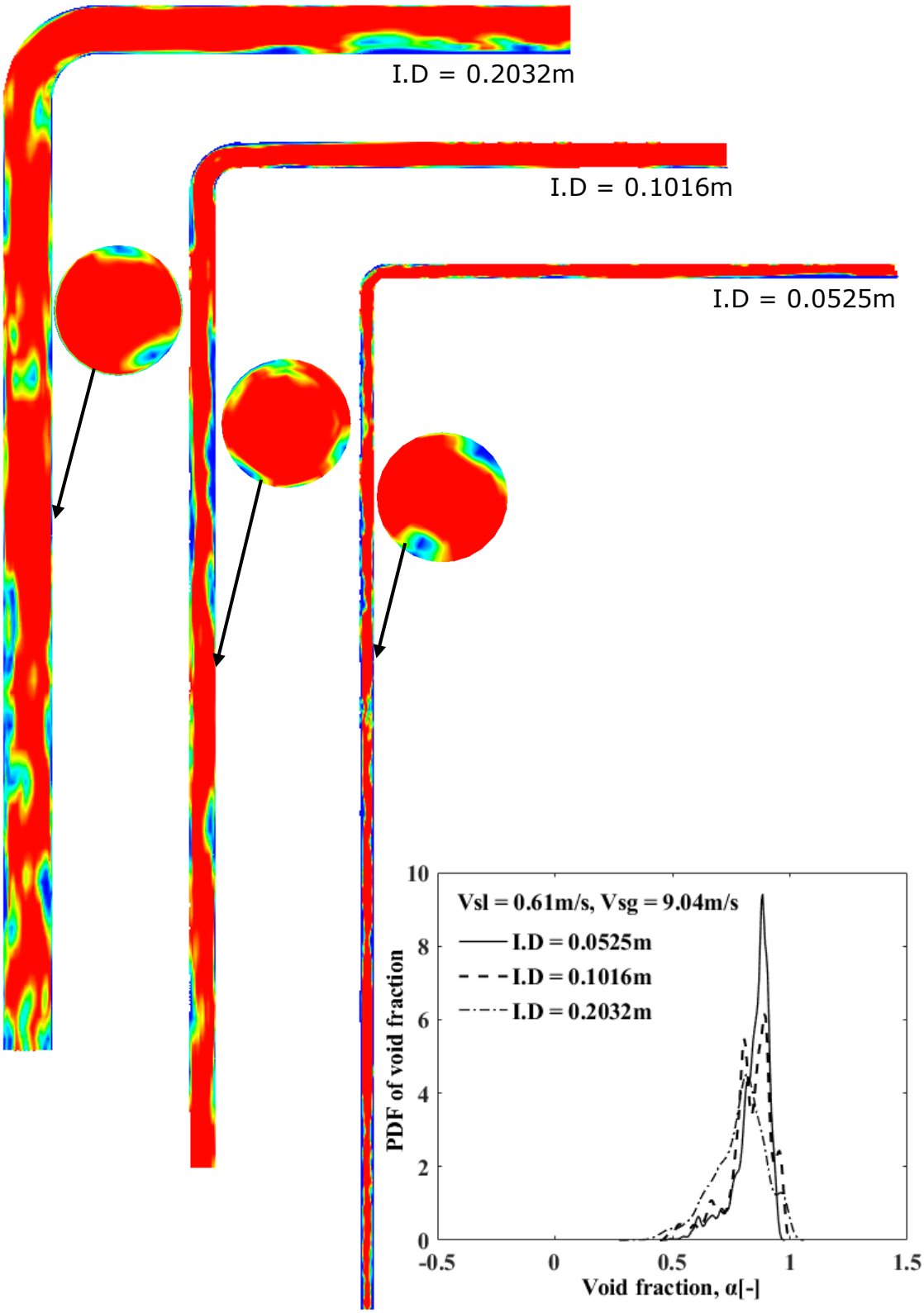

Figure 6.8: Contour of air volume fraction and PDF for Vsl=0.61m/s and Vsg=9.04m/s in the three pipe sizes.

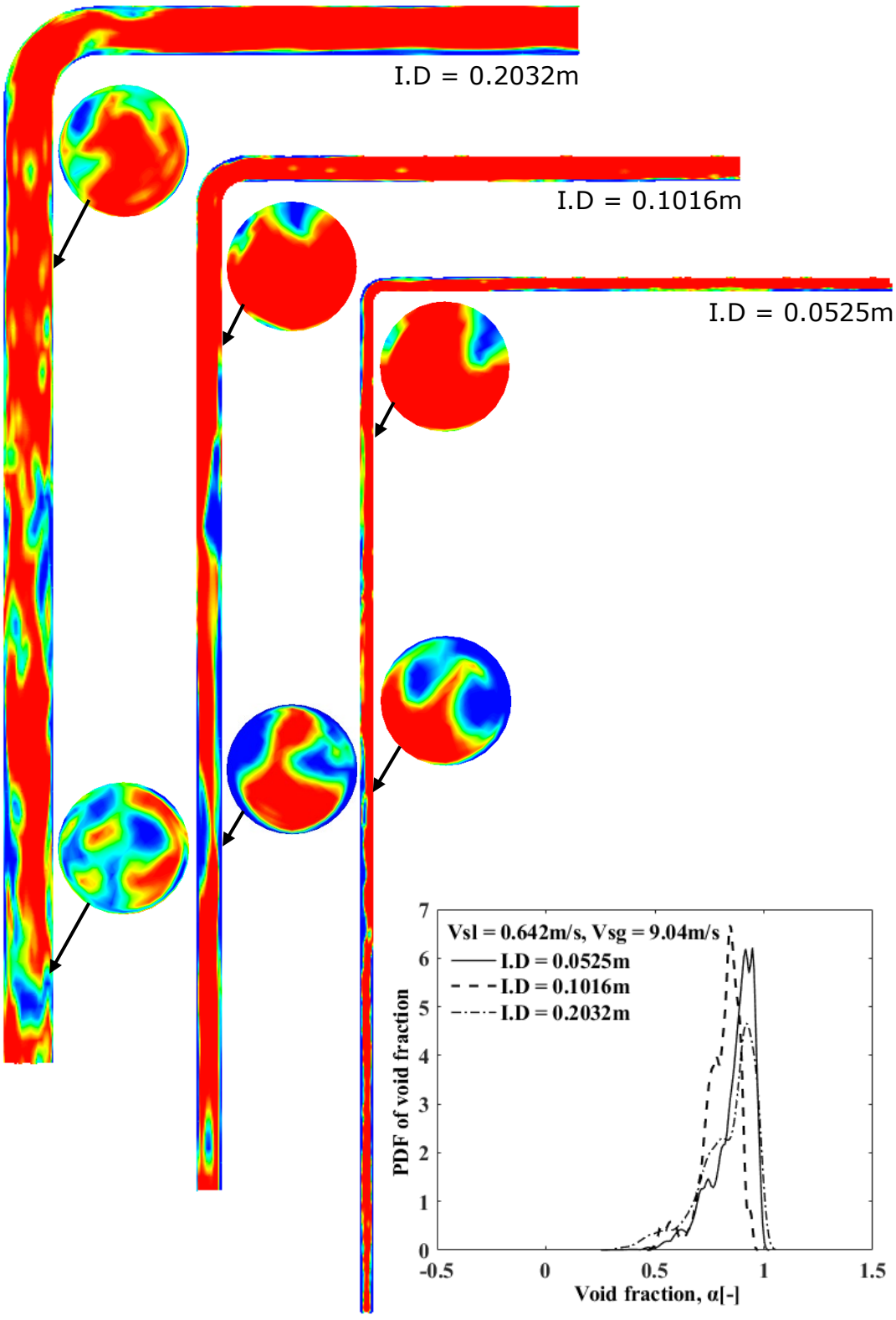

Figure 6.9: Contour of air volume fraction and PDF for Vsl=0.642m/s and Vsg=9.04m/s in the three pipe sizes.

Figures 6.10 (a) and (b) respectively show the comparisons of the time-history and PSDs of void fraction fluctuation for pipes of 0.1016m and 0.2032m I.Ds, while Figures 6.11 (a) and (b) show the comparisons of peak frequencies and RMS of void fraction fluctuation respectively for both pipes. In the case of the pipe of 0.2032m I.D, the trends in Figures 6.10(a) (i) – (ii) represent the distinct long liquid slugs with entrained smaller distorted bubbles and the leading or trailing much shorter cap-bubbles which are the defining characteristics of cap-bubbly flow regime in large pipes. Although this behaviour appears to be imitated in the pipe of 0.1016m I.D, it is however more obvious in the larger pipe and conforms to the findings of Schlegel et al. (2009). Generally, Figures 6.10(a) (i) – (v) show that the cross-sectional area average of the gas slugs in the 0.1016m I.D pipe which were up to values above 0.9 were consistently higher than that of the cap-bubbles in the pipe of I.D 0.2032m where values were typically less than 0.8. The trends are also consistent with the higher L/D of the gas slugs observed in the pipe of 0.1016m I.D compared to the larger pipe.

Figures 6.10(b) (i) – (v) show that in both pipes, the most important frequencies of fluctuations were below 2Hz. In addition, the energy in the fluctuations in the smaller pipe were consistently higher as seen in the PSDs. This behaviour is attributed to the presence of both long gas slugs and cap-bubbles co-existing in the pipe which has non-dimensional hydraulic diameter value of D_H^* = 37.2. This value lies in the transition region of $18.5<D_H^*<40$ within which both small pipe and large pipe behaviours could be present. These behaviours introduce more fluctuations in the pipe.

The time-history of the void fraction shown in Figure 6.10 (a) (vi) for the 0.1016m I.D. pipe show that at Vsg of 2.765m/s the flow is more unstable than is obtainable in the large pipe (0.2032m I.D.). The observation can be explained by the entry length phenomenon reported by Taitel et al. (1980) where the flow regime of Vsg = 2.765m/s is in the churn flow regime for the pipe of I.D = 0.1016m. The void fraction time-history in Figures 6.10(a) (vii) – (ix) show similar churn flow behaviours while the predominant frequencies in the PSDs are below 1.5 Hz and the range diminishing significantly from slug to churn flow regime.

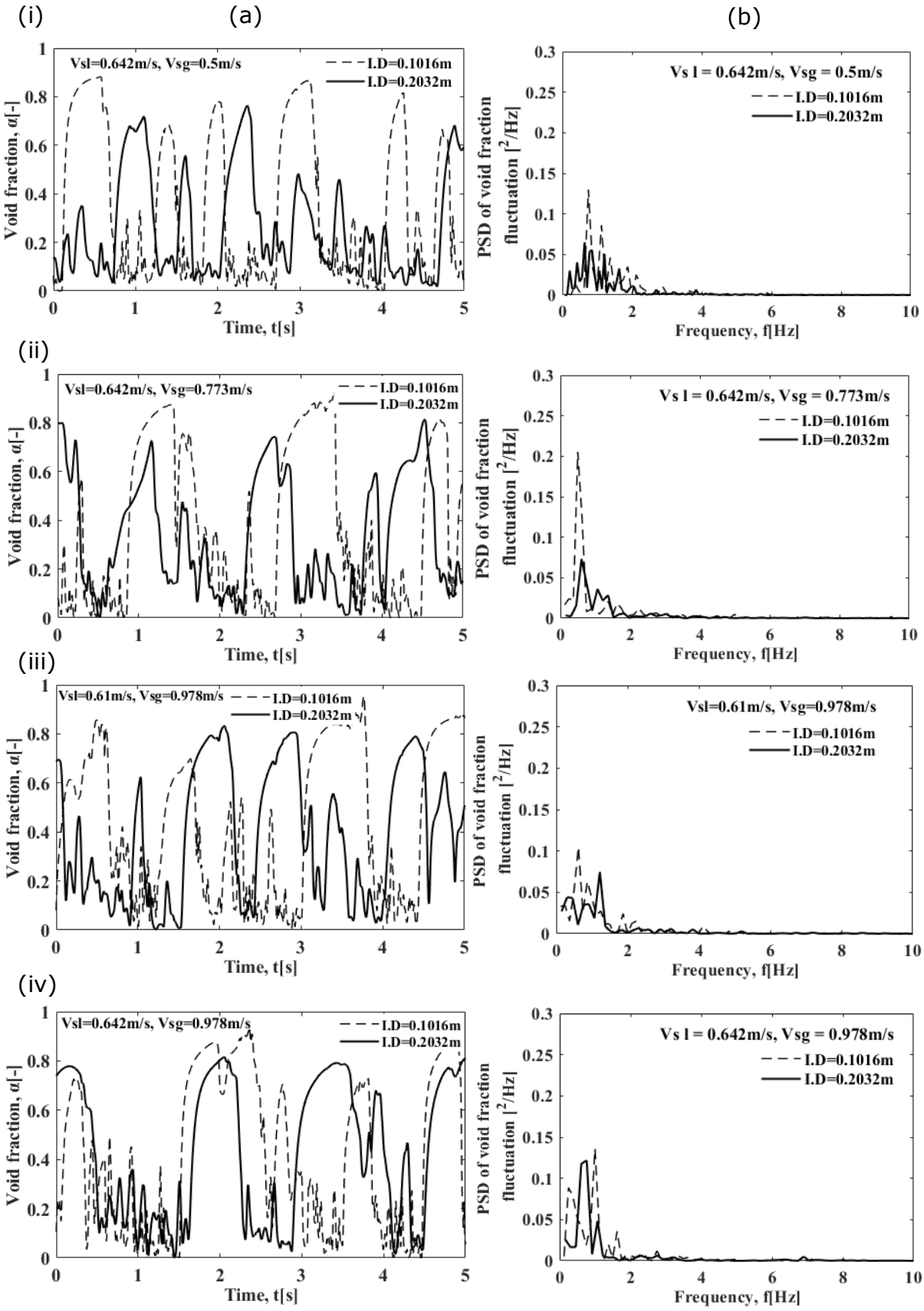
(i)
(a)
(b)
Vsl=0.642m/s, Vsg=0.5m/s
I.D=0.1016m
I.D=0.2032m
Void fraction, α[-]
Time, t[s]
Vs l = 0.642m/s, Vsg = 0.5m/s
PSD of void fraction fluctuation [²/Hz]
Frequency, f[Hz]
(ii)
Vsl=0.642m/s, Vsg=0.773m/s
Vs l = 0.642m/s, Vsg = 0.773m/s
(iii)
Vsl=0.61m/s, Vsg=0.978m/s
(iv)
Vsl=0.642m/s, Vsg=0.978m/s
Vs l = 0.642m/s, Vsg = 0.978m/s

(v)

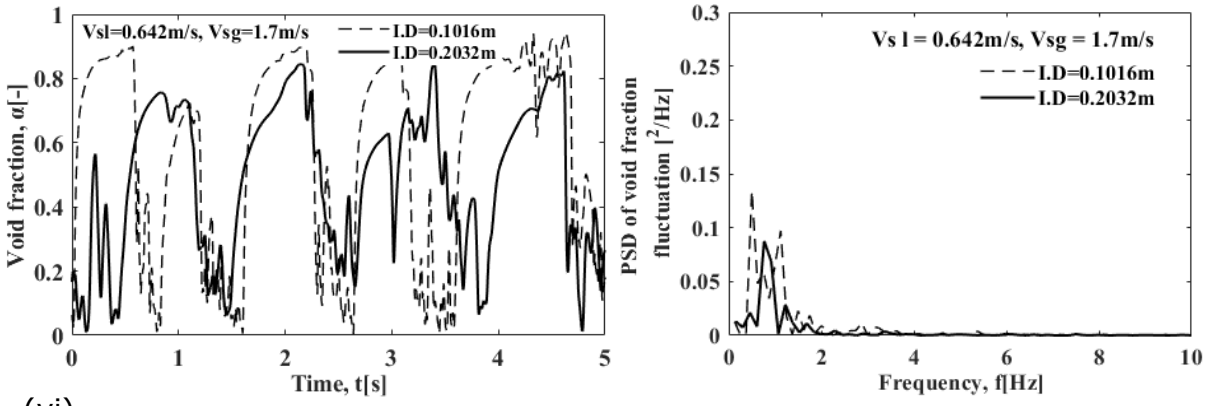
Vsl=0.642m/s, Vsg=1.7m/s
I.D=0.1016m
I.D=0.2032m
Void fraction, α[-]
Time, t[s]
Vs l = 0.642m/s, Vsg = 1.7m/s
I.D=0.1016m
I.D=0.2032m
PSD of void fraction fluctuation [2/Hz]
Frequency, f[Hz]

(vi)

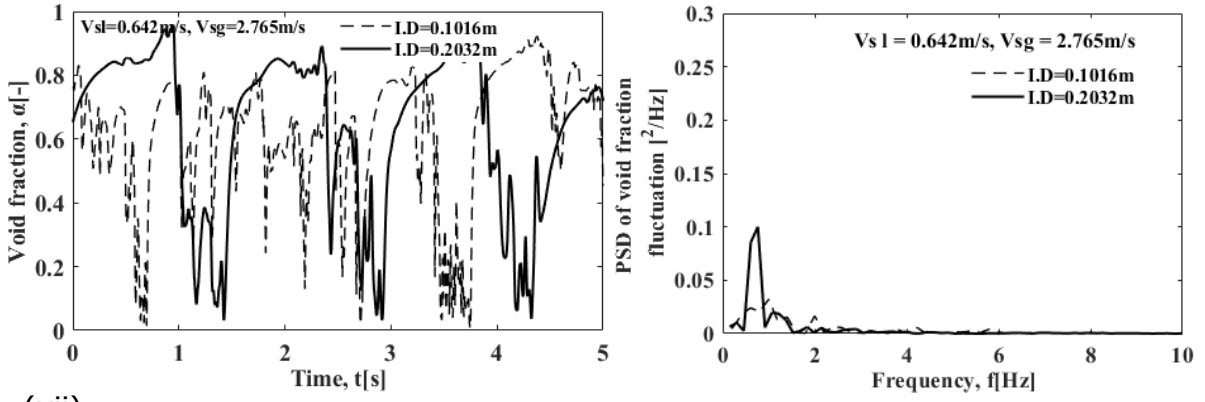
Vsl=0.642m/s, Vsg=2.765m/s
I.D=0.1016m
I.D=0.2032m
Void fraction, α[-]
Time, t[s]
Vs l = 0.642m/s, Vsg = 2.765m/s
I.D=0.1016m
I.D=0.2032m
PSD of void fraction fluctuation [2/Hz]
Frequency, f[Hz]

(vii)

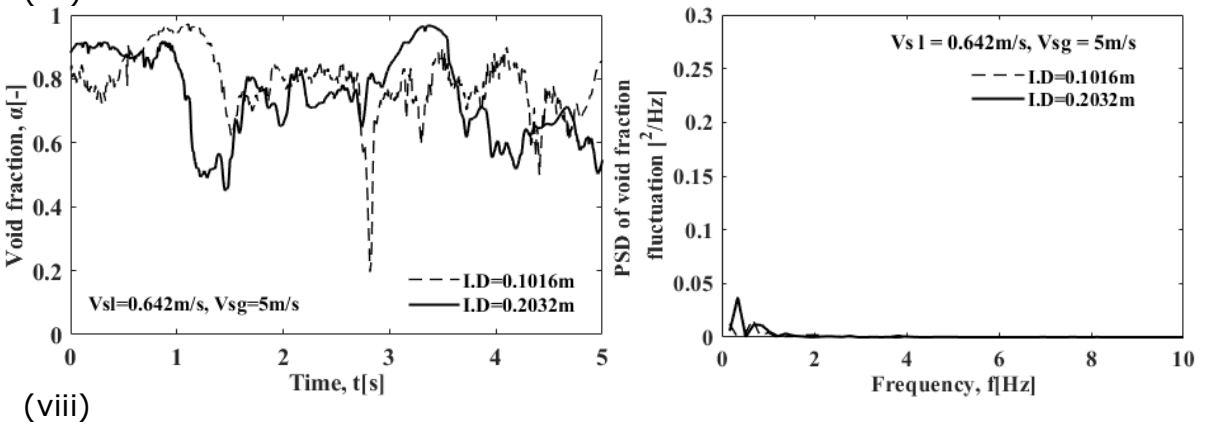
Vsl=0.642m/s, Vsg=5m/s
I.D=0.1016m
I.D=0.2032m
Void fraction, α[-]
Time, t[s]
Vs l = 0.642m/s, Vsg = 5m/s
I.D=0.1016m
I.D=0.2032m
PSD of void fraction fluctuation [2/Hz]
Frequency, f[Hz]

(viii)

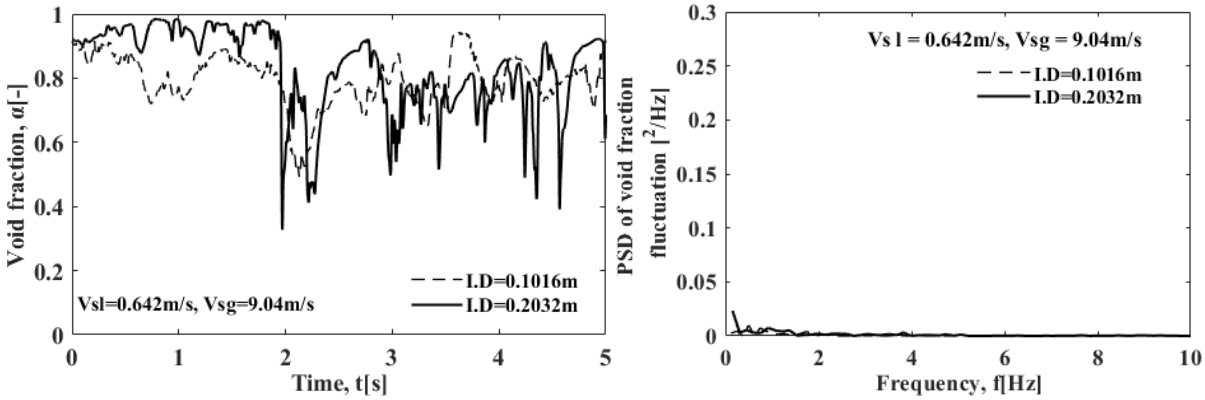
Vsl=0.642m/s, Vsg=9.04m/s
I.D=0.1016m
I.D=0.2032m
Void fraction, α[-]
Time, t[s]
Vs l = 0.642m/s, Vsg = 9.04m/s
I.D=0.1016m
I.D=0.2032m
PSD of void fraction fluctuation [2/Hz]
Frequency, f[Hz]

(ix)

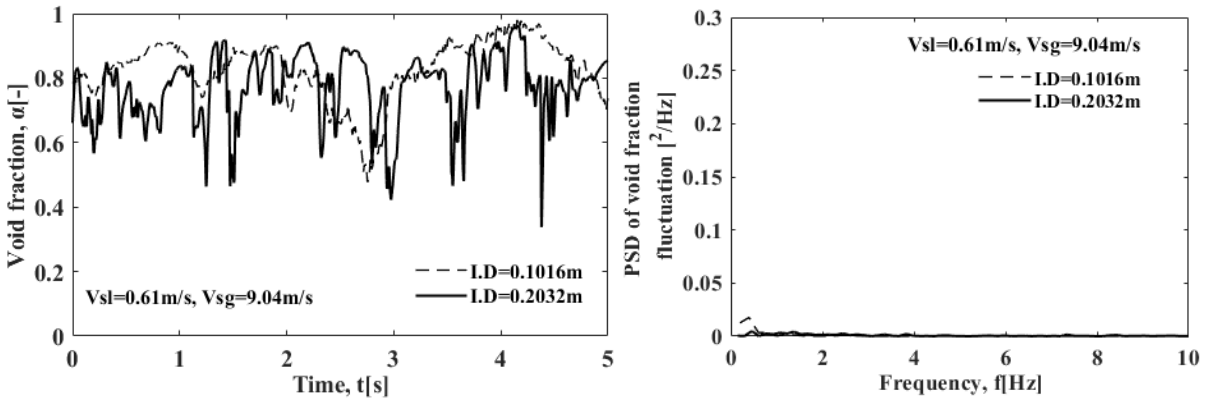

Figure 6.10: Comparison of (a) the time domain signal of void fraction fluctuation and (b) PSD for the pipes of I.D = 0.1016m and 0.2032m.

The trends in the predominant frequencies of void fraction fluctuation as a function of gas superficial velocity in Figure 6.11(a) is also consistent with the transition region behaviour between small and large pipes as described by Shen et al. (2014). This behaviour was identified to be mainly present within the superficial velocities corresponding to stable slug flow regime in small pipes. Therefore the predominant frequencies of void fraction fluctuation in the pipe of 0.1016m I.D varied much from Vsg of 0.773 – 2.75 which represent the limits of moderate/relatively stable slug flow regime. On the other hand, the predominant frequencies in the pipes of 0.0525m and 0.2032m I.D show more predictable trends within the stable slug flow regime. The former peaked at Vsg of 0.773m/s while the later peaked at Vsg of 0.978m/s which is on the transition line between cap-bubbly and churn turbulent flow regime. The peak value in the large pipe also remained constant for Vsg of 1.7m/s and 2.765m/s which are within the churn turbulent flow regime. As Vsg approached the churn flow regime, the trends of the peak frequencies became similar because the chaotic nature of churn flow are similar in the present three pipe sizes and the mechanism of churn to annular flow transition is also similar in the pipes.

The RMS of void fraction fluctuation as a function of superficial gas velocity is similar for all pipe sizes. The maximum RMS values are observed within the stable slug/cap-bubbly flow regime and then it diminishes as Vsg approaches churn flow

regime in all the pipes. The RMS of fluctuation was also slightly higher in the pipe of 0.1016m I.D ($D_H^* =$ 37.2) within the stable slug flow regime.

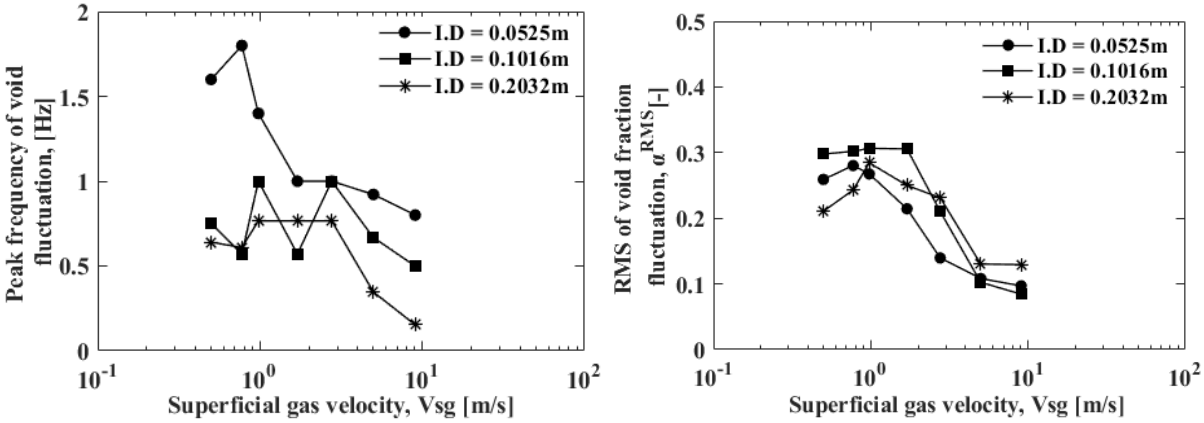

Figure 6.11: (a) Peak frequency and (b) RMS of void fraction fluctuation for increasing gas superficial velocities and constant liquid superficial velocity of 0.642 m/s for the three pipe sizes.

6.2 Two-phase flow induced force

The fluctuating force acting on the elbow in the pipes of 0.1016m and 0.2032m I.D are also calculated using Equations (5.2) – (5.4). Figures 6.12 – 6.20 show the simulated time-histories of force fluctuations and the corresponding PSDs of the fluctuations in each case for the flow regimes of interest.

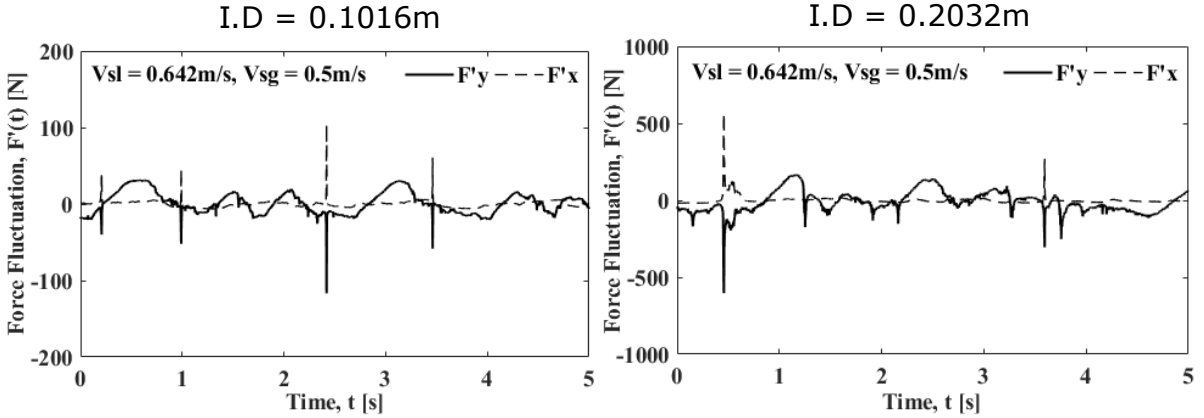

(a)

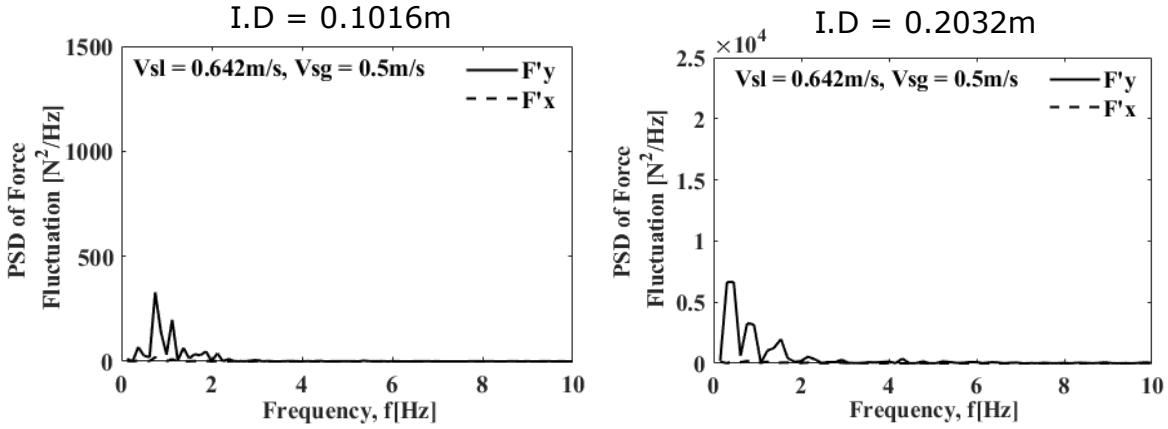

(b)

Figure 6.12: (a) Force fluctuation and (b) PSD for gas and liquid superficial velocities of 0.5m/s and 0.642 m/s respectively.

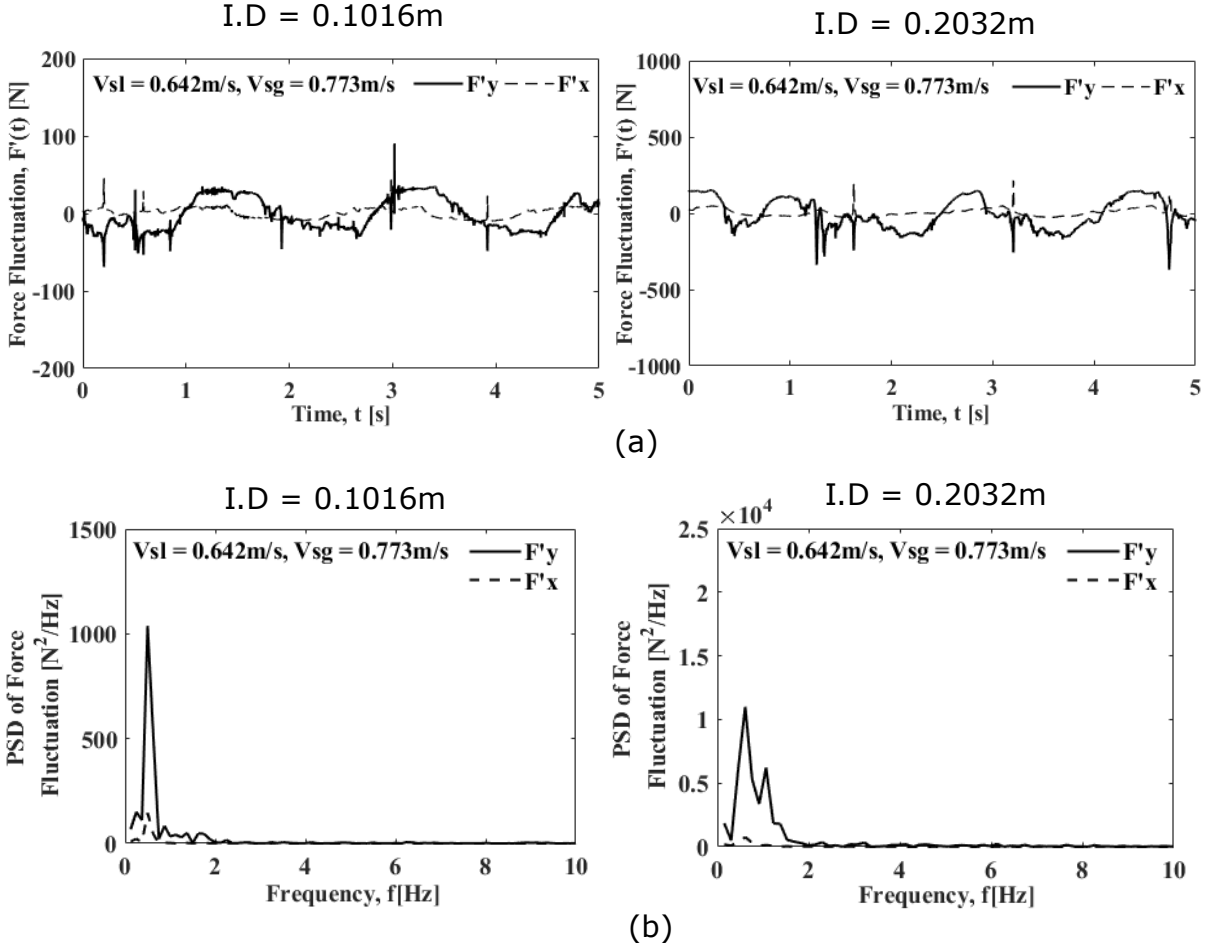

(a)

(b)

Figure 6.13: (a) Force fluctuation and (b) PSD for gas and liquid superficial velocities of 0.773m/s and 0.642 m/s respectively.

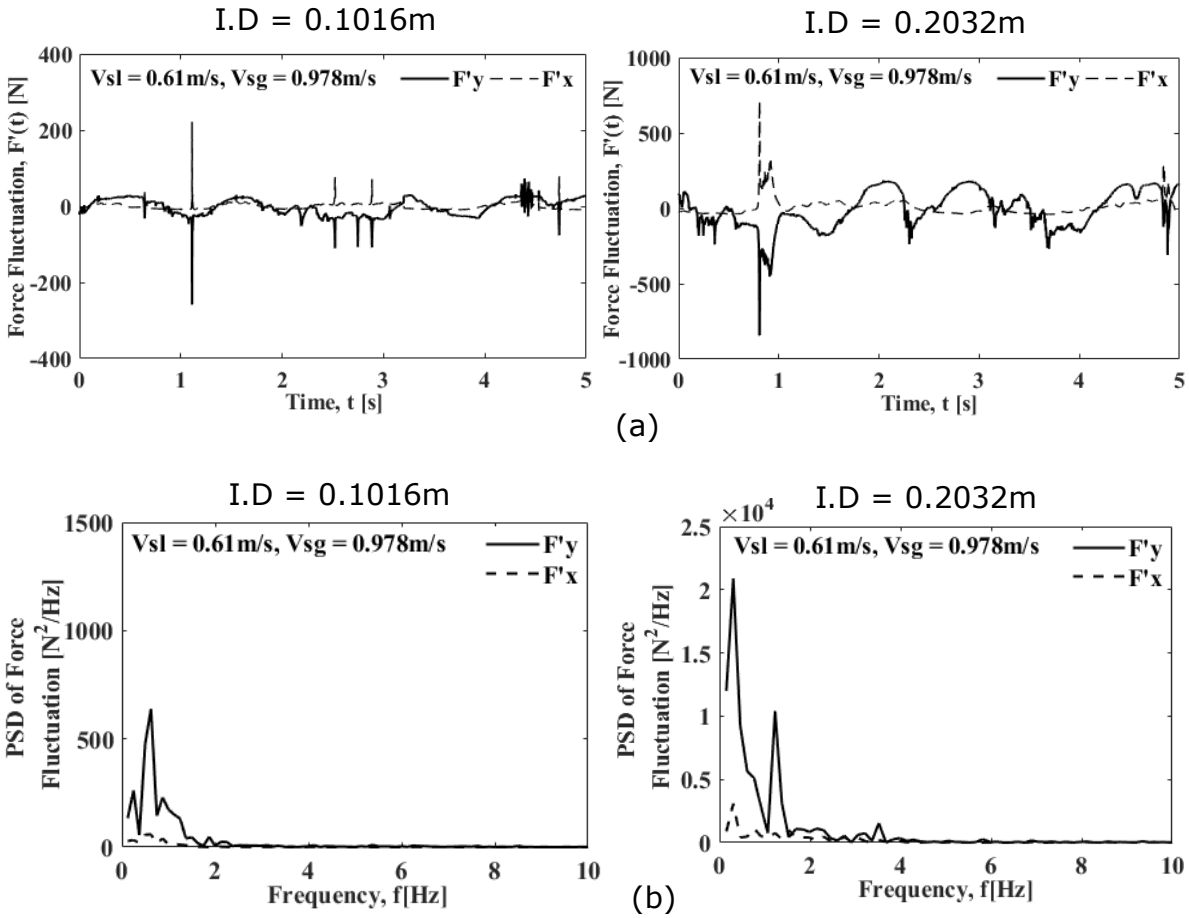

Figure 6.14: (a) Force fluctuation and (b) PSD for gas and liquid superficial velocities of 0.978m/s and 0.61 m/s respectively.

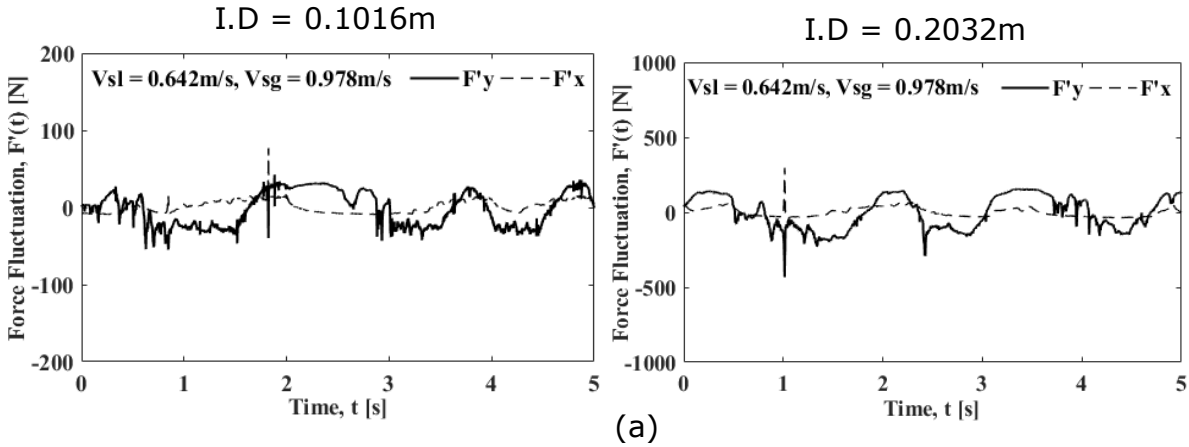

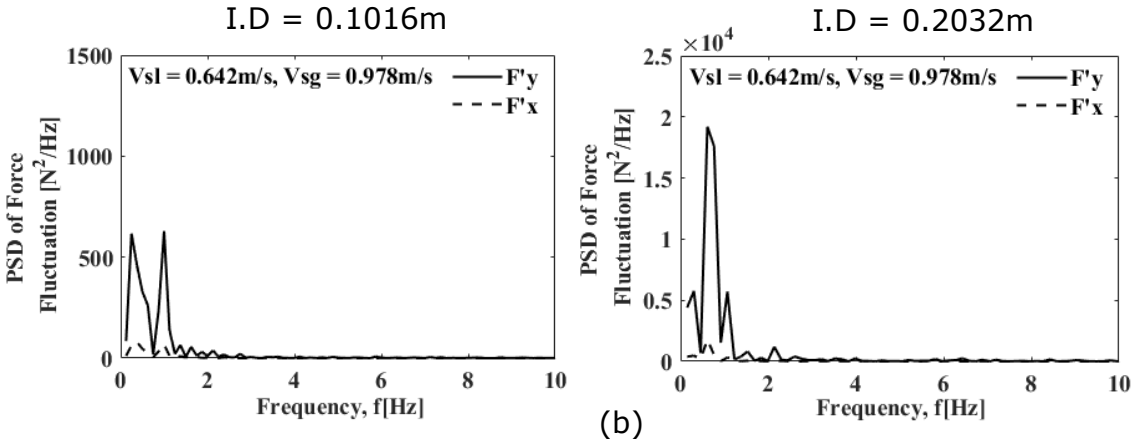

Figure 6.15: (a) Force fluctuation and (b) PSD for gas and liquid superficial velocities of 0.978m/s and 0.642 m/s respectively.

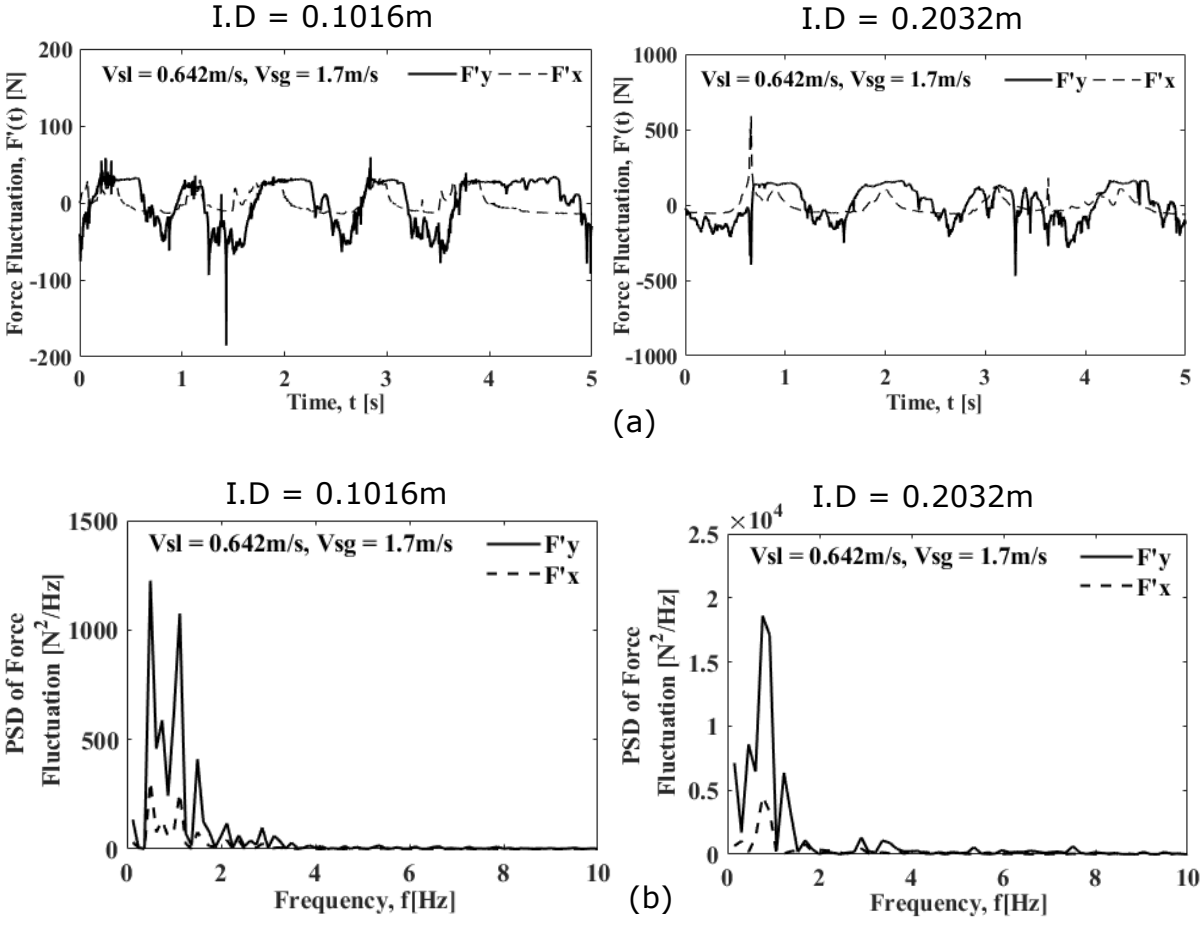

Figure 6.16: (a) Force fluctuation and (b) PSD for gas and liquid superficial velocities of 1.7m/s and 0.642 m/s respectively.

The time signals of force fluctuations in Figures 6.12(a) – 6.16(a) show that force fluctuations in the 0.1016m I.D pipe were generally within -100N to100N while a fluctuation range of -500N to 500N was observed in the pipe of 0.2032m I.D for the moderate slug flow regime up to Vsg of 1.7m/s. As gas superficial velocities increase from moderate slug to unstable slug and churn flow regimes represented by Vsg >1.7m/s, the fluctuation ranges increased to about -250N to 250N in the 0.1016m I.D pipe and -2000N to 2000N in the 0.2032m I.D pipe with the exception of Vsg = 5m/s which exhibited reduced force fluctuation amplitude range in both pipes. This can be explained by the transition behaviour observed in the contour plot in Figure 6.2 which showed that liquid slugs could no longer bridge the entire pipe diameter at Vsg = 5m/s meanwhile the characteristic large waves that are present in established churn flows and representing the main mechanism of fluctuations in churn flows were not consistent yet in the flow. The increasing amplitude of force signal is attributed to the increase in mass flow rate and hence the momentum flux with increase in pipe diameter.

Pontaza et al. (2016) obtained a force fluctuations range of -500 -1000 N for Vsg and Vsl of 10.45m/s and 1m/s respectively from their experiment. Although the test section is a horizontal 90^0 pipe bend of 0.154m I.D which is half-way between the 0.1016m and 0.2032m I.D. sizes, the measured force range conforms with present CFD observed force ranges. Assuming their measured force fluctuation for the reported geometry gives a good indication of force fluctuation in similar geometry positioned vertically, then the force range also falls about half-way between the observed force range for the 0.1016m I.D. (-250N - 250N) and 0.2032m I.D. (-2000N – 2000N) for similar flow superficial velocities of Vsg and Vsl of 9.04m/s and 0.642m/s.

The y-components of force fluctuations were consistently higher than the observed x-component fluctuations although, the magnitude of the difference reduced as the gas superficial velocity increased towards the churn flow regime (Vsg = 9.04m/s). This observation is consistent with the results reported for the pipe of 0.0525m I.D in Chapter 5. The high amplitude of the y-component is equally attributed to the impact of liquid slugs on the bend in the y-direction while the

lower amplitude of Fx fluctuation which is more prominent in the moderate slug flow cases up to Vsg of 1.7m/s (Figures 6.12 – 6.16) is as a result of the change in flow pattern into stratified/stratified wavy flow downstream of the bend.

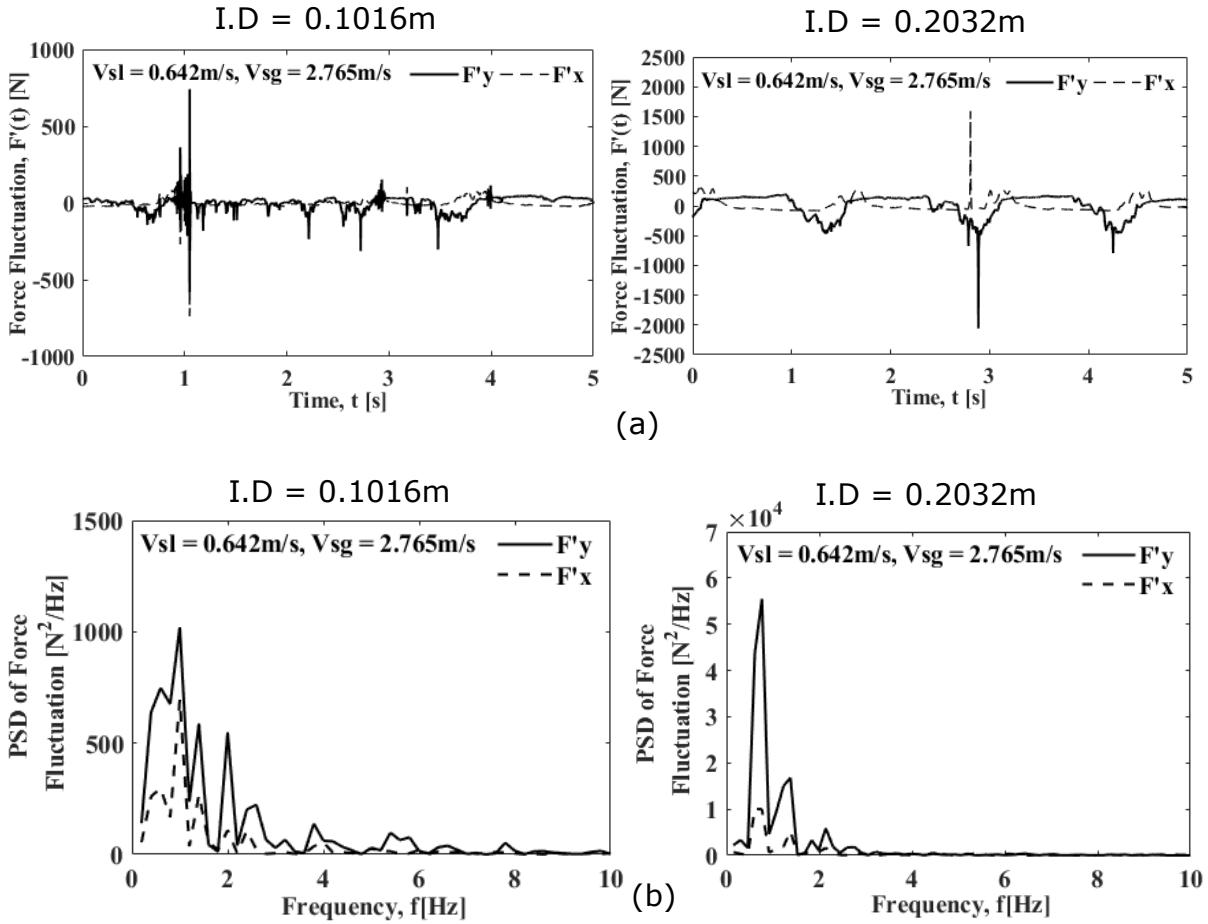

Figure 6.17: (a) Force fluctuation and (b) PSD for gas and liquid superficial velocities of 2.765m/s and 0.642 m/s respectively.

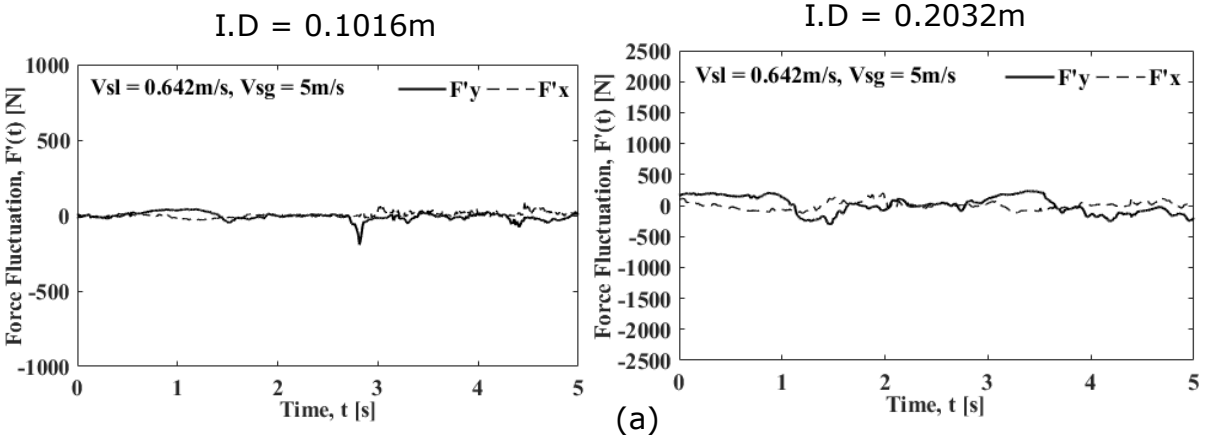

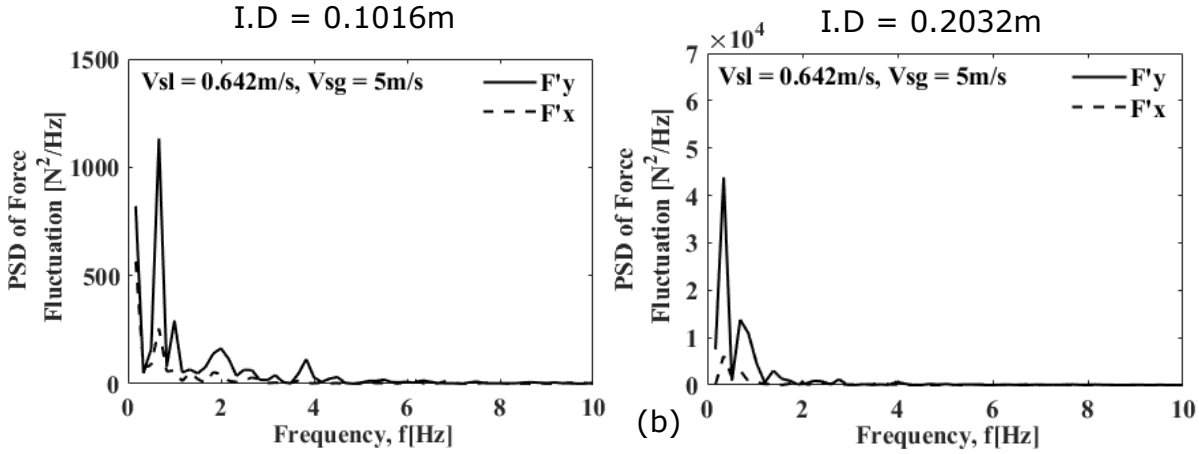

Figure 6.18: (a) Force fluctuation and (b) PSD for gas and liquid superficial velocities of 5m/s and 0.642 m/s respectively.

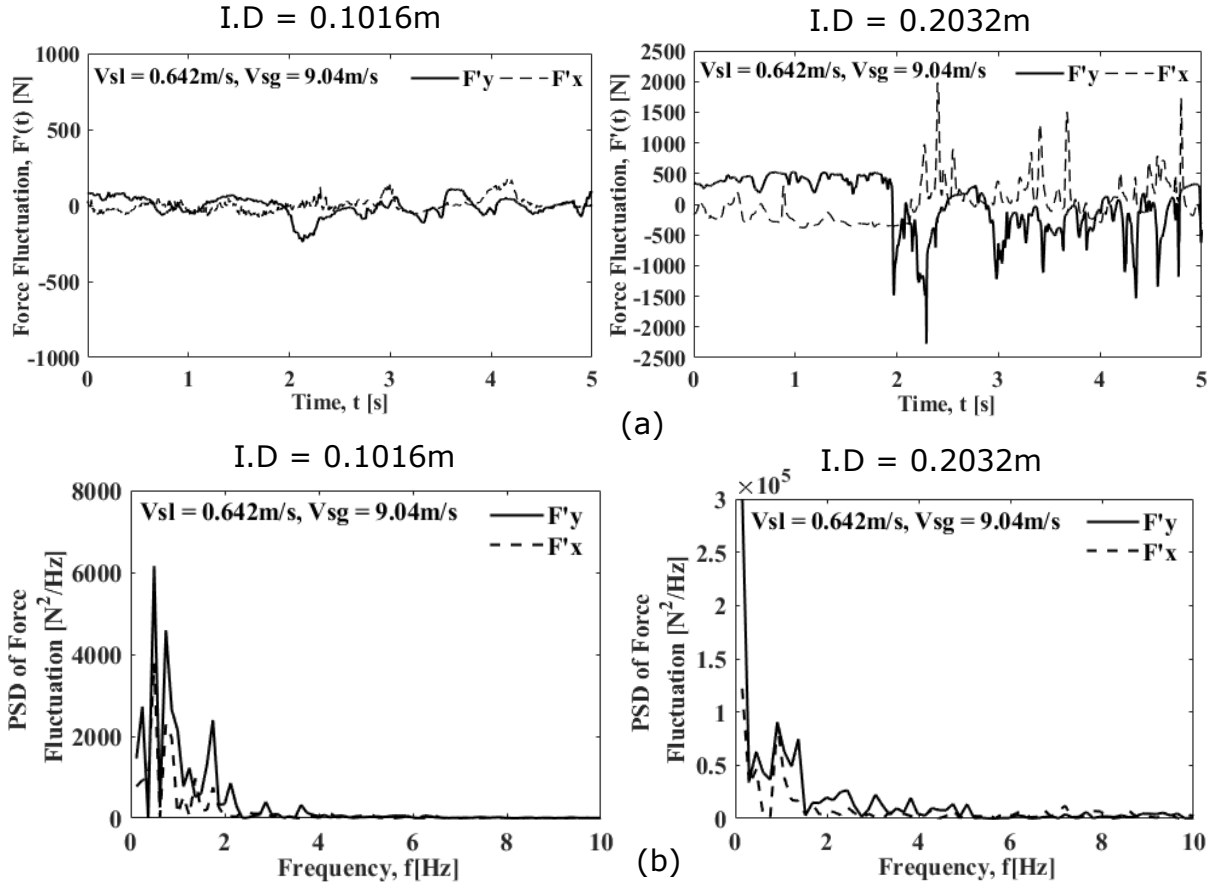

Figure 6.19: (a) Force fluctuation and (b) PSD for gas and liquid superficial velocities of 9.04m/s and 0.642 m/s respectively.

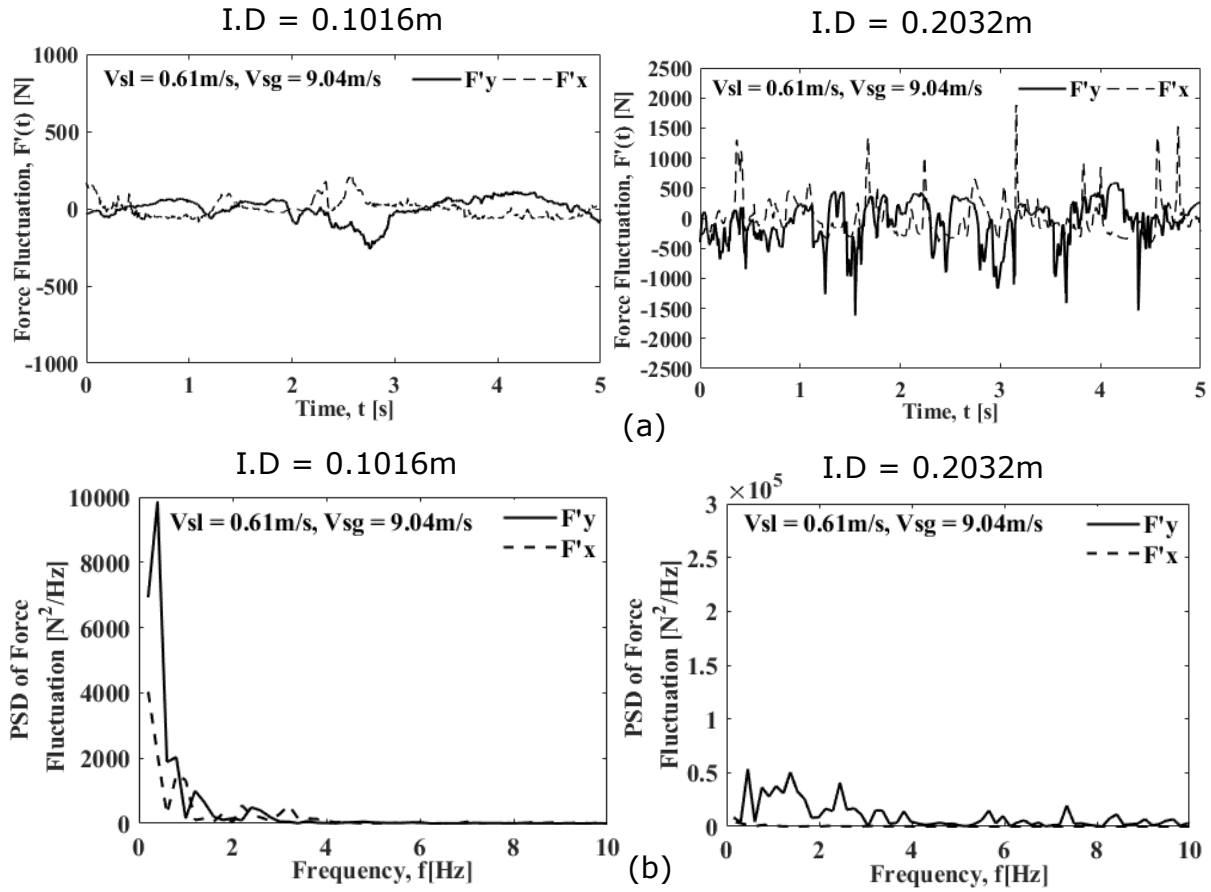

Figure 6.20: (a) Force fluctuation and (b) PSD for gas and liquid superficial velocities of 9.04m/s and 0.61 m/s respectively.

In both pipes, Figures 6.12 (b) to 6.20 (b) show that higher frequencies greater than 2Hz became more prominent as V_{sg} increased beyond 1.7m/s except at V_{sg} of 5m/s which showed less noise beyond 2Hz. This behaviour was also present in the 0.0525m I.D. pipe. However, in contrast to the findings in the case of 0.0525m I.D. pipe, force fluctuations PSD spread over larger frequency ranges compared to the void fraction fluctuations PSD (Figure 6.10 (b)) especially for the churn flows of Vsg = 9.04m/s. This behaviour indicates the following conclusions:

- Findings in Liu et al. (2012) and the Chapter 5 (Figure 5.18) of this study showed that the momentum flux fluctuation correlated very well with the force fluctuation compared to the pressure force fluctuation. The fluctuating

parameters in the momentum term ($\dot{m}(t)V(t)$ in Equations 5.2 - 5.3) and the mass flow rate ($\dot{m}(t)$ in Equation 5.4) are the $\alpha(t)$ and $V(t)$. Hence in the 0.0525m I.D. pipe, the time dependent velocity had a levelling out effect on the calculated momentum flux fluctuation and the force fluctuation by damping out values which would have appeared as higher frequency noise in the force fluctuation PSD due to the high frequency noise in the void fraction fluctuation PSD. Conversely, higher level of fluctuations in the velocity history contributed to the higher frequency noise observed in the force fluctuation in the larger pipes since the PSD of the corresponding void fraction parameter showed lesser high frequency noise compared to the force.

- The larger I.D. pipe bends allowed for enhanced flow streamlines mixing within the elbow control volume which contributed to enhanced velocity fluctuations compared to the small I.D. pipe whose walls would have a constricting and damping out effect on the flow streamlines similar to the effect that walls have on the gas slug surface instabilities and distortions.

Nevertheless, though the time domain signals of void fraction and force are different, the predominant frequencies ranges are the same- 0Hz to 2Hz. Liu et al. (2012) also reported similar findings between the time domain signals of their force fluctuations and void fraction. Generally, the PSD of force fluctuation is more than 1 order of magnitude higher in the 0.2032m I.D. pipe than the 0.1061m I.D. pipe.

Figures 6.21 and 6.22 show the predominant frequency and the RMS of force fluctuations in the x and y direction, respectively for all three pipe sizes. The trend in the present CFD predicted peak frequencies are similar in the smallest and largest pipes of 0.0525m and 0.2032m I.D respectively except for Vsg = 9.04m/s as seen in Figures 6.21(a) and 6.22(a). For the gas superficial velocities between 0.5 – 9.04m/s, peak frequencies of force fluctuations were within 0.1 – 1.7 Hz and were also higher in small pipes than large pipes for similar flow conditions. Conversely, the medium sized pipe having 0.1016m I.D showed irregular trend especially for the moderate slug flow regime up to Vsg = 1.7m/s for both x and y component forces. Additionally, peak frequencies peaked in slug flow regime for the small pipes and peaked in churn turbulent flow regime for the large pipe.

Therefore, while slug flow is critical for FIV in small pipes, churn turbulent flow is the critical flow regime for large pipes.

The RMS of force fluctuations showed similar behaviour in the three pipe sizes with increasing superficial gas velocities. The only exception was observed for Vsg = 5m/s which showed less fluctuation compared to other unstable slug or churn flow regimes. The RMS increased monotonically from 0.5m/s (slug/cap bubbly flow) to 2.765m/s (churn/churn turbulent flow) gas superficial velocities in the two larger pipes. For a mixture velocity of 1.142 – 9.682 m/s the range of RMS values for the x and y force components were 0.89 – 16.6 N and 2.5 – 18.5 N respectively for the pipe of 0.0525m/s, 3.8 – 57.3N and 13.9 – 72N for the pipe of 0.1016m/s and finally, 25.9 – 336N and 76 – 450N for the pipe of 0.2032m/s. Hence, in the present study having the largest to the smallest pipe diameter ratio of 4, the RMS of force fluctuation was about 1-order of magnitude (10X) higher in the large pipe than the small pipe.

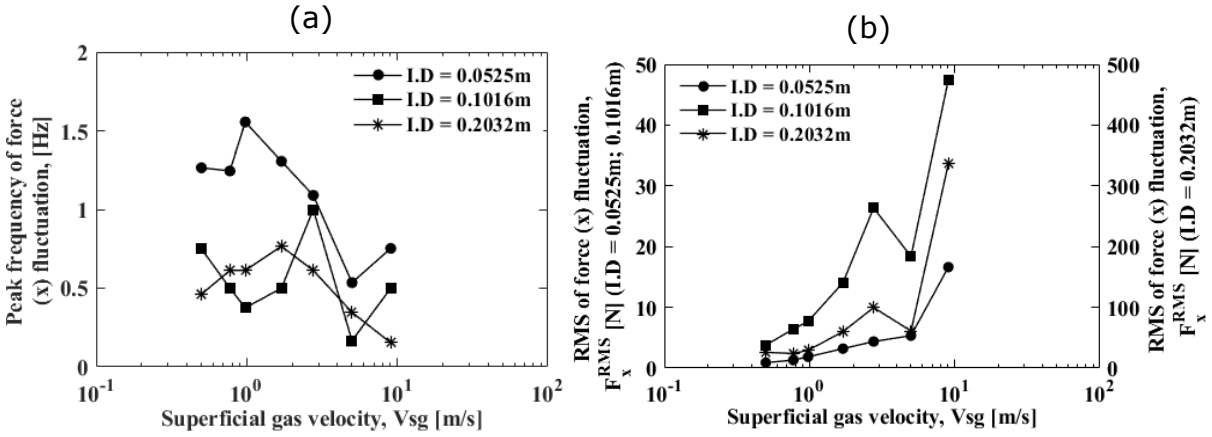

Figure 6.21: The effect of superficial liquid velocity on (a) peak frequency and (b) RMS values of x-component of force fluctuation for a fixed superficial liquid velocity at 0.642m/s in the three different pipe sizes.

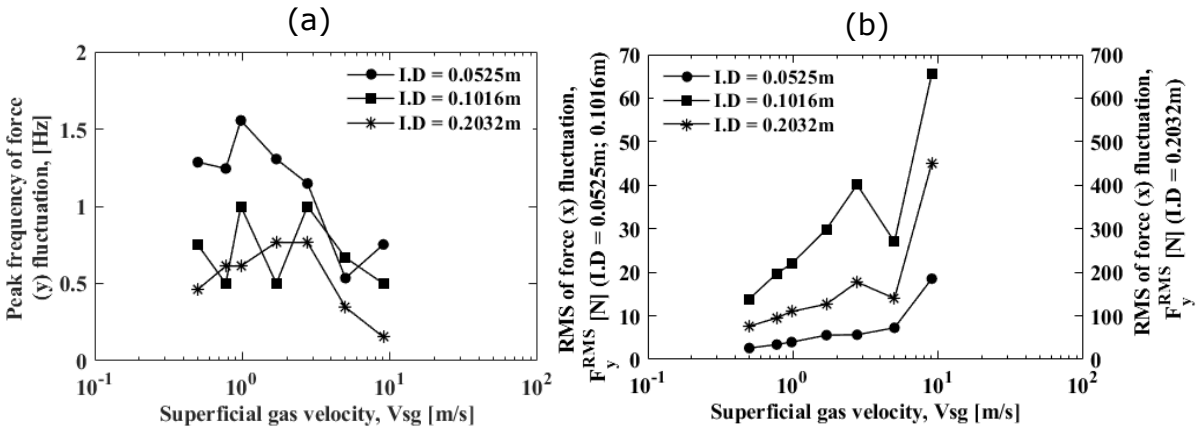

Figure 6.22: The effect of superficial gas velocity on (a) peak frequency and (b) RMS values of y-component of force fluctuation for a fixed superficial liquid velocity at 0.642m/s in the three different pipe sizes.

6.3 Performance of Riverin et al. (2006) correlation for non-dimensional RMS of excitation force in both small and large pipes

Figures 6.23 (a) and (b) present the comparisons of the non-dimensional RMS of force fluctuation for the three pipe sizes to the model by Riverin et al (2006). In Figure 6.23 (a), the constant C appearing in Equation 2.1 is left as its original value of 10. In Figure 6.23 (b), the correlation has been modified by setting the value of the constant C to be 20 in the present study in order to observe the performance of the model in estimating the RMS of excitation force in both small and large diameter pipes. The modified correlation is given as:

$$\overline{F_{rms}} = \frac{F_{rms}}{\rho V_t^2 (\frac{\pi D^2}{4})} = 20We^{-0.4} \qquad (6.1)$$

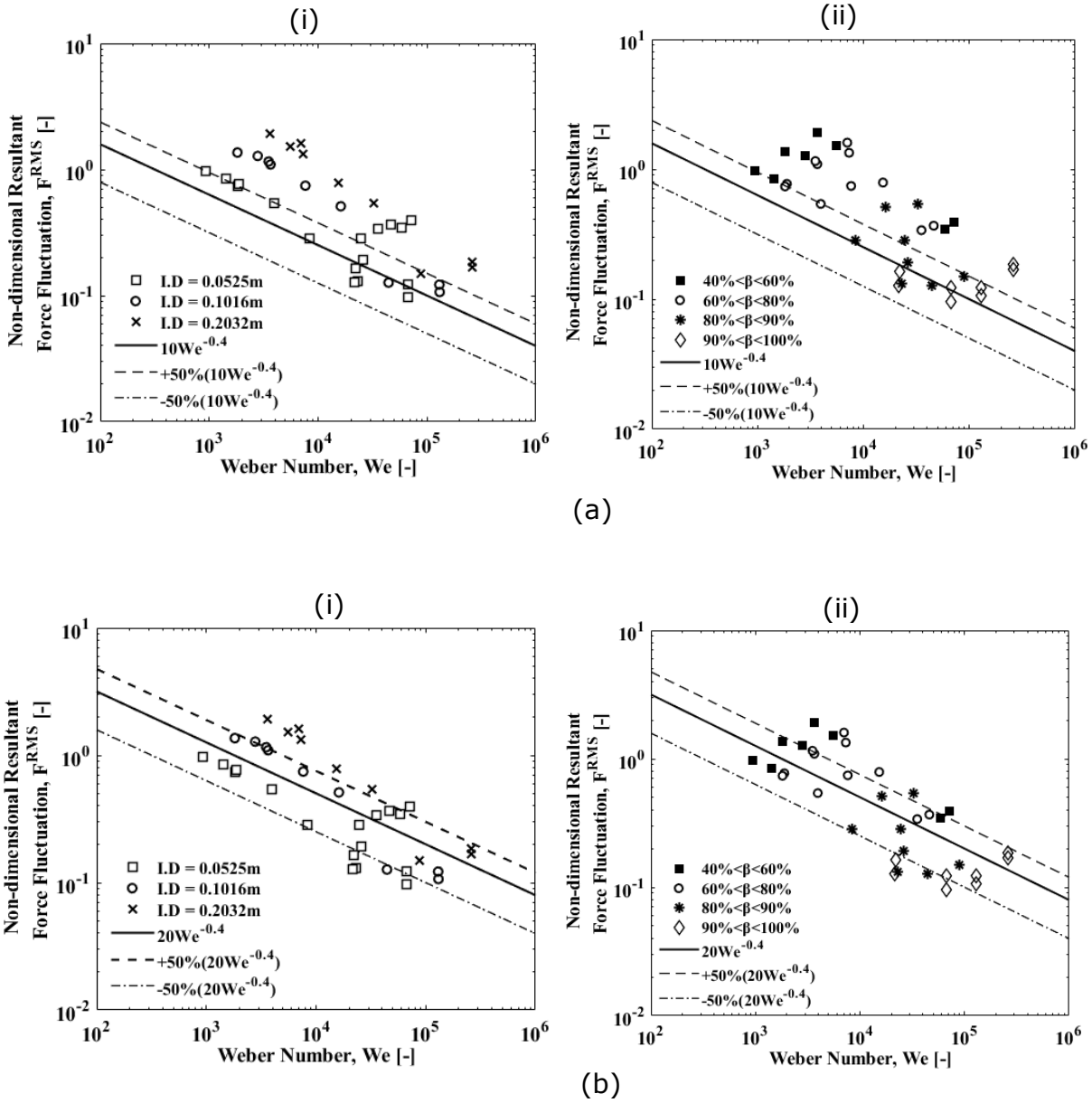

Figure 6.23: Comparison of RMS values of fluctuating forces with Riverin et al. (2006) correlation. The 17 cases of simulation data grouped according to volume fraction of gas.

As discussed in the preceding chapter, most of the present CFD predicted data in the small pipe of 0.0525m I.D fall within the $\pm 50\%$ accuracy margin of the correlation by Riverin et al. (2006). However, this is not the case for the two larger pipes. Figure 6.23 (a) (i) shows that close to 70% of the predicted data in the 0.1016m I.D fall outside the $\pm 50\%$ range while about 90% of predicted data in the 0.2030m I.D pipe fall outside the range. In addition, Figure 6.23 (a) (ii) in which

the predicted data have been grouped according to the global volume fraction β shows that pipe diameter has a stronger effect on $\overline{F_{rms}}$ compared to β. Generally, the correlation could not estimate about 50% of the combined 35 flow case studies across the three pipe sizes. The experimental findings by Belfroid et al. (2016a) for a large pipe of 0.1524m I.D match the present study findings. Most of their experimental data also fell outside the $\pm 50\%$ even for $40 < \beta < 80$ as was equally observed in the present study.

Therefore, the Riverin et al. (2006) was modified by adjusting the parameter C in the present study. This parameter is a function of the void fraction, ratio of liquid and gas densities, Weber number, Reynolds number and Froude's number. By fitting a slope to their measured result data which was plotted against Weber Number to be within $\pm 50\%$, they found the best fit for the parameter C, to be a constant value of 10. In literature, Cargnelutti et al. (2010) found the best fit for the constant C to be 3.51 for a pipe of I.D.=20.6mm while Belfroid et al. (2018) reported a range of 14 – 30 as the values of the constant for a pipe of 0.15m I.D. Hence, in the present study, C values of 15, 20 and 30 were initially tested to fit the result data set for pipes of three different I.D. Figures 6.23 (b) (i) and (ii) show that the modified correlation having constant C = 20 is able to estimate about 70% of the combined CFD/analytical predicted $\overline{F_{rms}}$ across the three pipe sizes within $\pm 50\%$ accuracy range.

CHAPTER 7

STRUCTURAL DYNAMICS AND MODAL ANALYSIS

The structural response in the form of stress fluctuations and total displacements of the pipe bends are presented and discussed in this chapter. The interaction between the magnitudes of force fluctuation and structural stress responses is also quantified based on pipe geometric scale for each flow regime case. The modal analysis is also presented for all pipe sizes with a discussion on the effect of the contained two-phase flow on the natural frequencies of the pipes. Finally, the risk of resonance is assessed by comparing the predominant frequencies of the characteristic fluctuations due to the two-phase flows to the natural frequencies of the pipe.

7.1 Equivalent (von-Mises) stresses, σ_e

Equivalent stress also known as von-Mises stress is an important stress value which is often used in design work to determine if a given material will yield or fracture. It is mostly used for ductile materials, such as metals. In practice, ductile materials exhibit higher resistances when subjected to arbitrary non-uniaxial stresses and tensions compared to resistances that could be observed if the same material is subjected to simple tension in laboratory experiments. Hence the maximum distortion energy theory involving the complete stress tensor was developed. This theory allows the arbitrary three-dimensional stress state to be represented as a single positive stress value known as equivalent stress or von-Mises stress. In the representation which is based on elasticity theory, the position of a minute element of material located randomly as part of a solid body can be adjusted such that only normal stresses will become present and all shear stresses seize to exist. The remaining three normal stresses called the principal stresses are given as:

σ_1 - Maximum

σ_2 - Middle

σ_3 - Minimum

Therefore, equivalent stress σ_e is given as:

$$\sigma_e = \left[\frac{(\sigma_1-\sigma_2)^2+(\sigma_2-\sigma_3)^2+(\sigma_3-\sigma_1)^2}{2}\right]^{1/2} \quad (7.1)$$

Then the von-Mises criterion states that a material will yield if the components of stress acting on it are greater than the simple tension yield stress limit of the material. This criterion is given as:

$$\sigma_e \geq S_y \quad (7.2)$$

where S_y is the simple tension elastic limit.

Therefore, equivalent stress represents an important parameter for quantifying the response of complex geometries due to loading. In the present study, the time history of the equivalent stress due to the fluctuating force at the pipe bend has been presented here. The calculated time signals of the flow induced force fluctuations presented in Chapter 5 for the small pipe of diameter 0.05252m and in Chapter 6 for the larger pipes of diameters 0.1016m and 0.2032m are applied to the inner surface of the elbow control volume within which the force predictions were based. Both the x-component and y-component of the force fluctuations were applied on the surface to produce a resultant effect of the combined forces. Figures 7.1 (a) shows the elbow control volume and the front view of the planes coinciding with the positions from which stress fluctuation signals were extracted for the three pipe sizes. The length b[m] in the figure have values of 0.2m, 0.4m and 0.6m for the pipes of I.D 0.0525m, 0.1016m and 0.2032m respectively. Figure 7.1 (b) presents the pipe cross section plane viewed from the pipe outlet to show the positions of stress evaluation. These positions are similar to the locations chosen by Yamano et al. (2011a) and Pontaza et al. (2013b) in their stress evaluations.

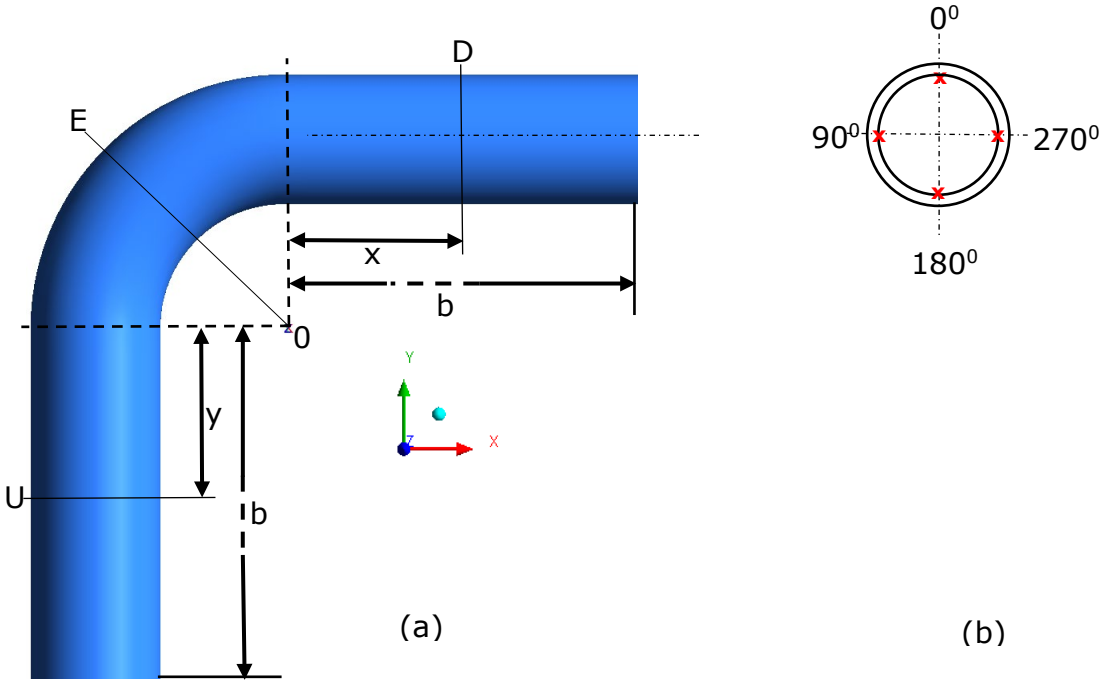

Figure 7.1: (a) Front view of the elbow control volume and (b) pipe cross section plane viewed from the pipe outlet to show the positions of stress evaluation.

Table 7.1: Positions of the planes from the elbow origin for each pipe.

S/N	Pipe I.D [m]	Plane U, y[m]	Plane E	Plane D, x[m]
1	0.0525	0.05	Angle 45^0 across the elbow	0.05
2	0.1016	0.1	Angle 45^0 across the elbow	0.1
3	0.2032	1.5	Angle 45^0 across the elbow	1.5

Figure 7.2 (a) – (h) present the time history of force induced stress fluctuations at the 0^0 and 180^0 positions at planes U, E and D in the pipe bend. The PSD of the stress fluctuations in the frequency domain are shown for the three 180^0 positions in Figure 7.3 (a) – (h). The 0^0 and 180^0 positions are respectively the extrados and intrados of the pipe. Figure 7.2 shows that higher stress fluctuation magnitudes were observed at the $E180^0$ and $E0^0$ positions compared to the other positions in the pipes of I.D 0.1016m and 0.2032m. Although, values at $E180^0$ were consistently higher in both pipes. On the other hand, higher stress fluctuations were observed at the $U180^0$ and $D180^0$ positions in the pipe of 0.0525m I.D.

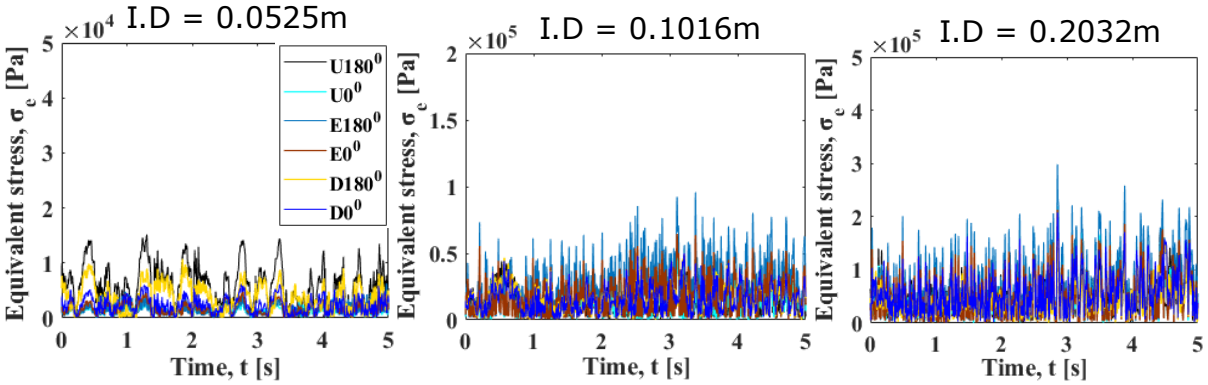

(a) Vsl=0.642m/s and Vsg=0.5m/s

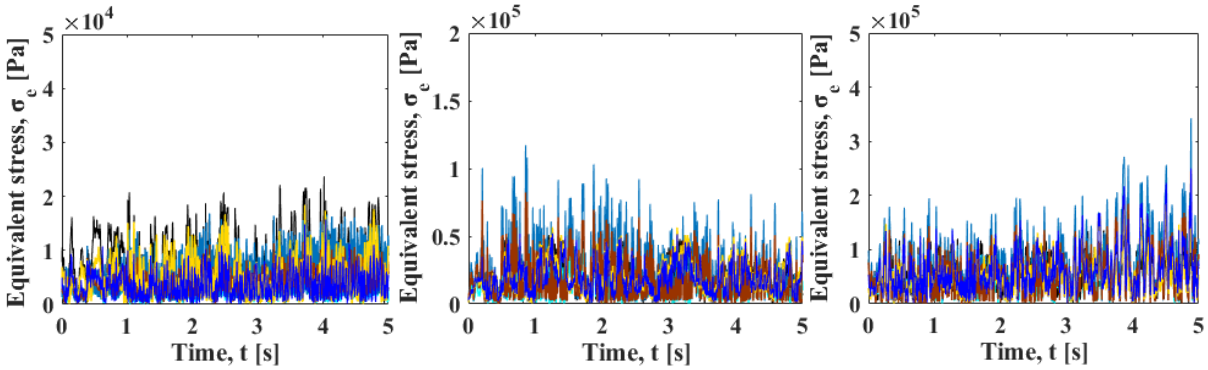

(b) Vsl=0.642m/s and Vsg=0.773m/s

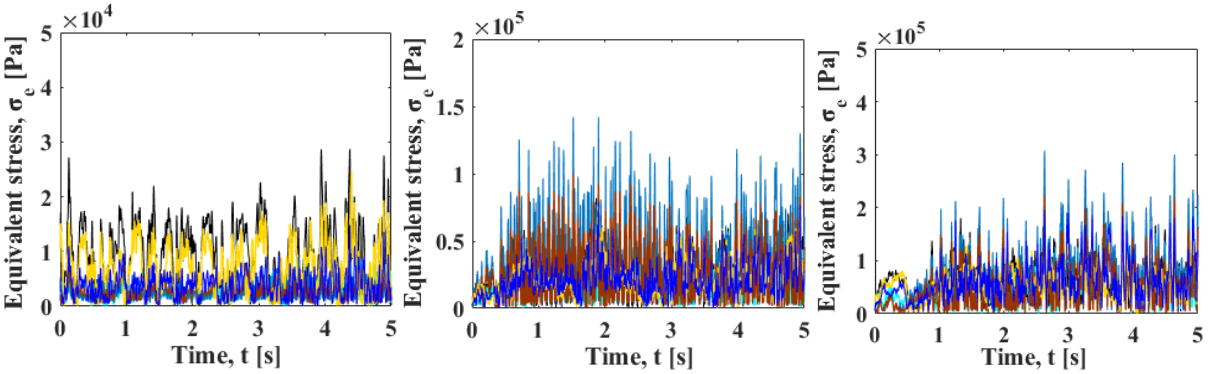

(c) Vsl=0.642m/s and Vsg=0.978m/s

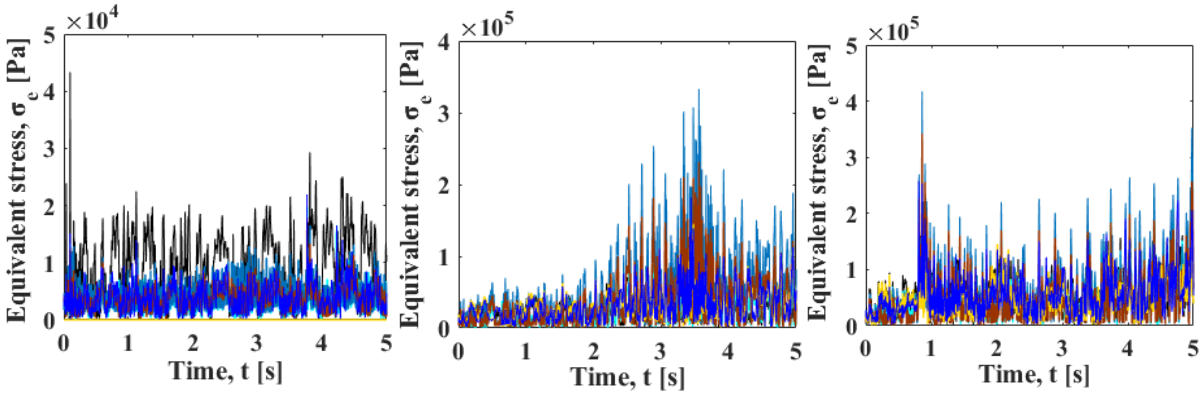

(d) Vsl=0.61m/s and Vsg=0.978m/s

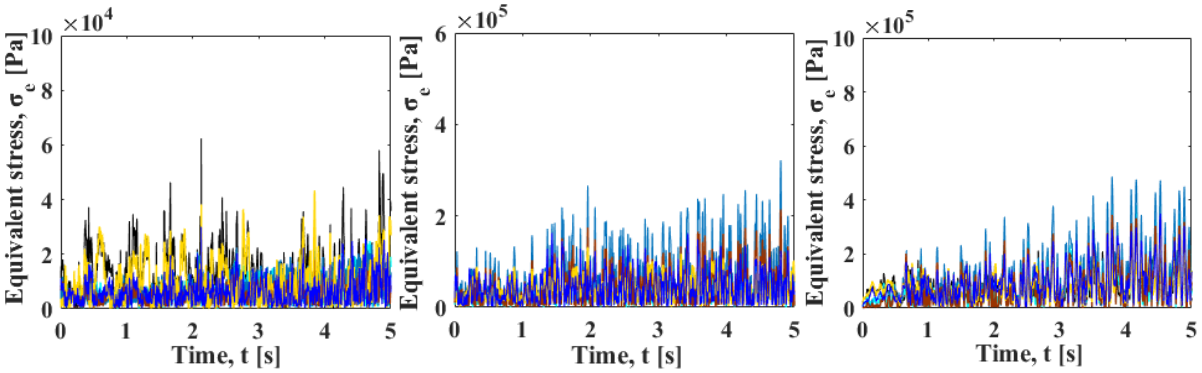

(e) Vsl=0.642m/s and Vsg=1.7m/s

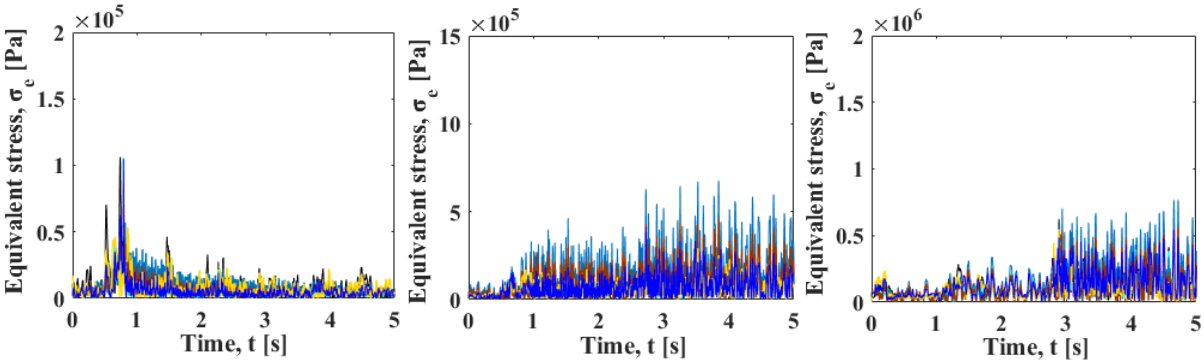

(f) Vsl=0.642m/s and Vsg=2.765m/s

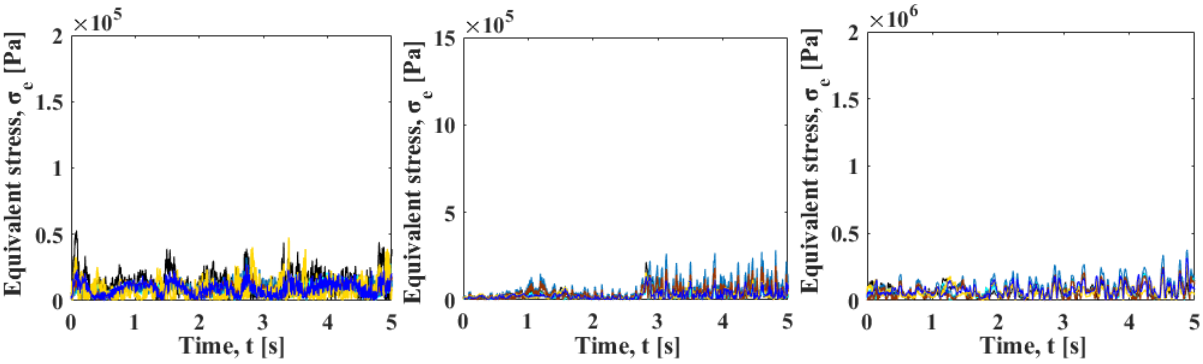

(g) Vsl=0.642m/s and Vsg=5m/s

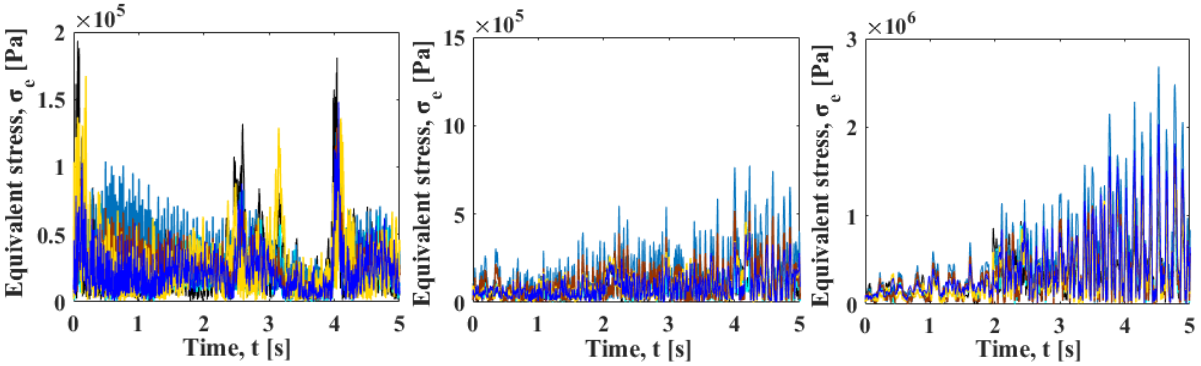

(h) Vsl=0.642m/s and Vsg=9.04m/s

Figure 7.2: Time histories of equivalent stress fluctuations due to the flow regimes (a) – (h) at the 0^0 and 180^0 positions at planes U, E and D for the three pipe sizes.

The stress fluctuation in Figure 7.2 (g) shows less fluctuation for the flow regime having Vsg of 5m/s compared to the preceding flow regime of Vsg = 2.765m/s (Figure 7.2 (f)) for the same Vsl of 0.642m/s. This observation is expected because the force fluctuation magnitudes in the flow of Vsg = 5m/s were equally observed to be lower than in the flow of Vsg = 2.765m/s as reported in the RMS of force fluctuations (Figure 6.21 (b)) and there is a strong feedback mechanism between equivalent stress response of the pipe structures and the flow induced force fluctuations. A consistent difference in the maximum stress fluctuation amplitude value of about 1-order of magnitude was also observed between the largest (0.2032m; 1.0 scale) and smallest pipes (0.0525m; ¼ scale) for all flow case studies.

Figures 7.3 (a) and (b) show the interaction of resultant force fluctuation and the equivalent stress response with pipe size, respectively. In the effort to develop models and correlations to predict MFIV in industrial scale pipework, it is crucial to establish the different relationships and interactions existing between characteristics properties of MFIV in laboratory scale pipes and the industrial scale pipes. Also, measurements of the amplitudes and frequencies of stress fluctuations are used to predict fatigue life of operational pipe works. Since the present pipes are geometrically similar, comparing their stress responses and the interaction with RMS of force fluctuation gives the accurate correlations that exist between the MFIV behaviours in small and large pipes. Hence using the ¼ scale as a

reference, Figure 7.3 (a) shows that the resultant force fluctuation RMS in the ¼ scale pipe increased by up to 1500% - 3000% in the pipe of 1.0 scale while Figure 7.3 (b) shows that the maximum amplitude of equivalent stress fluctuation increased by 500% - 2000%. On the other hand, the resultant force fluctuation RMS increased by a range of 200% – 600% in the ½ scale pipe while the maximum amplitude of equivalent stress response due to the resultant force increased by only 300% – 550%. Generally, the percentage increments in both stress and force dropped with increase in gas superficial velocity although it increased again in churn flow regime (Vsg = 9.04m/s). In addition, the increments in the ½ scale pipe from ¼ scale pipe is more gradual.

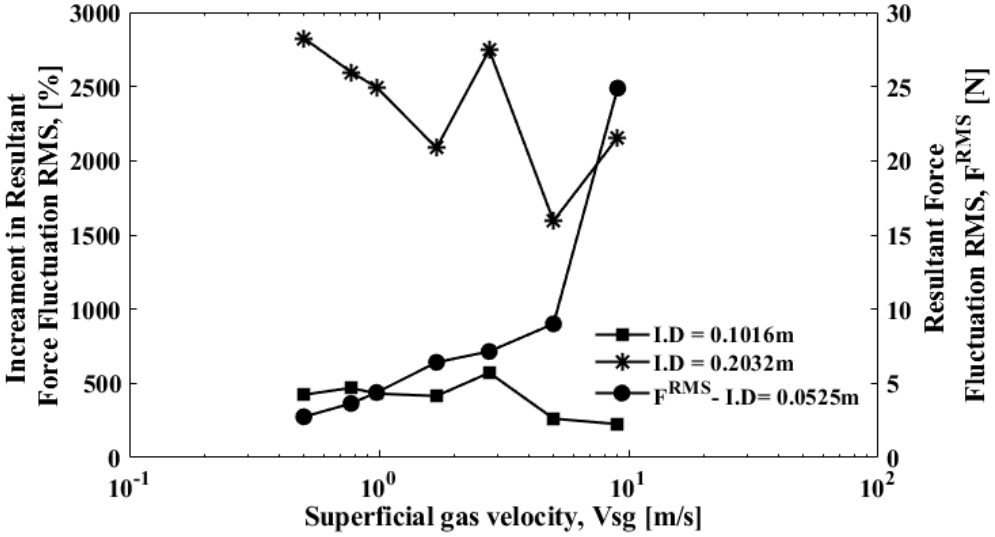

(a)

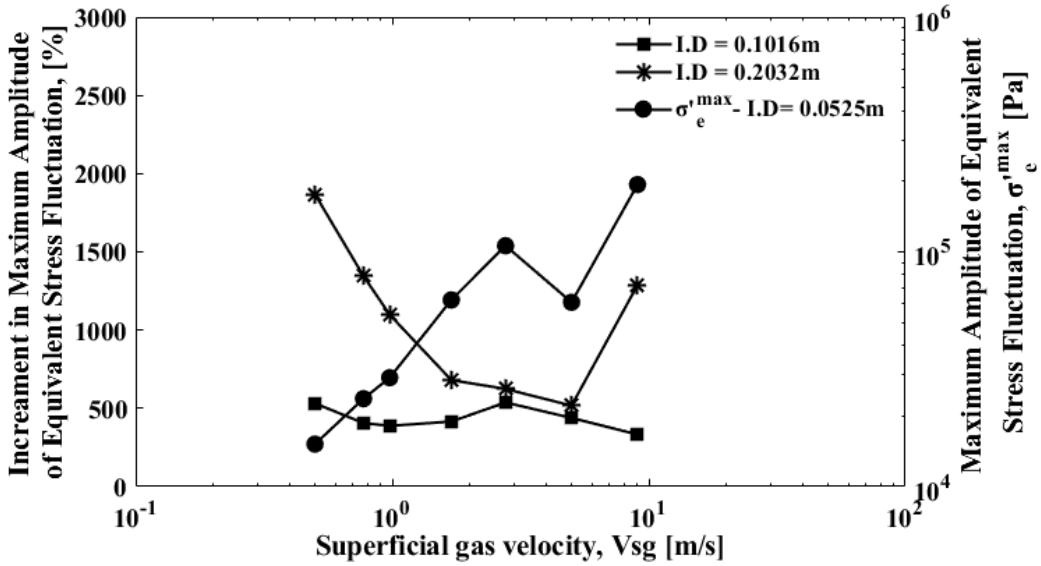

(b)

Figure 7.3: Interaction of (a) resultant force fluctuation RMS and (b) maximum amplitude of equivalent stress fluctuation with pipe diameter.

Figure 7.4 (a) - (h) show the frequency domain of the stress signals. Similar to the findings by Pontaza et al. (2013b), the significant frequencies generally spread over 0 – 80 Hz for all the pipe sizes. However, the frequency range in the 1.0 scale pipe did not exceed 60Hz.

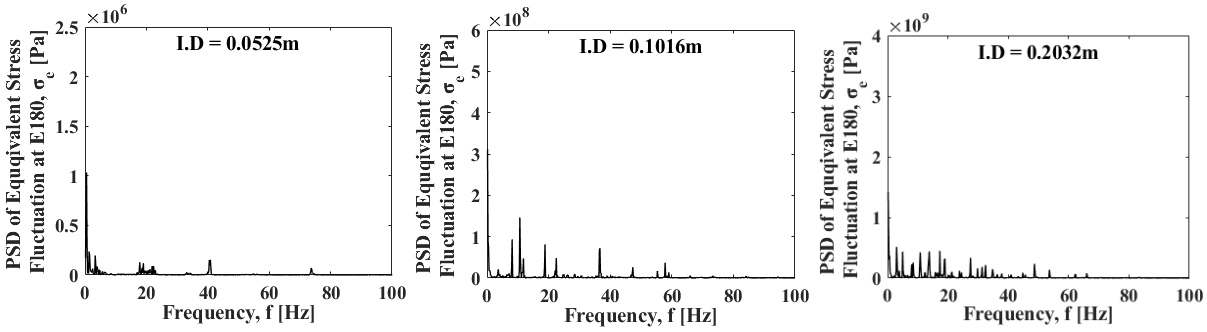

(a) Vsl=0.642m/s and Vsg=0.5m/s

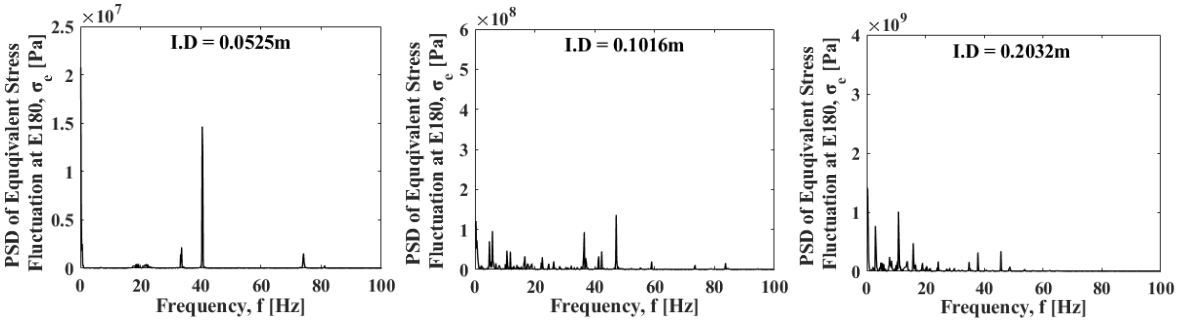

(b) Vsl=0.642m/s and Vsg=0.773m/s

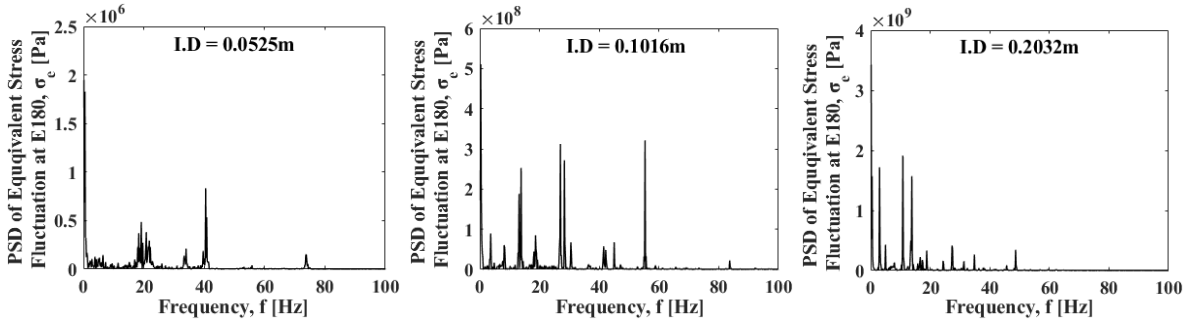

(c) Vsl=0.642m/s and Vsg=0.978m/s

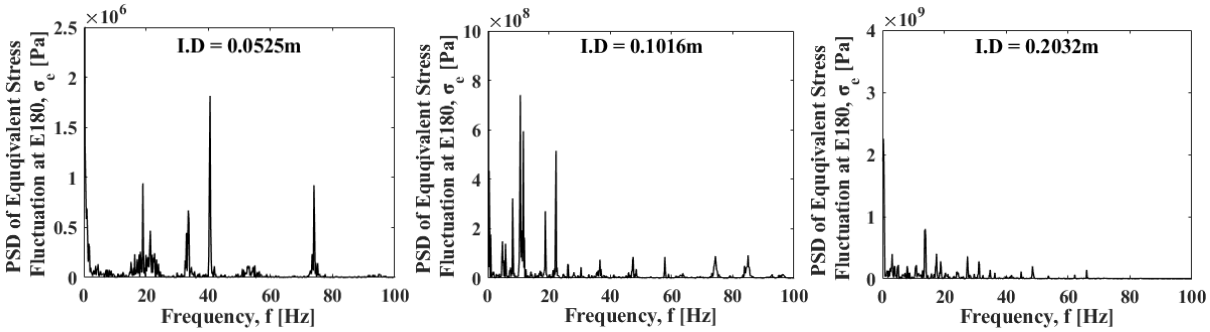

(d) Vsl=0.61m/s and Vsg=0.978m/s

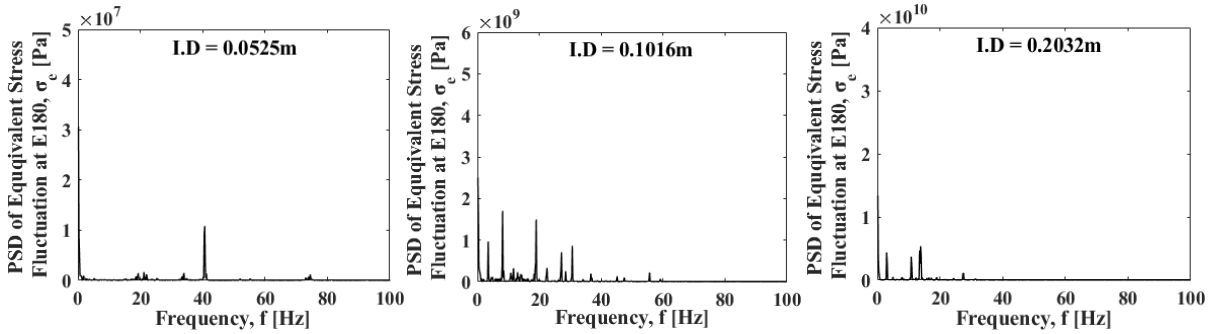

(e) Vsl=0.642m/s and Vsg=1.7m/s

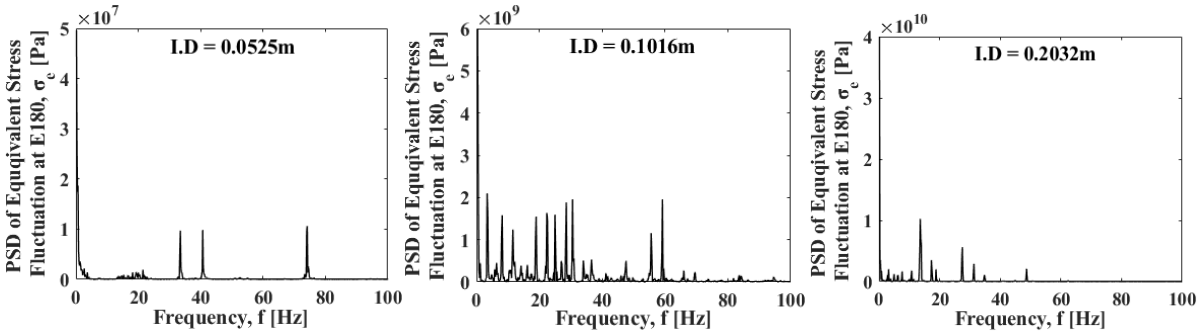

(f) Vsl=0.642m/s and Vsg=2.765m/s

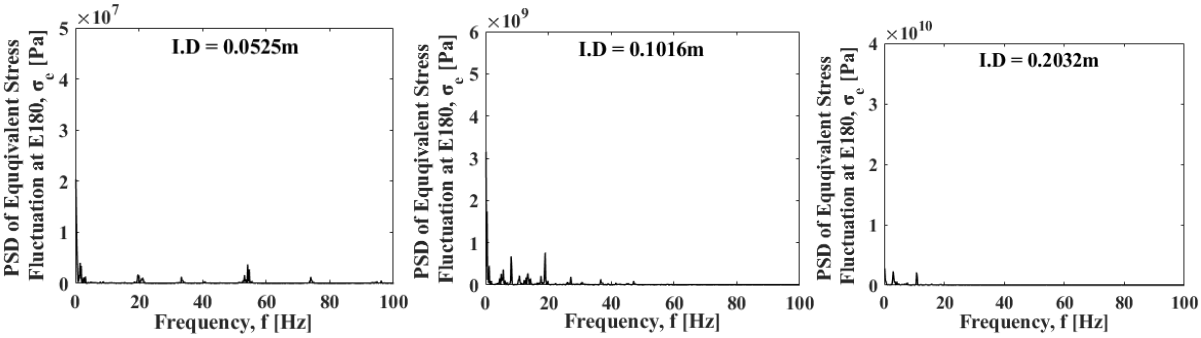

(g) Vsl=0.642m/s and Vsg=5m/s

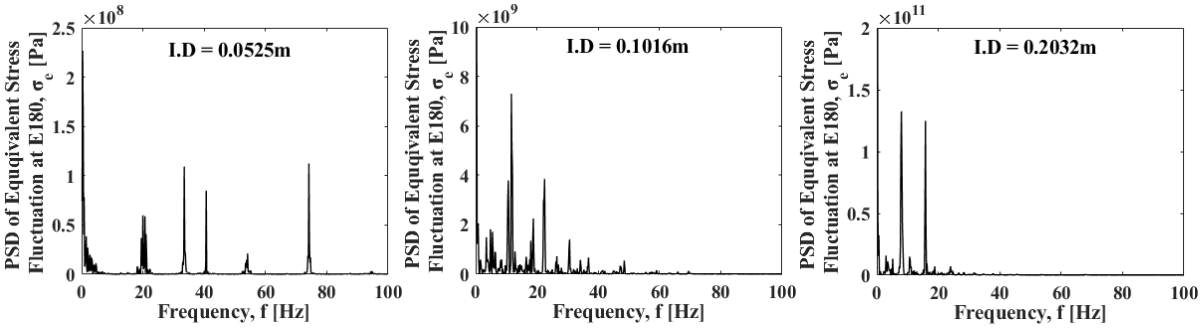

(h) Vsl=0.642m/s and Vsg=9.04m/s

Figure 7.4: PSD of stress fluctuations at E180^0 for the three pipe sizes.

Although the flow conditions and pipe material properties were exactly the same and the geometries were similar for the three different pipe sizes that has been studied, the behaviours seen in the PSD of the stress responses differ significantly. In the ¼ scale pipe, the dominant peaking frequencies of stress cycling were consistently 40Hz for the slug flows upto Vsg of 1.7m/s with the exception of $Vsg = 0.5m/s$ where predominant frequency was 1Hz. As the gas superficial velocity increased from 2.765m/s to 9.04m/s, the predominant frequencies were above 40Hz. On the other hand, predominant frequencies of stress cycling in the large

pipe (1.0 scale) were consistently below 20Hz for all the two-phase flow case studies that were simulated.

In the case of the ½ scale (0.1016 I.D.) pipe, the predominant frequencies did not show any consistent value or range of values for all flow case studies apart from the fact that the PSDs indicate more noise in the stress signal than is obtainable in the other two pipes. This observation also conforms to the random trend of the peak frequencies of F_x and F_y fluctuations shown in Figures 6.21 and 6.22 respectively. Hence, in practical industrial flowlines, extrapolating both quantitative and qualitative findings that were based on small laboratory scale experiments or numerical/analytical simulations to large scale flowlines will give erroneous design specifications. This could lead to either costly over engineering or less than optimum designs and monitoring procedures which would also be prone to costly and hazardous failures. However, a more replicable trend was observed in the stress fluctuation energy. The maximum PSDs in the 1.0 scale pipe were generally about 3-orders of magnitude higher than the maximums in the ¼ scale pipe and only about 1-order of magnitude higher than the corresponding values in the ½ scale pipe.

7.2 Pipe deformation

The calculated total pipe deformation is a resultant of the direction deformations in the x and y directions. Figures 7.5 (a) – (h) show the total distance of the pipe deformation for all flow cases. The signals are used to assess the level of vibration of the pipe. The total deformation increased from 0.0001m to 0.0015m in the pipe of 1.0 scale as the gas superficial velocity increased from 0.5m/s (slug/cap bubbly flow) to 9.04m/s (churn turbulent flow). In the ½ scale pipe, the total deformation increased from 0.00002m to 0.0002m as the gas superficial velocity increased. On the other hand, the increase was from 0.000001m to 0.00001m in the small pipe (¼ scale).

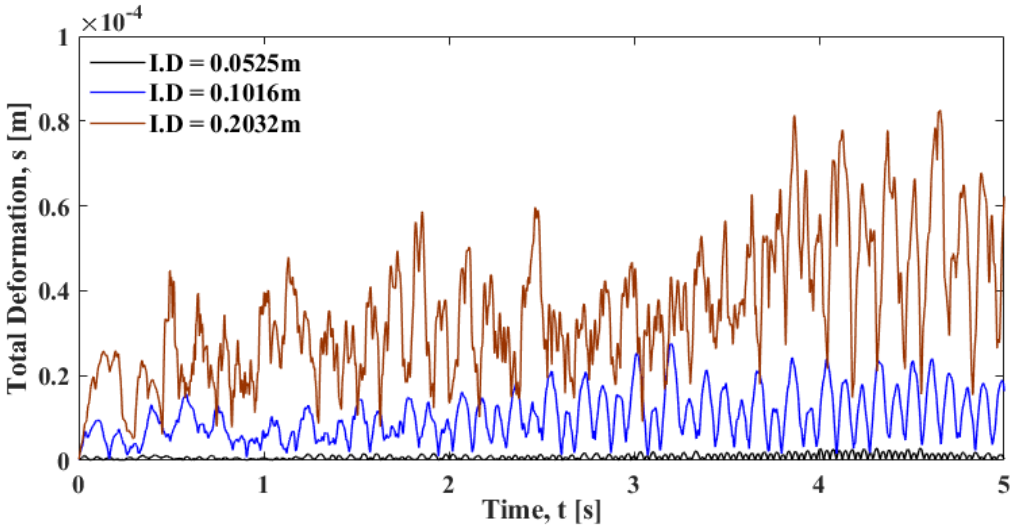

(a) Vsl=0.642m/s and Vsg=0.5m/s

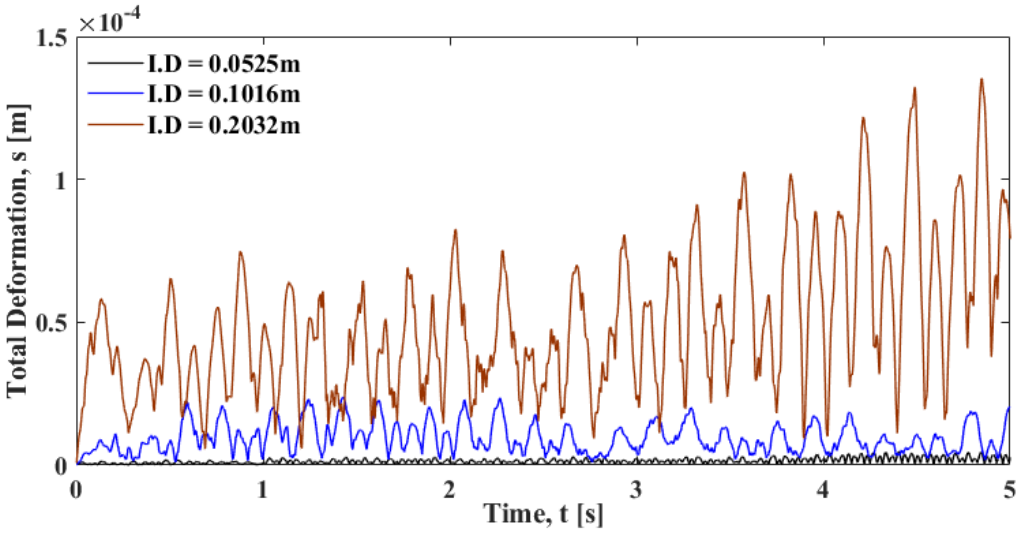

(b) Vsl=0.642m/s and Vsg=0.773m/s

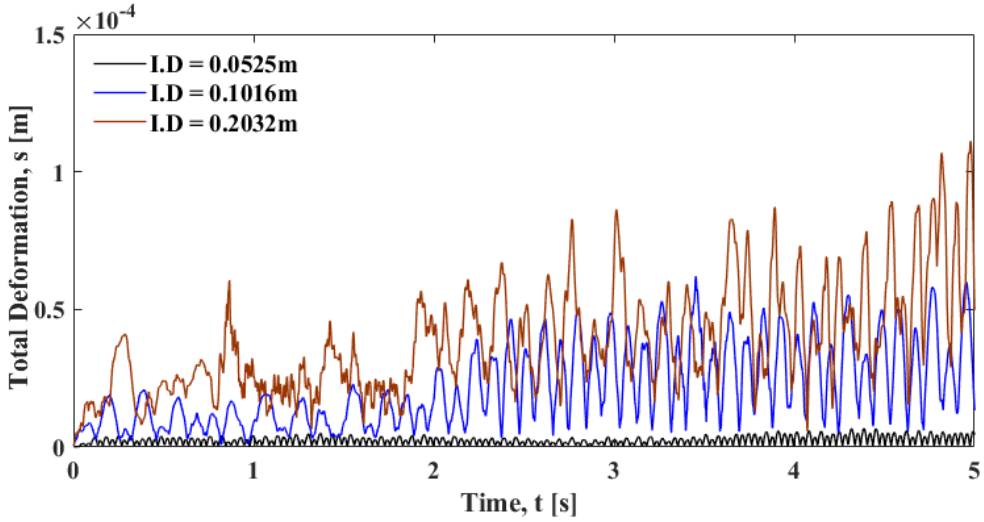

(c) Vsl=0.61m/s and Vsg=0.978m/s

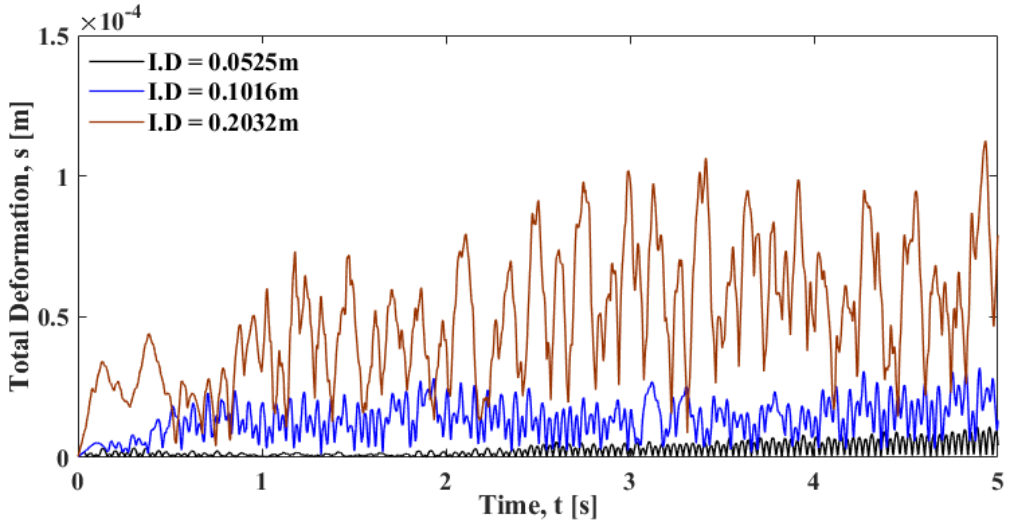

(d) Vsl=0.642m/s and Vsg=0.978m/s

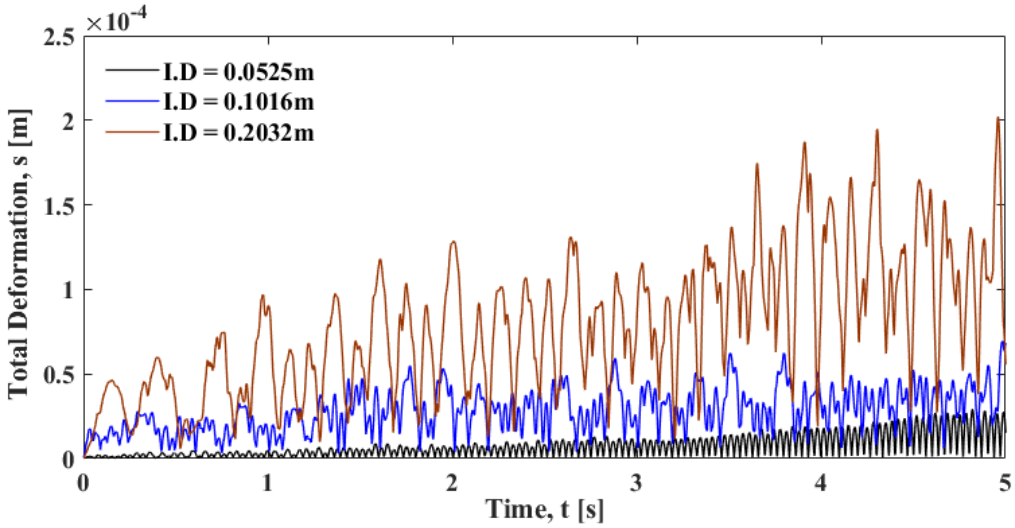

(e) Vsl=0.642m/s and Vsg=1.7m/s

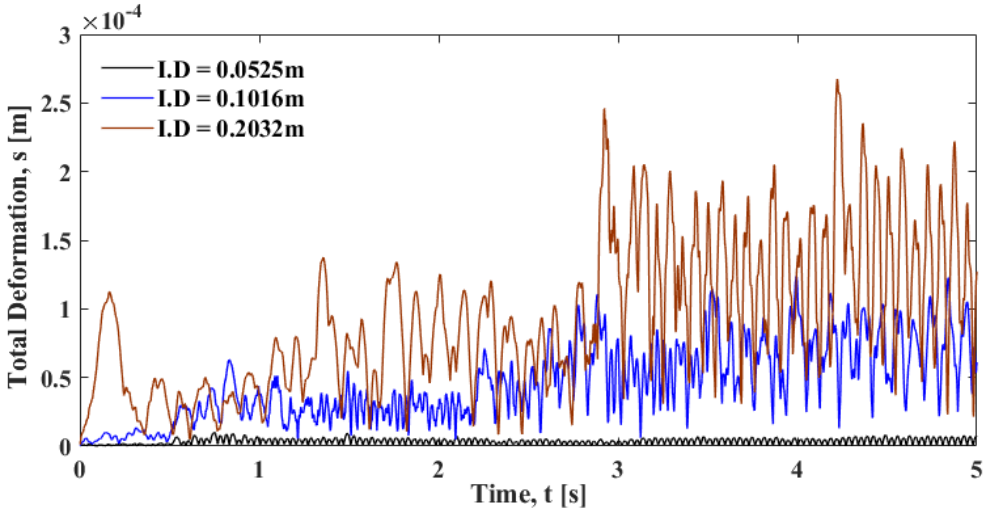

(f) Vsl=0.642m/s and Vsg=2.765m/s

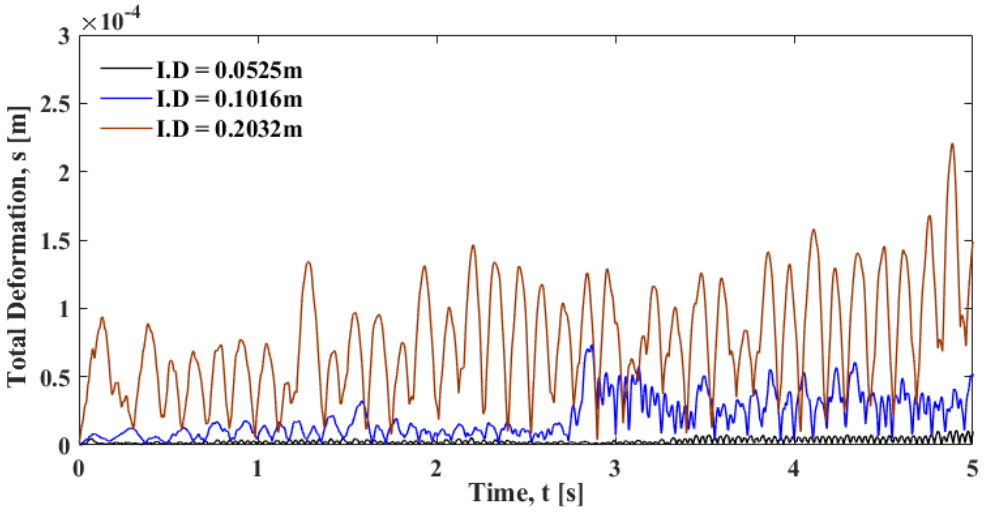

(g) Vsl=0.642m/s and Vsg=5m/s

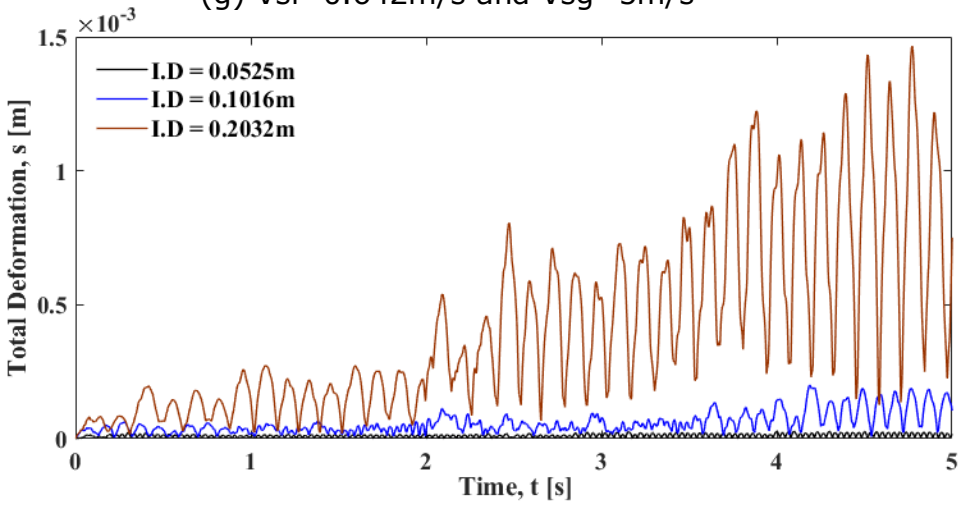

(h) Vsl=0.642m/s and Vsg=9.04m/s

Figure 7.5: Total deformation signal for the three pipe sizes due to each flow regime.

The PSDs of the total deformation signals are shown in Figures 7.6 (a) to (h). The most important frequency in the ¼ scale pipe is ~30Hz while the dominant frequency range in the largest pipe was 7.83Hz apart from the flow case having V_{sg} andV_{sl} = 0.978m/s and 0.61m/s respectively in which case 13.83Hz was observed as dominant frequency. The trends are also similar to observed predominant frequency of stress cycles were the ¼ scale pipe showed the maximum predominant frequency while the largest pipe of 1.0 scale showed the lowest range of predominant frequency. In addition, the dominant frequency in the ½ scale pipe only showed consistent value of approximately 11Hz for flow case

studies with V_{sg} given as 0.5m/s, 0.978m/s (V_{sg}=0.61m/s), 5m/s and 9.04m/s. The rest values in the ½ scale pipe were more or less random as seen in the predominant frequencies of the stress circles.

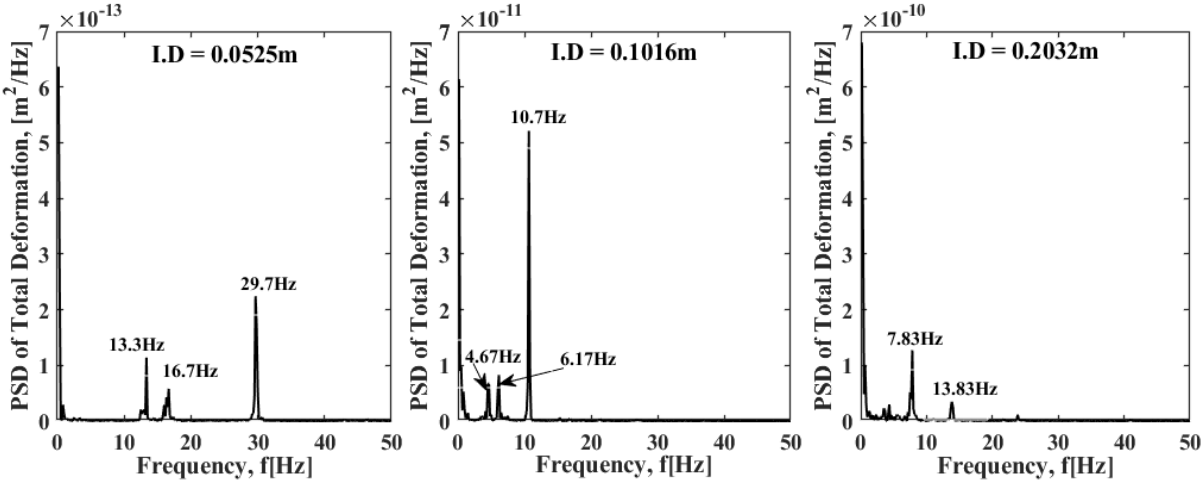

(a) Vsl=0.642m/s and Vsg=0.5m/s

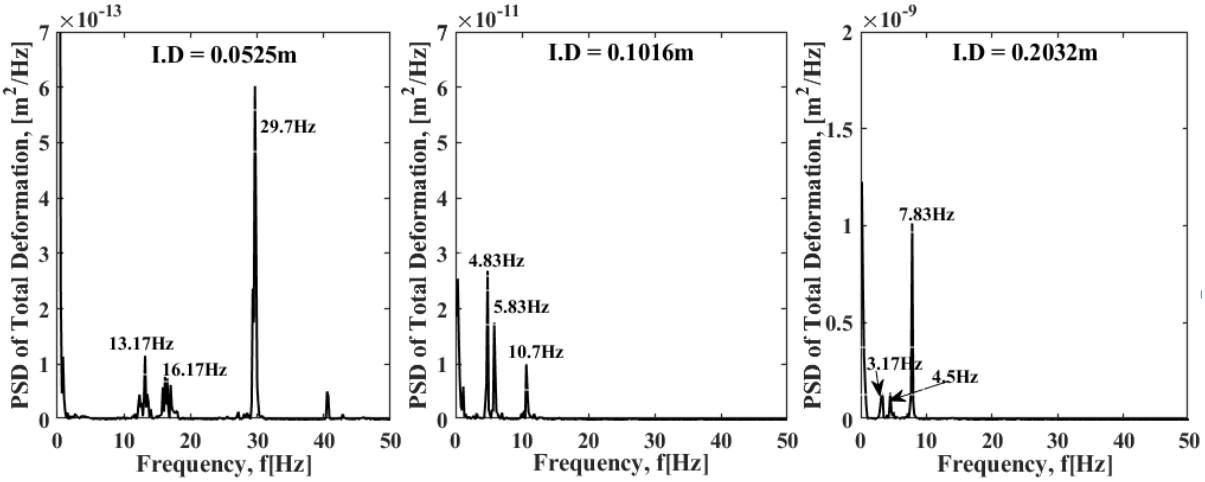

(b) Vsl=0.642m/s and Vsg=0.773m/s

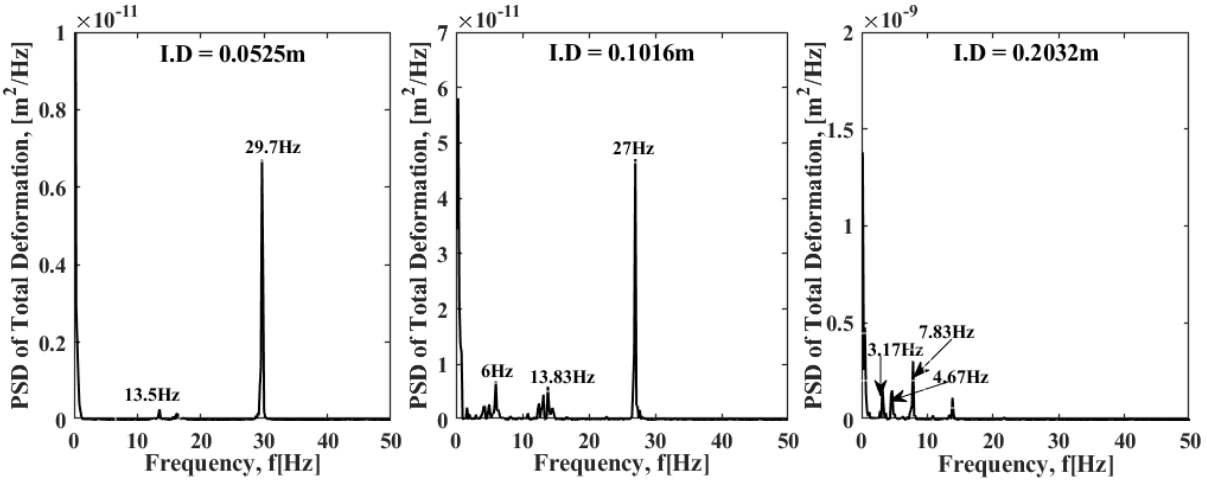

(c) Vsl=0.642m/s and Vsg=0.978m/s

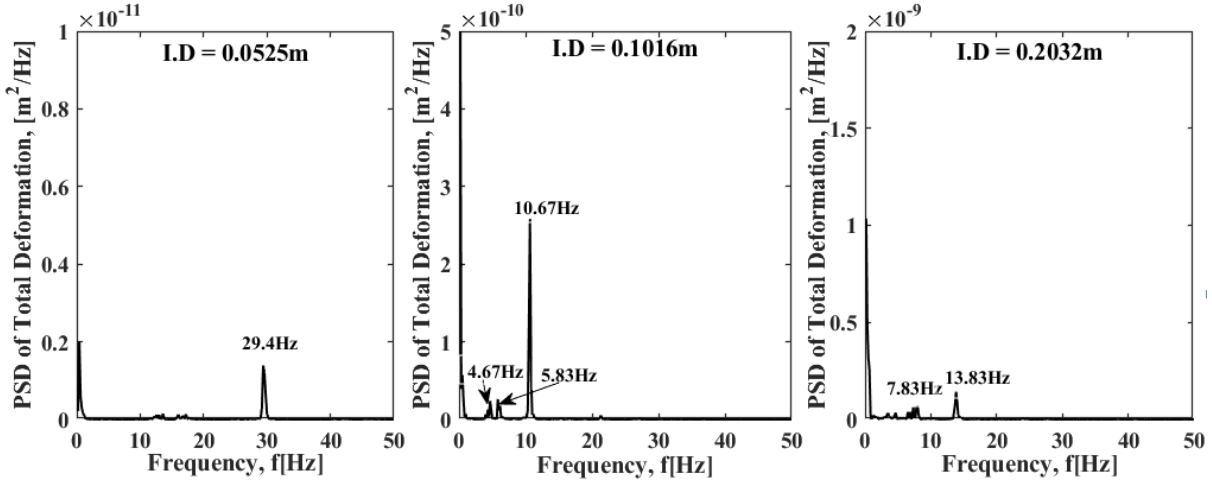

(d) Vsl=0.61m/s and Vsg=0.978m/s

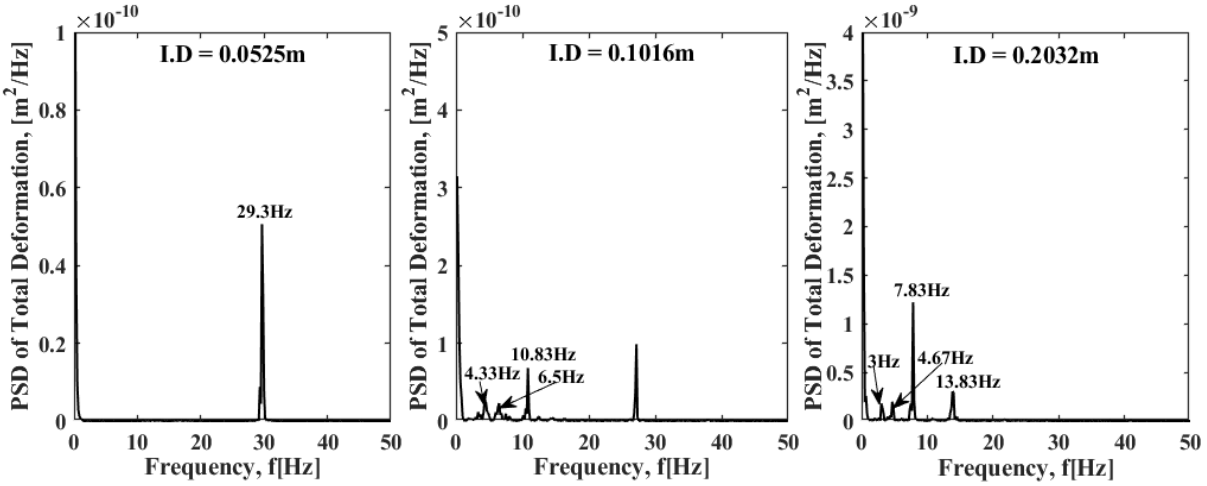

(e) Vsl=0.642m/s and Vsg=1.7m/s

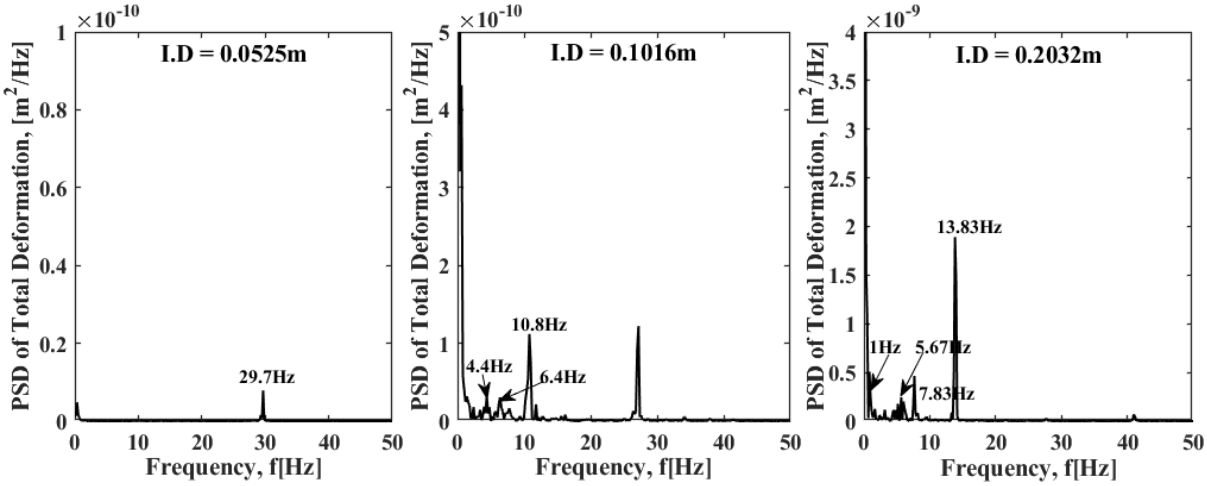

(f) Vsl=0.642m/s and Vsg=2.765m/s

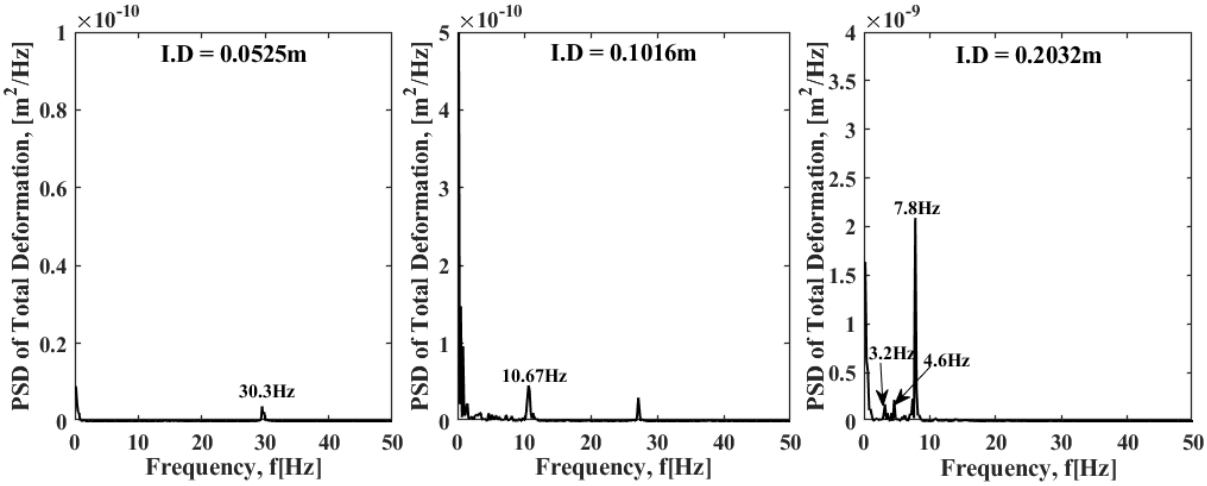

(g) Vsl=0.642m/s and Vsg=5m/s

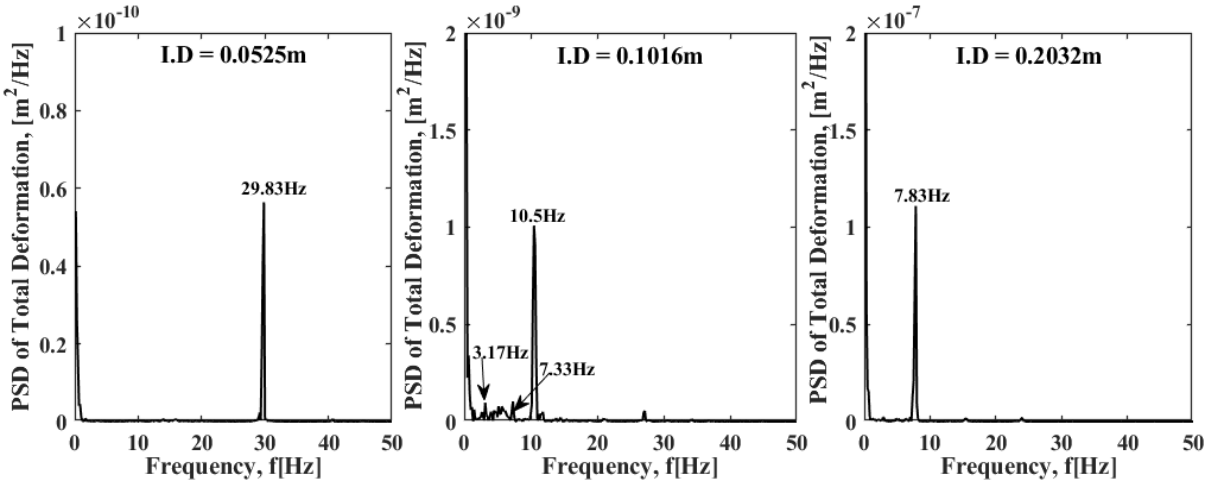

(h) Vsl=0.642m/s and Vsg=9.04m/s

Figure 7.6: PSD of total deformation signal for the three pipe sizes due to the each flow regime ((a) – (h)) and showing the prominent frequency peaks

7.3 Modal analysis

Figures 7.7 – 7.9 present the natural frequencies of the three similar pipe sizes. In the present analysis, the added mass effect due to contained fluid is captured by defining the global volumetric gas fraction at the pipe inlet. Generally, as the gas fraction increased corresponding to increasing gas superficial velocities, the natural frequencies of the first 3 modes of vibration increased approaching the natural frequencies of the pipes in cases where they didn't contain any fluid, β = 0. Wang et al. (2018) also reported that increasing gas volume fraction of inlet had similar effect on the first three natural frequencies of an acrylic material pipeline riser of 0.0514m I.D and thickness of 0.0058m conveying gas-liquid two-phase flow.

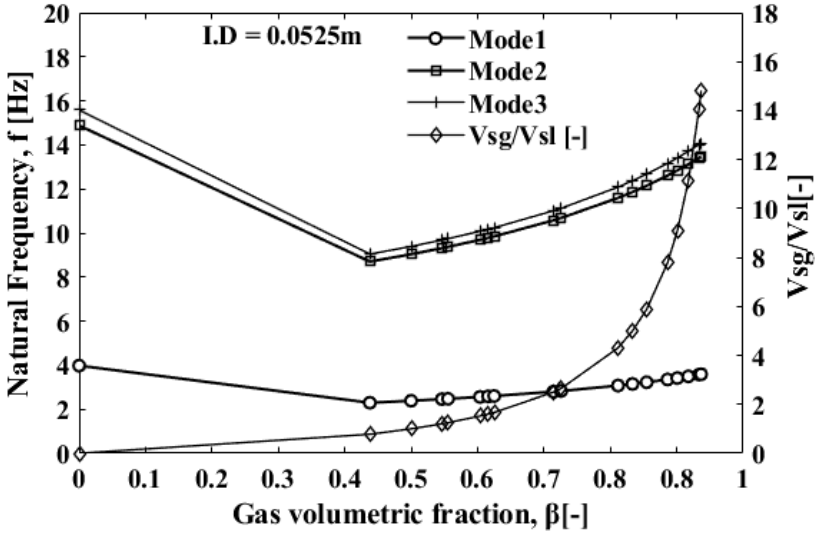

(a)

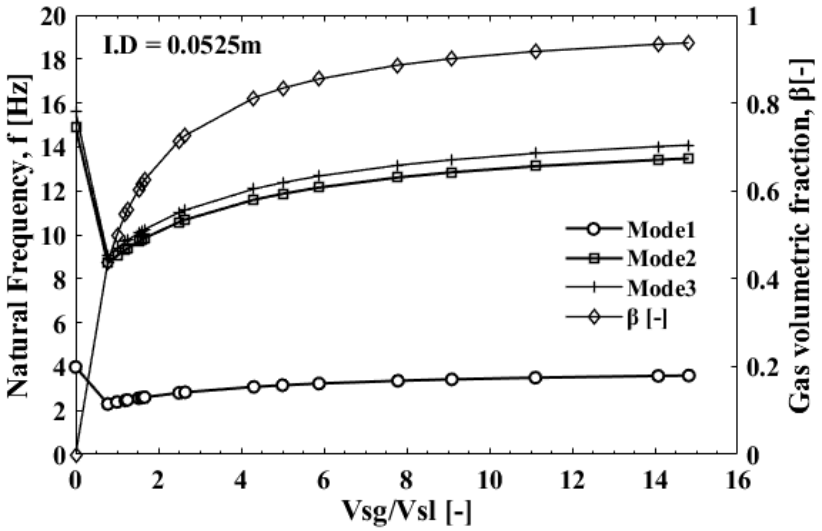

(b)

Figure 7.7: The effect of gas volume fraction at inlet and the ratio of superficial velocities on the natural frequencies of the pipe (I.D = 0.0525).

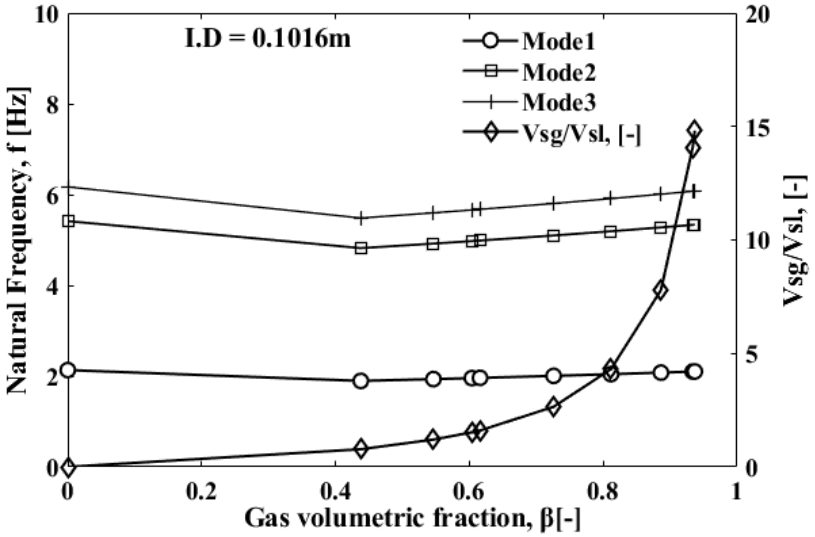

Figure 7.8: The effect of gas volume fraction at inlet and the ratio of superficial velocities on the natural frequencies of the pipe (I.D = 0.1016).

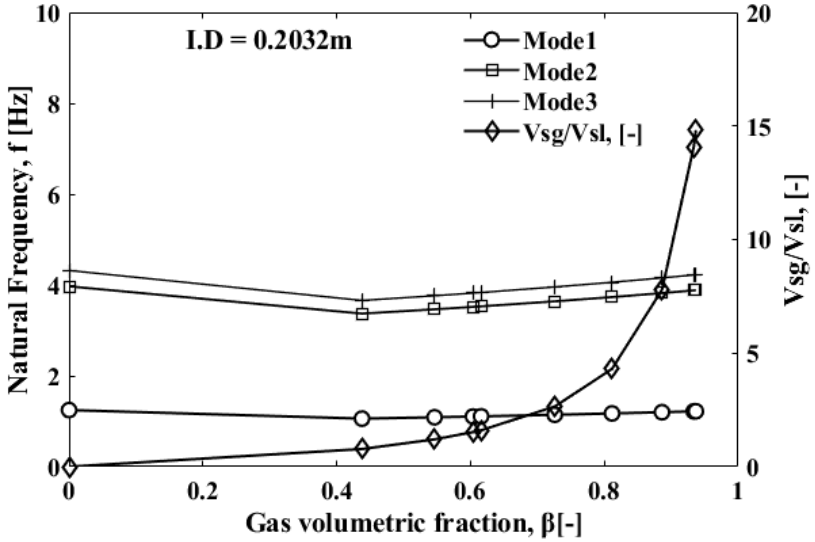

Figure 7.9: The effect of gas volume fraction at inlet and the ratio of superficial velocities on the natural frequencies of the pipe (I.D = 0.2032).

However, the increase in natural frequencies with gas superficial velocities were more significant in the smallest pipe of ¼ scale than the ½ and 1.0 scale pipes. Frequencies as low as 1Hz were recorded in the 1.0 scale pipe while the lowest frequency in the ½ scale pipe is ~2Hz.

7.3.1 Resonance risk assessment and comparison

Figures 7.10 to 7.12 present the comparison of the first three natural frequencies of the pipe bends with fixed supports representing Modes 1 – 3 as a function of gas superficial velocity and the dominant frequencies of force fluctuation and pipe total deformation. This discussion ultimately aims to assess the risk of resonance in pipes of similar geometry, subjected to the exact same internal multiphase flow conditions but having different size scales. The 1st, 2nd and 3rd level dominant frequencies of pipe deformation used in these figures represent the prominent peak frequencies shown in the PSD plots of the total deformation signal.

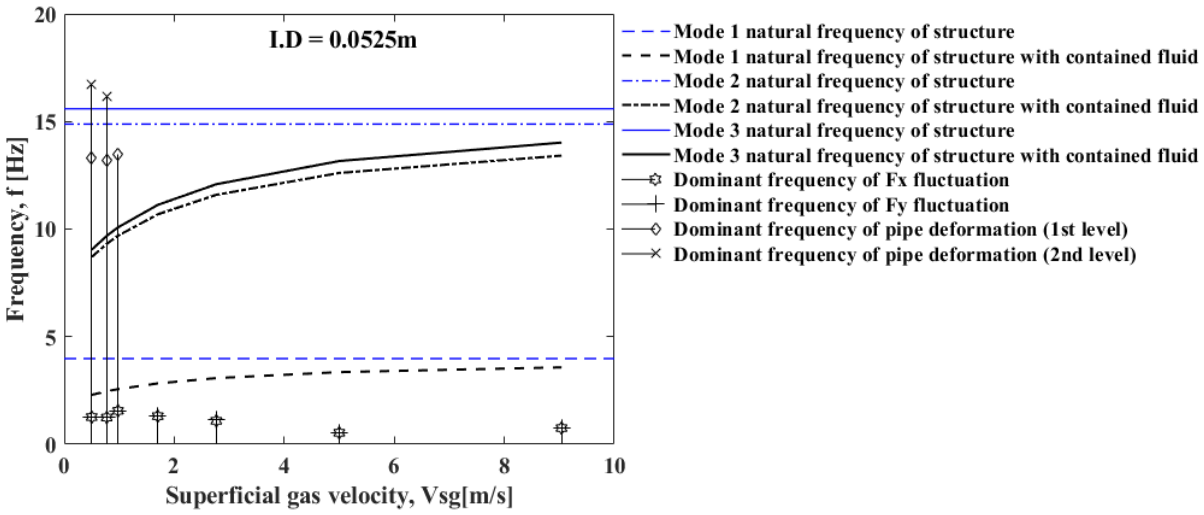

Figure 7.10: Comparison of the natural frequencies of pipe structure to the dominant frequencies of force fluctuation and pipe total deformation (1/4 scale).

None of the dominant frequencies overlap the first three natural frequencies of the pipe with and without contained fluid in the ¼ scale pipe. However, Figures 7.11 show that the 1st and 2nd levels of the dominant frequencies of pipe deformation overlap the 2nd and 3rd natural frequencies in the ½ scale pipe. The frequency matching occurred within the moderate slug flow regime up to gas superficial velocity of 0.978m/s.

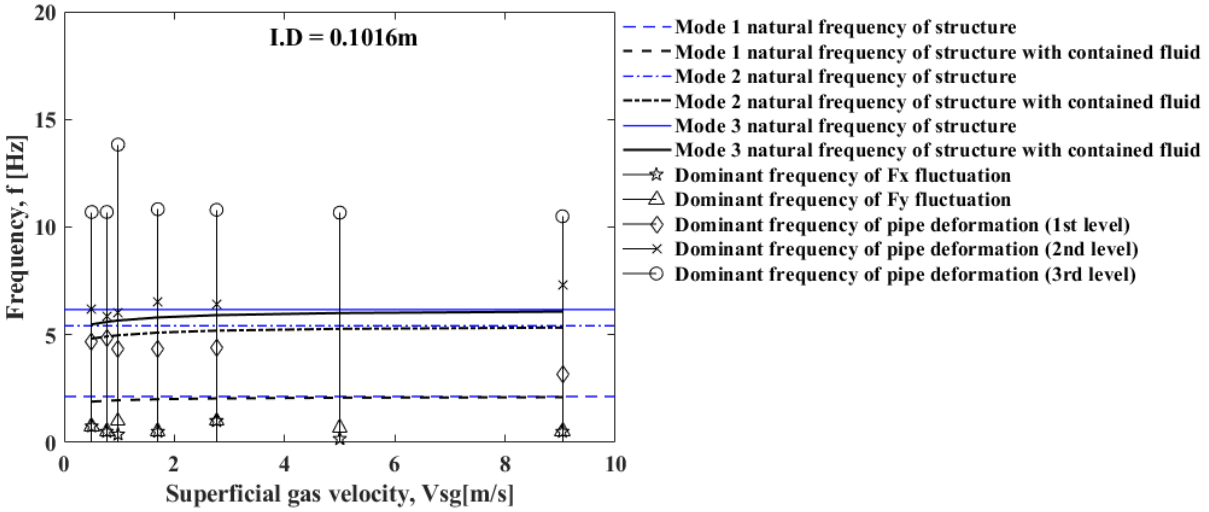

Figure 7.11: Comparison of the natural frequencies of pipe structure to the dominant frequencies of force fluctuation and pipe total deformation (1/2 scale).

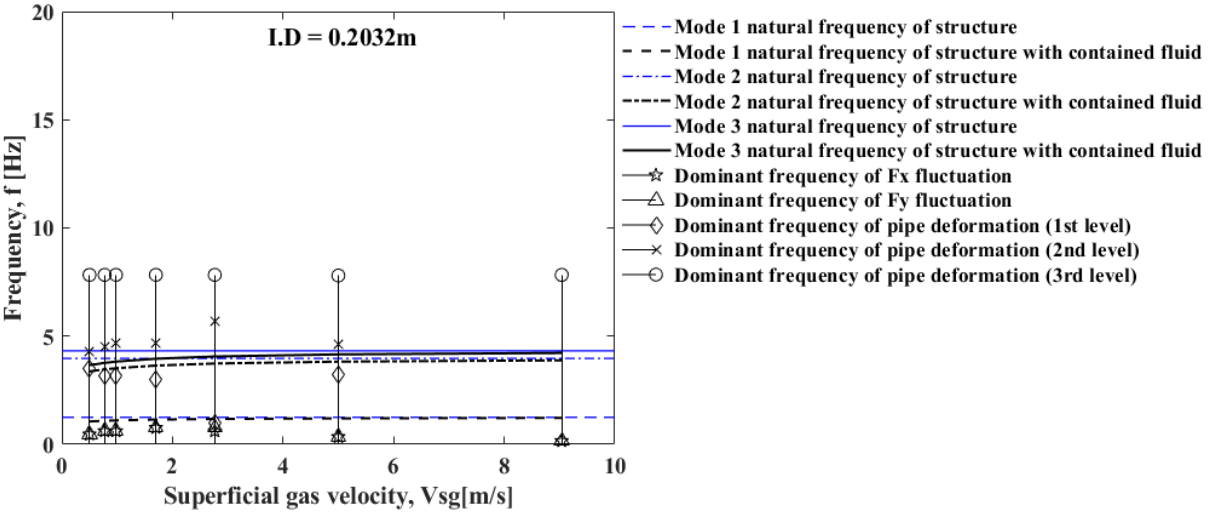

Figure 7.12: Comparison of the natural frequencies of pipe structure to the dominant frequencies of force fluctuation and pipe total deformation (1.0 scale).

Figure 7.12 shows that the 1.0 scale pipe present the highest resonance occurrence risk since both the dominant frequency of force fluctuation and pipe deformation overlap the first three natural frequencies of the pipe structure. The dominant frequencies of force fluctuation coincided with the first natural frequency of the pipe structure with and without contained fluid at gas superficial velocities

of 1.7m/s and 2.765m/s. The 1st and 2nd level dominant frequencies of pipe deformation coincided with the 2nd and 3rd natural frequencies of the pipe structure as well even at gas superficial velocity of 5m/s.

In summary, although the risk of resonance in the ¼ scale is unlikely, the high frequency stress circles observed in Figure 7.6 could also reduce the fatigue life of the structure. Conversely, the risk of resonance is high in the ½ scale pipe and higher in the 1.0 scale pipe. It was also observed that the only risks of resonance occurred within slug/cap bubbly and churn turbulent flow regimes up to V_{sg} of 5m/s. No risk at all existed at V_{sg} = 9.04m/s for all pipe sizes. Hence for pipes of similar geometry and the same internal multiphase flow conditions within slug-churn flow regimes, risk of resonance increased with pipe scale when matched with the first three natural frequencies of the pipe structure.

CHAPTER 8

CONCLUSION AND RECOMMENDATIONS FOR FURTHER WORK

8.1 Conclusions and contributions to development of industry standard

This project has developed an integrated high-fidelity CFD and FEA based numerical-analytical modelling framework for predicting the defining characteristics of MFIV in pipes of different sizes especially in cases where experimentation is impossible. The CFD simulations of slug, cap bubbly, churn and churn turbulent flow induced fluctuations at 90^0 pipe bend have been carried out using the volume of fluid (VOF) model for the two-phase flows and the $k-\epsilon$ model for turbulence modelling. Flow induced forces at the bend were calculated by carrying out momentum balance at the bend using the time signals of void fraction, velocity and pressure that were obtained from the simulation. Then the calculated time signal of flow induced forces were applied to the pipe structure in a one-way transient structural FEA analysis to predict the structural response in terms of equivalent (von-Mises) stress and displacement. Modal analysis was also carried out to obtain the natural frequencies of the pipe, investigate the effect of contained slug-churn flow regime on the natural frequencies and establish the risk of resonance.

In the process of carrying out this work, some important correlations and relationships were established between the defining characteristics of slug-churn flow and the resulting flow induced fluctuations due to such flows. Furthermore, very significant findings in this study included the establishment and quantification of correlating behaviours between small laboratory scale pipe bends and industry large scale pipe bends. This contribution is significant because based on the results of this study, experimental data that are based on small scale pipes can be used to estimate MFIV behaviours in scaled-up geometrically similar pipes of practical sizes. Initial investigations in this study focused on characterising the slug and churn flow induced forces on a 90^0 pipe bend of 0.0525 I.D. pipe represented as ¼ scale size in comparison with the larger pipes that were further investigated. The simulation results were compared with reported experiment data of time series of volume fraction and excitation forces and the results showed a very good

conformation of CFD results with experimental data. The findings in this study include:

1. The simulation results based on the 0.0525m I.D (1/4 scale) pipe show that the peak gas volume fraction frequency varies between 0.5–9 Hz with the values decreasing with the increase of superficial gas velocity, and increasing with the increase of superficial liquid velocity in the slug flow regimes. The gas volume fraction fluctuation frequencies drop as the flow approaches the transition boundary from slug flows to annular or bubbly flow. The frequency of gas volume fraction fluctuations is broadband and spreads over 30 Hz.

2. Also, in the ¼ scale pipe, the simulated time domain signal of forces for churn flow and its frequency domain PSD matched well with the experiment data. The peak frequency of the fluctuations of force varies between 0.5–1.7 Hz and drops with the increasing superficial gas velocity. The frequency of fluctuations of force spreads below 10 Hz and contrary to volume fraction fluctuations, the RMS of force fluctuations increases with the superficial gas velocity. With the increase of superficial liquid velocity, the peak frequency of fluctuations of force varies between 1–7 Hz and increases initially before dropping at higher superficial liquid velocity as the flow approaches bubbly flow. The PSD of fluctuation of force spreads over 20 Hz with the increase of superficial liquid velocity. The RMS of force fluctuations increases with the increase of superficial liquid velocity. It can be concluded that the increase of gas fraction narrows the range of frequency ranges, while increasing the liquid expands the frequency ranges of force fluctuations.

3. The CFD simulation technique using VOF multiphase model and $k-\epsilon$ turbulence model was able to reproduce the effect of Taylor instability on large bubbles in the slug and cap bubbly flow regimes flowing through larger ½ (0.1016m I.D) and 1.0 (0.2032m I.D) scale pipes. Both the slug length and cross-sectional area were lower in the 1.0 scale pipe having $\mathrm{D}_{\mathrm{H}}^{*}$ of 74.5.

4. The PSD of void fraction fluctuation showed higher fluctuation energy in the ½ scale pipe compared to the 1.0 scale for gas superficial velocities of 0.5

– 1.7m/s. Further increase in gas superficial velocity towards churn flow regime showed higher fluctuation energy in the larger pipe of 1.0 scale except at Vsg and Vsl pair of 9.04m/s and 0.61m/s respectively. In both pipes, the fluctuation frequency range was 0 – 4Hz and this range dropped significantly in churn flow regime. The interaction between the peak frequencies of void fraction fluctuation and gas superficial velocity is similar for both the ¼ and 1.0 scale pipes. The peak frequencies in both cases increased as gas superficial velocity increased from 0.5m/s to moderate slug flow regime and then dropped as the flow transited to churn flow regime. On the other hand, an irregular interaction was observed for the ½ scale pipe within the slug flow regime while a decreasing trend similar to the other two pipes was observed as the flow regime transited to churn flow from gas superficial velocity of 2.765m/s to 9.04m/s. Peak frequency values were within 0.1 – 0.8 Hz for the largest scale pipe and within 0.5 – 1Hz for the ½ scale pipe. RMS of void fraction fluctuation showed similar behaviour in the three pipe sizes. They all peaked within the moderate slug flow regime (cap bubbly in the largest scale pipe) and dropped in churn flow regime.

5. Peak frequencies of force fluctuations showed similar interactions with the gas superficial velocities as was established in the void fraction fluctuation. This behaviour was more prominent for the y-component of force fluctuation. The frequency ranges were also similar to the void fraction fluctuation frequencies. The RMS of force fluctuation in the three pipe sizes increased as gas superficial velocity increased except for the gas superficial velocity of 5m/s in the ½ scale and 1.0 scale pipes in which RMS of force fluctuation dropped. This velocity represents an important transition region between slug and churn flow where liquid slugs could no longer bridge the pipe cross-section and this behaviour appears to be more pronounced in large pipes. Generally, RMS of force fluctuation were a little above one-order of magnitude higher in the 1.0 scale pipe compared to the ¼ scale pipe. In addition, RMS of force fluctuations were up to four times higher in the ½ scale pipe compared to the ¼ scale pipe. Typical bounding limits of both x-component and y-component RMS values of the force fluctuations were 20 – 500N, 5 – 70N and 1 – 20N for the 1.0, ½ and ¼ scale pipes respectively.

6. A very good match of RMS of resultant force fluctuations with Riverin et al. (2006) correlation was obtained for the ¼ scale pipe where the constant C is assigned its original value of 10. However, when the larger pipe sizes were considered, the correlation using 10 as the value of C could not predict the non-dimensional RMS of forces well. A more satisfactory prediction was obtained by assigning C the value of 20.

7. The resultant force fluctuation RMS in the ¼ scale pipe was 2.5 – 25N for gas superficial velocity range of 0.5 – 9.04m/s and constant liquid superficial velocity of 0.642m/s. The corresponding maximum amplitude of equivalent stress fluctuation was 15000 – 200000Pa for the same pipe geometry. Using these values as references, observations in structural stress response to force fluctuation showed that as the resultant force fluctuation RMS in the ¼ scale pipe increased by up to 1500% - 3000% in the pipe of 1.0 scale, the maximum amplitude of equivalent stress fluctuation increased by 500% - 2000%. On the other hand, the resultant force fluctuation RMS increased by a range of 200% – 600% in the ½ scale pipe corresponding to a maximum amplitude of equivalent stress response of 300% – 550%.

8. Maximum pipe displacements due to vibration were up to 0.0015m, 0.0002m and 0.00001m in the 0.2032m, 0.1016m and 0.0525m I.D. respectively. In addition, the first three natural frequencies corresponding to the first three mode shapes of vibration increased as gas volumetric fraction at pipe inlet increased. This effect was more significant in the ¼ scale pipe.

9. For pipes of similar geometry and the same internal multiphase flow conditions within slug-churn flow regimes, risk of resonance increased with pipe scale when matched with the first three natural frequencies of the pipe structure.

This study has shown that the characteristics of MFIV in 0.0525m (2in) pipes differ from pipes of 0.1016m (4in) and 0.2032m (8in) I.D. corresponding to non-dimensional hydraulic diameters of 19.2, 37.2 and 74.5. Based on the

current findings, laboratory-scale test results and numerical results obtained using 2in pipes can easily be scaled up using high fidelity factors obtained in this study to predict the RMS of force fluctuation and maximum amplitude of equivalent stress fluctuation in 8in industrial scale pipes. Also, the slug/churn behaviours in the intermediary pipe size (4in) is more irregular and doesn't correlate very well with the 2in pipe. Hence extra caution and more investigation is recommended to characterise the irregular behaviours of pipes having non-dimensional hydraulic diameters of $18.5 < D_H^* < 40$.

In conclusion, the findings and MFIV assessment approach developed in this study can directly contribute to the development of industry pipeline integrity guidelines for predicting and assessing the risk of MFIV in new and existing rigid pipework with bends.

- The presented systematic approach can be incorporated in a guideline to show how identifying the prevailing flow regime and implementing the appropriate CFD modelling approach combined with analytical calculations could be used to accurately predict forces due to multiphase flow at bends for industrial scale pipes. This will provide cost effective method of pipeline integrity assessment compared to experimentation.
- The data on frequencies, magnitude and RMS of the flow induced forces and stresses generated in the present study could be referred to during initial integrity assessment of multiphase flow pipes with bends (I.5 R/D) having I.D. of $2in \leq D \leq 8in$ to estimate the likelihood of failure (LOF) and the risk of resonance and fatigue before deciding to invest in detailed assessment
- The values that have been reported here as the scale of the RMS of force fluctuation between the 0.0525m and 0.2032m pipes can be implemented in practical cases to scale up lab experiments which have been conducted to solve a site specific MFIV problem in a pipework of up to 0.2032 I.D.
- Finally, since this study compared results across lab-scale to real-life scale pipes sizes, the generated data makes a significant addition to the body of data in literature and JIPs findings that could be used to develop a more robust model/correlation for predicting frequencies, maximum

magnitude and RMS of the flow induced excitation forces, stresses and displacements in pipes.

8.2 Recommendation for further work

The present study has rigorously addressed the objectives that were defined in the first chapter of this thesis. However, more work needs to be done to completely solve the problem of MFIV in oil and gas flow lines both onshore and subsea. A complete solution will also be applicable to flow induced vibration in chemical and nuclear energy power plants. The following are the areas of future work proposed by this study:

- The accuracy of VOF decreases where the interface lengths of the smaller entrained bubbles are closer to the computational grid scale. In addition, coalescence due to wake entrainment and random collisions due to bubbles induced turbulence as well as Group 1 bubbles production due to shearing-off from Group 2 bubbles and break-up due to turbulent eddies impact are not accounted for in VOF method. Hence the density of the liquid slugs might have missed the effect of the very small dispersed bubbles. Although force fluctuation frequency due to alternating gas and liquid flow will not be affected, the upper limits of the fluctuation range could be affected. Hence. further work needs to be carried out on the effect of Group 1 bubbles on the flow induced forces due to cap bubbly flow regime in large pipes by comparing results obtained with present VOF model to that obtained by modelling the cap bubbly flow regime with Multifluid-VOF multiphase model.

- The application of DNS and LES turbulence models to the two-phase flow will help to account for the effect of large vortices and secondary flow induced pressure fluctuation and the corresponding induced stress at the separation and re-attachment zone downstream of bend. Such fluctuation has been reported in literature in cases of single-phase flows and the suggested future work will investigate this fluctuation mechanism for two-phase flows.

- The investigation could be extended to multiple bends and for cases where surrounding fluid is water while contained fluid is hydrocarbon to better represent practical subsea flowline scenario.

- Further studies could also focus on optimization of the Riverin et al. (2006) correlation by investigating how different fluid properties and flow properties affect the parameter C and the exponent -0.4 in the correlation.

- Finally, future work could consider the effect of pipe connections and joining methods such as flanges and welds on the stress response of the pipe and failure modes.

REFERENCES

ABDULKADIR, M., AZZI, A., ZHAO, D., LOWNDES, I.S., AZZOPARDI, B.J., 2014. Liquid film thickness behaviour within a large diameter vertical 180° return bend. *Chemical Engineering Science,* 107, pp. 137-148.

ABDULKADIR, M., HERNANDEZ-PEREZ, V., LO, S., LOWNDES, I.S., AZZOPARDI, B.J., 2013. Comparison of experimental and computational fluid dynamics (CFD) studies of slug flow in a vertical 90 bend. *The Journal of Computational Multiphase Flows,* 5(4), pp. 265-281.

ABDULKADIR, M., MBALISIGWE, U.P. ZHAO, D., HERNANDEZ-PEREZ, V., AZZOPARDI, B.J., TAHIR, S., 2019. Characteristics of churn and annular flows in a large diameter vertical riser. *International Journal of Multiphase Flow,* 113, pp. 250-263.

ABDULKADIR, M., ZHAO, D., AZZI, A., LOWNDES, I.S., AZZOPARDI, B.J., 2012. Two-phase air–water flow through a large diameter vertical 180^{o} return bend. *Chemical engineering science,* 79, pp. 138-152.

ABDULKADIR, M., 2011. *Experimental and computational fluid dynamics (CFD) studies of gas-liquid flow in bends* (Doctoral dissertation, University of Nottingham).

ABDULKADIR, M., HERNANDEZ-PEREZ, V., LO, S., LOWNDES, I.S., AZZOPARDI, B.J., 2015. Comparison of experimental and Computational Fluid Dynamics (CFD) studies of slug flow in a vertical riser. *Experimental Thermal and Fluid Science,* 68, pp. 468-483.

ABUALI, B., SMITH, F.J., BROWN, G.W. and PONTAZA, J.P., 2013. Flow-Induced Vibrations of Subsea Piping: A Screening Approach Based on Numerical Simulation. *SPE Offshore Europe Oil and Gas Conference and Exhibition.* Society of Petroleum Engineers.

AN, C. and SU, J., 2015. Dynamic behavior of pipes conveying gas–liquid two-phase flow. *Nuclear Engineering and Design,* 292, pp. 204-212.

ARAUJO, J.D.P., MIRANDA, J.M. and CAMPOS, J.B.L.M., 2015. CFD Study of the Hydrodynamics of Slug Flow Systems: Interaction between Consecutive Taylor Bubbles. *International Journal of Chemical Reactor Engineering,* 13(4), pp. 541-549.

ARNOLD, G.S., DREW, D.A. and LAHEY JR, R.T., 1989. Derivation of constitutive equations for interfacial force and Reynolds stress for a suspension of spheres using ensemble cell averaging. *Chemical Engineering Communications,* 86(1), pp. 43-54.

ASHRAFIZADEH, H., KARIMI, M. and ASHRAFIZADEH, F., 2013. Failure analysis of a high pressure natural gas pipe under split tee by computer simulations and metallurgical assessment. *Engineering Failure Analysis,* 32, pp. 188-201.

BAI, Y., XIE, W., GAO, X., XU, W., 2018. Dynamic analysis of a cantilevered pipe conveying fluid with density variation. *Journal of Fluids and Structures,* 81, pp. 638-655.

BELFROID, S., NENNIE, E., VAN WIJHE, A., PEREBOOM, H. and LEWIS, L., 2016. Multiphase forces on bend structures-overview large scale 6 inches experiments. *11th International Conference on Flow-Induced Vibration, The Hague, Netherlands.*

BELFROID, S., NENNIE, E. and LEWIS, M., 2016. Multiphase forces on bend structures-influence of upstream disturbance. *10th North American Conference on Multiphase Technology.* BHR Group.

BELFROID, S., NENNIE, E. and LEWIS, M., 2016. Multiphase forces on bend structures–critical gas fraction for transition single phase gas to multiphase flow behaviour.

BLEVINS, R.D., 1990. *Flow-induced vibration.* 2nd ed. New York: Van Nostrand Reinhold Co.

BOSSIO, V., BORIS, M., BLANCO, A., ARMANDO, J., CASANOVA, M. and EURO, L., 2014. Numerical modeling of the dynamical interaction between slug flow and vortex induced vibration in horizontal submarine pipelines. *Journal of Offshore Mechanics and Arctic Engineering,* 136(4), pp. 1-5.

BRACKBILL, J.U., KOTHE, D.B. and ZEMACH, C., 1992. A continuum method for modeling surface tension. *Journal of computational physics,* 100(2), pp. 335-354.

BRACKBILL, J.U., KOTHE, D.B. and ZEMACH, C., 1992. A continuum method for modeling surface tension. *Journal of computational physics,* 100(2), pp. 335-354.

BRATLAND, O., 2016. *The flow assurance site.* [online] Thailand: Available from: http://www.drbratland.com/PipeFlow2/chapter1.html [Accessed 01/15 2016].

BÜCKER, C., Jenisch, U., Lutter, S., Matz-Lück, N., Messner, J., Petersen, S., Rüpke, L.H., Schwarz-Schampera, U., Wallmann, K., Berndt, C., 2014. World

Ocean Review 2015: living with the oceans 3. Marine resources-opportunities and risks.

CARGNELUTTI, M.F., BELFROID, S.P.C., SCHIFERLI, W. and VAN OSCH, M., 2010. Multiphase fluid structure interaction in bends and T-joints. *ASME 2010 Pressure Vessels and Piping Division/K-PVP Conference, PVP2010, July 18, 2010 - July 22.* 2010. Bellevue, WA, United states: American Society of Mechanical Engineers. pp. 75-82.

CHUNG, T.J., 2010. *Computational fluid dynamics*. Cambridge university press.

COOPER, P., BURNETT, C. and NASH, I., 2009. Fatigue design of flowline systems with slug flow. *28th International Conference on Ocean, Offshore and Arctic Engineering, OMAE2009, May 31, 2009 - June 5.* 2009. Honolulu, HI, United states: American Society of Mechanical Engineers. pp. 207-212.

DA RIVA, E. and DEL COL, D., 2009. Numerical simulation of churn flow in a vertical pipe. *Chemical Engineering Science,* 64(17), pp. 3753-3765.

DELHAYE, J., 1968. Fundamental equations for two-phase flow. Part 1: general conservation equations. Part 2: complement and remarks; Equations fondamentales des ecoulements diphasiques. Premiere partie: equations generales de conservation. Deuxieme partie: complements et remarques.

DUDLEY, B., 2017. BP statistical review of world energy. *World Petroleum Congress: London.*

EMMERSON, P., LEWIS, M. and BARTON, N., 2016. CFD validation of flow induced forces in 6" piping caused by slugging flow. *11th International Conference on Flow-Induced Vibration, Hague.* 4-6 July 2016.

EMMERSON, P., LEWIS, M. and BARTON, N., 2016. Influence of multiple bends for multiphase flow induced forces in 6" piping: Measurements and CFD analysis. *11th International Conference on Flow-Induced Vibration.* 4-6 July 2016.

EMMERSON, P., LEWIS, M. and BARTON, N., 2015. Improving boundary conditions for multiphase CFD predictions of slug flow induced forces. *17th International Conference on Multiphase Production Technology.* BHR Group.

ENERGY INSTITUTE, 2008. *Guidelines for the avoidance of vibration induced fatigue failure in process pipework.* UK.

EXECUTIVE, S., 2018. *World Energy Outlook.* International Energy Agency.

GABBAI, R.D. and BENAROYA, H., 2004. An overview of modeling and experiments of vortex-induced vibration of circular cylinders. *Journal of Sound and Vibration*. 282 (2005), 575-616.

GAYET, C., N'DIAYE, M. and LINE, A., 2013. Behaviour of slug flow and pressure force induced in a spool: Numerical simulation of a Taylor bubble flowing in a liquid flow through a spool. *16th International Conference on Multiphase Production Technology 2013, June 12, 2013 - June 14.* 2013. Cannes, France: BHR Group Limited. pp. 255-266.

GHARAIBAH, E., BARRI, M. and TUNGEN, R., 2016. Flow Induced Vibration for Design and Operation of Subsea Systems-State of the Art, Limitations and Potential Developments. *Offshore Technology Conference Asia.* Offshore Technology Conference.

HILBER, H.M., HUGHES, T.J. and TAYLOR, R.L., 1977. Improved numerical dissipation for time integration algorithms in structural dynamics. *Earthquake Engineering & Structural Dynamics,* 5(3), pp. 283-292.

HILL, J., 2012. *Managing the integrity threat of subsea pipework fatigue failure.* [online] UK: Xodus Group. Available from: http://www.subseauk.com/documents/xodus%20group%20-%20subsea%20europe%20paris%202011.pdf [Accessed 11/27 2015].

HIRT, C.W. and NICHOLS, B.D., 1981. Volume of fluid (VOF) method for the dynamics of free boundaries. *Journal of computational physics,* 39(1), pp. 201-225.

HUA, C. and PAN, H., 2015. Wet gas flow regime identification based on flow-induced vibration and empirical mode decomposition. *Metallurgical and Mining Industry,* 7(4), pp. 18-26.

HUGHES, T.J., 1987. *The Finite Element Method Linear Static and Dynamic Finite Element Analysis.* New Jersey: Prentice-Hall.

ISAO, K. and MAMORU, I., 1987. Drift flux model for large diameter pipe and new correlation for pool void fraction. *International Journal of Heat and Mass Transfer,* 30(9), pp. 1927-1939.

ISHII, M. and MISHIMA, K., 1984. Two-fluid model and hydrodynamic constitutive relations. *Nuclear Engineering and Design,* 82(2-3), pp. 107-126.

ISHII, M., 1971. Thermally induced flow instabilities in two-phase mixtures in thermal equilibrium *(Doctoral dissertation, Georgia Institute of Technology).*

ISHII, M., 1977. *One-dimensional drift-flux model and constitutive equations for relative motion between phases in various two-phase flow regimes (No. ANL-77-47). Argonne National Lab., Ill.(USA).*

ISHII, M. and HIBIKI, T., 2010. *Thermo-fluid dynamics of two-phase flow.* Springer Science & Business Media.

JAKOBSEN, H.A., 2014. *Chemical reactor modeling.* Springer.

KAICHIRO, M. and ISHII, M., 1984. Flow regime transition criteria for upward two-phase flow in vertical tubes. *International Journal of Heat and Mass Transfer,* 27(5), pp. 723-737.

KIM, J. and SRINIL, N., 2018. 3-D Numerical Simulations of Subsea Jumper Transporting Intermittent Slug Flows. *ASME 2018 37th International Conference on Ocean, Offshore and Arctic Engineering.* American Society of Mechanical Engineers Digital Collection.

KOCAMUSTAFAOGULLARI, G., 1971. *Thermo-fluid dynamics of separated two-phase flow,*

LAUNDER, B.E. and SPALDING, D.B., 1974. The numerical computation of turbulent flows. 3, pp. 269-289.

LIU, Y. et al., 2012. Experimental study of internal two-phase flow induced fluctuating force on a 90 elbow. *Chemical Engineering Science,* 76, pp. 173-187.

LU, Y., LIANG, C., MANZANO-RUIZ, J., JANARDHANAN, K. and PERNG, Y., 2014. FSI analysis of flow-induced vibration in subsea jumper subject to downstream

slug and ocean current. *ASME 2014 33rd International Conference on Ocean, Offshore and Arctic Engineering, OMAE 2014, June 8, 2014 - June 13.* 2014. San Francisco, CA, United states: American Society of Mechanical Engineers (ASME). pp. Ocean, Offshore and Arctic Engineering Division

MEIROVITCH, L., 2001. *Fundamentals of Vibrations.* New York: McGraw-Hill.

MIWA, S., HIBIKI, T. and MORI, M., 2016. Analysis of Flow-Induced Vibration Due to Stratified Wavy Two-Phase Flow. *Journal of Fluids Engineering,* 138(9), pp. 091302.

MIWA, S., MORI, M. and HIBIKI, T., 2015. Two-phase flow induced vibration in piping systems. *Progress in Nuclear Energy,* 78, pp. 270-284.

MONTOYA-HERNANDEZ, D. et al., 2014. Natural frequency analysis of a marine riser considering multiphase internal flow behavior. *Ocean Engineering,* 92, pp. 103-113.

NENNIE, E.D. and BELFROID, S.P.C., 2016. Multiphase forces on bend structures. *9th International Conference on Multiphase Flow.* 22-27 Italy 2016

NENNIE, E., BELFROID, S. and O'MAHONEY, T., 2013. Validation of cfd and simplified models with experimental data for multiphase flow in bends. *ASME 2013 32nd International Conference on Ocean, Offshore and Arctic Engineering.* American Society of Mechanical Engineers Digital Collection.

NENNIE, E., BELFROID, S. and O'MAHONEY, T., 2013. Validation of cfd and simplified models with experimental data for multiphase fluid structure interaction with multiple bends. *8th International Conference on Multiphase Flow, ICMF 2013.* May 26 - 31.

NENNIE, E. and BELFROID, S., 2016. Multiphase forces on bend structures. *ICMF-2016, 9th International Conference on Multiphase Flow, 22–27 May 2016, Firenze, Italy.* TNO.

NEWMARK, N.M., 1959. A method of computation for structural dynamics. *Journal of Engineering Mechanics Division,* 85, pp. 67-94.

NICHOLS, B. and HIRT, C., 1975. Methods for calculating multidimensional, transient free surface flows past bodies. *Proc., 1st Int. Conf. Ship Hydrodynamics.* Naval Ship Research and Development Center, Bethesda, Md. pp. 253-277.

NICKLIN, D. and DAVIDSON, J., 1962. The onset of instability in two-phase slug flow. *Proceedings of the Symposium on Two-phase Fluid.*

OFFSHORE ENERGY TODAY.COM, 2013. *Petrofac launches KW subsea in malaysia.* [online] Available from: http://www.offshoreenergytoday.com/petrofac-launches-kw-subsea-in-malaysia/ [Accessed 02/03 2016].

OHNUKI, A. and AKIMOTO, H., 2000. Experimental study on transition of flow pattern and phase distribution in upward air–water two-phase flow along a large vertical pipe. *International Journal of Multiphase Flow,* 26(3), pp. 367-386.

OUTLOOK, B.E., 2019 edition. *London, United Kingdom2019.*

PAIDOUSSIS, M., 1970. Dynamics of tubular cantilevers conveying fluid. *Journal of Mechanical Engineering Science,* 12(2), pp. 85-103.

PARAMESHWARAN, R., DHULIPALLA, S.J. and YENDLURI, D.R., 2016. Fluid-structure interactions and flow induced vibrations: a review. *Procedia Engineering,* 144, pp. 1286-1293.

PARSI, M., VIEIRA, R., AGRAWAL, M., SRINIVASAN, V., MCLAURY, B., SHIRAZI, S., SCHLEICHER, E. and HAMPEL, U., 2015. Computational Fluid Dynamics (CFD) Simulation of Multiphase Flow and Validating Using Wire Mesh Sensor. *17th International Conference on Multiphase Production Technology.* BHR Group.

PARSI, M. Agrawal, M., Srinivasan, V., Vieira, R.E., Torres, C.F., McLaury, B.S., Shirazi, S.A., Schleicher, E., Hampel, U., 2016. Assessment of a hybrid CFD model for simulation of complex vertical upward gas–liquid churn flow. *Chemical Engineering Research and Design,* 105, pp. 71-84.

PAVLOU, D.G., 2015. *Essentials of the finite element method: for mechanical and structural engineers.* Academic Press.

PETTIGREW, M. and TAYLOR, C., 1994. Two-phase flow-induced vibration: An overview (survey paper). *Journal of Pressure Vessel Technology,* 116(3), pp. 233-253.

PONTAZA, J.P., KREEFT, J.J., ABUALI, B., SMITH, F.J. and BROWN, G.W., 2016. Flow-induced forces in piping due to multiphase flow prediction by CFD. *11th International conference on flow-induced vibration, FIV 2016.* July 4 - 6. Hague.

PONTAZA, J.P., MENON, R.G., OKEREMI, A., SPRITZER, J. and WIDJAJA, S., 2013. Flow-induced vibrations of high gas rate well jumpers: Tees vs. Bends. *ASME 2013 32nd International Conference on Ocean, Offshore and Arctic Engineering, OMAE 2013, June 9, 2013 - June 14.* 2013. Nantes, France:

American Society of Mechanical Engineers. pp. Ocean, Offshore and Arctic Engineering Division.

POPE, S.B., 2001. Turbulent flows*. Cambridge University Press, UK.*

RATKOVICH, N., MAJUMDER, S. and BENTZEN, T.R., 2013. Empirical correlations and CFD simulations of vertical two-phase gas–liquid (Newtonian and non-Newtonian) slug flow compared against experimental data of void fraction. *Chemical Engineering Research and Design,* 91(6), pp. 988-998.

RIVERIN, J., DE LANGRE, E. and PETTIGREW, M., 2006. Fluctuating forces caused by internal two-phase flow on bends and tees. *Journal of Sound and Vibration,* 298(4-5), pp. 1088-1098.

RIVERIN, J.-. and PETTIGREW, M.J., 2007. Vibration excitation forces due to two-phase flow in piping elements. *Journal of Pressure Vessel Technology, Transactions of the ASME,* 129(1), pp. 7-13.

SANCHIS, A., 2014. *Flow-induced vibration assessment of a subsea manifold branch for the Visund Nord field.* 1st International Conference on Flow Assurance - design and operation of multiphase systems, Norway.

SANCHIS, A. and JAKOBSEN, K.G., 2012. Flow-induced vibrations in subsea pipework. *Flow-induced vibration : proceedings of the 10th International Conference on Flow-Induced Vibration (& Flow-Induced Noise) ; FIV 2012, Dublin, Ireland.* 3-6 July 2012.

SCHLEGEL, J.P., SAWANT, P., PARANJAPE, S., OZAR, B., HIBIKI, T., ISHII, M, 2009. Void fraction and flow regime in adiabatic upward two-phase flow in large diameter vertical pipes. *Nuclear Engineering and Design,* 239(12), pp. 2864-2874.

SCHLEGEL, J., HIBIKI, T. and ISHII, M., 2010. Development of a comprehensive set of drift-flux constitutive models for pipes of various hydraulic diameters. *Progress in Nuclear Energy,* 52(7), pp. 666-677.

SHEN, X., SCHLEGEL, J.P., CHEN, S., RASSAME, S; GRIFFITHS, M.J., HIBIKI, T., ISHII, M, 2014. Flow characteristics and void fraction prediction in large diameter pipes. *Frontiers and Progress in Multiphase Flow I.* Springer. pp. 55-103.

SHUKLA, A. and KARKI, H., 2016. Application of robotics in offshore oil and gas industry—A review Part II. *Robotics and Autonomous Systems,* 75, pp. 508-524.

SIEMINSKI, A., 2018. *World Energy Outlook.* International Energy Forum: Kapsarc.

SIEMENS PLM Software, 2017. Introduction to pipeline flow-induced vibration. Siemens Digital Factory Division.

SWINDELL, R., 2013. New methods developed to manage subsea vibration-induced fatigue. *JPT, Journal of Petroleum Technology,* 65(8), pp. 32-35.

TAITEL, Y., BORNEA, D. and DUKLER, A., 1980. Modelling flow pattern transitions for steady upward gas-liquid flow in vertical tubes. *AIChE Journal,* 26(3), pp. 345-354.

TAKAYA, S., FUJISAKI, T. and TANAKA, M., 2017. Numerical Analysis of Flow-Induced Vibration of Large Diameter Pipe With Short Elbow. *ASME 2017 Pressure Vessels and Piping Conference.* American Society of Mechanical Engineers Digital Collection.

TAY, B.L. and THORPE, R.B., 2014. Hydrodynamic forces acting on pipe bends in gas–liquid slug flow. *Chemical Engineering Research and Design,* 92(5), pp. 812-825.

TAY, B.L. and THORPE, R.B., 2004. Effects of liquid physical properties on the forces acting on a pipe bend in gas-liquid slug flow. *Chemical Engineering Research and Design,* 82(3), pp. 344-356.

TER HOFSTEDE, E., KOTTAPALLI, S. and SHAMS, A., 2017. Numerical prediction of flow induced vibrations in nuclear reactor applications. *Nuclear Engineering and Design,* 319, pp. 81-90.

TONG, X., ZHANG, G., WANG, Z., WEN, Z., TIAN, Z., WANG, H., MA, F., WU, Y. 2018. Distribution and potential of global oil and gas resources. *Petroleum Exploration and Development,* 45(4), pp. 779-789.

VERNIER, P. and DELHAYE, J., 1968. General two-phase flow equations applied to the thermohydrodynamics of boiling nuclear reactors. *Energie Primaire,* 4(1), pp. 3-43.

VERSTEEG, H.K. and MALALASEKERA, W., 2007. *An introduction to computational fluid dynamics: the finite volume method.* Pearson education.

WANG, L., YANG, Y., LI, Y., WANG, Y, 2018. Resonance analyses of a pipeline-riser system conveying gas-liquid two-phase flow with flow-pattern evolution. *International Journal of Pressure Vessels and Piping,* 161, pp. 22-32.

WOOD, W., BOSSAK, M. and ZIENKIEWICZ, O., 1980. An alpha modification of Newmark's method. *International Journal for Numerical Methods in Engineering,* 15(10), pp. 1562-1566.

XU, M., XU, S. and GUO, H., 2010. Determination of natural frequencies of fluid-conveying pipes using homotopy perturbation method. *Computers & Mathematics with Applications,* 60(3), pp. 520-527.

YAMANO, H., TANAKA, M., KIMURA, N., OHSHIMA, H., KAMIDE, H. and WAKATABE, O., 2009. Unsteady hydraulic characteristics in large-diameter pipings with elbow for JSFR (1) current status of flow-induced vibration evaluation methodology development for the JSFR pipings. *Proceedings of the 13th International Topical Meeting on Nuclear Reactor Thermal Hydraulics (NURETH-13).*

YAMANO, H., TANAKA, M., KIMURA, N., OHSHIMA, H., KAMIDE, H., WATANABE, O., 2011. Development of flow-induced vibration evaluation methodology for large-diameter piping with elbow in Japan sodium-cooled fast reactor. *Nuclear Engineering and Design,* 241(11), pp. 4464-4475.

YAMANO, H., TANAKA, M., Murakami, T., Iwamoto, Y., Yuki, K., Sago, H., Hayakawa, S., 2011. Unsteady elbow pipe flow to develop a flow-induced vibration evaluation methodology for Japan Sodium-Cooled Fast Reactor. *Journal of Nuclear Science and Technology,* 48(4), pp. 677-687.

YIH, T.S. and GRIFFITH, P., 1968. Unsteady momentum fluxes in two-phase flow and the vibration of nuclear reactor components (No. DSR-70318-58). Massachusetts Inst. of Tech., Cambridge. Engineering Projects Lab.

YI-MIN, H., YONG-SHOU, L., BAO-HUI, L., YAN-JIANG, L., ZHU-FENG, Y., 2010. Natural frequency analysis of fluid conveying pipeline with different boundary conditions. *Nuclear Engineering and Design,* 240(3), pp. 461-467.

YOUNGS, D.L., 1982. Time-dependent multi-material flow with large fluid distortion. *Numerical methods for fluid dynamics.*

ZHANG, D. and PROSPERETTI, A., 1994. Averaged equations for inviscid disperse two-phase flow. *Journal of Fluid Mechanics,* 267, pp. 185-219.

ZHANG, D. and PROSPERETTI, A., 1994. Ensemble phase-averaged equations for bubbly flows. *Physics of Fluids,* 6(9), pp. 2956-2970.

ZHU, H., TANG, Y., WANG, J., TANG, L., 2017. Flow erosion and flow induced vibration of gas well relief line with periodic fluctuation of boosting output. *Journal of Loss Prevention in the Process Industries,* 46, pp. 69-83.

ZHU, H., Wang, J., Ba, B., Wu, Z., Wang, W., 2015. Numerical investigation of flow erosion and flow induced displacement of gas well relief line. *Journal of Loss Prevention in the Process Industries,* 37, pp. 19-32.

ZUBER, N., 1967. *Steady State and Transient Void Fraction in Two Phase Flow Systems: Final Report for the Program of Two-phase Flow Investigation.* Atomic Power Equipment Department, General Electric.

ZUBER, N., 1964. On the dispersed two-phase flow in the laminar flow regime. *Chemical Engineering Science,* 19(11), pp. 897-917.

APPENDIX A: ANSYS MECHANICAL HSFLD242 ELEMENTS CODE FOR MODELLING CONTAINED FLUID

```
fini
/prep7
*get,typemax,ETYP,,NUM,MAX   ! max defined element type
*get,realmax,RCON,,NUM,MAX   ! max defined real constant
*get,mat_max,MAT,,NUM,MAX    ! max defined material
*get,nodemax,NODE,,NUM,MAX ! highest numbered node in model
! Create a new higher number for element type, real, and material
newnode=nodemax+1000 ! number for pressure node for HSFLD242
newnumber=typemax+1
*if,realmax,ge,newnumber,then
newnumber=realmax+1
*endif

*if,mat_max,ge,newnumber,then

newnumber=mat_max+1
*endif

et,newnumber,HSFLD242 ! 3-D Hydrostatic Fluid Element
keyopt,newnumber,1,0 ! UX, UY, UZ, plus HDSP at pressure node
keyopt,newnumber,5,1 ! Fluid mass calculated based on the volume of the fluid
!element
keyopt,newnumber,6,1 ! Incompressible
mp,dens,newnumber,Density value ! Density of fluid, kg/m^3
! Ignoring thermal expansion in this example
! Ignoring TB,FLUID in this example
r,newnumber ! Ignoring Reference pressure for compressible gas
type,newnumber
mat,newnumber
real,newnumber
!
cmsel,s,Inside_Faces ! Select nodes on interior
esln ! Select elements that touch these nodes
n,newnode,Centroid ! Pressure node at Centroid (automatically moved to
centroid?)
ESURF,newnode ! ESURF HSFLD242 elements over solid element faces
! Extra node "newnode" with ESURF with HSFLD242
allsel
fini
/solu ! return to solving
```